



THE UNIVERSITY *of* EDINBURGH

This thesis has been submitted in fulfilment of the requirements for a postgraduate degree (e.g., PhD, MPhil, DClinPsychol) at the University of Edinburgh. Please note the following terms and conditions of use:

This work is protected by copyright and other intellectual property rights, which are retained by the thesis author, unless otherwise stated.

A copy can be downloaded for personal non-commercial research or study, without prior permission or charge.

This thesis cannot be reproduced or quoted extensively from without first obtaining permission in writing from the author.

The content must not be changed in any way or sold commercially in any format or medium without the formal permission of the author.

When referring to this work, full bibliographic details including the author, title, awarding institution and date of the thesis must be given

Utility of Animal Models for Studying the Human Neuromuscular Junction in Health and Disease

Abrar Fawzi Alhindi

A thesis submitted for the degree of
Doctor of Philosophy

The University of Edinburgh
2023

Declaration

- a) That the thesis has been composed by the student, and
- b) Either that the work is the student's own, or, if the student has been a member of a research group, that the student has made a substantial contribution to the work, such contribution being clearly indicated, and
- c) That the work has not been submitted for any other degree or professional qualification except as specified, and
- d) That any included publications are the student's own work, except where indicated throughout the thesis and summarized and clearly identified on the declarations page of the thesis.

Signature

Date

Abstract

The neuromuscular junction (NMJ) is a synapse formed between a lower motor neuron (LMN) and a skeletal muscle fibre. It comprises three major components: a motor nerve terminal, acetylcholine receptors (AChRs) at the motor endplate, and one or more terminal Schwann cells (tSCs). Structural and functional disruption of the NMJ is one of the earliest signs of neurodegeneration in motor neuron diseases (MND) such as amyotrophic lateral sclerosis (ALS), a fatal condition with no effective cure. ALS is characterized by progressive muscle weakness that eventually leads to paralysis and death from respiratory failure. Study of the NMJ is therefore critical to develop an understanding of both the disease process and the development of novel therapeutic interventions. For many decades, research has relied heavily on rodent models to study the NMJ. However, recent studies have revealed fundamental differences between rodents and humans in the cellular and molecular organization of the neuronal and muscular parts of the NMJ, as well as in the response to pathological events and therapeutic agents.

The first aim of this project was to extend our knowledge of human NMJ morphology by presenting the first detailed structural analysis of human tSCs. The findings demonstrated notable morphological differences between mouse and human tSCs. Despite having a similar number of tSCs per NMJ, human tSCs were significantly smaller in size and had more extended cytoplasm compared to murine tSCs. Furthermore, the positioning of the cell bodies relative to the endplate, which has clinical implications, was different between the two species: while mouse tSCs had significantly more synaptic nuclei, human nuclei were more widely distributed. These results provide further evidence for the stark morphological differences between mouse and human NMJs, encouraging the identification of alternative models that better represent the morphology of the human NMJ.

Based on these findings, the second part of the project explored NMJ morphology across several large mammalian species. The NMJs of the cat, dog, sheep, and pig were examined in a range of pelvic limb muscles, and baseline inter-species reference

data were generated. These observations revealed that the morphology of sheep and pig NMJs more closely resembles that of the human NMJ compared with those of mice. As such, sheep and pigs may represent better models for translational work than either mice or rats.

Finally, to emphasize the critical role of the NMJ as an early target in MND, a thorough analysis of NMJ morphology was performed in an ALS mouse model (*Thy1-hTDP-43*). This part of the study aimed to characterize the morphological changes and the time course of denervation along with the differential vulnerability of NMJs in distinct body regions. Morphological assessment of NMJs was performed at three disease stages: pre-symptomatic, early symptomatic and end-stage; and in pelvic limb, cranial, thoracic limb muscles and abdominal muscles. Characteristically, muscle denervation was present in the pelvic limb from an early symptomatic stage. The disease progressed rapidly, and by the end-stage, all pelvic limb muscles showed severe denervation and loss of tSCs. In contrast, cranial muscles were only mildly denervated, whilst thoracic limb and abdominal muscles were remarkably preserved. Pathological features were mainly apparent in the pre-synaptic structures (nerve terminals and tSCs), whereas the post-synaptic structures (endplates and muscle fibres) were relatively unaffected. This comprehensive analysis and time course of NMJ pathology can be built-on to determine the sequence of pathological events occurring at the NMJ in ALS.

Overall, this project significantly deepens our understanding of differences between human NMJs and NMJs in other mammals, particularly mice. These differences must be considered when attempting to translate animal research to the human context. The project also emphasises the necessity of finding an appropriate animal model to accurately replicate the human NMJ in health and disease, encouraging further exploration of sheep and pig for future NMJ studies. And finally, it further emphasises the importance of the NMJ in MND and its early involvement in the pathogenesis of ALS.

Lay summary

The neuromuscular junction (NMJ) is the place for signal transmission to occur between nerve and muscle which is required to initiate movement. It consists of three components: the far end of the nerve, called nerve terminals; the region of the muscle that can detect signals released from the nerve, called acetylcholine receptors; and supporting cells located on top of nerve terminals, called terminal Schwann cells (tSCs). It is known that motor neuron diseases (MNDs) lead to structural and functional disruption of the NMJ. The most common MND in adults is amyotrophic lateral sclerosis (ALS), which is characterized by muscle weakness and paralysis. There is no cure for this disease and death usually occurs within 5 years when the muscles of respiration become affected. Therefore, studying the NMJ is crucial for understanding disease processes and aiding better drug discovery. However, obtaining muscle samples from human patients is technically difficult and raises ethical issues. Therefore, animal models (mainly rodents such as mice and rats) have been commonly used for NMJ research. Importantly, however, recent studies showed remarkable differences in the structure of the NMJs between rodents and humans.

The first part of this project focused on exploring further structural differences between mouse and human NMJs by focussing on tSCs. The presented data represents the first detailed description of human tSCs. It showed that human tSCs were much smaller compared to the mouse, and large parts of their cell structure were found to lie beyond the boundaries of the NMJ. These results provide more evidence for notable differences between mouse and human NMJs and emphasize the need to develop alternative models that may better represent the human NMJ.

In the second part of this project, the structure of NMJs in muscles from a variety of non-rodent animals (cat, dog, sheep, and pig) was studied and compared to those of the human. Of these animals, sheep and pig NMJs were found to have the most similar characteristic features to human NMJs, which makes them potential models to consider for future NMJ studies.

Lastly, to highlight the importance of the NMJ as an early target in MND, an analysis of NMJ pathology was performed in an ALS mouse model across different body regions and at different disease stages. These data showed that NMJ disruption in pelvic limb muscles coincided with the start of symptoms and worsened with disease progression. By the end-stage of disease, all pelvic limb muscles were severely affected, although to variable degrees. In contrast, muscles from the head region showed only mild disruption of NMJ structure, and muscles from the thoracic limbs and the abdomen were remarkably unaffected.

Overall, this project clearly illustrates the differences in NMJ structure between mammals and highlights the importance of finding better animal models for human targeted NMJ research projects. It directs future research towards the use of sheep and pig as models for human NMJs. The project also further confirms the importance of studying NMJs as a key structure involved in early disease processes in ALS.

Acknowledgements

“In the name of ALLAH, the Most Gracious, the Most Merciful”

First and foremost, I would like to thank ALLAH (God) almighty for his help and generosity. For giving me the strength and guidance to keep going and face the challenges and struggles through this long journey. Thank you, ALLAH, for giving me the knowledge and the opportunity to achieve my goal and to be successful in this part of my life. Without your blessings this achievement would not have been possible.

Second, I would like to express my gratitude to my supervisors; Professor Thomas Gillingwater and Dr. Ross Jones. Thank you for giving me the opportunity to be part of your great laboratory team. Thank you for your guidance, kindness, and support at all times. Your invaluable advice, expertise, and positive criticism enabled me to improve myself and to be better in what I do.

I would also like to thank my university in Saudi Arabia; King Abdulaziz University, for funding me and for giving me the opportunity to study abroad. To the head of the anatomy department Dr. Emad Hindi, thank you for your support and help.

To my beloved mother and lovely brothers and sister, the biggest source of my strength. Thank you for your continuous love and support to help me reach this stage in my life. Thank you for your patience towards me being away for years and for encouraging me to follow my dreams and get my PhD. Without your prayers and support I would not have been where I am today and what I am today.

A special thanks to everyone in the Gillingwater laboratory who has been part of my academic journey. To Helena Chaytow and Megan Shand, thank you both for your help in my last project. To Nikky Huang, Rachel James, Dinja Van Der Hoorn, Kiterie Faller, Leire Ledahawsky, Hannah Smith, Anna Motyl, Hannah Crick, Federica Genovese, and Hattie McHale-Owen; thank you all very much for your help and advice, thank you for making working in this group enjoyable.

A special thanks to Ines Boehm who supervised me at the start of my PhD and taught me everything from laboratory work to data analysis. And to Rizwan Farrukh who was

always there for me whenever I need. Thank you for all the support that you gave me during stressful times and for helping me editing some parts of this thesis.

My acknowledgment would be incomplete without thanking my faithful friends and colleagues in Edinburgh. Afnan Abdulmajeed and her lovely kids: Soso and Azoz, and Abeer Alshehri, I am very grateful to have you in my life. Abdulaziz Alomairi, Abdullah Ramadan, Yusif Almajed, Mohammad Alqarni, and Zaid Alturkistani who accompanied me through this journey and provided me with a lot of help, advice, and support. I am very honoured to know all of you.

And of course, to my beloved friends in Saudi Arabia. Weaam Felemban, Abdulaziz Almutairy, and Ghazi Alenezi, although we are miles apart from each other, you were always there for me till the last minute. I cannot thank you enough for your massive support especially during the tough months of thesis writing. Thank you for giving me hope and keeping me think positive all the time. Thank you for your consistent encouragement from the beginning up until the completion of my PhD thesis. Can't wait to get back home to celebrate this achievement together.

Many thanks to my Ph.D. examiners: Dr. Eddie Clutton and Dr. Robin Highley for examining me and providing constructive feedback on my thesis.

Last but not least, as Snoop Dogg said: *"I want to thank me. I want to thank me for believing in me. I want to thank me for doing all this hard work. I want to thank me for having no days off. I want to thank me for never quitting. I want to thank me for trying to do more right than wrong. I want to thank me for just being me at all times".*

To all of us, thanks from all my heart.

Table of Contents

Declaration	3
Abstract	4
Lay summary	6
Acknowledgements	8
Table of Contents	10
Figures	13
Tables	15
Abbreviations	16
Chapter 1: General Introduction	17
<i>The Neuromuscular Junction</i>	17
<i>Morphological differences of the NMJ between species</i>	21
<i>Pathological changes at the NMJ</i>	25
<i>Amyotrophic lateral sclerosis (ALS)</i>	27
Historical perspectives	27
Risk factors and clinical presentation of ALS	28
Pathogenesis of ALS	29
1. The dying-forward hypothesis	30
2. The dying-back hypothesis	31
Mechanisms of NMJ disruption in ALS	37
Impaired axonal transport	37
Mitochondrial dysfunction	38
Mutated proteins	39
Selective vulnerability in ALS	40
<i>Aims of the project</i>	42
<i>Nomenclature and terminology</i>	43
Chapter 2: Morphology of terminal Schwann cells at mouse and human NMJs	44
<i>Introduction</i>	44
<i>Methods</i>	45
<i>Results and discussion</i>	50
1. Validation of tSC labelling at human NMJs	50

3. Murine and human NMJs have similar numbers of tSCs	53
4. Human tSCs are smaller in size, with relatively less synaptic area, but relatively more non-synaptic area	54
5. Humans have lower numbers of synaptic nuclei compared to mice	55
<i>Conclusions</i>	58
Chapter 3: The NMJ morphology of non-rodent mammals	60
<i>Introduction</i>	60
<i>Methods</i>	61
<i>Results and discussion</i>	66
1. NMJ morphology of pelvic limb muscles	66
2. Sheep and pigs have a similar NMJ morphology to humans	69
3. The relationship between size of NMJ, size of muscle fibre and body mass	72
<i>Conclusions</i>	75
Chapter 4: Pathological changes at the NMJ in the Thy-1 hTDP-43 ALS mouse model	76
<i>Introduction</i>	76
<i>Methods</i>	78
<i>Results and discussion</i>	83
1. Clinical phenotype correlated with spinal cord hTDP-43 expression and MN loss	
2. Severe disruption of NMJ morphology in pelvic limb muscles at disease end-stage	87
3. Within-region assessment of NMJ pathology at disease end-stage	93
4. Selective involvement of pre-synaptic structures during NMJ pathology	96
5. Timeline of NMJ denervation in pelvic limb muscles	97
<i>Conclusions</i>	100
Chapter 5: Histological changes in muscle fibres of the Thy-1 hTDP-43 ALS mouse model	101
<i>Introduction</i>	101
<i>Methods</i>	102
<i>Results and discussion</i>	104
1. Gross skeletal muscle atrophy with no regenerative changes in hTDP-43 mice	104
2. Muscle fibre atrophy in the absence of compensatory changes in the pelvic limb muscles of hTDP-43 mice	107

<i>Conclusions</i>	110
Chapter 6: General Discussion	111
<i>Morphological comparison of mouse and human terminal Schwann cells</i>	111
<i>Comparative anatomy of NMJ morphology in larger mammals</i>	113
<i>Pathological characterization of the NMJ and skeletal muscle in the Thy-1 hTDP-43 mouse model</i>	116
<i>Conclusions</i>	121
Appendices	124
Publications	143
References	144

Figures

Figure 1: The structure of the neuromuscular junction (NMJ).	18
Figure 2: Variations of endplate distribution in assorted muscles in cats and ponies	25
Figure 3: Morphological analysis of terminal Schwann cells.	49
Figure 4: Reliability of anti-S100b labelling to identify human tSCs.	50
Figure 5: The distribution of tSCs processes closely match their respective nerve terminals at the human NMJ	51
Figure 6: Similar morphological characteristics of tSCs in PB and RA muscles.	52
Figure 7: Terminal Schwann cells at mouse and human NMJ.	53
Figure 8: Morphological differences between mouse and human tSCs.	55
Figure 9: Different position of nuclei in mouse and human tSCs.	56
Figure 10: AChR area significantly correlates with the morphological variables of tSCs in mice and humans	58
Figure 11: Conservation of NMJ morphology between pelvic limb muscles of non-rodant mammals	67
Figure 12: NMJ morphology is largely conserved between muscles in cats, dogs, sheep, and pigs.	68
Figure 13: Heterogeneity of NMJ morphology between mammals.	69
Figure 14: the sheep and pig NMJ and muscle fibre diameter are the most similar to those of humans.	70
Figure 15: Animal's body mass is not a determining factor of NMJ or muscle fibre size.	73
Figure 16: Correlation of NMJ size with muscle fibre and axon diameter in non-rodant mammals	74
Figure 17: A plateau in body mass gain and a decrease in survival in mice expressing hTDP-43.	84
Figure 18: Progressive increase in hTDP-43 protein expression in the spinal cord of hTDP-43 mice.	84
Figure 19: MN death and mislocalisation of TDP-43 in symptomatic hTDP-43 mice.	86
Figure 20: Regional assessment of NMJ pathology shows severe denervation in pelvic limbs at disease end-stage in WT and hTDP-43 mice.	89
Figure 21: tSC pathology in pelvic limb and cranial muscles of hTDP-43 mice at disease end-stage	92

Figure 22: Selective vulnerability in the pelvic limb and cranial muscles of hTDP-43 mice	95
Figure 23: NMJ denervation at early symptomatic stages in plantaris	98
Figure 24: Progression of pathological changes in the hTDP-43 mouse model.	99
Figure 25: Decreased muscle mass in hTDP-43 mice.	105
Figure 26: No evidence of centrally located nuclei in hTDP-43 muscles.	106
Figure 27: No difference in total muscle fibre count or percentage of slow- to fast-twitch fibres between WT and hTDP-43 mice.	108
Figure 28: Significant muscle fibre atrophy in hTDP-43 mice at disease end-stage.	109

Tables

Table 1: A comparison of the NMJ morphology between frog, mouse, and human	22
Table 2: A reference dataset of mammalian NMJ morphology and muscle fibre diameter	71
Table 3: Selective disruption of the pre-synaptic structures in hTDP-43 mice	97

Abbreviations

AAL: M. adductor auris longus	MN: motor neuron
ACh: acetylcholine	MND: motor neuron disease
AChE: acetylcholinesterase	NMJ: neuromuscular junction
AChR: acetylcholine receptor	NT: nerve terminals
ALS: amyotrophic lateral sclerosis	OCT: optimal cutting temperature
ANOVA: analysis of variance	P: postnatal day
AS: M. Auricularis superior	PB: M. peroneus brevis
BTX: Bungarotoxin	PBS: phosphate-buffered saline
BSA: bovine serum albumin	PCR: polymerase chain reaction
C9orf72: chromosome9 open reading frame 72	PFA: paraformaldehyde
CNS: central nervous system	PL: M. peroneus longus
DAPI: 4',6-diamidino-2-phenylindole	RA: M. rectus abdominis
EDL: M. extensor digitorum longus	sALS: sporadic Amyotrophic lateral sclerosis
EOM: extraocular muscles	SEM: standard error of the mean
fALS: familial Amyotrophic lateral sclerosis	SMA: spinal muscular atrophy
FDB: M. flexor digitorum brevis	SOD1: superoxide dismutase 1
FF: fast fatigue	SOL: M. soleus
FR: fatigue resistant	SV2: Synaptic vesicle glycoprotein 2A
FTD: frontotemporal lobe dementia	TA: M. tibialis anterior
FUS: fused in sarcoma	TARDBP gene: transactivating response element DNA- binding protein gene
GC: M. gastrocnemius	TDP-43: transactivating response element DNA- binding protein 43 kDa.
hTDP-43: human TDP-43	Thy-1: thymocyte differentiation antigen 1
IS: M. interscutularis	tSC: terminal Schwann cell
LALc: M. levator auris longus – caudal	TVA: M. transverses abdominus
LALr: M. levator auris longus – rostral	UMN: upper motor neuron
LMN: lower motor neuron	
mEPP: miniature endplate potential	

Chapter 1: General Introduction

The Neuromuscular Junction

Motor neurons (MNs) are divided into upper and lower motor neurons (UMN and LMN). The cell bodies of UMNs are in the brain and their axons synapse directly or indirectly, through interneurons, onto LMNs in the spinal cord (Sherrington, 1929). The axons of the LMNs project onto skeletal muscles and carry signals to initiate muscle contraction. Each LMN innervates several muscle fibres. Together, these fibres and their innervating LMNs form a single motor unit (Sherrington, 1929).

Innervation takes place at a specialized synapse called the neuromuscular junction (NMJ) where signals carried by axons pass to muscle fibres to initiate contraction (Figure 1). Nerve signals upon reaching nerve terminals cause Ca^{+2} influx which in turn causes the release of hundreds of acetylcholine (ACh) molecules from the synaptic vesicles. ACh travels through the synaptic cleft and binds to the postsynaptic ACh receptors (AChR) located within the motor endplate of the muscle fibre. The binding of ACh onto AChRs causes Na^{+} influx and depolarization of the muscle fibre and triggers an action potential. To end the activation, ACh is catalysed by acetylcholinesterase (AChE) into reusable acetate and choline (il Lee and Thompson, 2012).

The motor axon is supported by two types of Schwann cells: myelinating Schwann cells and non-myelinating terminal Schwann cells (tSCs). Although both cells arise from the same progenitor (loghen *et al.*, 2020), they are functionally different; myelinating Schwann cells are located proximal to nerve terminals and enwrap the MN axon completely (loghen *et al.*, 2020). They are mainly responsible for the production of myelin and the formation of endoneural tubes that guide the axons during regeneration after nerve injury (Faweett and Keynes, 1990). In contrast, tSCs are located at the NMJ, and their processes extend to cover the unmyelinated nerve terminals without enwrapping them, otherwise they would interrupt neurotransmission (Monk, Feltri and Taveggia, 2015). Although they are not necessary for the initial nerve-muscle contact, they are required for NMJ maturation, growth and maintenance (Herrera, Qiang and Ko, 2000).

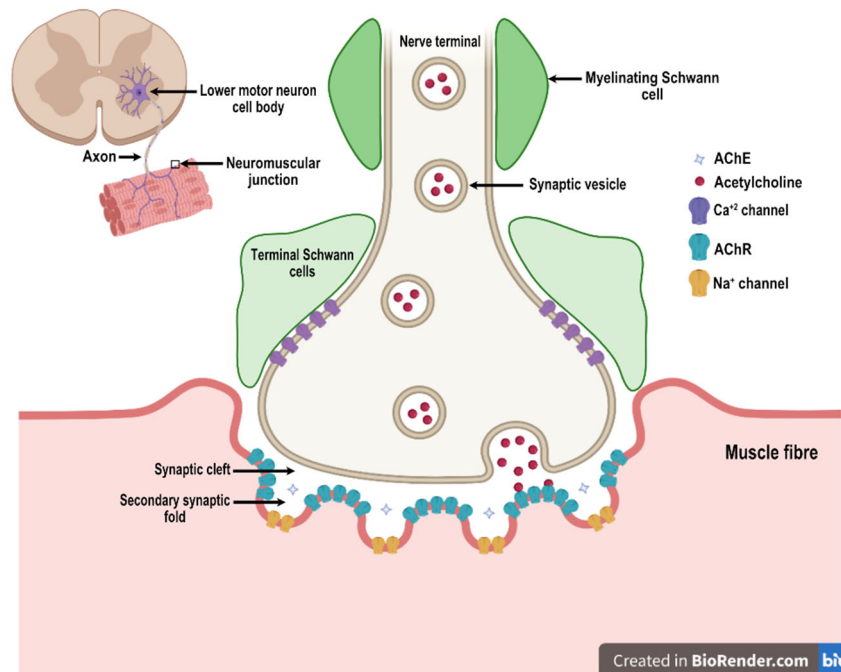


Figure 1: The structure of the neuromuscular junction (NMJ).

A schematic diagram illustrating the general morphology of the NMJ in mammals. The small top left diagram illustrates a single motor unit (motor neuron cell body is not to scale). The large diagram illustrates the main components of the NMJ. The NMJ consists of presynaptic components: nerve terminals capped by terminal Schwann cells (tSCs), and a postsynaptic component: the opposed folded part of the muscle fibre with AChRs clustered at the top of the secondary synaptic folds and sodium channels at the bottom of the folds. The two components are separated by a 100 nm gap (the synaptic cleft) containing acetylcholine esterase (AChE). Nerve terminals contain synaptic vesicles (50 nm vesicles, each filled with 5000 – 10000 acetylcholine molecules). A 10 – 20 nm gap separate nerve terminals from their capping tSCs.

1.1. Terminal Schwann cells at the NMJ

a) Synapse elimination and maturation

Synapse elimination is the term that describes the early post-natal changes in the NMJ morphology that occur as it matures (Brown, Jansen and Van Essen, 1976). In mice, the endplate is transformed from multi-innervated-plaques to mono-innervated pretzel-shaped structures (Marques and Lichtman, 2000; Chung and Barres, 2009). The changes in the endplate architecture are mediated through nerve signals (Marques and Lichtman, 2000), while the transformation from polyneuronal innervation to mononeuronal innervation is mediated through tSCs (Alvarez-Suarez, Gawor and Prószyński, 2020). TSCs contribute to synaptic elimination through: 1) detection and decoding of neuronal activity through their muscarinic AChRs to identify and promote

the strongest competing axon (Todd, Darabid and Robitaille, 2010; Darabid, Arbour and Robitaille, 2013). 2) TSCs eliminate the weakest axons by sending invasive processes that either penetrate and degrade them, or extend underneath and physically separate them from the endplate (Smith *et al.*, 2013). 3) Finally, tSCs have the ability to engulf the degraded axonal remnants (Bishop *et al.*, 2004; Smith *et al.*, 2013).

In addition to their roles in synaptic elimination, tSCs contribute to NMJ maturation through several tSC-derived factors (Escher *et al.*, 2005). For instance, neuregulin 1 (NRG1) which is released by nerve terminals and tSC, binds to the post-synaptic ErbB receptors (receptor tyrosine kinase) and increases the levels of the post-synaptic proteins: rapsyn, MUSK, and AChR (Lin *et al.*, 2000; Escher *et al.*, 2005) Another factor that is expressed by tSCs is the transforming growth factor- β 1 (TGF β 1), which induces synaptogenesis and the expression of agrin by nerve terminals (Feng and Ko, 2008). Agrin activates the postsynaptic lipoprotein receptor-related protein 4 and muscle-specific receptor tyrosine kinase (Lrp4-MuSK). The activation of this complex promotes AChR clustering and post-synaptic maturation (DeChiara *et al.*, 1996; Glass *et al.*, 1996; Yang *et al.*, 2001).

b) Synaptic growth and maintenance

In the frog, during development, tSCs send sprouts that extend beyond the synapse, along the same muscle fibre and to newly formed fibres. These sprouts form pathways for nerve terminals to grow leading to the enlargement of the NMJ to adult size, and to the formation of NMJs on the newly developed muscle fibres (Herrera, Qiang and Ko, 2000).

TSCs play a critical role in NMJ stabilization. Studies on mice and frogs showed that selective ablation of tSCs leads to nerve terminal retraction and MN degeneration (Reddy *et al.*, 2003; Halstead *et al.*, 2005). Nerve terminal retraction occurs due to a lack of serpins (Gould *et al.*, 2019). Thrombin, which is released from muscle fibres after muscle contraction (Coughlin, 2000), is a known axonal destabilizer and causes denervation (Turgeon *et al.*, 1998). A recent study has found that the serpins secreted by tSCs inhibit muscle-released thrombin and therefore stabilize nerve terminals and maintain NMJ health (Gould *et al.*, 2019).

c) Re-innervation after nerve injury

After denervation, tSCs immediately cover the vacant synapse and form sprouts to the neighbouring innervated NMJs (Reynolds and Woolf, 1992; Kang *et al.*, 2007, 2014). These sprouts serve as tracks to guide neuronal processes from the innervated NMJs to the denervated ones (Herrera, Qiang and Ko, 2000; Kang, Tian and Thompson, 2019). The newly formed branching pattern of nerve terminals is determined by the distribution of tSCs processes. Sites that were not initially covered by tSCs do not get reinnervated, resulting in synaptic remodelling (Kang *et al.*, 2014; Kang, Tian and Thompson, 2019).

1.2. Methods for studying tSCs at the NMJ in mammals.

Although research has made great progress in the understanding of the functional properties of tSCs, the lack of a specific protein marker for tSCs in mammals has hindered the advancement of our knowledge of molecular mechanisms underlying their various functions. The majority of tSC studies on mammals have been performed using an antibody against the Ca⁺² binding protein S100b (Brockes, Fields and Raff, 1979). This antibody is, however, a non-specific marker that labels all types of Schwann cells i.e., immature Schwann cells, pro-myelin Schwann cells, myelinating Schwann cells, and non-myelinating Schwann cells (Liu *et al.*, 2015). Recently, Castro *et al.*, found that neuron-glia antigen 2 (NG2) is expressed by tSCs, but not by the myelinating Schwann cells. Thus, anti-NG2 and anti-S100b can be used in combination to selectively label tSCs in mouse (Castro *et al.*, 2020).

Other less commonly used tSCs protein markers include LNX-1, which is only expressed by tSCs at early developmental stages (Young *et al.*, 2005), TrkC proteins and the sodium channel Nav 1.6, which are also expressed by the myelinating Schwann cells and nodes of Ranvier, respectively (Musarella *et al.*, 2006; Hess *et al.*, 2007), and the low-affinity nerve growth factor receptor (p75) which is upregulated in tSCs during nerve injury (Hassan *et al.*, 1994).

A more advanced technique for studying tSC in mammals is sequential photobleaching (fading) (Brill, Marinković and Misgeld, 2013). In transgenic mice expressing enhanced green fluorescent protein (EGFP) driven by the mouse myelin proteolipid protein (PLP) gene promoter, using a confocal microscope, a single tSC could be photobleached by applying the maximum laser power to the centre of its

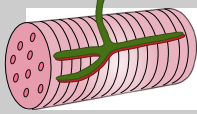
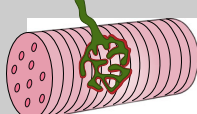
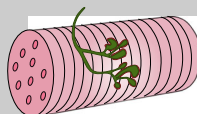
nucleus for a few second. The morphology of the bleached tSC is then reconstructed by image subtraction (Brill, Marinković and Misgeld, 2013). Although this method allows the visualization of a single tSC, it is limited by using explanted muscles which are utilized for a maximum of 3-6 hours. Another consideration when using this method is that when a tSC is photo-bleached nearby tSCs expand to occupy the vacated territory, which could affect the overall interpretation of results (Brill *et al.*, 2011).

Finally, the electron microscope has been widely used for decades to study the morphological changes of tSCs (Desaki and Uehara, 1981). The most significant advantage of using the electron microscope is its ability to visualize tSC processes intruding into the synaptic cleft. This has been observed during synaptic elimination (Smith *et al.*, 2013), ageing (Wokke *et al.*, 1990), and neuromuscular disorders (Bruneteau *et al.*, 2015). Unlike mammalian tSCs, amphibian tSCs can be specifically labelled using either peanut agglutinin (PNA) or monoclonal antibody 2A12 which labels the extracellular matrix around tSCs and the cell surface, respectively (Ko, 1987; Astrow, Qiang and Ko, 1998).

Morphological differences of the NMJ between species

The structure and function of NMJs has been extensively studied in vertebrates and invertebrates (Sanes and Lichtman, 1999; Wood and Slater, 2001; il Lee and Thompson, 2012; Slater, 2015) with the assumption that human NMJs will exhibit the same features as other, lower, mammals. However, several studies have shown a huge difference in NMJ morphology between humans and other species (Wood and Slater, 2001; Slater, 2008; Jones *et al.*, 2017) (Table 1). Additionally, many of the NMJ-targeted therapeutic modalities that showed promise in mouse disease models, such as amyotrophic lateral sclerosis (ALS), did not translate well to humans (Mitsumoto, Brooks and Silani, 2014; Tosolini and Sleight, 2017), indicating that the mouse NMJ might not be the best representative of the human NMJ in health and disease. One possible solution is the use of large mammals, such as the cat, dog, sheep, pig, and horse.

Table 1: A comparison of the NMJ morphology between frog, mouse, and human

	Frog NMJ	Mouse NMJ	Human NMJ
Schematic diagram			
Axon and Nerve terminals (NT)	1-3 axons (due to incomplete synaptic elimination or continues remodelling/growth) ¹⁹ . NTs (30-200 μm long, 0.8-2.3 μm wide) ³ .	One axon (3 μm in diameter), complex NTs, with 65% overlap between NT and AChR ² .	One axon (<1 μm in diameter). NTs are less complex than in mouse, with 50% overlap between NT and AChR ² .
Endplate morphology	Long strands that run parallel to the muscle fibre (1000 - 1200 μm^2 and twice the width of NTs) ^{1, 18} .	678 μm^2 , compact, smaller than frog NMJ. Pretzel – shaped endplate, consists of 2.6 AChR clusters ² .	351 μm^2 , compact, half the size of mouse NMJ. Nummular – shaped endplate, consists of 3.9 AChR clusters ² .
Post-synaptic folds	Increase the surface area by twofold ⁷ .	Increase the surface by area fourfold ⁷ .	Highly folded, increase the surface area by eightfold ⁷ .
Quanta per impulse	200 ACh per impulse ⁷	50 – 75 ACh per impulse ⁷	20 ACh per impulse ⁷
Terminal Schwann cell (tSC)	Enwrap NTs and form interdigitations between active zones to allow the release of ACh ³ .	Lie on top of NTs and form a 10 – 20 nm gap that does not contain basal lamina ^{4,5} .	Lie on top of NTs ^{4,6} .
Synapse elimination	Takes up to 4-6 months. The process slows with age and could persist until adulthood ^{8,19} .	Occurs during the first 2 post-natal weeks, with changes from plaque to pretzel-shape endplate ⁹ .	Occurs from 16 th – 25 th week of development with no evidence of changes in endplate shape ¹⁰ .
Age-related degenerative changes	Accumulation of abandoned gutters and increase in NMJ size and complexity ²⁰ .	Occur from the age of 12 – 36 months. The following structural changes were observed in limb muscles: denervation, poly-innervation, endplate	Increase endplate length, fragmentation and intrusion of tSC processes into the synaptic cleft were observed in intercostal muscles ^{14,15} .

		fragmentation (increased number of AChR clusters), decrease AChR density, axonal thinning, sprouting and preterminal swellings ^{12,13} .	Others did not observe changes (intercostal, posterior cricoarytenoid, laryngeal, and lower limb muscles ^{2,15-17}).
Muscle fibre diameter	<i>Sartorius</i> : 25-90 µm, correlates with endplate size ^{1,19} .	<i>Limb muscles</i> : 40 µm, no correlation with NMJ variables ² .	<i>Limb muscles</i> : 60 µm, correlates with most of NMJ size variables ² .
¹ (Kuno, Turkanis and Weakly, 1971), ² (Jones, 2017), ³ (Pawson, Grinnell and Wolowske, 1998), ⁴ (Griffin and Thompson, 2008) ⁵ (Fuertes-Alvarez and Izeta, 2021), ⁶ (Bruneteau et al., 2015), ⁷ (Slater, 2008) ⁸ (Letinsky and Morrison-Graham, 1980), ⁹ (Marques and Lichtman, 2000), ¹⁰ (Hesselmans et al., 1993), ¹² (Valdez et al., 2010), ¹³ (Valdez et al., 2012), ¹⁴ (Oda, 1984), ¹⁵ (Wokke et al., 1990), ¹⁶ (Gambino, Malmgren and Gacek, 1990), ¹⁷ (Périé, St Guily and Sebille, 1999), ¹⁸ (Desaki and Uehara, 1981), ¹⁹ (Herrera and Werle, 1990), ²⁰ (Jans, Salzmann and Wernig, 1986).			

A group of researchers have recently quantitatively analysed the morphological features of the pony NMJ in *M. tibialis cranialis*, *M. extensor digitorum longus* (EDL), and *M. soleus* (SOL) (Cahalan, Perkins, et al., 2022). Qualitative assessment of the NMJ morphology revealed *en plaque* terminals (plate or pretzel shape terminals) in *M. tibialis cranialis* and EDL, and *en grappe* terminals (grape-like or spherical clustered terminals) in SOL (Cahalan, Perkins, et al., 2022). Quantitative assessment of the morphological variables revealed remarkable inter-muscular heterogeneity; SOL had significantly smaller NMJs, with less complex nerve terminals, and smaller muscle fibre diameter than both *M. tibialis cranialis* and EDL (Cahalan, Perkins, et al., 2022). Similar to the human NMJ, the pony has fragmented, nummular-shaped endplates (coin-shaped). Nonetheless, the overall size of pony NMJs and axon diameter were larger than that of the human (Cahalan, Boehm, et al., 2022).

Whilst NMJ morphology in other mammals, such as cat, dog, sheep, and pig, has not been thoroughly characterized before now (Boehm, Alhindi, et al., 2020), several studies have investigated the topographical distribution of NMJs in different large mammals (Figure 2). *Tensor tympani* and *stapedius* in cat and dog (Mascarello et al., 1982), SOL in rabbit and monkey (Paul, 2001) and *M. sternomastoideus* in monkeys (Paul, 2001) are focally innervated (one endplate per fibre) with a single band of endplate running across the entire muscle (Figure 2D). The distribution of the endplates is more complex in the multipennate (multiple tendons) *M. flexor carpi*

radialis in the cat. *M. Flexor carpi radialis* is composed of short fibres that run from origin to insertion. It is divided into four compartments based on the attachment and direction of muscle fibres (Galvas and Gonyea, 1980). This muscle is focally innervated, but each compartment has a distinct endplate band with different orientations depending on the direction of their muscle fibres (Figure 2A). In other muscles, such as the dorsal neck muscles in cat (*M. splenius*, *M. biventer cervicis*, and *M. complexus*) (Richmond and Abrahams, 1975), the long pelvic limb muscles in the cat (*M. tenuissimus*, *M. sartorius*, and *M. semitendinosus*) (Loeb *et al.*, 1987), the *diaphragm* in cats and dogs (Gordon *et al.*, 1989; Boriek, Miller and Rodarte, 1998), and equine pelvic limb muscles (*M. tibialis cranialis*, EDL, and SOL) (Cahalan, Perkins, *et al.*, 2022), fibres do not run all the way from origin to insertion. Instead, they run in a series of short fibres along the muscle. Therefore, the endplate bands are distributed throughout the entire length of the muscle, at regular intervals. Due to this architecture, muscles appear to be multi-innervated (more than one endplate per muscle fibre) despite being focally innervated (a single endplate per muscle fibre) (Figures 2B, C). Several muscles in different species contain fibres that are truly multi-innervated, making them more resistance to degeneration, such as the extraocular muscles (EOMs) in cats and dogs (Mascarello *et al.*, 1982; Dimitrova *et al.*, 2009), *M. sternomastoidus* in rabbits (Paul, 2001), *M. semitendinosus* and *M. gracilis* in rabbits and monkeys (Paul, 2001), and *M. sternocephalicus* in horses (Zenker, Snobl and Boetschi, 1990) (Figure 2E).

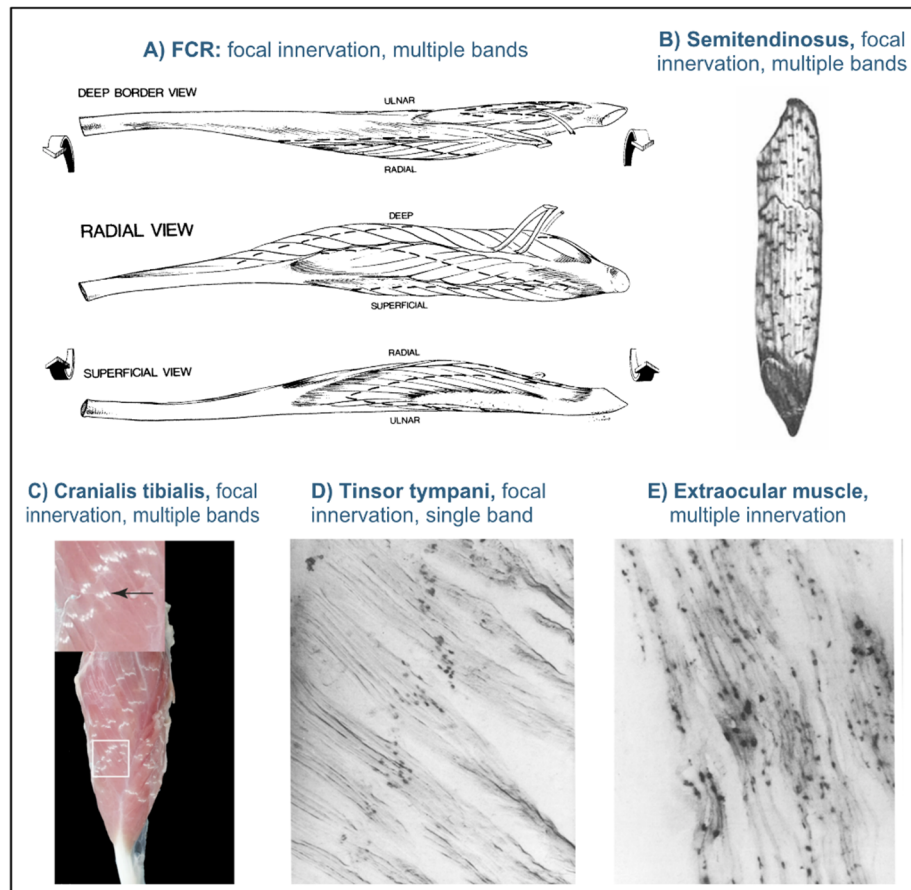


Figure 2: Variations of endplate distribution in assorted muscles in cats and ponies

A) A schematic diagram illustrating the four compartments of *M. flexor carpi radialis* in the cat. Each compartment has a distinct endplate band (dotted lines) with different orientation based on the orientation of muscle fibres (*adapted from: Galvas and Gonyea, 1980*). **B)** The *semitendinosus* in cat (*adapted from: Loeb and Chanaud, 1987*) and **C)** The *tibialis cranialis* muscle in pony (*adapted from: Cahalan et al., 2022*) is comprised of a series of short fibres that are focally innervated but appear to be multi-innervated because of the muscle fibre arrangement. **D)** *Tensor tympani* in cat shows the classic location of endplates: a single band across the middle part of the muscle, **(E)** the *lateral rectus* (an extraocular muscle) in cat contains multi-innervated fibres (*D, E adapted from: (Mascarello et al., 1982)*).

Pathological changes at the NMJ

NMJ's are highly dynamic structures; continuous remodelling occurs throughout their lifespan starting with synaptic elimination and maturation (Marques and Lichtman, 2000), to growth (Herrera, Qiang and Ko, 2000), and ageing (Valdez *et al.*, 2012). External factors such as exercise and training can also induce functional and structural

changes in the pre- and post-synaptic structures of the NMJ (Deschenes *et al.*, 2016; Deschenes, 2019). In addition, the NMJ has been identified as a pathological target in many neuromuscular diseases, including myasthenia gravis (Albuquerque *et al.*, 1976), Charcot-Marie-Tooth disease (Cipriani *et al.*, 2018), and motor neuron diseases (MND) (Murray, Talbot and Gillingwater, 2010).

Myasthenia Gravis is an autoimmune disease caused by an antibody-mediated neurotransmission block. It primarily affects the extra-ocular muscles and causes fatigable muscle weakness that worsens during the day and improves upon rest (Vincent, 2002). Morphological NMJ changes have been observed in patients including decreased AChR density, degeneration of the post-synaptic folds and nerve terminals, and the invasion of the synaptic cleft by leukocytes (Albuquerque *et al.*, 1976).

Another example of neuromuscular disease that compromises the function and alters the structure of the NMJ is Charcot-Marie-Tooth disease (Spaulding *et al.*, 2016; Cipriani *et al.*, 2018), which is the most common inherited neuromuscular disorder in human (Saporta, 2014). It is caused by peripheral nerve demyelination which leads to reduced nerve conduction velocity. Patients present with progressive muscle weakness that starts in the distal lower limbs before affecting the upper ones (Ruskamo *et al.*, 2017). Mouse models have shown severe NMJ denervation with an increase in nerve terminal complexity and endplate fragmentation, a decrease in overlap percentage between nerve terminals and AChRs, and the formation of axonal sprouts (Ang *et al.*, 2010; Cipriani *et al.*, 2018).

Motor neuron disease (MND) constitutes a group of disorders characterized by progressive muscle weakness caused by upper and/or lower MN death, including amyotrophic lateral sclerosis (ALS; affects both upper and lower MNs), primary lateral sclerosis (affects only UMNs), progressive muscular atrophy (affects only LMNs), and spinal muscular atrophy (SMA; affects the LMNs in children) (Talbot, 2009).

The morphological changes of NMJ in SMA are suggestive of a developmental delay pathology such as the presence of small, non-perforated endplates, and lack of nerve terminal arborization (Kariya *et al.*, 2008; Harding *et al.*, 2015), nerve terminal sprouting (Murray *et al.*, 2010), denervation and accumulation of neurofilaments in the

MN axon (Murray *et al.*, 2008), and loss of tSCs and endplate coverage with a significant reduction of the secondary folds and synaptic vesicles (Lee *et al.*, 2011; Murray *et al.*, 2013).

Amyotrophic lateral sclerosis (ALS)

Amyotrophic lateral sclerosis (ALS) also known as *Charcot's disease* or *Lou Gehrig's disease*, is the most common acquired MND in adults (Tiryaki and Horak, 2014). In the presence of a family history, the mean age of onset is 46 years, and without a known family history, the mean age of onset is 56 years (Tiryaki and Horak, 2014). ALS is characterized by the degeneration of both upper and lower MNs. UMN degeneration produces muscle spasticity and hyper-reflexia, while LMN degeneration causes progressive muscle weakness and atrophy, leading eventually to severe paralysis (Rowland, 2001). It starts with a focal onset, i.e., one body region, e.g. right leg, that spreads with disease progression to involve most skeletal muscles, including respiratory muscles, leading to respiratory failure and death within 3-5 years (Brown and Al-Chalabi, 2017).

Historical perspectives

Jean-Martin Charcot (1825 – 1893) who the disease is named after, was the first to explain the basic pathology and distinguish it from other progressive muscle weakness disorders (Rowland, 2001). Although many scientists have contributed to our understanding of the disease, arguably the greatest achievements were based on his observations using anatomical-clinical methods on a case series of 20 patients (a life-long follow-up of patients, linking the neurological signs to structural neuroanatomical lesions and histological findings after death) (Katz, Dimachkie and Barohn, 2015). His first observation was the degeneration of the lateral column of the spinal cord in a female patient with spastic contracture of the limbs. This patient had no muscle atrophy or loss of sensation, nor urinary incontinence. Four years later, Charcot made his second observation of infantile paralysis and muscle atrophy with anterior horn cell atrophy found at an autopsy. These two observations were the basis for the concept of upper and lower MN lesions. He proposed that the motor system is of two parts; a lateral column from which originates the spasticity, and anterior horn cells which are responsible for muscle atrophy. The third patient, who had both muscle atrophy and

spastic contracture with anterior horn cells lesion and sclerosis of the lateral columns, confirmed his hypothesis. Five years later, in 1874, Charcot described the disease and named it ALS - the term alludes to the involvement of both the grey matter (amyotrophic, referring to muscle atrophy) and the white matter (lateral sclerosis) (Rowland, 2001; Goetz, 2009; Katz, Dimachkie and Barohn, 2015).

Risk factors and clinical presentation of ALS

ALS is an idiopathic disease i.e., the exact cause of MN degeneration is unknown. The majority of ALS cases are caused by a combination of genetic mutations and environmental factors, and only 5-10% of cases are familial (fALS) with an autosomal dominant pattern of inheritance (Wang *et al.*, 2017). An ALS case is considered familial if at least two first- or second-degree relatives have the disease (Ingre *et al.*, 2015). The only established risk factors for ALS are advanced age, with a peak incidence at 70-79 years (Chiò *et al.*, 2001; Huisman *et al.*, 2011), male sex (male to female ratio ranges from 2.5 at younger ages to 1.4 at older ages) (Manjaly *et al.*, 2010), and a family history of ALS (Ingre *et al.*, 2015).

As of 2018, there are over 150 genes that are known to be associated with ALS (Nguyen, Van Broeckhoven and van der Zee, 2018), with *SOD1* (Cu/Zn-binding superoxide dismutase 1), *C9ORF72* (chromosome 9 open reading frame 72), *FUS* (fused in sarcoma) and *TARDBP* (transactivating response element DNA-binding protein gene) being the most commonly mutated genes (Mejzini *et al.*, 2019). The frequency of involved genes varies according to geographical location. In Europe, *C9ORF72* is the most mutated gene (40% in fALS, 7-11% in sALS), followed by *SOD1* (10-20% in fALS, 1-5% in sALS) and *TARDBP* (5% in fALS, 1% in sALS) (Zou *et al.*, 2017), while in Asia, the *SOD1* gene represents 30% of fALS cases, followed by *FUS* (6.4%), *C9ORF72* (2.3%) and *TARDBP* (1.5%) (Zou *et al.*, 2017). Other associated environmental risk factors include smoking (Armon, 2009; Gallo *et al.*, 2009), continuous exposure to pesticides and chemicals such as formaldehyde (Malek *et al.*, 2012; Seals *et al.*, 2017), high levels of physical fitness (Mattsson *et al.*, 2012), and professional sports (Blecher *et al.*, 2019). Other less established factors that require further investigation include a previous history of enteroviral infection (Berger *et al.*, 2000) and a history of autoimmune disease (Turner *et al.*, 2013).

The diagnosis of ALS is purely clinical. A combination of imaging and electrophysiological tests is used to support the diagnosis and exclude the possibility of other differential diagnoses (Ferguson and Elman, 2007). A definite diagnosis of ALS is made when the patient presents with evidence of UMN and LMN lesions in three spinal regions or two spinal regions plus bulbar involvement (impairment of the corticobulbar fibre tract resulting in a dysfunction of speech and swallowing) (Picher-Martel *et al.*, 2016).

Phenotype is highly variable; nonetheless, it is important to identify the phenotype as it helps predict prognosis (Kiernan *et al.*, 2011). The bulbar onset of ALS occurs in 30% of cases and is characterized by facial muscle weakness, dysarthria, tongue fasciculations and slow speech (Logroscino *et al.*, 2010). It is associated with a poorer prognosis than spinal onset ALS due to an earlier involvement of respiratory muscles (Logroscino *et al.*, 2010). Other factors associated with shorter survival include old age, late-onset, malnutrition, smoking and the presence of co-morbidities such as cardiovascular diseases, Parkinson's disease, dementia and depression (Wang *et al.*, 2017).

Although ALS is mainly a motor disease, patients can also develop other non-motor manifestations such as mental impairment, ranging from mild cognitive impairment to frontotemporal lobe dementia, insomnia, depression and subclinical sensory deficits (Choquer *et al.*, 2020).

Pathogenesis of ALS

Charcot, who originally described the disease, proposed that lateral column sclerosis induces the death of anterior horn cells (Katz, Dimachkie and Barohn, 2015), implying that degeneration is trans-neuronal and that LMN degeneration is secondary to cortical neuron pathology. Later, several researchers suggested that upper and lower MN degeneration occur independently. The latter argument is based on the failure of most neuropathological studies to find a correlation between UMN and LMN pathology (Kiernan and HUDSON, 1991; Pamphlett, Kril and Hng, 1995). The lack of correlation in these studies is attributed to the complexity of the human central nervous system - a single LMN soma receives input from several UMNs, and a single UMN cell innervates multiple LMNs (Porter and Lemon, 1995). Thus, it is extremely difficult to correlate upper and lower MN loss. In contrast, more recent studies have favoured the

trans-neuronal degeneration process (Eisen, Kim and Pant, 1992; Chou and Norris, 1993). Nevertheless, there is still much debate as to whether degeneration starts in the UMN and spreads down the LMN (the dying-forward pathogenesis) or starts in the LMN and spreads up to the UMN (the dying-backward pathogenesis).

1. *The dying-forward hypothesis*

In 1990, Eisen re-emphasised Charcot's concept and proposed that ALS is a disease of the corticomotor neurons that causes anterograde degeneration of the LMNs (dying-forward pathology) (Eisen, Kim and Pant, 1992). The degenerative influence of corticomotor neurons on LMNs is mediated through glutamate excitotoxicity (Rothstein *et al.*, 1993; Rosenblum and Trotti, 2017). Glutamate is the most abundant excitatory neurotransmitter in the brain and is secreted by neurons to stimulate the post-synaptic glutamate receptors (Zhou and Danbolt, 2014). To terminate neuronal transmission, glutamate is cleared (via re-uptake) through glutamate transporters that are located on the astrocytes surrounding the synapse (Arriza *et al.*, 1994). Up to 90% of glutamate re-uptake is mediated through the glutamate transporters GLT1 (in rodents) and EAAT2 (in humans) (Lauriat and McInnes, 2007). A defect in these transporters leads to excessive accumulation of glutamate and overstimulation (excitotoxicity) of post-synaptic glutamate receptors (Bristol and Rothstein, 1996; Eisen and Weber, 2001). Glutamate excitotoxicity increases Ca^{+2} influx into the post-synaptic MN which adversely affects mitochondrial function and leads to the formation of reactive oxygen species and subsequent degeneration of MNs (Eisen, Kim and Pant, 1992; Rothstein *et al.*, 1993; Van Den Bosch *et al.*, 2006). Up to 50% reduction in GLT1 transporters has been found in the motor cortex and the spinal cord of SOD1 rodent models (Bruijn *et al.*, 1997; Bendotti *et al.*, 2001; Howland *et al.*, 2002). Elevated plasma and cerebrospinal fluid glutamate levels were reported in ALS patients (Camu, Billiard and Baldy-Moulinier, 1993; Spreux-Varoquaux *et al.*, 2002; Andreadou *et al.*, 2008).

Further evidence supporting the dying-forward hypothesis is the early involvement of muscles with larger cortical representations. For example, in the hand, the thumb muscles (thenar complex) and the fifth finger muscles (hypothenar complex) receive their innervation from the same spinal segment (C8, T1) through the median and ulnar nerves (Standring, Wiseman and Brennan, 2019). However, several studies have found preferential involvement of the thenar muscles in ALS patients. This gives the impression of a "split hand" (Wilbourn and Sweeney, 1994; Wilbourn, 2000; Kim *et al.*,

2015; Fang *et al.*, 2016). As they are required for precise and fine movement, thenar muscles have a larger cortical representation, and so, their LMNs receive more corticospinal input; they are thus more susceptible to glutamate excitotoxicity (Penfield and Boldrey, 1937). Similarly, an assessment of orofacial muscles revealed that tongue muscles, which have a large cortical representation, were more affected than lip and jaw muscles (DePaul and Brooks, 1993; Langmore and Lehman, 1994).

2. The dying-back hypothesis

In contrast, Chou and Norris argued against the dying-forward hypothesis. In 1993, they proposed that ALS is a disease of the LMN with secondary involvement of the UMN (Chou and Norris, 1993). Their argument was based on early histopathological findings observed more commonly in the LMNs than in the UMNs, such as swelling of the initial axonal segment (Carpenter, 1968; Sasaki *et al.*, 1988) caused by an accumulation of neurofilaments (Schmidt *et al.*, 1987; Sobue *et al.*, 1990) and the presence of intracytoplasmic aggregates (Leigh *et al.*, 1988) which leads to intra-axonal and intra-dendritic blockade (Karpati, Carpenter and Durham, 1988). Moreover, A post mortem study results revealed a pronounced loss of LMNs compared to UMNs, indicating that LMN pathology develops earlier in the disease process and is therefore primary rather than secondary (Chou, 1991, 1992).

In general, the “dying-back” hypothesis has received more attention. During the past few decades, several studies have focused on studying the LMN in ALS. These studies found early pathological changes at the NMJ including impaired neurotransmission (Chand *et al.*, 2018), ultrastructural changes (Vinsant *et al.*, 2013b) and morphological disruption and denervation of the NMJ (Frey *et al.*, 2000; Fischer *et al.*, 2004). These changes precede MN loss and symptom onset. These observations suggests that pathology starts at the periphery and progress retrogradely toward the cell body (Gould *et al.*, 2006; Vinsant *et al.*, 2013b; Liu *et al.*, 2015). These findings have been observed in ALS patients (Maselli *et al.*, 1993; Fischer *et al.*, 2004; Clark *et al.*, 2016) and most ALS mouse models including SOD1 (Frey *et al.*, 2000; Fischer *et al.*, 2004; Gould *et al.*, 2006; Martineau *et al.*, 2018), TDP-43 (Walker *et al.*, 2015; Chand *et al.*, 2018), FUS (Sharma *et al.*, 2016; Picchiarelli *et al.*, 2019), and C9orf72 (Riemslogh *et al.*, 2021) mutations.

Furthermore, therapeutic interventions attempting to delay neuronal death have failed to prevent denervation, slow disease progression or improve survival. For instance, although MNs were rescued in the SOD1 mice after *bax* deletion (a key gene involved in apoptosis) there was no significant improvement in muscle denervation or prolongation of the animal's lifespan (Gould *et al.*, 2006). Similarly, sodium valproate, a neuroprotective drug, and inhibition of p38 MAPK (a protein kinase involved in cell death) enhanced MN survival but had no significant effect on disease progression, NMJ disruption or animal survival (Dewil *et al.*, 2007; Rouaux *et al.*, 2007).

The next sections discuss the pathological alterations of the NMJ observed in ALS patients and the most commonly used ALS mouse models (SOD1, C9orf72, FUS, and TDP-43). The selected studies demonstrate that ALS is a distal axonopathy, where axonal withdrawal and NMJ degeneration are the earliest morphological changes and precede MN loss, both of which are in agreement with the dying-back hypothesis of disease progression.

A. NMJ disruption in ALS patients

Early NMJ dysfunction and morphological changes are commonly observed in ALS patients. Impaired neurotransmission has been reported in muscle biopsies (M. anconeus) of patients with disease duration ranging from 6 months – 6 years (Maselli *et al.*, 1993). Electrophysiological assessment of NMJ function showed a significant decrease in mEPP (miniature endplate potential) amplitude and quantal content indicating presynaptic pathology (Maselli *et al.*, 1993). Endplate denervation with preservation of post-synaptic folds was evident in all samples. Normally innervated endplates were occupied by small nerve terminals indicating early degeneration or re-innervation. Pathological muscular changes, including predominance of type 1 fibres, muscle fibre atrophy, and fibre type grouping, were observed in most samples (Maselli *et al.*, 1993).

The first evidence that NMJ pathology precedes MN death in ALS patients came from the post mortem examination of muscles and spinal cord of a patient who died 6 months after onset of progressive muscle weakness (Fischer *et al.*, 2004). Electromyography was performed 2 weeks before death and revealed changes indicative of denervation of upper and lower limb muscles and paraspinal muscles (Fischer *et al.*, 2004). Histological examination of leg and thoracic muscle samples

showed muscle fibre atrophy and fibre type grouping. More importantly, there was no evidence of MN loss at any level of the spinal cord, nor degeneration of the corticospinal tract or motor cortex (Fischer *et al.*, 2004).

Other morphological changes that have been reported in ALS patients include endplate fragmentation (Bjornskov *et al.*, 1975; Bjornskov, Norris and Mower-Kuby, 1984), decreased area of nerve terminals and endplate (Tsujihata *et al.*, 1984), flattening of the synaptic cleft with preservation of the post-synaptic folds (Yoshihara *et al.*, 1998), reduced S100b labelling at tSCs (Liu *et al.*, 2013), extension of tSC cytoplasmic processes into the synaptic cleft (Bruneteau *et al.*, 2015) and decreased numbers of mitochondria at nerve terminals (Tsujihata *et al.*, 1984).

B. NMJ disruption in SOD1 mouse models

The *SOD1* mutation was the first gene to be associated with ALS and was described in 1993 (Rosen *et al.*, 1993). It has been extensively used in research, particularly in the form of the SOD1^{G39A} mouse model, which expresses mutant human SOD1 with glycine to alanine substitution at position 93 (Gurney *et al.*, 1994). SOD1 is a cytosolic enzyme that catalyses reactive free radicals. The mutated gene causes abnormal aggregation of misfolded SOD1 protein in muscles and MNs and a gain of cytotoxic function (Johnston *et al.*, 2000; Turner, Lopes and Cheema, 2003). Over 200 *SOD1* gene mutations have been discovered, as described on the ALS online data website: <https://alsod.ac.uk>, with a remarkable heterogeneity of clinical phenotype between variants (Renton, Chiò and Traynor, 2014). The A4V variant is one of the most aggressive mutations causing death within one year after disease onset (Cudkowicz *et al.*, 1997), in contrast to patients with G37R, G41D, G93C, and D90A mutations who have much longer survival (up to 10 years after disease onset) and are therefore at higher risk of developing cognitive impairment (Andersen *et al.*, 1996; Cudkowicz *et al.*, 1997; Turner *et al.*, 2005). The G37R, L106V, and L38V mutations are associated with a younger age of onset (around 40 years), whereas the I113T mutation is linked to a more advanced age (over 55 years) (Cudkowicz *et al.*, 1997).

NMJ pathology is well characterized in the SOD1^{G39A} mouse model. NMJ changes have been observed as early as day 7 post-partum (P7) with abnormal mitochondria at abnormally rounded nerve terminals (Gould *et al.*, 2006; Vinsant *et al.*, 2013b). Muscle denervation starts at the pre-symptomatic stage (P14 – P30) in fast-twitch

muscles only, while denervation of slow-twitch muscles occurs after the onset of symptoms (Narai *et al.*, 2009). Moreover, some NMJs displayed shorter post-synaptic folds, and nerve terminals showed a reduced number of docked synaptic vesicles and contained mitochondria that were larger in size and fewer in number (Gould *et al.*, 2006; Vinsant *et al.*, 2013b). Although MN loss was not evident at the early stages, there was evidence of pathologies in the spinal cord such as astrogliosis, cytoplasmic vacuoles and swollen mitochondria in the MNs (Fischer *et al.*, 2004; Gould *et al.*, 2006; Vinsant *et al.*, 2013b). TSCs showed variable degrees of pathology; some tSCs were normally labelled but showed displaced nuclei, some NMJs were totally devoid of tSC coverage; while others were only covered by the cytoplasmic processes of the pre-terminal Schwann cells (Liu *et al.*, 2013; Carrasco, Seburn and Pinter, 2016; Harrison and Rafuse, 2020).

C. NMJ disruption in C9orf72 mouse models

The *C9orf72* mutation was identified in 2011 (DeJesus-Hernandez *et al.*, 2011; Renton *et al.*, 2011) and is the most common mutation in European ALS patients (Zou *et al.*, 2017). It is characterized by a massive expansion of the GGGGCC (G₄C₂) repeat in a non-coding region (intron 1) of C9ORF72. While the normal repeat of G₄C₂ is 23 at maximum, ALS patients can carry hundreds to thousands of repeats leading to a loss of function and a toxic gain of function (DeJesus-Hernandez *et al.*, 2011; Renton *et al.*, 2011).

Because of the large discrepancy between models with different expansions/repeats, reported findings on NMJ pathology are not consistent between studies. While O'Rourke *et al.* found no evidence of motor dysfunction, denervation or NMJ structural changes in mice expressing a high copy number of G₄C₂ (O'Rourke *et al.*, 2015), Liu *et al.* reported significant denervation of TA and diaphragm in the C9-500 and C9-500/32 models at the age of 5-7 months (Liu *et al.*, 2016). Similarly, HRE-102 (mice expressing 102 hexanucleotide repeat expansions) showed pronounced NMJ pathology in lumbrical muscles at the age of 12 months, including neurofilament accumulation, blebbing of nerve terminals and reduced density of AChRs (Herranz-Martin *et al.*, 2017). Denervation of EDL, alterations in endplate morphology and disorganized axonal projections were also observed within 4 weeks of doxycycline-induced expansion of 36x G₄C₂ repeats using the hnRNP-rtTA promoter (Riemslogh

et al., 2021). C9-500 and C9-500/32 mice demonstrated significant MN loss (Liu *et al.*, 2016) whereas HRE-102 and 36x G₄C₂ mice showed no change in MN count (Herranz-Martin *et al.*, 2017; Riemsлагh *et al.*, 2021).

D. NMJ disruption in FUS mouse models

Another gene linked to ALS is *FUS* (Kwiatkowski *et al.*, 2009). *FUS* mutations are far less common than other gene mutations (Zou *et al.*, 2017). The *FUS* gene codes for a DNA/RNA binding protein that is involved in splicing, mRNA transport, and microRNA processing (Lagier-Tourenne *et al.*, 2012). It is mainly localized at the nucleus but mutations lead to cytoplasmic mislocalization and aggregation (Kwiatkowski *et al.*, 2009).

NMJ pathology has been recognized in the *FUS*^{ΔNLS} mouse model, in which the nucleus localization signal is removed to transport *FUS* to the cytoplasm (Scekic-Zahirovic *et al.*, 2017). Homozygous mice (*FUS*^{ΔNLS/ΔNLS}) die shortly after birth. Loss of synaptic vesicles, presynaptic mitochondria and postsynaptic folds were evident in pelvic limb muscles at embryonic day (E)18.5 and a significant reduction in the size and number of endplates was found at birth (Scekic-Zahirovic *et al.*, 2017; Picchiarelli *et al.*, 2019). Heterozygous mice (*Fus*^{ΔNLS/+}) showed milder phenotypes and developed motor deficits at age of 10 months (Picchiarelli *et al.*, 2019). Progressive denervation started in TA at the age of 1 month, prior to symptom the onset and MN loss, with a significant reduction in the size, but not in the number, of endplates (Picchiarelli *et al.*, 2019).

In mice overexpressing WT human *FUS* (*hFUS*^{+/+}) presynaptic disruption not only preceded symptom onset but also MN loss (So *et al.*, 2018). A slight, non-significant reduction in mitochondrial number was observed in nerve terminals as early as P6, with some morphological alterations including vacuolation, an abnormal arrangement of cristae and 'onion-ring' membranous structures (So *et al.*, 2018). At P15, MN degeneration became more apparent, with disruption and fragmentation of nerve terminals, dramatic loss of mitochondria and synaptic vesicles and extension of tSC processes into the synaptic cleft. Immunohistochemistry revealed smaller NMJs with loss of synaptophysin labelling (a pre-synaptic marker) indicating NMJ denervation (So *et al.*, 2018). Despite all these degenerative changes at nerve terminals, endplates appeared normal with no structural or ultrastructural changes. MN loss was only

significant at a later stage (P56) (So *et al.*, 2018). Likewise, NMJ denervation and ultrastructural changes at nerve terminals were detected at P20 and P40, while MN loss was not significant until P30 and P60 in the hFUS^{P525L} and hFUS^{R521C} models, respectively (Sharma *et al.*, 2016).

E. NMJ disruption in TDP-43 mouse models

TDP-43 is another DNA/RNA binding protein encoded by the *TARDBP* gene and is mainly localized to the nucleus (Ou *et al.*, 1995). Although ALS-linked mutations of this gene are rare and account for only 1% of fALS cases (Zou *et al.*, 2017), the majority of ALS patients (~97%) have TDP-43 positive cytoplasmic aggregations (Versluys *et al.*, 2022).

The involvement of the NMJ in ALS pathogenesis has been reported in several TDP-43 models. For example, induced cytoplasmic accumulation of TDP-43 in hTDP-43^{ΔNLS} mice led to severe denervation in TA muscle which was reversed in two weeks after restoring nuclear TDP-43 (Walker *et al.*, 2015). Moreover, MN-specific deletion of TDP-43 caused progressive motor impairment at the age of 50 weeks followed by NMJ denervation and grouped muscle fibre atrophy in GC. Although MN loss was not observed, significant MN atrophy of the lumbar region of spinal cord and astrogliosis were found at around 100 weeks of age (Iguchi *et al.*, 2013).

NMJ pathology has also been explored in other models of ALS-linked TDP-43 mutations such as TDP-43^{M337V} and TDP-43^{G298S} (Ebstein, Yagudayeva and Shneider, 2019). Assessment of muscle innervation and MN count in homozygous TDP-43^{M337V} and TDP-43^{G298S} mice showed mild denervation of TA and SOL that was accompanied by astrogliosis and microgliosis in the lumbar segment of the spinal cord. NMJ denervation in the TA was only evident by the age of 1.5 years and 2.5 years in the TDP-43^{G298S} and TDP-43^{M337V}, respectively, and in SOL by the age of 2.5 years in both models. With the exception of one animal that showed the greatest degree of denervation, there was no significant MN loss at any time point (Ebstein, Yagudayeva and Shneider, 2019).

The TDP-43^{Q331K} mutant model has also been assessed in three published studies and considerable differences have been found. Arnold *et al.* reported onset of symptoms at the age of 3 months and a significant reduction in motor axons and NMJ

number in GC by the age of 10 months (Arnold *et al.*, 2013). In contrast, Chand *et al.* reported motor deficits and loss of MNs by the age of 10 months, which was preceded by impaired neurotransmission in EDL and the presence of poly-innervated endplates in TA at 3 months (Chand *et al.*, 2018). In contrast to the TDP-43^{Q331K} model, TDP-43^{WTxQ331K} mice exhibited a rapidly progressive disease course where they reached the humane endpoint by the age of 10 weeks. Impaired motor function was detected at 3 weeks and was followed by a significant loss of motor axons at 5 weeks, and a reduction in the AChR area was seen at 8 weeks (Mitchell *et al.*, 2015).

Mechanisms of NMJ disruption in ALS

Studies on human subjects and mouse models have demonstrated that the NMJ is an early target in ALS. Therefore, focusing research on the NMJ and understanding the mechanism of its disruption is crucial for the development of therapeutic approaches aiming to stabilize the synapse. Although the exact mechanism of NMJ degeneration is not well understood, several molecular changes have been observed in mouse models during early disease stages - even before clinical signs are apparent. These observations suggest that such molecular changes are likely to be linked to disease causation rather than represent consequent or subsequent events. These molecular changes include impaired axonal transport (Collard, Côté and Julien, 1995; Williamson and Cleveland, 1999), mitochondrial dysfunction (Verma *et al.*, 2022) and the accumulation of mutated proteins (McGown *et al.*, 2013; Altman *et al.*, 2021).

Impaired axonal transport

Axonal transport is the movement of organelles, proteins and lipids to and from the cell body through the axon. It is a dynamic process - organelles continually move in an anterograde and a retrograde direction. This process is essential for the integrity of the NMJ, - as proteins are almost completely produced at the cell body (and at dendrites, glia and axons (Batista and Hengst, 2016), and are then transported distally (Morfini *et al.*, 2012). Disturbances of axonal transport cause insufficient supply of nutrients/organelles and elimination of waste/degradative products which leads to nerve terminal degeneration in the form of a “dying-back” pathology (Verma *et al.*, 2022). Impaired axonal transport has been implicated in the pathogenesis of several neurodegenerative diseases (Roy *et al.*, 2005; Morfini *et al.*, 2009) including ALS

(Collard, Côté and Julien, 1995; Williamson and Cleveland, 1999), Huntington's disease (Li and Li, 2004) and Alzheimer's disease (LaPointe *et al.*, 2009).

Mitochondria, neurotransmitters, membrane proteins and lipids are moved by fast transport, while metabolic enzymes, neurofilaments and microtubules are moved by slow transport (Morfini *et al.*, 2012). Deficits of both fast and slow axonal transport has been reported as one of the earliest pathological features of ALS (Williamson and Cleveland, 1999; Bilsland *et al.*, 2010). In vivo assessment of axonal transport in the sciatic nerve of SOD1^{G93A} mice revealed progressive impairment of fast retrograde transportation at the pre-symptomatic stage, prior to NMJ denervation and MN loss (Bilsland *et al.*, 2010). Earlier studies have observed swelling of the initial axon and accumulation of neurofilaments, suggesting impaired slow axonal transport (Chou and Norris, 1993; Williamson and Cleveland, 1999). Furthermore, impaired anterograde transport results in mitochondria misdistribution. ALS patients, SOD1, FUS and TDP-43 mice models showed reduced mitochondrial number along the axon and at nerve terminals, and pronounced accumulation at the MN cell body (Tsujihata *et al.*, 1984; De vos *et al.*, 2007; Bilsland *et al.*, 2010; Shan *et al.*, 2010; Vinsant *et al.*, 2013a; Wang *et al.*, 2013; Magrané *et al.*, 2014; So *et al.*, 2018).

Axonal impairment is selective for MNs while sensory neurons are preserved (Bilsland *et al.*, 2010). It is also MN-type specific; in a murine study, fast-fatigue (FF) MNs were affected around P35, leading to accumulation of synaptic vesicles within intramuscular nerve branches and a decrease in their number at the NMJ. Twenty days later, similar pathology was observed in fatigue-resistant (FR) MNs (Pun *et al.*, 2006). The daily application of ciliary neurotrophic factor (an axon-protecting agent) successfully preserved the integrity of axons and NMJs (Pun *et al.*, 2006).

Mitochondrial dysfunction

Nerve terminals are densely populated by mitochondria which are transported from the MN soma by fast axonal transport (Morfini *et al.*, 2012). Mitochondria play key roles in ATP production and Ca⁺² buffering (Barrett, Barrett and David, 2011). Mitochondrial abnormalities and dysfunction have been linked to ALS pathogenesis (Verma *et al.*, 2022) and it has been proposed that mitochondrial damage, caused by increased energy demand and the presence of misfolded and mutant proteins (Siklós

et al., 1996; Pickles *et al.*, 2016; Moller *et al.*, 2017), triggers motor decline in ALS (Kong and Xu, 1998).

In addition to the reduced number of mitochondria at nerve terminals (So *et al.*, 2018) (Magrané *et al.*, 2014), arising from axonal transport defects, morphological mitochondrial abnormalities have also been observed in human patients and mouse models (Siklós *et al.*, 1996; Vinsant *et al.*, 2013b). Both SOD1 and TDP-43 mouse models demonstrated abnormal morphological changes of mitochondria at the pre-symptomatic stage including mega-mitochondria, fragmentation, dilated and disorganized cristae and disturbance of the outer membrane (Kong and Xu, 1998; Vinsant *et al.*, 2013b; Magrané *et al.*, 2014). Similarly, disorganised cristae, large vacuoles, and mitochondrial swelling were the earliest ultrastructural changes observed at the NMJ in hFUS mice (So *et al.*, 2018).

These structural changes were associated with functional mitochondrial impairment. Reduced membrane potential and ATP production were reported in SOD1 mice (Vinsant *et al.*, 2013b), as well as impaired mitophagy as evidenced by reduced expression of mitophagy-related proteins (Rogers *et al.*, 2017). Furthermore, dysfunctional mitochondria lose their ability to sequester Ca^{+2} and form reversible insoluble complexes after nerve stimulation. This leads to increased levels of cytosolic Ca^{+2} and the activation of protease pathways which are detrimental to nerve terminals (Barrett, Barrett and David, 2011).

Mutated proteins

NMJ disruption in ALS is largely attributed to mutant proteins which cause structural and functional impairment at nerve terminals. For instance, the main function of the SOD1 enzyme is the clearance of superoxide radicals. Thus, mutated SOD1 causes neuronal stress and loss of the inhibitory effect of interneurons, which in turn generates stress on the LMN and leads to nerve terminal retraction (McGown *et al.*, 2013). Suppressing the expression of SOD1 in motor neurons of SOD1^{G93A} mice maintained NMJ integrity, prolonged survival times and delayed disease onset (Dirren *et al.*, 2015). Similarly, mutant FUS accumulates at the rough endoplasmic reticulum and causes neuronal stress and loss of cellular proteostasis through altering gene expression associated with ribosomes, mitochondria and proteasomes (Devoy *et al.*, 2017; López-Erauskin *et al.*, 2018). Furthermore, mutated FUS affects

synaptic transmission by downregulating the expression of transporters and ion channels at the NMJ (López-Erauskin *et al.*, 2018).

Mutant TDP-43 also downregulates genes associated with the ubiquitin proteasome pathway which is essential for maintaining cellular homeostasis (Fratta *et al.*, 2018). Moreover, cytoplasmic mislocalization and accumulation of phosphorylated TDP-43 in MN axons and NMJs form ribonucleoprotein condensates which impair mRNA transportation and thus reduce localized protein synthesis in MNs axon and NMJs (Altman *et al.*, 2021). Axonal TDP-43 accumulation affects the local translation of nuclear-encoded mitochondrial proteins, Cox4i1 and ATP5A1 (Altman *et al.*, 2021). As the NMJ is densely packed with mitochondria and relies on their activity and local protein synthesis, disturbed synaptic protein synthesis causes the shortage of local energy that ultimately leads to NMJ denervation (Altman *et al.*, 2021).

Selective vulnerability in ALS

Selective vulnerability, in which particular neuronal populations show greater susceptibility to functional and structural alterations, is a well-known feature of normal ageing (Valdez *et al.*, 2012) and neurodegenerative diseases (Fu, Hardy and Duff, 2018). This feature of selective vulnerability helps clinicians diagnose and differentiate ALS from other neuromuscular disorders. For example, in ALS, distal pelvic limb muscles are the most vulnerable, while in SMA, axial and proximal pelvic and thoracic limb muscles are the most affected (Valdez *et al.*, 2012; Woschitz *et al.*, 2022). The involvement of distal muscles in ALS might be related to impaired axonal transport (Collard, Côté and Julien, 1995; Williamson and Cleveland, 1999); MNs that supply the legs have very long axonal processes that might reach up to one meter in length hence their susceptibility to transport deficit-induced MN degeneration.

The inter-muscular vulnerability has also been reported in the pelvic limb muscles in mice. Several studies provided evidence for the temporal loss of different motor units with disease progression. In general, FF MNs are the most vulnerable and degenerate at the pre-symptomatic stage, followed by the FR motor units which start to degenerate during the symptomatic stage, and finally, the slow motor units which are highly resistant and have higher compensatory ability that only shows mild degeneration at the disease end-stage (Frey *et al.*, 2000; Fischer *et al.*, 2004; Schaefer, Sanes and

Lichtman, 2005; Pun *et al.*, 2006; Hegedus, Putman and Gordon, 2007; Hegedus *et al.*, 2008; Sharma *et al.*, 2016; Ebstein, Yagudayeva and Shneider, 2019).

FF MNs are fast firing, possess a large axonal calibre, and supply more muscle fibres than FR and slow MNs (Nijssen, Comley and Hedlund, 2017). Thus, they have higher metabolic demand, and are, therefore, more prone to oxidative stress and undernourishment in the setting of impaired mitochondria and/or axonal transport (Bradley *et al.*, 1983; Hegedus, Putman and Gordon, 2007). By contrast, slow-twitch muscle fibres, which are supplied by slow MNs, contain more mitochondria and have a greater capacity to compensate for oxidative stress (Pun *et al.*, 2006; Hegedus, Putman and Gordon, 2007; Vinsant *et al.*, 2013b).

Another example that clearly demonstrates inter-muscular vulnerability in ALS is the “split hand” phenomenon, which refers to the preferential involvement of the thenar (thumb) muscles, including the first dorsal interosseous and abductor pollicis brevis muscles, compared to the hypothenar (fifth digit) muscle, abductor digiti minimi (Wilbourn, 2000; Kim *et al.*, 2015; Fang *et al.*, 2016). It has been proposed that differences in the volume of corticospinal projections to LMN account for this phenomenon - as the thenar muscles are required for precise and fine movement, they have a larger cortical representation and receive more corticospinal input than other hand muscles. This makes their LMNs more susceptible to degeneration induced by glutamate cytotoxicity (Bae *et al.*, 2014; Menon, Kiernan and Vucic, 2014).

The oculomotor, trochlear and abducens nuclei, which are located in the brainstem and innervate EOMs, also show marked resistance to degeneration (Nijssen, Comley and Hedlund, 2017). They remain unaffected even at later disease stages allowing patients to use eye movements to communicate with others (Ahmadi *et al.*, 2010; Valdez *et al.*, 2012; Comley *et al.*, 2016). These MNs are unique. Compared with spinal nerves MNs, cranial nerves MNs have a smaller soma with less complex dendrites (Grant *et al.*, 1979; Ulfhake and Kellerth, 1981), higher resting membrane potentials (-60mV as opposed to -70mV for spinal MNs) (Torres-Torrelo *et al.*, 2012; Torres-Torrelo, Torres and Carrascal, 2014) and higher discharge frequency (100-600Hz compared with 100Hz for spinal MNs) (Robinson, 1970). They have less extensive motor units, with innervation ratios of 1:5-13, compared to spinal MN with innervation ratios of 1:300-2000 (Robinson, 1970; Niimi *et al.*, 1979; Brull and Naguib,

2011). It was found that MNs of larger motor unit size are more susceptible to degeneration, particularly the higher order (distal) branches, due to increased energetic overload (Pacelli *et al.*, 2015; Martineau *et al.*, 2018). Additionally, cranial nerve MNs have higher levels of proteasome activity compared to spinal nerves, making them more resistant to proteostasis stress (An *et al.*, 2019).

The EOMs are also unique and have special characteristics that distinguish them from other skeletal muscles. Each EOM consists of two layers: an inner global layer and a thin orbital layer (Mayr, 1971). Some muscle fibres, mainly of the global layer, are multi-innervated, therefore, loss of some MNs might not lead to loss of function (Mayr, 1971). Unlike other skeletal muscles which are focally innervated and express a single isoform in each fibre, the muscle fibre composition of EOMs is highly complex and some fibres co-express multiple myosin isoforms. In addition to the regular myosin heavy chain isoforms expressed in skeletal muscles (I, IIa, and IIb) EOMs express special isoforms such as embryonic, slow tonic, extraocular and cardiac (Wieczorek *et al.*, 1985). However, further investigations are required to determine whether this distinctive composition of EOM fibres contribute to their high level of resistance in MND.

Aims of the project

The stark differences between murine and human NMJs and the failure of most ALS therapies to translate from rodent models to humans have raised several questions regarding the usefulness of the murine NMJ to model the human NMJ, and the validity of the currently used ALS mouse models for studying the disease's pathogenesis and developing novel therapeutic interventions. With the current knowledge of human NMJ morphology, it is still unknown whether the human tSC has morphological features that distinguishes it from the murine equivalent, and whether other mammalian species would exhibit an NMJ morphology that is more representative of the human NMJ. Therefore, the current project aims to answer the following questions:

1. What are the similarities and differences in tSC morphology between mice and humans? (Chapter 2).

2. Would larger mammalian species, i.e., the cat, dog, sheep and pig, be more suitable for studying the human NMJ? (Chapter 3).
3. Would the *Thy1-TDP-43* ALS mouse model provide a better means for understanding: i) the pathological mechanisms of MN degeneration; ii) and selective vulnerability between different muscles in ALS, in order to expedite the development of new therapeutic approaches? (Chapters 4 and 5).

Nomenclature and terminology

Different terminologies are used in research to describe the same structure/condition. This section clarifies some of the terminology used in this thesis in order to avoid any possible misinterpretation.

Animal limbs are known as “thoracic limbs” and “pelvic limbs” which correspond to the upper limbs and lower limbs in humans, respectively. There are some publications that refer to the limbs by the terms “forelimbs and hindlimbs” rather than by their veterinary terms “pelvic and thoracic limbs”. In this thesis, the limbs have been described using veterinary terminology.

The muscles “tibias anterior” which is one of the muscles of the anterior compartment of the leg, and “plantaris” which is one of the superficial muscles located in the posterior compartment of the leg in humans, are known as “tibialis cranial” and “flexor digitorum superficialis” in mice, respectively. However, in this thesis to facilitate comparison with the human and to be consistent with the MND research, the terms “tibias anterior” and “plantaris” were used. Similarly, the term “symptoms” describes the clinical manifestations reported by patients, whereas “clinical signs” is used in veterinary medicine to refer to the manifestations of disease observed in animals. However, the term “symptom” is widely used in the literature when discussing different diseases stages in rodent, e.g., pre-symptomatic stage, early symptomatic stage, ... etc. Therefore, to keep this thesis consistent with the published literature of MND, this thesis used the term “symptoms”.

Chapter 2: Morphology of terminal Schwann cells at mouse and human NMJs

Introduction

Terminal Schwann cells (tSCs) also known as perisynaptic Schwann cells, or teloglia are one of the key components of the NMJ, and are involved in NMJ maturation, synaptic competition, and elimination. They are also essential for the development and maintenance of the NMJ. More importantly, they are involved in cell repair and are required for nerve sprouting and reinnervation following denervation. Consequently, tSCs contribute to the pathogenesis of many neurodegenerative diseases. For example, sprout formation, and invasion of the cytoplasmic processes into the synaptic cleft have been reported in ALS (Winter *et al.*, 2006; Arbour *et al.*, 2015; Bruneteau *et al.*, 2015), with reduction or absence of the S100 labelling and increased sprouting in SMA (Lee *et al.*, 2011; Murray *et al.*, 2013; Neve *et al.*, 2016), full wrapping of nerve terminals and tSC lysis in Miller-Fisher syndrome (Halstead *et al.*, 2005) and lack of sprout formation in Duchenne muscular dystrophy (Personius and Sawyer, 2005).

Most of our understanding of the NMJ comes from studies using rodent models. However, as discussed in the general introduction, there are stark differences between mouse and human NMJs. The murine NMJ is approximately twice the size of the human NMJ and is distinguished by its pretzel-shaped endplate, thick axon, and complex nerve terminals. The human NMJ, on the other hand, is substantially smaller, with a fragmented, nummular-shaped endplate, thin axon, and less complex nerve terminals. Moreover, human NMJ morphology is stable over many decades of life, whereas the mouse NMJ is known for its susceptibility to age-related degeneration or remodelling (Valdez *et al.*, 2010; Jones *et al.*, 2017). As most researchers rely on mice as primary models for the human NMJ and given the importance of tSCs for NMJs in health and disease, it is appropriate to investigate whether the differences observed at the nerve terminals and endplates result in corresponding differences in tSCs.

Study hypothesis:

Based on the current literature, it is expected to observe a huge difference in the morphology of tSC between mouse and human.

Aims of this study:

- To quantify and compare the morphology of human and murine (*Mus musculus*) tSCs.
- To determine whether the size of the NMJ influences the size and/or number of tSCs in mice and humans.

Methods

Ethics - human and animal material

Human tissue samples were obtained in accordance with the appropriate consent and requisite ethical approvals (NHS Lothian REC: 2002/1/22, 2002/R/OST/02; NHS Lothian BioResource: SR719, 15/ES/0094 and SR589, 15/SS/0182). The murine analyses were carried out in accordance with the Animals (Scientific Procedures) Act 1986. Animal work was carried out under the regulations of the Animals (Scientific Procedures) Act 1986 in compliance with the three Rs: “replace” animal models with alternative models, “reduce” the number of animals used in experiments as far as possible and “refine” experiments to minimise suffering for animals and improve animal welfare.

Tissue sampling

Human tissue samples were obtained from a tissue bank curated and managed by the Gillingwater laboratory at the University of Edinburgh. Based on tissue availability *peroneus brevis* (PB) was selected for this study (Jones *et al.*, 2017). Samples were collected from five male patients (mean age = 69.3 years) who underwent above-knee leg amputation for peripheral vascular disease. Within 30 minutes of the procedure, full-length muscle fibres (2-3 cm in length) were dissected from the proximal healthy end of the discarded amputated limb and placed immediately in 4 % paraformaldehyde (PFA, Electron Microscopy Sciences, 15710) for 1 hour, then washed thoroughly with 1x PBS. The health of muscle samples was confirmed grossly by the absence of

necrotic tissue and the presence of spontaneous twitching and back bleeding during dissection. Biopsies of *rectus abdominus* (RA) were collected for inter-muscular comparisons from two healthy, age-matched patients during abdominal surgery (Boehm, Miller, *et al.*, 2020).

Six wild-type mice (C57/BL6J, 3 males and 3 females, 2 months old) were euthanised by an overdose of inhaled isoflurane. PB was dissected from each side and placed in 4 % PFA (Electron Microscopy Sciences, 15710) for 30 minutes, then washed thoroughly with 1x PBS.

Tissue processing and NMJ labelling.

Muscle fibres were micro-dissected into small bundles of 10-15 individual fibres. Connective tissue was removed as much as possible to reduce background staining. Muscle fibres were moved into a 48 well-plates and incubated in the following sequence of solutions (made-up in 1xPBS unless otherwise specified): glycine (Sigma-Aldrich, 410225-50G) for 15 minutes (to decrease tissue auto-fluorescence); then washed for 15 minutes in PBS; α -bungarotoxin conjugated to tetramethyl-rhodamine isothiocyanate (TRITC α -BTX, 2 μ g/ml, BTIU00012, VWR International Ltd.) for 15 minutes to label the AChR, and samples were subsequently processed and kept in the dark (covered by a box) to protect them from photobleaching.

To visualize the pre-synaptic components (neve terminals, axons, and tSCs), samples were incubated in 4 % Triton X-100 (for 90 minutes for permeabilization, from Sigma Aldrich) then placed in a blocking solution of 4 % bovine serum albumin (BSA, from Sigma Aldrich) and 2 % Triton X-100 for 30 minutes. Tissue was then incubated overnight at room temperature with the primary antibodies, all prepared in the same block solution (4% BSA and 2% Triton X-100). To label tSCs, the following antibody were used as required, the ready-to-use rabbit polyclonal anti-S100b IgG (from Dako Omnis); mouse anti-S100b antibody (at 1:100 dilution, ab7852, Abcam); and rabbit monoclonal anti-NG2 IgG (neuron-glia protein 2; at 1:100 dilution, ab255811, Abcam). Samples were also incubated in mouse anti-SV2 IgG and mouse anti-2H3 IgG to label synaptic vesicles and neurofilaments, respectively (both at 1:50 dilution, from Developmental Studies Hybridoma Bank).

Subsequently, samples were washed with 1x PBS for 4 x 20 minutes, then incubated in the corresponding secondary antibodies for 5 hours at room temperature or overnight at 4°C: AlexaFluor-488-conjugated donkey anti-rabbit IgG antibody (1:400, A21206, Life Technologies), AlexaFluor-680-conjugated donkey anti-rabbit IgG antibody (1:400, A10043, Life Technologies), AlexaFluor-488-conjugated donkey anti-mouse IgG antibody (1:400, A21202, Life Technologies), followed by 4 x 20 minutes washes with 1x PBS. Finally, samples were stained with DAPI nucleic acid staining for 15 minutes (1:1000, D1306, Life Technologies) followed by 1x PBS 3 x 10 minutes washes, then mounted on a glass slide in Mowiol (an anti-fading media), and stored at 4°C.

NMJ imaging

A Nikon A1R FLIM confocal laser scanning microscope with 60x/1.4 oil immersion objective. Images were captured at 16-bit pixel, 512 × 512 frame size, with 0.5 - 1 μm Z-stack intervals. Red channel – 561 nm excitation, green channel – 488 nm excitation, and blue channel – 405 nm excitation were used.

Morphological analysis of tSCs

Fiji software (an open-source image processing package based on ImageJ) was used for morphological analysis. The number of tSCs per NMJ was counted manually. Because multiple nuclei exist at the synaptic region, counting tSCs was performed by carefully examining the confocal z-stacks manually above and below the endplate and only counting nuclei (DAPI stained) that co-localized with a cytoplasmic halo (labelled by S100b) over or near the endplate (TRITC α -BTx labelling) (Appendix 1). For the morphological analysis, aNMJ-morph, the semi-automated version of NMJ-morph, was used (Jones *et al.*, 2016; Minty *et al.*, 2020). NMJ-morph is a robust tool that facilitates morphological comparison of NMJs within and between species by generating 21 morphometric variables (Jones *et al.*, 2016). ANMJ-morph is a simple macro that was developed to accelerate the analysis and minimize data transfer errors (Minty *et al.*, 2020). Both tools have been used in several studies to characterize NMJ morphology in different species, in health and in disease (Jones *et al.*, 2017; Cipriani *et al.*, 2018; Genin *et al.*, 2019; Boehm, Miller, *et al.*, 2020; Mech *et al.*, 2020; Sleigh, Mech and Schiavo, 2020; Cahalan, Perkins, *et al.*, 2022).

To gain and validate the required analytical skills, hands-on training was initially undertaken by analysing a set of 120 mouse NMJs (obtained from an existing image bank) using NMJ-morph (Jones *et al.*, 2016) and the results were compared to a reference dataset (Appendix 2). After completion of training, another set of images (465 cat NMJs) was analysed by NMJ-morph and aNMJ-morph (Minty *et al.*, 2020) and the data generated from the two approaches was correlated. Strong correlations were observed across all variables, which established training competence and validated the use of aNMJ-morph as a robust tool for NMJ analysis ($r = 0.7090-0.998$; all $P \leq 0.0001$; Appendix 3).

Subsequently, the workflow of aNMJ-morph was slightly modified to make it suitable for tSC analysis rather than nerve terminals. In addition to tSC number, the following 6 morphological variables were measured: 1) size-related variables: the “total area of tSCs” and “the total perimeter of tSCs”. 2) The relationship of tSCs processes to the endplate: “synaptic area” of tSCs (defined as the area in contact with AChR) with the percentage “coverage” being derived from it, and “non-synaptic area” of tSCs (defined as the extended area beyond the boundaries of AChR) with the percentage “extension” being derived from it. 3) The position of the tSC cell body in relation to the endplate: “synaptic nuclei” was defined by those whose cell body was located over-arching the endplate while “non-synaptic nuclei” were positioned mostly external to the endplate margins. Measurements of the post-synaptic region were also obtained, including AChR area and perimeter, number of AChR clusters and endplate fragmentation (Figure 3).

These parameters were chosen to be measured and analysed because of their clinical significance in MNDs. For instance, the number of tSCs per NMJ could be altered in response to pathology (Love and Thompson, 1998; Snyder-Warwick *et al.*, 2018). Also, tSC coverage is significantly reduced in neurodegenerative diseases (Lee *et al.*, 2011; Liu *et al.*, 2013) while the presence of non-synaptic nuclei is significantly increased (Carrasco, Seburn and Pinter, 2016).

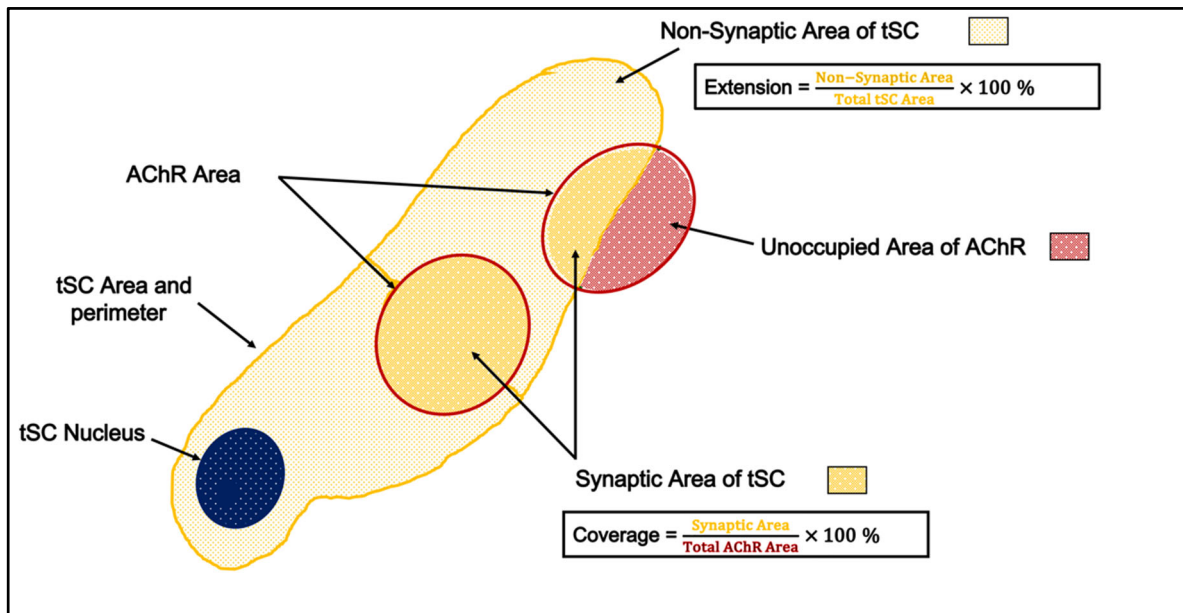


Figure 3: Morphological analysis of terminal Schwann cells.

Schematic diagram illustrating the variables for examined tSC analysis – tSC in yellow, AChRs in red, tSC nucleus in blue. The area of tSCs that is directly overlying AChRs (dark yellow) is defined as the synaptic component of the tSC and was used to calculate % ‘coverage’ of the AChRs by tSC. The area of tSC that extends beyond AChRs (light yellow) is defined as the non-synaptic component of the tSC and was used to calculate % ‘extension’ of the tSC. Other measurements included: tSC number (identified by counting tSC nuclei), total tSC area and perimeter, and unoccupied area of AChR. *Adapted from (Alhindi et al., 2021).*

Statistical analysis

GraphPad Prism Software (Version 8) was used for all statistics. Unpaired t-test was used to compare the continuous variables (total tSCs area and total tSCs perimeter) between the two groups (mice and humans), and Mann–Whitney test was used to compare the non-continuous variables (number of tSCs per NMJ, coverage and extension). To assess the relationship between NMJ morphology and tSC morphology correlation analysis were performed. Pearson’s correlation coefficient (r) was used when both variables are continuous, and Spearman correlation was used when one of the variables is non-continuous. $P < 0.05$ was considered statistically significant.

Results and discussion

1. Validation of tSC labelling at human NMJs

First, to confirm that the use of anti-S100b antibody to label human tSCs revealed the true morphology of the cell, NG2, another tSC marker that co-expresses with the S100b at murine tSCs, was used (Castro *et al.*, 2020). Applying the NG2 marker to human tSCs revealed similar morphology to the S100b marker (Figure 4). However, the strong intensity of the S100b marker made it more reliable for quantitative analysis.

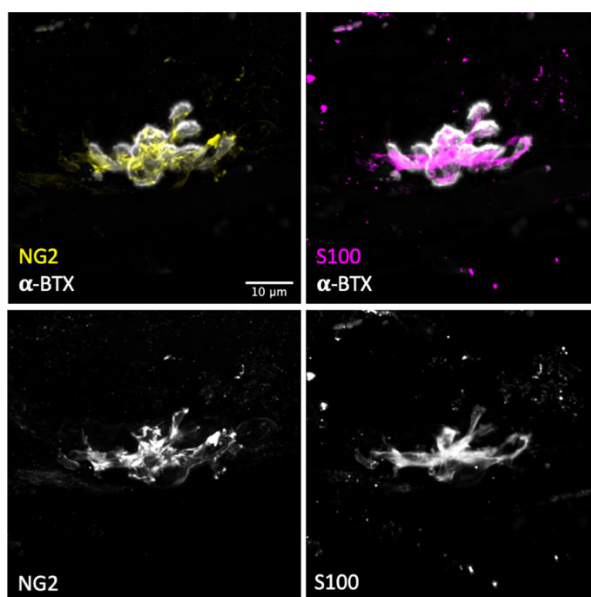


Figure 4: Reliability of anti-S100b labelling to identify human tSCs.

Double immunolabelling with anti NG2 (yellow) and anti-S100b (magenta) antibodies showed co-localization and revealed similar morphology of human tSCs. The use of anti S100b antibody gave more intense and evenly distributed staining. AChRs were labelled with α -BTX (α -bungarotoxin) (grey). The scale bar = 10 μ m. Adapted from (Alhindi *et al.*, 2021).

Secondly, axons and nerve terminals were additionally labelled in all human tissue samples to confirm that their NMJs were healthy and not modified as a consequence of an underlying pathology, and/or sampling techniques. Qualitative analysis showed that all examined NMJs had the typical healthy appearance with no apparent pathological signs such as denervation, nerve terminal sprouting or retraction, or tSC sprouting (Figure 5). Furthermore, tSCs were also examined in samples from the M.

rectus abdominus muscle. Those samples were collected during surgery for abdominal aortic aneurysm from two otherwise healthy, age-matched individuals (Boehm, Miller, *et al.*, 2020). The inspection of 52 RA NMJs revealed similar morphology to that previously identified in samples from PB (Figure 6).

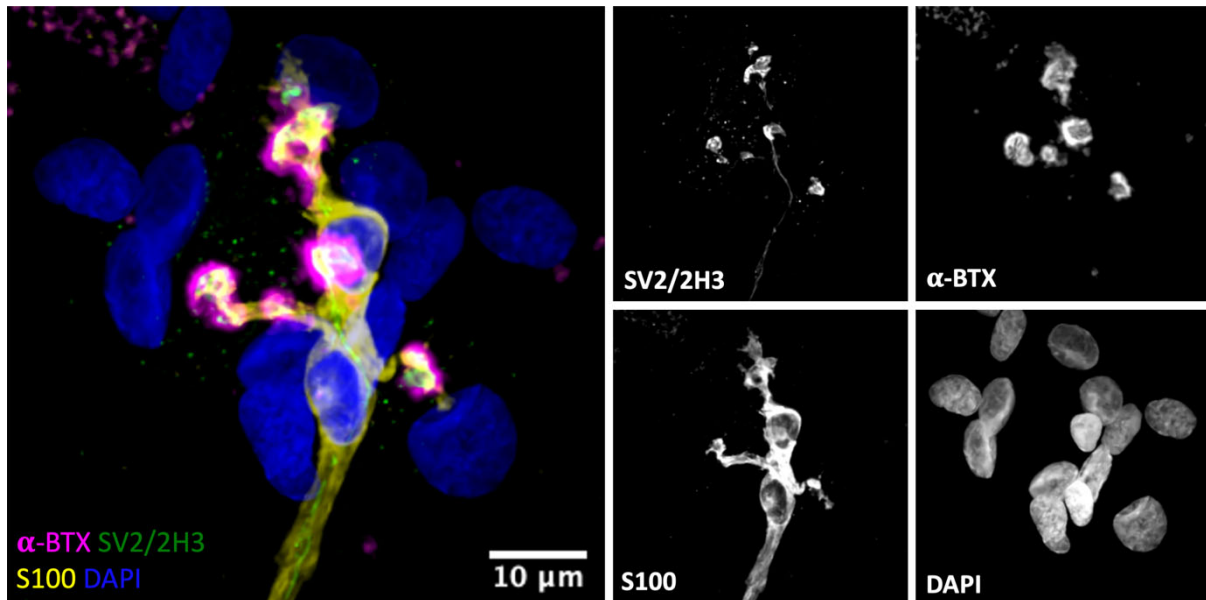


Figure 5: The distribution of tSCs processes closely match their respective nerve terminals at the human NMJ

Terminal Schwann cells (tSCs) were labelled with anti S100b antibody (yellow); AChR were labelled with α -BTX (α -bungarotoxin) (magenta); nerve terminals and axon were labelled with anti SV2 and anti 2H3, respectively; and nuclei were stained with DAPI (blue). The scale bar = 10 μ m. *Adapted from (Alhindi et al., 2021).*

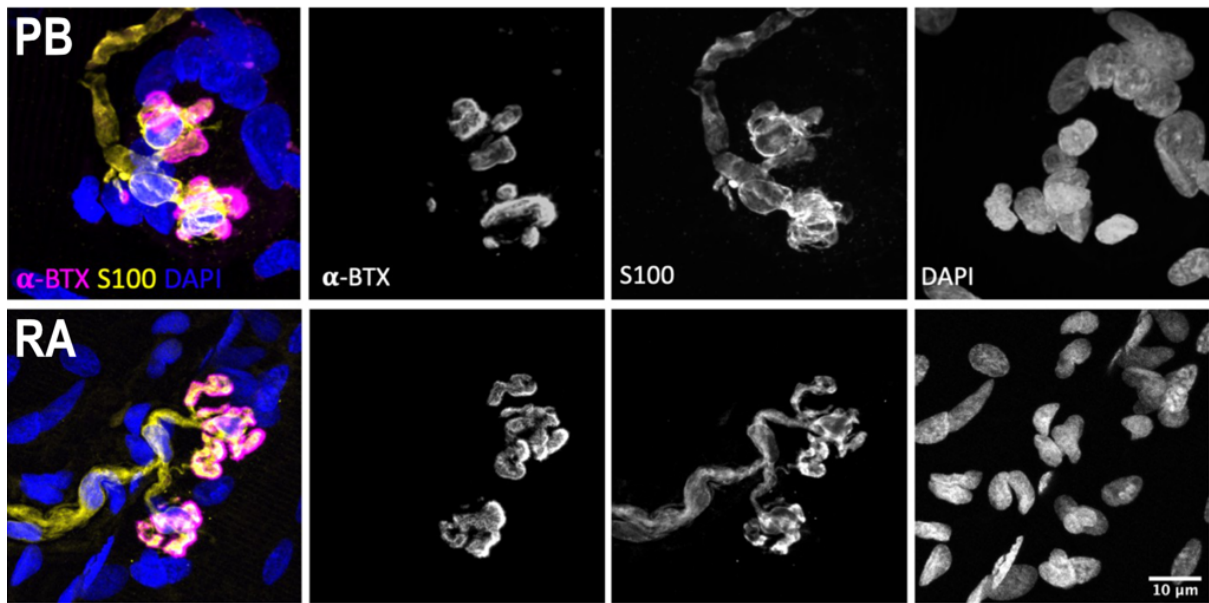


Figure 6: Similar morphological characteristics of tSCs in PB and RA muscles.

Representative confocal micrographs of human tSCs in PB and RA muscles. Terminal Schwann cells (tSCs) were labelled with anti S100b antibody (yellow); AChR were labelled with α -BTX (α -bungarotoxin) (magenta); and nuclei were stained with DAPI (blue). The scale bar is the same in all images = 10 μ m. PB: *peroneus brevis*, RA: *rectus abdominus*. Adapted from (Alhindi et al., 2021).

2. Morphological differences of tSCs between murine and human

All NMJs were covered by the cytoplasmic processes of tSCs and had at least one overlying cell body. In mice, as previously described (O'Malley, Waran and Balice-Gordon, 1999), the cytoplasmic processes were perfectly aligned with AchRs and rarely extended beyond their margins, while in humans, the distribution of cytoplasmic processes rarely matched those of neighbouring AchRs and did not cover the whole synaptic area (Figure 7).

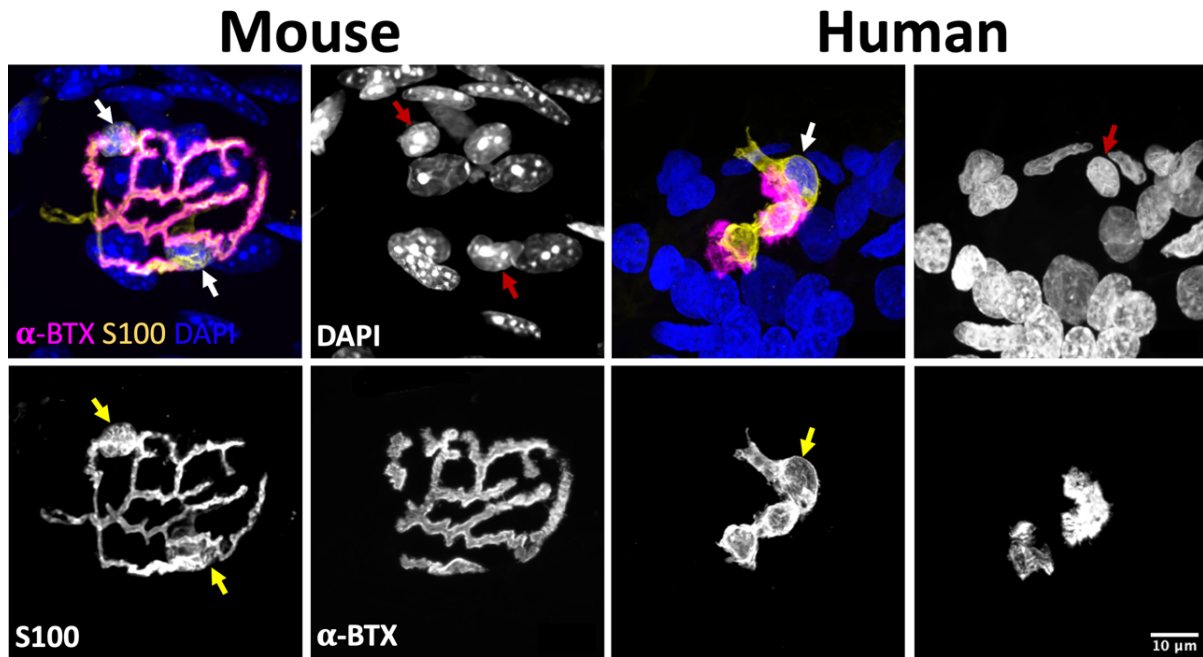


Figure 7: Terminal Schwann cells at mouse and human NMJ.

Representative confocal micrographs of murine and human NMJs showing tSCs (yellow), AchRs (magenta) and nuclei (blue). In murine NMJs, tSC cell bodies are located over the endplate and can be identified by co-localizing the cytoplasmic halo of S100b (yellow arrows) and nuclei (red arrows). Cytoplasmic processes are perfectly matched to AchRs. Human tSCs show peripherally located nuclei and less congruence between cytoplasmic processes and AchRs. Terminal Schwann cells (tSCs) were labelled with anti S100b antibody (yellow); AchRs were labelled with α -BTX (α -bungarotoxin) (magenta); and nuclei were stained with DAPI (blue). The scale bar is the same in all images. *Adapted from (Alhindi et al., 2021).*

3. Murine and human NMJs have similar numbers of tSCs

To gain a deeper understanding of the morphological similarities and differences between mouse and human tSCs, a quantitative analysis was conducted and the number of tSCs per NMJ was counted manually. Given the large difference in size between murine and human NMJs, it was not clear whether similar number of tSCs would be found in both. It was expected that the large mouse NMJ would be supported by more tSCs than the small human NMJ. Unexpectedly, both species showed a similar number of tSCs per NMJ (1-4 tSCs with an average of 1.7 tSCs per NMJ; Figure 8A, Appendix 4). This discrepancy between the size of NMJ and the number of tSCs might suggest that mouse tSCs have more functional capacity to support a larger area of NMJ than human tSCs. Future studies are therefore warranted to investigate

whether there is a maximal area of NMJ that a single tSC can cover, both in mice and in humans.

The number of tSCs at rodents' NMJs is dynamic and is subjected to alterations throughout life and in response to pathology (Love and Thompson, 1998; Snyder-Warwick *et al.*, 2018). Differences might also exist between different mouse strains and muscles. For example, higher numbers have been recorded (2-5 tSCs/NMJ) in M. sternomastoideus of strain-matched mice (C57BL/6J) (O'Malley, Waran and Balice-Gordon, 1999; Snyder-Warwick *et al.*, 2018), as well as in younger mice of a different strain (P13 FVB mice: 3.6 tSCs/NMJ in SOL, and 4.9 tSCs/NMJ in M. sternomastoideus) (Lee *et al.*, 2011).

4. Human tSCs are smaller in size, with relatively less synaptic area, but relatively more non-synaptic area

Despite having a similar number of tSCs per NMJ, human tSCs were significantly smaller (human: $199.15 \mu\text{m}^2 \pm 7.11$ vs. mouse: $258.51 \mu\text{m}^2 \pm 8.48$, $P \leq 0.01$; Figure 8B, Appendix 4). Moreover, the cytoplasmic processes of murine tSCs were more restricted to AchRs; only 28% of the total area extended beyond the boundaries of AchRs compared to more than 50% in human NMJs ($P \leq 0.01$; Figure 8C, Appendix 4). The smaller size and larger proportion of extended cytoplasm in human tSCs resulted in a significant reduction of AChR coverage (human: $54.14 \% \pm 1.06$ vs. mouse: $68.89 \% \pm 0.71$, $P \leq 0.05$; Figure 8D, Appendix 4).

The observed differences in the morphology of tSCs were in accordance with the differences in the overall NMJ morphology between the two species. The small size of human tSCs corresponds with the overall smaller synapse, and the distinctive endplate configuration in each species (the continuous pretzel-shaped mouse endplate vs. the highly fragmented human endplates) might be responsible for the difference in the synaptic and non-synaptic areas (Jones *et al.*, 2017). Also, since tSCs are closely associated with nerve terminals, the difference in AChR coverage matched the difference in the overlap: human NMJs had a 50 % overlap with a 54 % coverage, while murine NMJs had a 64 % overlap with a 69 % coverage (Jones, 2017). As both nerve terminal overlap and tSC coverage are significantly reduced in neurodegenerative diseases (Lee *et al.*, 2011; Liu *et al.*, 2013), a clear understanding

of the normal morphology and the differences between species is imperative to avoid misinterpretation of the results.

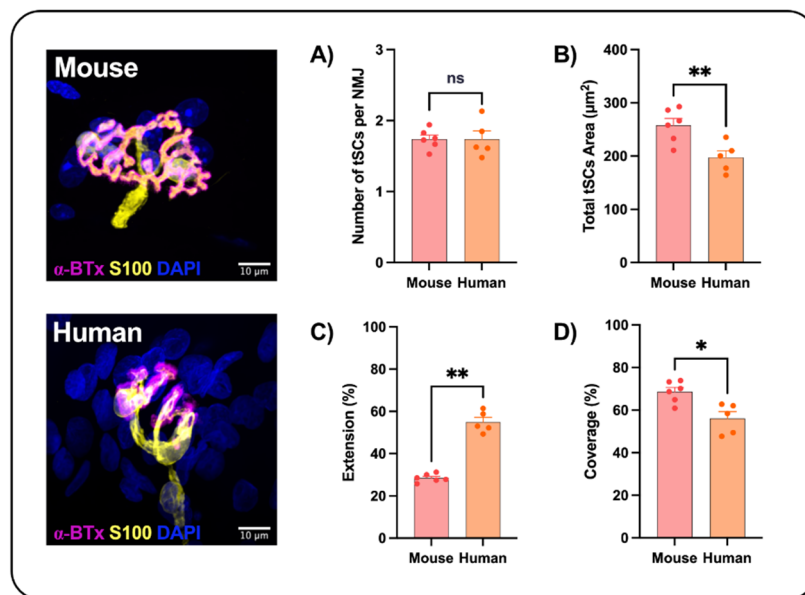


Figure 8: Morphological differences between mouse and human tSCs.

Representative confocal micrographs showing remarkable differences between the morphology of murine and human tSCs. **(A)** Despite having similar numbers of tSCs/NMJ, human and mouse tSCs were significantly different in terms of size and pattern. Human tSCs were significantly smaller **(B)** with less area covering AchRs **(D)** but greater area extending beyond them **(C)**. Bar charts are mean \pm SEM. Each data point represents an individual muscle (human PB; N = 5, murine PB; N = 6; a minimum of 17 NMJs per muscle; in total n = 126 mouse NMJs; n = 151 human NMJs). Unpaired t-test for parametric variables (total tSCs area); Mann–Whitney test for non-parametric variables (number of tSCs per NMJ, extension, coverage). * $P \leq 0.05$, ** $P \leq 0.01$. Terminal Schwann cells (tSCs) were labelled with anti S100b antibody (yellow); AChR were labelled with α -BTX (α -bungarotoxin) (magenta); and nuclei were stained with DAPI (blue). *Adapted from (Alhindi et al., 2021).*

5. Humans have lower numbers of synaptic nuclei compared to mice

Displaced ‘non-synaptic’ nuclei are a pathological feature that has been reported in ALS mice (Carrasco, Seburn and Pinter, 2016). Therefore, the position of nuclei was investigated in both species. Nuclei that were placed within the AChR boundaries were classified as ‘synaptic’ nuclei, while those placed outside the AChR boundaries were classified as ‘non-synaptic’ nuclei (Figure 9A). A significant difference was found between the two species, with mice having a significantly larger proportion of synaptic

nuclei (mouse: 85.9 % \pm 3.9 vs. human: 57 % \pm 5, $P \leq 0.01$; Figure 9B). In line with previous work (Carrasco, Seburn and Pinter, 2016), the majority of mouse tSC nuclei (85.9 %) tend to have a synaptic position (Figure 9C), while in humans, tSCs nuclei tend to be more evenly distributed (synaptic nuclei: 57 % vs. non-synaptic nuclei: 43 %, $P > 0.05$; Figure 9D). The presence of a higher proportion of non-synaptic nuclei in the human is more likely related to the small, fragmented nature of the endplates. The observed distribution of tSCs nuclei in the healthy human tissue samples was similar to that previously reported in ALS mice (Carrasco, Seburn and Pinter, 2016). Therefore, caution must be taken when translating findings from mice to humans.

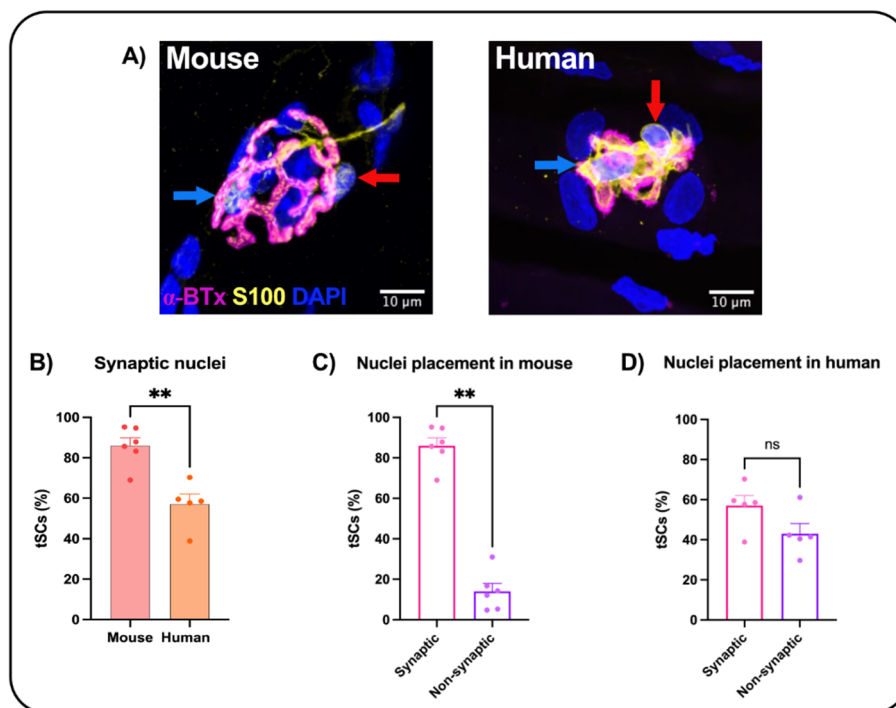


Figure 9: Different position of nuclei in mouse and human tSCs.

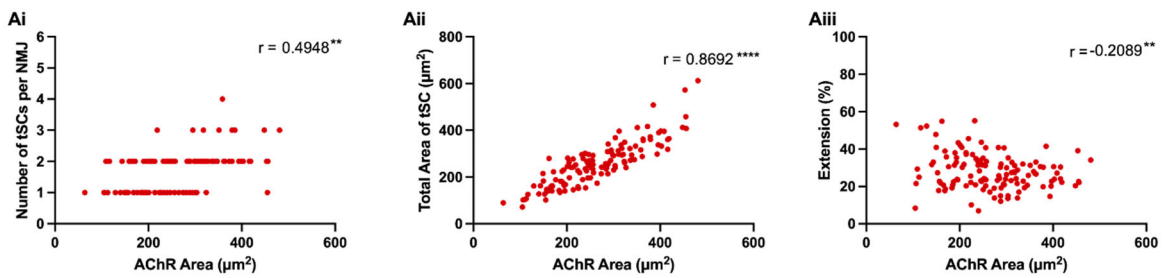
Representative confocal micrographs of mouse and human tSCs illustrating examples of synaptic (blue arrows) and non-synaptic nuclei (red arrows) in both species. B) mouse tSCs have a significantly larger proportion of synaptic nuclei compared to human tSCs. C) While murine tSCs have significantly more synaptic nuclei (>80%), human tSCs have an almost even proportion of synaptic (approximately 60%) and non-synaptic (approximately 40%) nuclei (D). Bar charts are mean \pm SEM; each data point represents an individual muscle; mouse: N = 6; n = 214 tSCs; human: N = 5; n = 247 tSCs. Mann–Whitney test for non-parametric variables. $**P \leq 0.01$. Terminal Schwann cells (tSCs) were labelled with anti S100b antibody (yellow); AChR were labelled with α -BTX (α -bungarotoxin) (magenta); and nuclei were stained with DAPI (blue). The scale bar = 10 μ m. Adapted from (Alhindi et al., 2021).

6. The relationship between NMJ size and tSC morphology

TSCs help in synaptic stabilization and regulating transmission. It is most likely that any increase in NMJ size will require a corresponding increase in tSC area and/or number to adequately cover and support the synapse. Multiple studies have demonstrated that tSCs are highly dynamic in rodents; a small increase in endplate area (by 20%) was accompanied by an increase in tSC area in mice (O'Malley, Waran and Balice-Gordon, 1999). In rats, a significant correlation was found between tSC number and endplate area during development and throughout adulthood (Hirata *et al.*, 1997; Love and Thompson, 1998; Lubischer and Thompson, 1999; Jordan and Williams, 2001).

Thus, to investigate how NMJ morphology (AChR area) influences tSC characteristics in mouse and human endplates, a series of correlation analyses were performed (Figure 10). Whilst the results showed a significant correlation between AChR area and the number of accompanying tSCs in both species, the strength of correlation was lower in humans (mouse: $r = 0.49$, $P \leq 0.01$ vs. human: $r = 0.25$, $P \leq 0.01$; Figure 10 Ai and Bi). A stronger association was found between the area of AChR and tSCs; in both species, an increase in AChR area was accompanied by an increase in tSC area (mouse: $r = 0.87$, $P \leq 0.0001$ vs. human: $r = 0.70$, $P \leq 0.0001$; Figure. 10 Aii and Bii) and a modest decrease in their cytoplasmic extension percentage (mouse: $r = 0.20$, $P \leq 0.01$ vs. human: $r = 0.44$, $P \leq 0.0001$; Figure 10 Aiii and Biii) thus representing more congruence between tSC processes and AchRs. These findings might suggest similarities in the mechanisms regulating the size, but not the number, of tSCs between the two species. Thus, further studies are needed to investigate the mechanisms regulating tSC size and number at murine and human NMJs. Other post-synaptic variables (unoccupied AChR area, number of AChR clusters, and endplates fragmentation) did not show any correlation with tSC number or area in either species (data not shown).

Mouse



Human

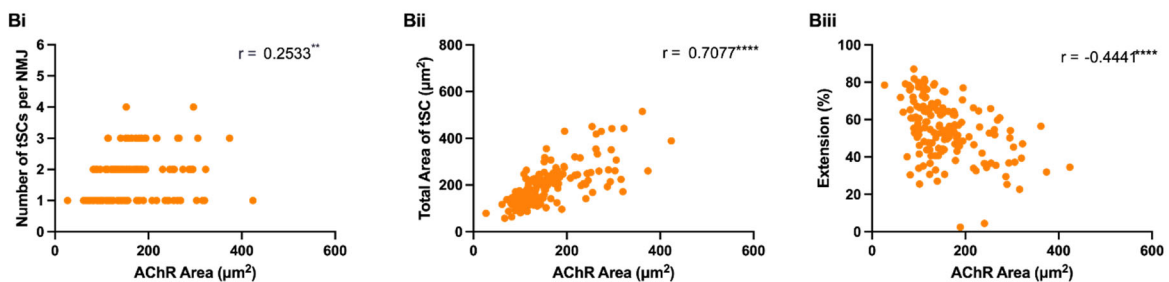


Figure 10: AChR area significantly correlates with the morphological variables of tSCs in mice and humans

The number of tSCs per NMJ showed modest correlation with AChR area in mice (**Bi**) and a weak correlation in humans (**Bi**). However, in both species, increased AChR area strongly correlated with the increase in the total area of tSCs (**Aii**, **Bii**) and a modest reduction in cytoplasmic extension percentage (**Aiii**, **Biii**). Each data point represents a single NMJ and its tSCs ($n = 126$ mouse NMJs; $n = 151$ human NMJs). Spearman correlation coefficients was used to correlate number of tSCs per NMJ (Ai, Bi) and extension percentage (Aiii, Biii) against AChR area, and Pearson's correlation coefficients was used to correlate total area of tSCs against AChR area (Aii, Bii). $^{**}P \leq 0.01$; $^{****}P \leq 0.0001$. Adapted from (Alhindi et al., 2021).

Conclusions

The present study represents, to the best of our knowledge, the first detailed morphological comparison of murine and human tSCs. In line with species differences in NMJ morphology, human tSCs were found to be smaller in size compared to the mouse; other features characteristic of human tSCs included greater cytoplasmic extension, lower AChR coverage, and greater numbers of non-synaptic nuclei. Future studies on tSCs must consider these differences in order to accurately interpret NMJ pathology and translate potentially therapeutic approaches. Therefore, a search for

other mammalian NMJ models that are more representative of the human NMJ is also required.

Chapter 3: The NMJ morphology of non-rodent mammals

Introduction

The use of animal models in NMJ research is commonplace because of the ethical and technical difficulties in acquiring human tissue samples. For example, obtaining pre- and postnatal samples for studying developmental and remodelling changes is challenging. In addition, deeply located muscles in adults, such as the diaphragm, EOMs, and the deeper muscles of the limbs, are extremely difficult to access and sample. Post mortem sampling is also limited by the narrow time window from the time of death until sampling (Jones *et al.*, 2017). Furthermore, studying degenerative changes in pre- and early symptomatic MND patients is not possible due to the difficulty of identifying those at high-risk and the long duration to a confirmed diagnosis (up to 16 months) (Dengler *et al.*, 2005; Kraemer, Buerger and Berlit, 2010). Therefore, the use of transgenic animal models has solved the ethical and practical limitations, and facilitated a wide array of scientific research, including monitoring early pathological changes in multiple diseases to drug development.

Rodents are the most used laboratory animals for studying the NMJ. However, as discussed previously, rodent and human NMJs are remarkably different, reducing the translatability of studies in animal models to human conditions. Therefore, alternative animal models that mimic the human NMJ as accurately as possible are needed. Large mammals, such as the cat, dog, sheep, and pig may be more suitable alternatives so are worth studying. Sheep and pigs are already used in research as a model of Batten's disease, peripheral nerve injuries (Starritt, Kettle and Glasby, 2011; Weber and Pearce, 2013), ALS (Holm, Alstrup and Luo, 2016) and SMA (Duque *et al.*, 2015). However, the morphology of their NMJs has not been fully assessed yet, as well as the morphology of NMJ in cats and dogs. Therefore, the goal of this study is to explore the structural differences in the morphology of NMJ between these species and to identify the one that most resembles the human NMJ.

Aims of this study:

- To generate a reference dataset derived from mammalian NMJs, characterising NMJ morphology in a range of pelvic limb muscles from the cat (*Felis catus*), dog (*Canis familiaris*), sheep (*Ovis aries*), and pig (*Sus scrofa*).
- To identify the animal model that most resembles the human NMJ.
- To investigate factors that might influence the NMJ size in cat, dog, sheep, and pig, such as muscle fibre type and diameter, axon diameter, and body mass.

Methods

[This study was undertaken in collaboration with undergraduate and postgraduate students who contributed to sample collection, imaging, and data analysis under the supervision of the author. Acknowledgment for their contributions is stated in the corresponding sections].

Ethics - human and animal material.

Procedures involving animals were conducted, when necessary, according to the Animals (Scientific Procedures) Act 1986 in compliance with the three Rs. Animal tissue samples were provided by an established institute in Edinburgh. No animals were sacrificed specifically for this project, as samples were taken from a group of animals submitted for euthanasia for veterinary purposes. Sheep and pigs had been euthanized using techniques permitted by the Animals (Scientific Procedures) Act 1986 although as acts of veterinary surgery, i.e., during flock and herd management, respectively. The cat and dog tissue samples were obtained as surplus from a veterinary necropsy facility.

Four mammals were included in this study: **cats** (N = 3; *domestic short-haired*, females, mean age = 12.6 years, mean mass = 4.3 kg, culled for aggression, hyperthyroidism, chronic kidney disease); **dogs** (N = 3; *Labrador, Staffordshire Bull terrier, Lurcher*, 2 males, 1 female, mean age = 6.6 years, mean mass = 39 kg, culled for aggression, neoplasia, joint pain); **sheep** (N = 3; *Texel crosses*, males, mean age = 16 months, mean mass = 75 kg, culled for colony management); and **pigs** (N = 3; *Large white X landrace*, females, mean age = 18 months, mean mass = 75.6 kg, culled for colony management).

All animals were of adult age (Okut *et al.*, 1999; Cozzi *et al.*, 2017) to permit comparison with the mouse (N = 3; CD1, females, mean age = 12 weeks, mean mass

= 19 g) and human data (N = 20; 15 males, 5 females, 34-92 years-old) (Jones *et al.*, 2017).

Tissue sampling.

[Tissue samples from sheep and pigs were collected in collaboration with Ines Boehm]

Textbooks and atlases of veterinary anatomy were used to identify muscles during dissection (Aspinall and Cappello, 2009; Done *et al.*, 2009; Fails and Magee, 2018). To allow direct comparison with mice and humans, previously studied muscles were selected (Jones *et al.*, 2017); M. peroneus longus (PL), M. peroneus brevis (PB), M. extensor digitorum longus (EDL), and soleus (SOL). The cat is the only animal that has all four muscles, while the dog lacks soleus, and sheep and pigs both lack PB (Aspinall and Cappello, 2009; Done *et al.*, 2009; Worne, 2011; Fails and Magee, 2018).

Animals were sedated and euthanised with non-neuromuscular blocking agents. Full-length muscle fibre samples were excised within one hour post-mortem and immediately fixed in 4 % PFA (Electron Microscopy Sciences, 15710) for 3-4 hours.

Tissue processing and NMJ labelling.

Samples were washed thoroughly with 1x PBS, then micro-dissected into small bundles of 10-15 individual fibres. Connective tissue was removed as much as possible to reduce background staining. NMJs were labelled by modifying a previous protocol (Jones *et al.*, 2016). Muscle fibres were moved into a 48 well-plates and incubated and placed in glycine (Sigma Aldrich, 410225-50G) for 15 minutes to reduce tissue auto-fluorescence, then washed in PBS. Fibres were then placed in tTRITC α -BTX (1:500; BTIU00012, VWR International Ltd) for 15 minutes to label AChR. Samples were subsequently processed and kept in the dark (covered by a box) to protect them from photobleaching.

To visualize the pre-synaptic components (nerve terminals and axons), samples were incubated in 4% Triton-X for 90 minutes for permeabilization (Sigma Aldrich), then placed in a blocking solution of 4% BSA (Sigma Aldrich) and 2% Triton X-100 for 30 minutes. Tissue was then incubated overnight at room temperature in the following primary antibodies made in the same blocking solution: mouse anti-SV2 IgG and

mouse anti-2H3 IgG (at 1:50 dilution, Developmental Studies Hybridoma Bank) to label synaptic vesicles and neurofilaments, respectively. Followed by 4 x 20 minutes 1x PBS washes and incubation overnight at 4°C in the secondary antibody: Alexa 488-donkey anti-mouse IgG (1:400 in PBS; A21202, Life Technologies). Finally, samples were washed by 1x PBS for 4 x 20 minutes, then mounted on a glass slide in Mowiol (an anti-fading media), and stored at 4°C.

NMJ and muscle fibre imaging

[Sheep and pig tissue samples were processed and imaged in collaboration with Ines Boehm]

NMJs were imaged on a Nikon A1R FLIM confocal laser scanning microscope equipped with a Nikon Apochromat 60× / 1.4 NA oil immersion objective (Nikon Instruments Europe BV, Netherlands), Images were captured at 16-bit pixel, 512 × 512 frame size, with 0.5 - 1 μm Z-stack intervals. Red channel - 561 nm excitation and green channel - 488 nm excitation were used. As suggested previously, 30-40 *en face* NMJs per muscle were imaged where possible, as plateauing of the mean was observed with a higher sample size (Jones, 2017). Muscle fibres were imaged from the same slides on an Olympus IX71 microscope attached to a Hamamatsu C4742-95 camera with Openlab Improvision software. To match the number of analysed NMJs, a minimum of 40 fibres per muscle were imaged at x20 magnification. Because muscle fibres and NMJs were not imaged at the same time on the same microscope, it was not possible to assign NMJs to their muscle fibres. Therefore, for correlation analysis, the average of NMJs was correlated against the average value of muscle fibre diameters.

Morphological analysis of NMJ and muscle fibre diameter measurement

[Analysis of ovine NMJs was performed in collaboration with Ana S. Leite. Analysis of porcine NMJs and imaging and measuring of sheep and pig muscle fibre diameters was performed in collaboration with Ines Boehm, Alyssa Gibbs (analysed PL), Olivia Murray (analysed EDL), and Rizwan Farrukh (analysed SOL)]

A total of 1565 NMJs were analysed across all 4 species using aNMJ-morph (Minty *et al.*, 2020) (the automated version of NMJ-morph (Jones *et al.*, 2016)) which facilitates comparative analysis of NMJ morphology within and between species (full training was done on using both tools as explained earlier in chapter 2).

A total of 19 morphological variables were measured or calculated (all variables and their means of calculation, where necessary, are summarized in Appendix 5). These variables are divided into:

1. **Pre-synaptic variables** of the pre-terminal axon and nerve terminals. These variables include:
 - a. Size-related parameters (axon diameter (μm), nerve terminal area (μm^2), and nerve terminal perimeter (μm)).
 - b. Nerve terminals branching analysis (number of terminal branches, number of branch points and total length of branches (μm)).

2. **Post-synaptic variables** of AChR (referring to BTx positive area only) and the endplate (referring to the whole endplate area, including AChR devoid area i.e., the footprint). These variables include:
 - a. Size-related parameters (AChR area (μm^2), AChR perimeter (μm), endplate area (μm^2), endplate perimeter (μm) and endplate diameter (μm)).
 - b. Number of AChR clusters: a continuous labelling of BTx is referred to as one cluster of AChR. The increase in number of AChR gives the appearance of a more fragmented endplate.

3. **Derived variables**: these are the variables that are calculated from the measured pre- and post-synaptic variables. These variables include:
 - a. Nerve terminal complexity which is calculated from the variables of branching analysis and provides an overall view of branching pattern of nerve terminals. This variable could give an insight about species differences. For example, mice have more complex nerve terminals than humans (Jones *et al.*, 2017). Also, increase nerve terminals complexity was observed in some neurodegenerative diseases (Ang *et al.*, 2010; Cipriani *et al.*, 2018).

- b. Average area of AChR clusters (μm^2), endplate fragmentation, and endplate compactness (%) (density of AChR). These post-synaptic derived variables are important to distinguish between different species as well as different developmental stages within a species. For example, human NMJs are more fragmented and compact than rodents (Jones *et al.*, 2017), and rodents acquire compact, plaque-shaped endplates during the first two week of life that develop into a pretzel-shaped endplates during adulthood (Marques and Lichtman, 2000). Moreover, increase endplate fragmentation is associated with MND and ageing (Ang *et al.*, 2010; Valdez *et al.*, 2010; Cipriani *et al.*, 2018).
- c. Area of synaptic contact and overlap percentage which describe nerve terminal coverage of endplate. These variables are extremely beneficial in the context of MND as an indicator of denervation (Lee *et al.*, 2011; Liu *et al.*, 2013).

In addition to the morphological analysis of NMJ, muscle fibre diameter was also recorded. Measurements were taken manually using the straight-line tool in Fiji. A total of 6,000 muscle fibres were analysed across all 4 species.

Statistical analysis

GraphPad Prism Software (Version 8) was used for all statistics. To compare NMJ morphology between muscles (PL, PB, SOL, and EDL) within each species, the mean of each muscle variable per species was used. To compare the NMJ morphology of each species to the NMJ morphology of human, data were pooled across all muscles for each species and the mean of each species was used. A one-way ANOVA with Dunnett's correction for multiple comparisons were performed for the continuous variables (area, perimeter, and diameter). Non-continuous variables (NT complexity, counts such as number of branch points, and percentages such as overlap) were analysed by Kruskal-Wallis test with Dunn's multiple comparison test. All results were expressed as mean \pm standard error of the mean (SEM). $P < 0.05$ was considered to be statistically significant.

To assess the influence of axon diameter and muscle fibre diameter on the size of NMJ in each species, the mean of each muscle was used. The values for muscle fibre diameter and axon diameter were correlated against each NMJ size-related variable including the nerve terminal area, the AChR area, the endplate area and the endplate diameter. Pearson's correlation coefficient (r) was used. $P < 0.05$ was considered to be statistically significant.

Results and discussion

1. NMJ morphology of pelvic limb muscles

In total, 465 feline NMJs (N=3, PL, PB, EDL, SOL), 341 canine NMJs (N=3, PL, PB, EDL), 313 ovine NMJs (N=3, PL, EDL, SOL), and 366 porcine NMJs (N=3, PL, EDL, SOL) were analysed. Qualitative assessment revealed a large degree of interspecies similarity in terms of size and shape, and all endplates were fully innervated and supplied by a single axon as expected in the healthy, adult mammalian NMJ (Figure 11).

NMJ were labelled using the same protocol that was previously used in the mouse and human study to facilitate comparison between species (Jones *et al.*, 2017). Although the nerve terminals and AChRs were satisfactorily labelled, axons in large mammals did not always stain as well as those in mice and humans: they were either unlabelled or heterogeneously stained (Figure 11). This may indicate that large mammals possess different types or quantities of neurofilaments. Furthermore, intense spots of SV2 labelling in the nerve terminals were observed in all mammals. These spots may represent dense areas of active zone proteins. Similar "hot spots" were previously observed in human NMJs but were almost absent in the mouse. These "hot spots" corresponded with intense labelling of SNAP25, an active zone protein, and using super-resolution imaging, the authors found larger and denser puncta in human NMJs compared to murine NMJs (Jones *et al.*, 2017). The same possibility might also apply to the large species used in this study and needs to be explored in future studies.

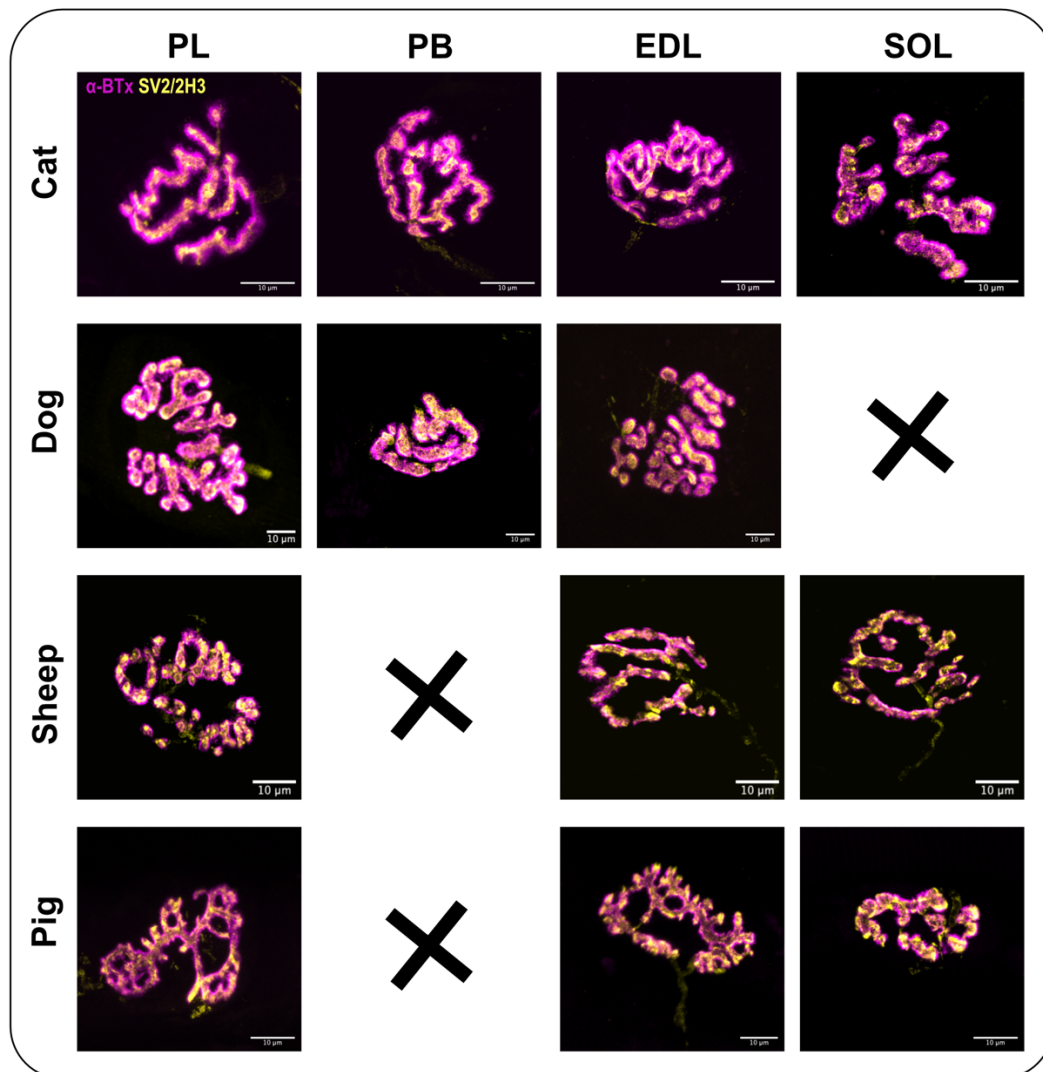


Figure 11: Conservation of NMJ morphology between pelvic limb muscles of non-rodent mammals

Representative confocal micrographs of NMJs from pelvic limb muscles in the cat, dog, sheep, and pig. Dogs do not have a SOL, and sheep and pigs do not have a PB. α -BTX (α -bungarotoxin) was used to label AChR (magenta), while anti SV2 and anti 2H3 antibodies were used to label synaptic vesicles (to visualize nerve terminals) and neurofilaments (to visualize axon), respectively (yellow). The scale bar = 10 μ m in all images.

Quantitative analyses using aNMJ-morph confirmed the initial observations and showed that the overall morphology of NMJs was conserved between muscles in all species (Figure 12). Only a few variables were significantly different in PL; in the cat, PL had a greater number of branch points and highly compacted endplates compared to EDL and SOL, respectively. In sheep and pigs, the average cluster area of AChRs

was significantly greater in PL than in SOL. Additionally, in pigs, the average branch length was longer than that of SOL and EDL (Appendix 6-9).

The preservation of NMJ morphology between pelvic limb muscles has also been reported in mice and humans (Jones et al., 2017), while in ponies, SOL NMJs were significantly smaller than EDL and M. tibialis cranialis (Cahalan, Perkins, et al., 2022). It has been proposed that NMJ size and morphology are influenced by muscle fibre type; fast-twitch muscle fibres are associated with larger, more complex NMJs (Fahim, Holley and Robbins, 1984; Ogata, 1988; Prakash et al., 1996; Mantilla and Sieck, 2001; Cahalan, Perkins, et al., 2022). The proportion of slow-twitch fibres was reported in previous studies in cats (SOL = 100%, EDL = 14%, PL = 6%, and PB = 20%) (Ariano, Armstrong and Edgerton, 1973) and sheep (SOL = 100%, EDL = 25%, and PL = 22%) (Konno and Watanabe, 2012). Although in this study NMJ size was not found to significantly differ between muscles, there was a trend towards larger NMJs in the fast muscles (PL in all 4 mammals, PB in the cat, and EDL in the dog, sheep, and pig) than in the slow muscle (SOL) (Figure 12, Appendix 6-9), which is consistent with the general belief.

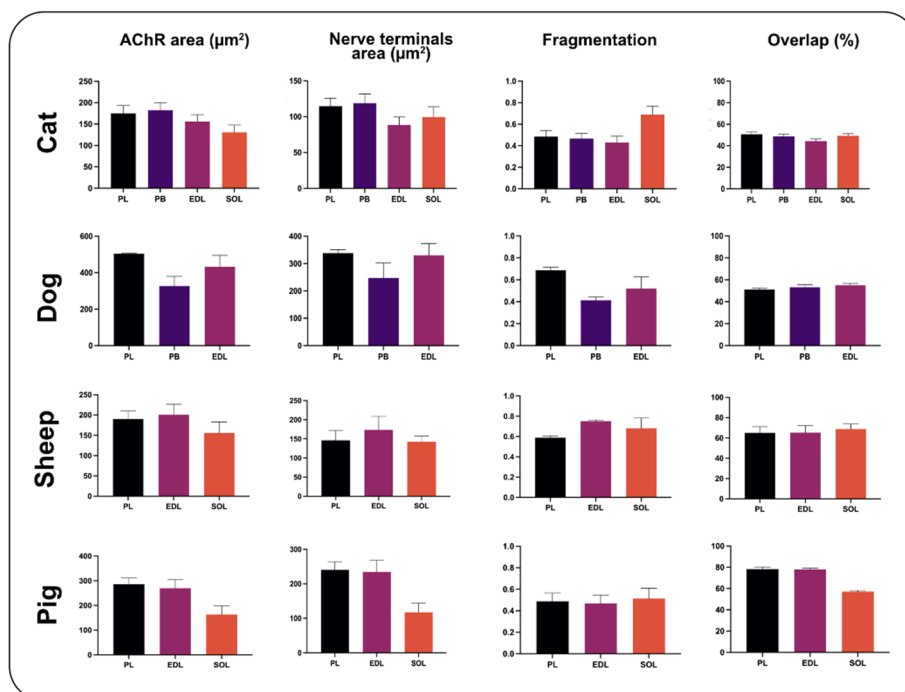


Figure 12: NMJ morphology is largely conserved between muscles in cats, dogs, sheep, and pigs.

Comparison of NMJ morphology between pelvic limb muscles in cats, dogs, sheep, and pigs. Dogs do not have a SOL, and sheep and pigs do not have a PB. Each bar depicts the mean (\pm SEM) of 40 NMJs. Other variables are illustrated in Appendix 6-9. One-way ANOVA for the parametric variables: nerve terminals area, and AChR area. Kruskal–Wallis test for non-parametric variables: overlap and fragmentation.

2. Sheep and pigs have a similar NMJ morphology to humans

To identify the species with NMJs with greater similarities to the human NMJ, data from each of the non-rodent mammals, in addition to the mouse, were compared to a reference dataset of the human NMJ (mouse and human data were obtained from Jones *et al.*, 2017). The initial observation revealed both similarities and differences between the species (Figure 13). murine and canine NMJs appeared similar; they both had pretzel-shaped endplates and were remarkably larger than the other species. The feline NMJ was the smallest overall, while porcine and ovine NMJs had similar morphology that closely resembled the human NMJ in size and shape.

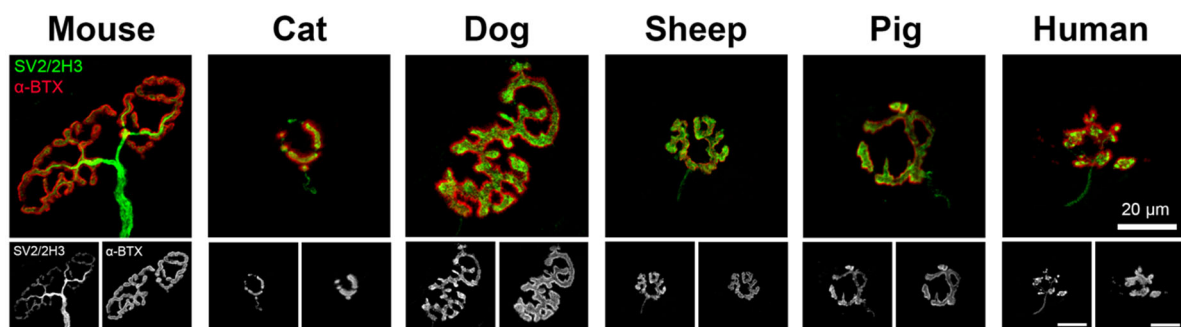


Figure 13: Heterogeneity of NMJ morphology between mammals.

Representative confocal micrographs of pelvic limb NMJ from different species, arranged in order of body size from the least to the greatest. Mouse and dog (porcine) NMJs are the largest among the species studied, while the cat (feline), which has an intermediate body mass had a remarkably smaller, less complex NMJ. In comparison, the 3 largest mammals (sheep, pigs, and humans) have similar NMJ morphologies and size. α -BTX (α -bungarotoxin) was used to label AChR (red), while anti SV2 and anti 2H3 antibodies were used to label synaptic vesicles (to visualize nerve terminals) and neurofilaments (to visualize axon), respectively. The scale bar = 20 μ m (across all images). Adapted from (Boehm, Alhindi, *et al.*, 2020).

Following qualitative assessment, data were pooled across all muscles (PL, PB, EDL, and SOL) in each species, and a statistical comparison was made with the human NMJ (Figure 14, Table 2). In keeping with the observed variations (Figure 13), sheep and pig NMJs were the most similar to the human NMJ. The majority of NMJ variables (17/19 in sheep; 16/19 in pig) in addition to the muscle fibre diameter, showed no statistically significant differences from the human. Sheep showed only significantly larger nerve terminals and AChR perimeters than the human. This increase in perimeters is not necessarily indicative of a larger synapse, as it was not associated with a corresponding increase in area. It may, however, be explained by the high number of AChR clusters (sheep: 4.9 ± 0.40 vs. human: 3.9 ± 0.18 , $P > 0.05$). Pig NMJs were significantly different to the human NMJ in only 3 variables that were reflective of slightly more complex pre-synaptic structures. Feline NMJs had a smaller area but a significantly larger perimeter and a more complex branching pattern than the human NMJ. In contrast, the dog and mouse had the largest, most complex synapses, and the largest axons among the species examined. Compared to the human NMJ, 14/19 and 10/19 NMJ variables were significantly greater in dog and mouse NMJs, respectively.

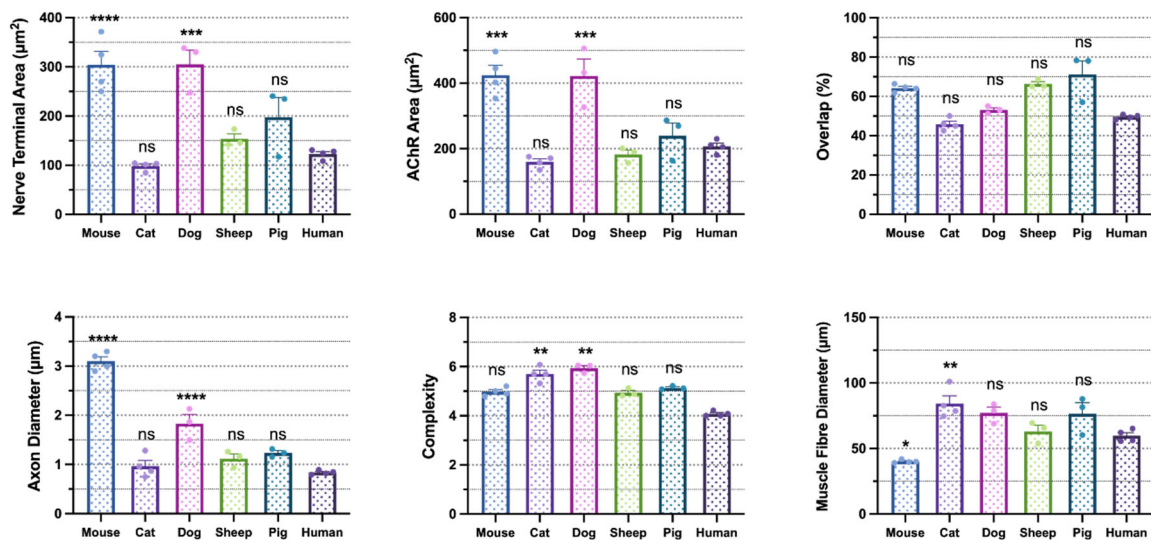


Figure 14: the sheep and pig NMJ and muscle fibre diameter are the most similar to those of humans.

Bar charts showing selected variables of NMJ morphology and muscle fibre diameter of each animal compared to humans (see Table 2 for all variables). The bars depict the mean (\pm SEM)

of pooled data from pelvic limb muscles. In total, 5,385 individual NMJs were analysed [cat: N = 3 animals, n = 12 muscles, 465 NMJs; dog: N = 3, n = 9, 341 NMJs; sheep: N = 3, n = 9, 313 NMJs; pig: N = 3, n = 9, 446 NMJs; mouse: N = 3, n = 24, 960 NMJs; human: N = 21, n = 72, 2860 NMJs]. Murine and human data were pooled from (Jones *et al.*, 2017). One-way ANOVA with Dunnett's post hoc analysis for parametric variables: nerve terminals area, AChR area, axon diameter, and muscle fibre diameter. Kruskal–Wallis test with Dunn's post hoc analysis for non-parametric variables: overlap and complexity. The P values are for the differences between each animal and human. *P ≤ 0.05; **P ≤ 0.01; ***P ≤ 0.001; ****P ≤ 0.0001.

	Mouse N = 3 960 NMJs	Cat N = 3 465 NMJs	Dog N = 3 341 NMJs	Sheep N = 3 313 NMJs	Pig N = 3 366 NMJs	Human N = 21 2860 NMJs
Presynaptic Core variables						
Axon diameter	3.1**** ± 0.05	0.96 ± 0.08	1.8**** ± 0.22	1.1 ± 0.09	1.2 ± 0.05	0.84 ± 0.02
NT Area (µm ²)	304.0**** ± 11.71	98.5 ± 5.44	305.1**** ± 24.93	153.9 ± 14.27	197.6 ± 24.70	122.7 ± 5.98
NT Perimeter (µm)	327.4**** ± 9.39	272.1**** ± 13.85	441.0**** ± 31.71	231.7* ± 12.28	234.7* ± 18.60	151.1 ± 6.53
Number of Terminal Branches	30.0 ± 1.24	101.4**** ± 7.36	95.6**** ± 8.54	45.5 ± 4.38	40.0 ± 5.95	28.0 ± 1.40
Number of Branch Points	26.0 ± 0.94	57.6**** ± 6.87	62.9**** ± 3.48	26.4 ± 2.55	38.5' ± 3.16	14.0 ± 0.85
Total Length of Branches (µm)	166.7**** ± 4.83	128.7** ± 7.71	215.7**** ± 13.54	109.5 ± 8.05	134.5** ± 12.02	69.3 ± 3.28
Average Length of Branches (µm)	6.7**** ± 0.21	1.4 ± 0.05	2.6 ± 0.155	3.0 ± 0.38	4.4 ± 0.59	3.0 ± 0.10
postsynaptic Core variables						
AChR Area (µm ²)	424.2*** ± 14.14	159.6 ± 9.29	420.8*** ± 35.07	182.2 ± 14.00	239.5 ± 25.18	206.7 ± 7.96
AChR Perimeter (µm)	275.8** ± 8.84	332.7**** ± 16.52	536.5**** ± 41.73	241.6' ± 15.23	221.7 ± 18.56	152.2 ± 5.79
Endplate Area (µm ²)	678.2*** ± 24.25	333.2 ± 19.86	858.9**** ± 85.03	365.4 ± 16.79	384.2 ± 38.48	351.5 ± 14.36
Endplate Perimeter (µm)	118.8 ± 2.93	91.4 ± 3.03	139.1** ± 10.18	85.1 ± 3.83	95.5 ± 7.25	98.7 ± 2.60
Endplate Diameter (µm)	42.2 ± 1.19	30.9 ± 1.06	48.1** ± 3.41	30.3 ± 1.41	32.2 ± 2.00	36.0 ± 0.93
Number of AChR Clusters	2.6 ± 0.15	3.2 ± 0.37	3.8 ± 0.53	4.9 ± 0.40	3.7 ± 0.46	3.9 ± 0.18
Derived variables						
NT Complexity	4.9 ± 0.05	5.7** ± 0.11	5.9** ± 0.09	4.9 ± 0.10	5.1 ± 0.11	4.1 ± 0.07
Average Area of AChR Clusters (µm ²)	238.5**** ± 8.53	75.8 ± 8.58	175.4**** ± 12.57	54.8 ± 6.84	113 ± 12.87	71.7 ± 2.66
Endplate Fragmentation	0.40 ± 0.02	0.51 ± 0.03	0.53 ± 0.05	0.67 ± 0.03	0.48 ± 0.04	0.58 ± 0.01
Endplate Compactness (%)	64.4 ± 0.58	49.5 ± 1.07	50.4 ± 1.76	51.0 ± 3.10	64.5 ± 2.33	61.6 ± 0.63
Pre and post synaptic Overlap (%)	64.2 ± 0.49	45.9 ± 1.13	53.1 ± 1.08	66.4 ± 3.03	71.1 ± 3.59	49.6 ± 1.05
Area of Synaptic Contact (µm ²)	267.9**** ± 9.48	72.4 ± 4.48	224.4** ± 18.13	122.0 ± 13.38	175.0 ± 24.19	105.2 ± 5.11
Associated variables						
Muscle Fibre Diameter	40.2' ± 0.52	84.3** ± 3.54	77.2 ± 3.33	63.0 ± 3.29	76.6 ± 6.72	59.9 ± 2.08

Table 2: A reference dataset of mammalian NMJ morphology and muscle fibre diameter

The listed values represent the mean ± SEM for the complete dataset pooled across all muscles in each species. One-Way ANOVA with post hoc analysis (Dunnett's test) for the continuous variables (diameter, length, area, and perimeter), and Kruskal-Wallis test with Dunn's test for non-continuous variables (counts, percentages, and NT complexity). The P values are for the differences between each animal and human. *P ≤ 0.05; **P ≤ 0.01; ***P ≤ 0.001; ****P ≤ 0.0001.

3. The relationship between size of NMJ, size of muscle fibre and body mass

The variations in NMJ size observed across species raises the question of what may be causing these differences. Several factors have been previously proposed and explored, including the body size of the species (Slater, 2017), the muscle fibre diameter (Kuno, Turkanis and Weakly, 1971; Oda, 1985; Jones, 2017), and the size of the MN axon (Jones, 2017).

Studies of NMJs in amphibians, rodents, and humans revealed a trend toward a smaller NMJs in larger species, suggesting an inverse relationship between NMJ size and body size (Slater, 2017). However, in the present study, no trend was observed between NMJ size and body mass (Figure 15). The larger size of dog NMJs, did not confirm this belief as dogs are intermediate in body mass between cat and sheep. Additionally, two recent studies have also shown a similarity in NMJ size between species of different body weights, i.e., mice compared to rats, with average adult males mass around 19 g and 550 g, respectively (Quinn, 2005; Jones, 2017), and humans compared to ponies, with an average adult male mass around 82 kg and 312 kg, respectively (Quinn, 2005; Cahalan, Boehm, *et al.*, 2022). Taken together, the presented findings in conjunction with the previous studies, are all suggestive of no association between body weight and NMJ size.

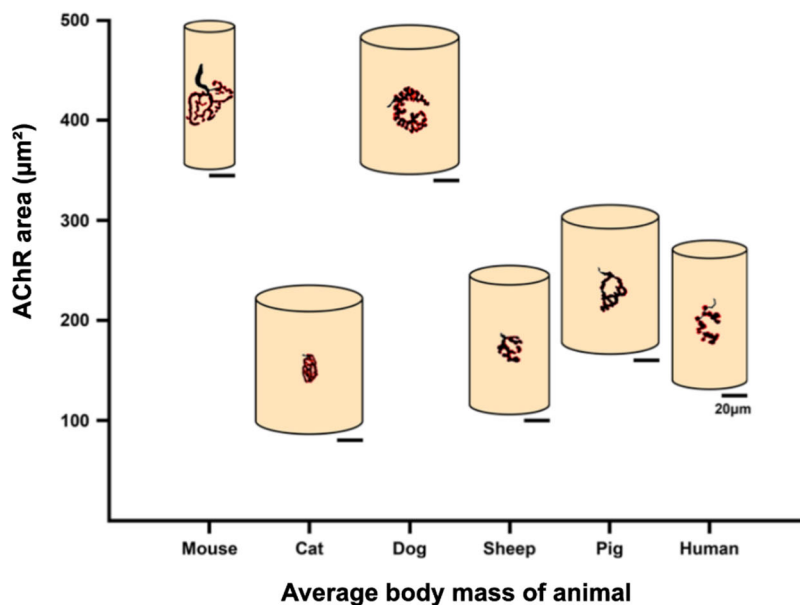


Figure 15: Animal's body mass is not a determining factor of NMJ or muscle fibre size.

The schematic diagram illustrates the mean values for AChR area and muscle fibre diameter of different mammals. Animals are arranged based on their average body mass from the least to the greatest. Overall, both NMJ and muscle fibre size appear to be unrelated to body mass. A stark contrast is seen between the two smallest animals; mice have the largest NMJs on the smallest muscle fibres while cats have the smallest NMJs on the largest muscle fibres. Sheep NMJs are the most similar to the human NMJ. The scale bar = 20 μm . Adapted from (Boehm, Alhindi, et al., 2020).

Previous studies have shown a correlation between NMJ size and muscle fibre diameter in different species, and a similar relationship has been proposed for the MN axon diameter. During NMJ development, AChRs are initially formed on the muscle fibre surface, then the MN axon approaches the muscle fibre surface and restructures the endplate by releasing agrin (an AChR-stabilizer factor) and ACh (a declustering factor) (Valdez, 2020). This might indicate that NMJ size is determined by the size of the MN axon. One study has investigated this relationship and found that NMJ size correlated with the axon diameter in mice and humans (Jones, 2017).

The influence of muscle fibre size has been reported by several studies and showed a positive correlation with NMJ size in several species: humans (PL, PB, EDL, and SOL), mice (small calibre muscles only: palmar lumbricals, Interscutularis (IS), levator auris longus – caudal (LALc), and levator auris longus – rostral (LALr) (Jones, 2017), rats (EDL, M. sternomastoideus, and M. levator palpebrae superioris) (Oda, 1985), frogs (M. sartorius) (Kuno, Turkanis and Weakly, 1971), and ponies (M. tibialis cranialis, EDL, and SOL) (Cahalan, Perkins, *et al.*, 2022).

To evaluate whether the size of the muscle fibre or the MN axon affects the NMJ size in the non-rodent mammalian species studied, a series of correlation analyses were performed. The average values of muscle fibre and axon diameters were correlated against the average values of NMJ size-related variables, i.e., the nerve terminal area, the AChR area, the endplate area and diameter, in each muscle. Interestingly, muscle fibre diameter correlated strongly with the NMJ size in the pig (4/4 variables) and, to a lesser extent, in sheep (AChR area only). Feline and canine NMJs showed an absence of correlation (Figure 16A, Appendix 10A). In contrast, increasing axon diameter was strongly associated with an increase in endplate and nerve terminal area in sheep.

The NMJ size in cats, dogs, and pigs showed no correlation with axon diameter (Figure 16B, Appendix 10B).

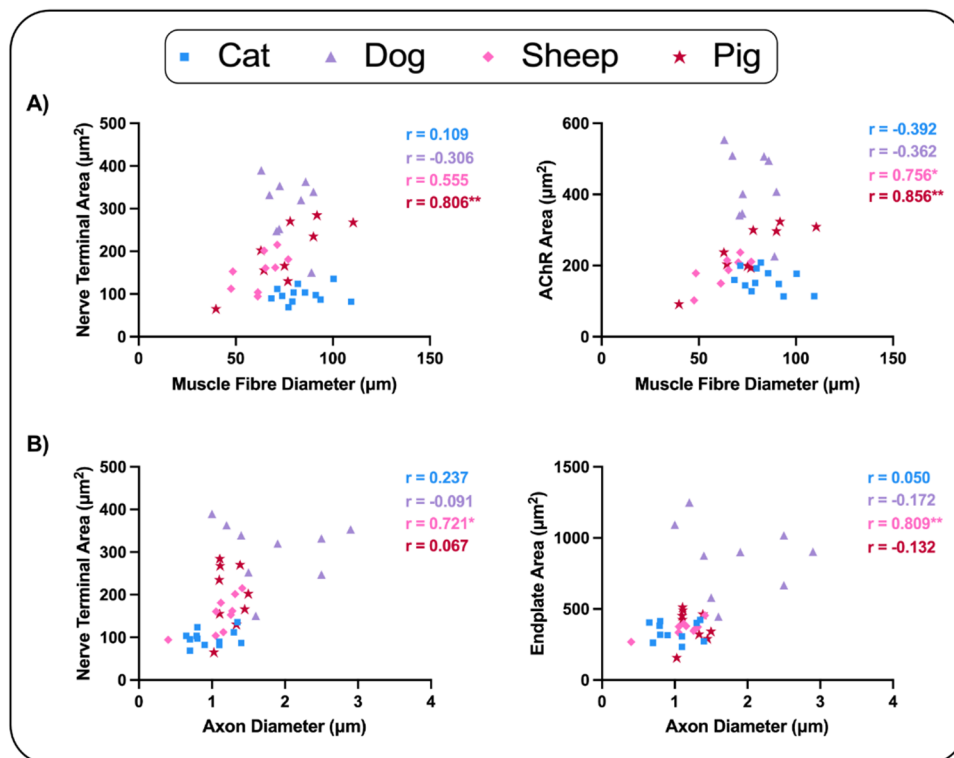


Figure 16: Correlation of NMJ size with muscle fibre and axon diameter in non-rodant mammals

Each data point represents the mean value of 40 NMJs for an individual muscle. **Cat**: n = 12 muscles; **dog**: n = 9 muscles; **sheep**: n = 9 muscles; **pig**: n = 9 muscles. **A)** Muscle fibre diameter correlated strongly with nerve terminal area and AChR area in sheep and pigs, while **B)** axon diameter showed positive correlation in sheep only. the Cats and dogs NMJ variables showed no significant correlation with neither muscle fibre nor axon diameter. Cat = blue squares; dog = purple triangles circles; sheep = pink diamonds; pig = red stars. Pearson's correlation coefficients. *P ≤ 0.05; **P ≤ 0.01. Adapted from (Boehm, Alhindi, et al., 2020).

These findings revealed species-specific differences in NMJ morphology, with muscle fibres and axon diameters being associated only with the NMJs of sheep and pigs. Accordingly, neither the size of the muscle fibre nor the size of the axon is a global factor that affects NMJ size in mammals, and the factors affecting NMJ size might vary from species to species.

Conclusions

The primary objective of this study was to find a more representative mammalian model for the human NMJ. It provided the first baseline data and comparative anatomy of the NMJ in non-rodent mammalian species. The data showed that sheep and pig NMJs were the most like the human NMJ, with sheep bearing the closest resemblance to the human, making it an attractive subject of future studies. Findings from the study also disprove the widely held belief of an inverse relationship between NMJ size and body weight and showed that NMJ size only correlates with the size of the muscle fibre in sheep and pigs, and the size of the MN axon in sheep.

Chapter 4: Pathological changes at the NMJ in the Thy-1 hTDP-43 ALS mouse model

Introduction

In general introduction (Chapter 1) the NMJ was identified as one of the critical structures involved in the pathogenesis of ALS (Murray, Talbot and Gillingwater, 2010). The dying-back phenomenon, in which MN death starts peripherally at the NMJ and progresses in a retrograde fashion towards the cell body, has been extensively studied in the SOD1 mouse model (Dadon-Nachum, Melamed and Offen, 2011). In comparison, studies on models of other forms of ALS are lacking, yet are necessary, for understanding different patterns of clinical presentation in human patients. There are several reasons for this gap in the literature. First and foremost, ALS phenotypes in humans are highly heterogeneous. Second, ALS-associated SOD1 mutations are only found in 10% of familial cases and 1.5% of sporadic cases (Zou *et al.*, 2017). Therefore, it may be imprudent to draw conclusions from the findings of a single model, until other models are similarly explored and characterized. Moreover, the fact that most therapies that showed promise in the SOD1 models failed to translate to humans further supports the need for investigating other models (Mitsumoto, Brooks and Silani, 2014; Tosolini and Sleight, 2017).

TDP-43 pathology is a characteristic feature of ALS. TDP-43 protein is encoded by the *TARDBP* gene located on chromosome 1. TDP-43 is a ubiquitously expressed, multifunctional DNA/RNA binding protein. It is involved in multiple steps of transcriptional and post-transcriptional regulation of gene expression. TDP-43 is essential for embryonic and postnatal survival; *TARDBP*^{-/-} embryos die early during development (Sephton *et al.*, 2010), and postnatal deletion of *TARDBP* causes progressive weight loss of body mass and rapid death (Chiang *et al.*, 2010). TDP-43 is also critical for MN health and maintenance; postnatal MN-specific TDP-43 knockout in mice leads to MN atrophy, ALS-like motor dysfunction, muscle atrophy, and denervation (Iguchi *et al.*, 2013).

TDP-43 is predominantly a nuclear protein, but continuously shuttles to and from the cytoplasm (Ayala *et al.*, 2008). However, in some neurodegenerative diseases,

including ALS, cytoplasmic transport increases, leading to nuclear depletion (Scotter, Chen and Shaw, 2015). As a result, the cell produces more TDP-43 to increase its nuclear level leading to more cytoplasmic accumulation. Both toxic “gain-of-function” and “loss-of-function” occur as a consequence of the formation of cytoplasmic aggregates and nuclear depletion respectively (Baralle, Buratti and Baralle, 2013). Although a small fraction of ALS cases are caused by *TARDBP* gene mutations (3% of fALS and 1.5% of sALS), cytoplasmic aggregates of TDP-43 are present in nearly 97% of all types of ALS independent of genetic background, indicating that TDP-43 is a key protein in ALS that warrants focussed investigation (Versluys *et al.*, 2022).

There is still much to learn about the aetiology and pathogenesis of ALS. Identifying the sequence of pathological events and distinguishing the primary from the secondary pathologies is the first step toward a better understanding of this. MN death, axonal degeneration, NMJ disruption, and muscle atrophy are all characteristics of the disease, but the sequence of changes and correlates with onset of symptoms are unknown. Whether compensatory mechanisms exist, and if so, to what extent and for how long they are able to compensate is also unknown.

In this study, NMJ disruption and MN loss (the main pathologies in ALS) were investigated in a severe mouse model of ALS that overexpresses human TDP-43 (hTDP-43) protein in the MNs under the control of a *Thy-1* promoter. This model was chosen because of its availability in our laboratory at the time and because it shows rapid disease progression with complete paralysis and death by P19-22 (Wils *et al.*, 2010). The short lifespan of this model facilitates the full characterization of pathology over a short period of time.

Hypothesis of this study:

Based on the findings from previous studies that showed structural and functional impairment of the NMJ in ALS patients and ALS mouse models, it is expected to observe a progressive NMJ denervation and tSCs loss in the pelvic limb muscles of the TDP-43 ALS mouse model, associated with a progressive MN atrophy and death in the lumbar spinal cord.

Aims of this study:

- To determine the onset and the progression of MN atrophy and death. This was achieved by examining MNs in the ventral horn of the lumbar spinal cord at 3 time points: i) the pre- symptomatic stage, ii) the symptomatic stage, iii) the disease end-stage.
- To identify the most vulnerable body regions. This was achieved by performing a full body characterization of NMJ denervation comparing muscles from the head, pelvic limbs, thoracic limbs, and abdomen, at the disease's end-stage.
- To investigate selective vulnerability between muscles from different body regions. This was achieved by comparing NMJ denervation and tSCs loss across a range of pelvic limb and cranial muscles at disease end-stage.
- To determine the onset and progression of NMJ loss. This was achieved by examining NMJs at 3 time points: i) the pre- symptomatic stage, ii) the symptomatic stage, iii) the disease end-stage.
- To investigate the extent of NMJ pathology during the course of the disease. This was achieved by examining the morphological changes affecting both pre- and post-synaptic structures using NMJ-morph.

Methods

Animal model

The daily inspection of animals, daily clinical assessment, and culling were conducted by personal license holders under the appropriate project license (P92BB9F93). This work was performed in accordance with University of Edinburgh and UK Home Office regulations.

Transgenic mice overexpressing the human wild-type *TARDBP* gene (hTDP-43^{wt}) under the control of the neuronal murine *Thy-1* (m *Thy-1*) promoter to selectively express the transgene in all neurons (Wils *et al.*, 2010) were obtained from the Jackson Laboratory B6;SJL-Tg(*Thy1-TARDBP*)4Singh/J (RRID:IMSR JAX stock #012836). Animals were maintained at the animal facility at the University of Edinburgh from the start of the experiments under standard conditions in a 12-hour light/dark cycle. The colony was maintained as a heterozygous cross. Both sexes were used. Wild-type (WT) littermates were used as controls. Homozygous mice (referred to as

hTDP-43) were monitored daily for body weight changes and signs of progressive muscle weakness, and paralysis. Clinical scoring was performed from the onset of ALS-like symptoms (at around P14-15) until disease end-stage (at around P19-21). The scoring system ranges from 0 to 3, where 0 refers to normal gain in body mass and muscle strength, while a score of 3 indicates a significant loss of body mass and severe paralysis (Appendix 11). Disease end-stage was defined as a 20% reduction in body mass from previous days (Talbot *et al.*, 2019), severe paralysis that compromises movement to the extent that the animal moves by dragging itself on the floor (Yerger *et al.*, 2022), a full retraction of both pelvic limbs when suspended by the tail (Yerger *et al.*, 2022), and when the animal is placed on its back and takes more than 30 seconds to right itself (Gurney *et al.*, 1996).

Spinal cord dissection and sectioning

[performed in collaboration with Megan Shand under my project management].

Mice were culled by either an intraperitoneal injection of pentobarbital (P3 - P12 mice) or by cervical dislocation (P15 – P19 mice) and their spinal cords were dissected out.

For protein analysis, spinal cords were flash-frozen on dry ice and stored at -80°C until processing. For immunohistochemistry, spinal cords were pinned straight on a dish and fixed with 4 % PFA (Electron Microscopy Sciences, 15710) for 24 hours, then immersed in 30 % sucrose for 24 hours, followed by rolling for 1 hour in a 1:1 mixture of 30% sucrose and OCT (optimum cutting temperature, from Cell Path). The lumbar region was trimmed and embedded in blocks with the same mixture (1:1 30% sucrose:OCT) on dry ice and stored at -80°C until sectioning. To ensure that each section had entirely a new pool of MNs, 20 µm thick sections, 160 µm apart were collected onto charged slides.

Western blotting

[performed in collaboration with Megan Shand under my project management].

The spinal cord was homogenised in RIPA buffer containing protease inhibitor (89900, Life Technologies), centrifuged, and the protein supernatant was collected. A Pierce™ BCA Protein Assay Kit (Thermo Fisher Scientific) was used for total protein measurement. 20 µg of protein was loaded on NuPAGE™ 4 to 12%, Bis-Tris Mini Protein Gels. An iBlot 2 Transfer Device (Thermo Fisher Scientific) was used to

transfer the gel to PDVF membranes. Immediately after transfer, the membrane was incubated with Revert 700 Total Protein Stain (LiCor) for 5 minutes then blocked in a 5% BSA buffer for 30 minutes, before being incubated overnight at 4°C with primary antibody - human TDP-43 (1:1000 in BSA; Abnova Cat# H00023435-M01, RRID:AB_425904) - followed by 3 x 5 TBS-T washes on the next day, and an incubation in IR 800 secondary antibody for 1 hour at room temperature (1:5000; LICOR Biosciences) and washing 3 x 30 in TBS-T. Finally, after drying the membrane, it was imaged using a LiCOR Odyssey scanner. Protein was quantified by normalizing the signal against the Total Protein Stain for each sample.

Motor neuron labelling, imaging, and analysis.

[performed in collaboration with Megan Shand under my project management].

Lumbar sections of spinal cords were permeabilized for 10 minutes with 4% Triton X-100. They were then stained with NeuroTrace 500/525 to label MNs (a fluorescent Nissl stain; 1:200 in PBS; N21480 ThermoFisher), counter stained with DAPI (ThermoFisher; 300 nM), then mounted on a glass slide in Mowiol. Steps were performed in the dark to prevent photobleaching.

For the analysis, slides were imaged on a Leica DMI8 fluorescent microscope at 10x magnification. To obtain representative micrographs, a Nikon A1R confocal laser scanning microscope was used with 20x and 60x objectives.

A total of three mice were used from each genotype and at each timepoint, except for P19, where four mice from each genotype were used. The presence of a positive Nissl label along with DAPI staining or dark nucleoli was used to identify MNs. Only cell bodies with a minimum diameter of 20µm were included in the analysis. The MN count was done manually by calculating the average of both sides in 6 spinal cord sections per animal. The area of MN cell bodies was measured using CellProfiler (Version 4.2.1). The investigator was unaware of the genotype while preparing and examining the sections and analysing the data.

Muscle selection for NMJ analysis

To perform a full characterization of NMJ pathology in the hTDP-43 model, 16 muscles were selected from four different anatomical regions. The following cranial muscles were dissected: M. Adductor auris longus (AAL); M. Auricularis superior (AS), M.

interscutularis (IS), M. levator auris longus rostral (LALr) and M. levator auris longus caudal (LALc). From the abdomen: M. transversus abdominus (TVA). From the thoracic limbs: Mm. lumbricales. And from the pelvic limbs: Mm. lumbricales, M. flexor digitorum brevis (FDB), M. tibialis anterior (TA), M. extensor digitorum longus (EDL), M. peroneus longus (PL), M. peroneus brevis (PB), M. gastrocnemius (GC), M. soleus (SOL), and M. plantaris.

These are representative muscles from the most affected regions in ALS in mouse and human. A wide range of cranial and pelvic limb muscles were selected to facilitate a comprehensive analysis of the extent of pathology within these two regions and explore selective vulnerability between muscles. Palmar lumbricals were chosen because they are distally (peripherally) located, and in ALS, distal muscles are more affected than the proximal muscles. The TVA is an abdominal muscle that is routinely used in NMJ/muscle studies.

Tissue processing and NMJ labelling.

NMJ pathology was characterized at three time points: pre-symptomatic stage (P8; WT: N = 3, males : females = 2:1; hTDP-43: N = 3, males : females = 3:0), early symptomatic stage (P15, WT: N = 4, males : females = 2:2; hTDP-43: N = 4, males : females = 3:1) and disease end-stage (P19-21, WT: N = 6, males : females = 3:3; hTDP-43: N = 6, males : females 4:2).

Mice were euthanised either by cervical dislocation (P15 and P19-21 mice) or by an intraperitoneal injection of pentobarbital (P8 mice). Muscles were immediately dissected bilaterally and fixed in 4% PFA (Electron Microscopy Sciences, 15710) for 15-60 minutes depending on the muscle size, then washed thoroughly with 1xPBS. Large muscles (TA, EDL, PL, PB, GC, SOL, and plantaris) were micro-dissected into small bundles containing 10 – 20 muscle fibres, while small and flat muscles (cranial muscles, TVA, lumbricals, and FDB) were whole-mounted after clearing connective tissue. The following protocol was used to label all NMJ components: axons, nerve terminals, tSCs, and AChRs (Alhindi *et al.*, 2021). Muscle fibres were moved into a 48 well-plate and incubated and placed in glycine (Sigma Aldrich, 410225-50G) for 15 minutes to reduce tissue auto-fluorescence, then washed in PBS. Fibres were then placed in TRITC α -BTX (1:500; BTIU00012, VWR International Ltd) for 15

minutes to label AChR. Samples were subsequently processed and kept in the dark (covered by a box) to protect them from photobleaching.

To visualize the pre-synaptic components (nervous terminals, axons, and tSCs), samples were incubated in 4 % Triton X-100 (from Sigma Aldrich) for 90 minutes for permeabilization (2% Triton X-100 for 30 minutes was used for P8 mice muscles). Samples were then placed in a blocking solution of 4% BSA (Sigma Aldrich) and 2% Triton X-100 for 30 minutes. Tissue was then incubated with the following primary antibodies over 48 hours at 4°C: ready-to-use rabbit polyclonal anti-S100b IgG (from Dako Omnis) to label tSCs, mouse anti-SV2 IgG and mouse anti-2H3 IgG (in BSA at 1:50 dilution, Developmental Studies Hybridoma Bank) to label synaptic vesicles, and neurofilaments, respectively, followed by 4×20 minutes PBS washes. Tissue was then incubated with the corresponding secondary antibodies overnight at 4°C: AlexaFluor-488-conjugated donkey anti-mouse IgG antibody (1:500 dilution, A21202, Life Technologies), AlexaFluor-680-conjugated donkey anti-rabbit IgG antibody (1:500 dilution, A10043, Life Technologies), and washed for 4×20 minutes with 1x PBS. Finally, samples were stained with DAPI for 15 minutes (1:1000, D1306, Life Technologies) followed by 3×10 minutes PBS washes, then mounted on a glass slide in Mowiol (an anti-fading media), and stored at 4°C.

NMJ Imaging

A minimum of 40 NMJs per muscle (only NMJs in an *en face* orientation) were captured using a Nikon A1R FLIM confocal laser scanning microscope equipped with a Nikon Apochromat 60× / 1.4 NA oil immersion objective (Nikon Instruments Europe BV, Netherlands), Images were captured at 16-bit pixel, 512 × 512 frame size, with 0.5 - 1 μm Z-stack intervals. Red channel - 561 nm excitation, green channel - 488 nm excitation, far red channel - 650 excitation, and blue channel - 405 nm excitation was used. Subsequent analyses were performed using maximum intensity projection images.

Qualitative and quantitative analysis of NMJs

Based on the overlap between nerve terminals and the endplate, innervation was first assessed visually and NMJs classified as fully innervated (endplates are entirely occupied by nerve terminals), partially denervated (part of the endplate is vacant), and

vacant NMJs (fully empty endplates). The term “denervation” was used to describe both partially denervated and vacant NMJs combined. Second, for tSC analysis, NMJs were classified as: fully covered (complete labelling of S100b over the endplate), partially covered (partial loss of the S100b labelling over the endplate) or uncovered (total loss of the S100b labelling over the endplate). Finally, to investigate morphological changes in the pre- and post-synaptic structures, quantitative analysis was carried out using aNMJ-morph (Minty 2020). The following variables were measured to assess changes in NMJ size: axon diameter, nerve terminal area and perimeter, AChR area, endplate area, and number of AChR clusters. The complexity of nerve terminals was quantified in order to assess changes in nerve terminal branching patterns. Endplate compactness and fragmentation were calculated to investigate any degenerative changes of the endplate and overlap percentage to determine the degree of denervation (see chapter 3 for more details on aNMJ-morph).

Statistical analysis

Statistical analysis was performed using GraphPad Prism Software (version 9). The percentage of NMJ denervation was calculated for each muscle and Mann Whitney test was used to compare between the two groups (WT and hTDP-43 mice). All results were expressed as mean \pm standard error of the mean (SEM). P values < 0.05 were considered statistically significant.

Results and discussion

1. Clinical phenotype correlated with spinal cord hTDP-43 expression and MN loss

[performed in collaboration with Megan Shand].

Mice were monitored daily for changes in body mass and muscle strength. As previously described (Wils *et al.*, 2010), around P14-15, mice began to develop an ALS-like phenotype (tremor, cessation of gain in body mass, and impaired gait and grip strength) and developed severe paralysis and significant loss of body mass around P19-21. This was considered the humane endpoint at which mice were euthanised (Figure 17).

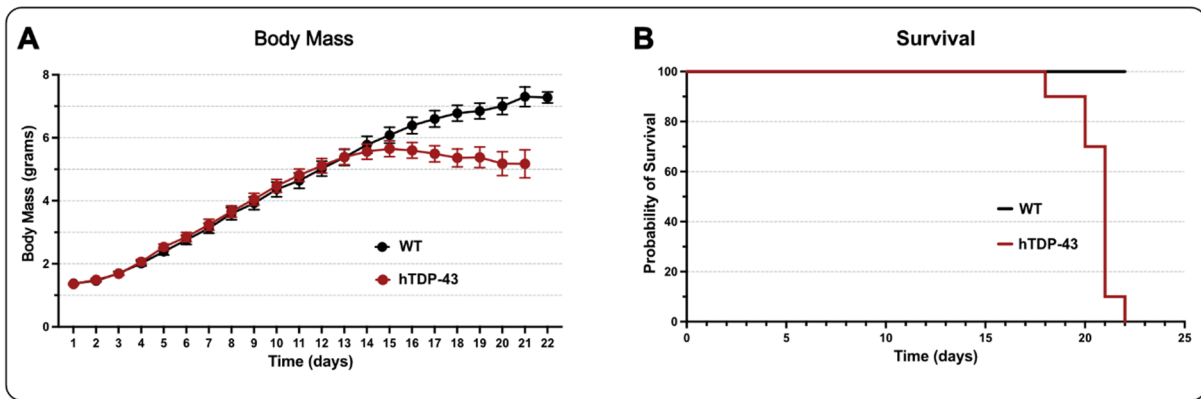


Figure 17: A plateau in body mass gain and a decrease in survival in mice expressing hTDP-43.

A) Line chart shows the daily assess of body mass in hTDP-43 (red line) and WT (black line) mice. While WT mice demonstrated normal gain of body mass, that of hTDP-43 animals showed little further gains from P14-17 followed by a slight reduction in body weight. **B)** Kaplan-Meier survival curve of hTDP-43 (red line) and WT (black line) mice. There was no death in the WT group, while hTDP-43 mice reached end-stage at p18-22 and were euthanised. *Adapted from (Alhindi et al., 2023)*

Using an antibody against human TDP-43, changes in the expression of hTDP-43 in the spinal cord were monitored across the lifespan (pre- symptomatic stage: P3, 5, 8, 12; symptomatic stage: P15, 17; and end-stage: P19) in hTDP-43 and WT mice. At P19, protein expression had increased by 2x from the earliest point analysed (P3). hTPD-43 mice showed a gradual increase in protein expression with age. In contrast, WT mice only had a negligible amount of the protein during the time course of the study as they did not possess the transgene (Figure 18).

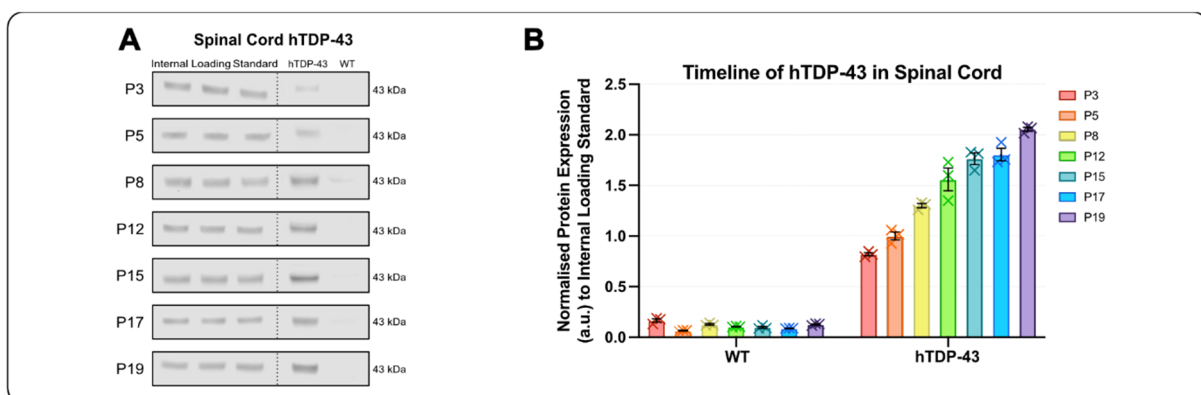
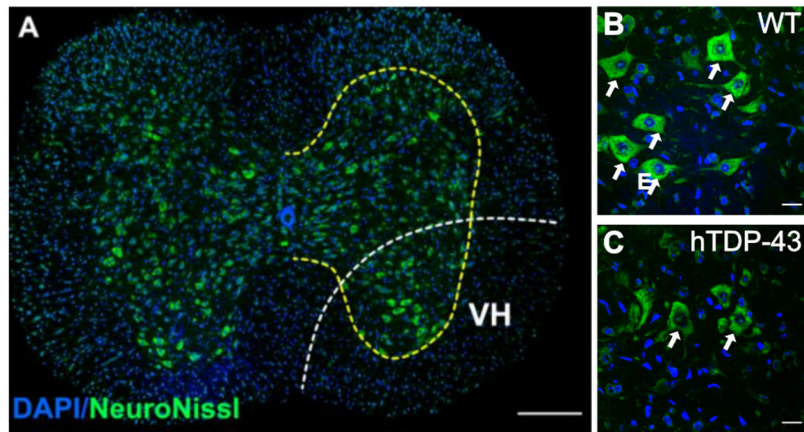


Figure 18: Progressive increase in hTDP-43 protein expression in the spinal cord of hTDP-43 mice.

A) Representative Western blot images of hTDP-43 expression in the spinal cord of hTDP-43 and WT mice and triplicates of the internal loading standard. **B)** Bar chart shows the amount of hTDP-43 in the spinal cord of hTDP-43 and WT mice. Data are normalized against the internal loading standard to allow comparison between blots. Bars depict the mean \pm SEM of 3 animals. *Adapted from (Alhindi et al., 2023)*

As ALS is caused by progressive loss of MNs, sections of the lumbar spinal cord were stained using a fluorescent Nissl stain to track changes in the size and number of α MNs at P8, 15, 17, and 19 (Figure 19A-C). While no change in MN cell body area was found (Figure 19F), a significant gradual loss of MNs was evident in hTDP-43 mice from P15 onwards (Figure 19G), which corresponds with the onset of a clinical phenotype. Additionally, lumbar spinal cord sections were also labelled with antibodies against TDP-43, revealing cytoplasmic mislocalization in MNs of hTDP-43 mice (Figure 19D, E).



D Lumbar Spinal Cord Cell Soma Size in Ventral Horn at P19

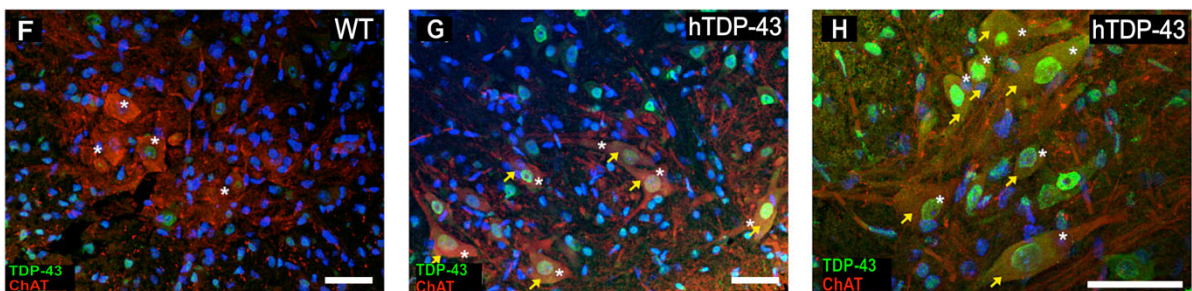
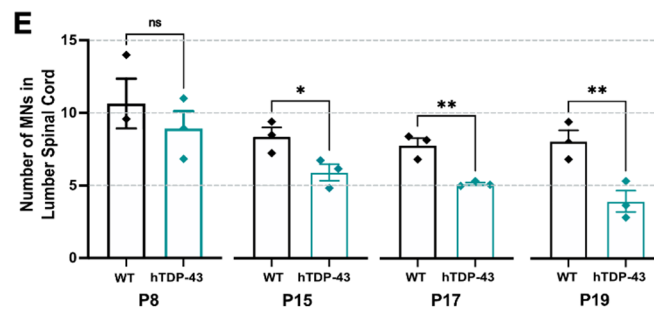
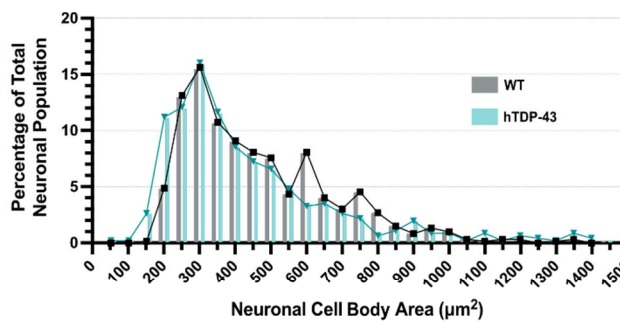


Figure 19: MN death and mislocalisation of TDP-43 in symptomatic hTDP-43 mice.

(A) A representative confocal micrograph of a cross-section from the lumbar spinal cord stained with NeuroNissl (green) and DAPI (blue) to label neuronal cells and nuclei respectively. The yellow dotted line depicts grey matter. The ventral horn (VH), the area from which MNs were analysed, is outlined by the yellow and white dotted lines. Only MNs with the

shortest diameter exceeding 20 μm were analysed. Scale bar = 200 μm (**B and C**) Example images from the VH in WT and hTDP-43 mice at P19 show fewer MNs (white arrows) in the hTDP-43 mouse compared to WT. Scale bar = 20 μm (**D**) Bar and line chart show no difference in the distribution of MN area between WT and hTDP-43 mice at P19 (a left shift of the hTDP-43 bars would indicate atrophy, while a right shift indicates hypertrophy) (**E**) The average number of MNs in WT and hTDP-43 mice at different time points. The number of MNs was similar in both groups at the pre- symptomatic stage (P8). However, at the early- symptomatic stage (P15), a significant reduction in the number was found in the hTDP-43 mice (5.92 ± 0.57 MNs compared to 8.39 ± 0.63 MNs in WT). MN loss gradually increased with disease progression and over 50% of MNs were lost by disease end-stage (P19) (3.94 ± 0.73 MNs compared to 8.36 ± 0.41 MNs in WT). Each data point represents the average of 6 spinal cord sections (20 μm thick, 160 μm apart from one another) in one animal. Bars are the averages \pm SEM. Mann Whitney test, * $P \leq 0.05$, ** $P \leq 0.01$. (**F – H**) Representative confocal micrographs of a cross-section from the lumbar spinal cord of WT (**F**) hTDP-43 (**G, H**) mice labelled by anti-choline acetyltransferase antibody (anti ChAT antibody in red) and anti-TDP-43 antibody (in green) reveal cytoplasmic mislocalisation of TDP-43 in hTDP-43 but not in the WT mice. Stars indicate ChAT-positive motor neurons, and arrows indicate TDP-43 cytoplasmic localisation. Scale bars in (F – H) = 50 μm . Adapted from (Alhindi et al., 2023)

2. Severe disruption of NMJ morphology in pelvic limb muscles at disease end-stage

To characterize denervation in different body regions, NMJ components were first labelled in cranial muscles, palmar lumbricals, TVA, and a range of pelvic limb muscles (lumbricales, FDB, TA, EDL, PL, PB, GC, SOL, and plantaris). It is known that in spinal onset ALS, the most common form of ALS (Logroscino *et al.*, 2010), muscle weakness and atrophy are more evident distally in the lower limbs in humans and hindlimbs in rodents, and with disease progression, the pathology extends proximally and spreads to the upper limbs in humans and forelimbs in rodents (Chiu *et al.*, 1995). Consistent with this phenotype, this study found that pelvic limbs were the most severely affected body region in the hTDP-43 model; only 40% of NMJs in pooled pelvic limb muscles remained innervated, compared to 80% in pooled cranial muscles (Figure 20). Thoracic limb lumbricals and TVA were the most disease-resistant muscles, with only 5% denervation in the former and 15% in the latter, not reaching statistical significance in either (Figure 20).

Previous studies have shown similar results. For example, in SOD1^{G39A} rodents, denervation was earlier and more severe in pelvic limb muscles (GC) than thoracic limb extensor muscles and neck muscles (M. sternomastoideus) (Smittkamp *et al.*, 2010; Clark *et al.*, 2016). Moreover, at the symptomatic stage, trunk muscles and most cranial muscles remained relatively innervated to pelvic limb muscles. While EOMs, frontalis muscle, and M. levator palpebrae superioris were completely spared (Valdez *et al.*, 2012). By contrast, in SMA, the distal pelvic limb and foot muscles are relatively spared compared to the thoracic limbs, abdominal muscles, and proximal pelvic limb muscles (Woschitz *et al.*, 2022). The mechanism(s) underlying such regional vulnerability are still not well understood. However, the pattern of selective vulnerability can help in the clinical diagnosis of MNDs.

Signs of reinnervation, such as poly-innervated endplates and nerve terminal sprouts, were not observed in the hTDP-43 mice. Previous studies found that the number of axons per NMJ (poly-innervation) increases with disease duration and decreases with the rate of progression (Kang *et al.*, 2014; Bruneteau *et al.*, 2015). It was, therefore, not surprising that these changes were not observed in the hTDP-43 model.

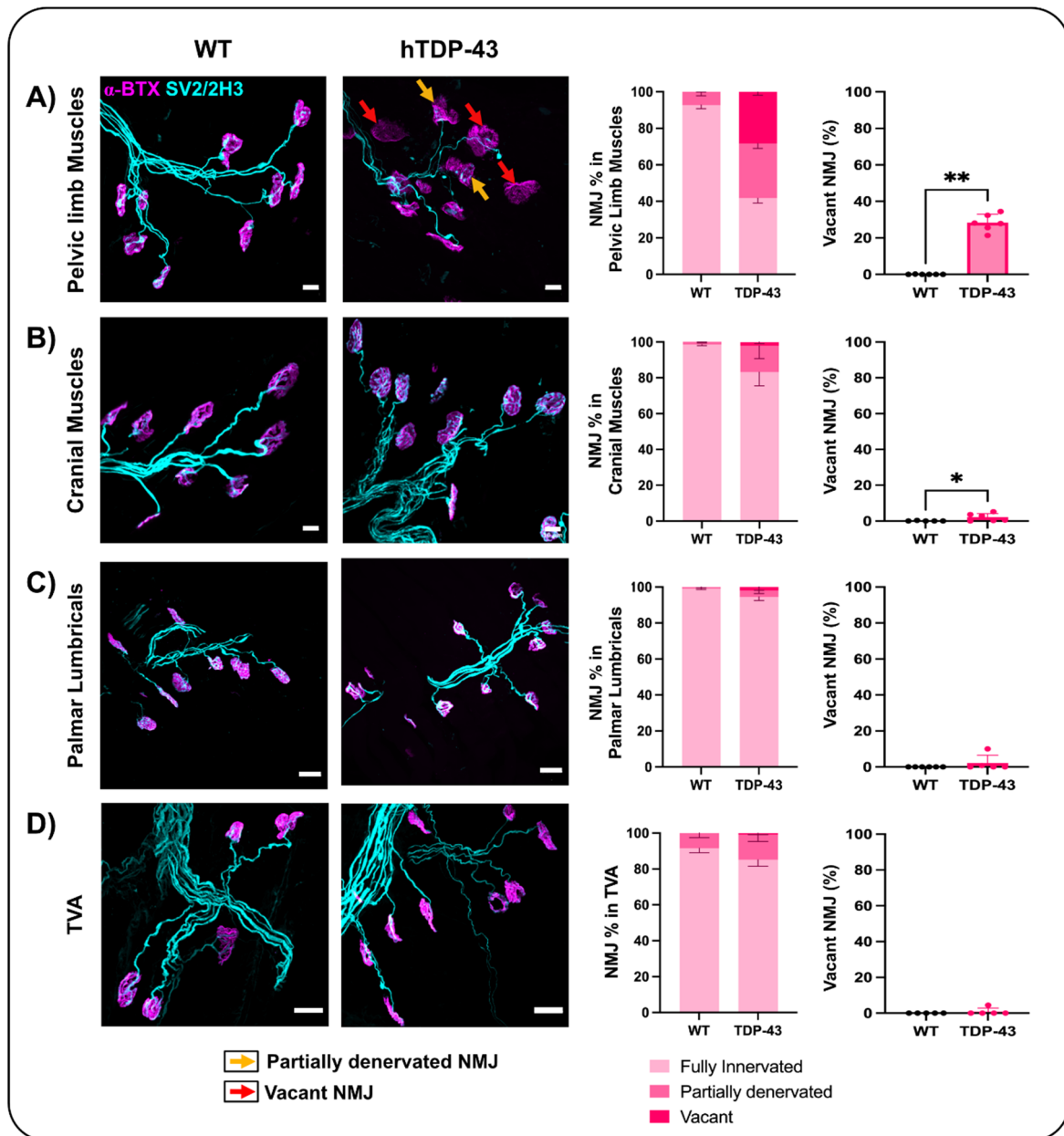


Figure 20: Regional assessment of NMJ pathology shows severe denervation in pelvic limbs at disease end-stage in WT and hTDP-43 mice.

First two columns: show representative confocal images of WT and TDP-43 NMJs from the corresponding body region. WT example images show intact NMJs in all muscles. While in the hTDP-43, pelvic limb shows partially (orange arrows) and vacant NMJs (red arrows), as well as thin pre-terminal axons (**A**). Images from the other body regions show healthy innervated NMJs in the hTDP-43 mouse (**B-D**). Bar charts showing the percentage of NMJs from (**A**) pooled pelvic limb muscles, (**B**) pooled cranial muscles, (**C**) palmar lumbricals, and (**D**) TVA (*M. transversus abdominus*). NMJs were classified as fully innervated, partially denervated, or vacant. The charts show severe NMJ pathology in the pelvic limb muscles (**A**); more than 50% of the NMJs were denervated, being either partially denervated (30%) or

vacant (25%). **(B)** Pooled data from cranial muscles also showed significant pathology, although this was less severe than that affecting the pelvic limb muscles. **(C, D)** NMJs of palmar lumbricals and TVA were preserved. NMJ (%) bars are the averages of pooled muscles of 6 - 8 animals. Bars representing vacant NMJs (%) indicate means \pm SEM. Results of the data (data points) represents the pooled muscles from one animal, N = 5 animals, Mann Whitney test, *P \leq 0.05, **P \leq 0.01. AChR are labelled by α -BTX (α -bungarotoxin) (magenta), and nerve terminals and axons are labelled by anti-SV2 and anti-2H3 antibodies, respectively (cyan). Red arrows indicate vacant NMJs, and orange arrows indicate partial denervation. Scale bars = 10 μ m in pelvic limb and cranial muscles, and 20 μ m in palmar lumbricals and TVA. *Adapted from (Alhindi et al., 2023).*

TSC changes were then investigated in the pelvic limb and cranial muscles, as these were the most severely affected. Overall, loss of tSC labelling at the NMJ (revealed with antibodies against S100b) was more pronounced in the pelvic limbs than the cranial muscles (Figure 21A-C). In many cases of partial loss of S100b labelling, the Schwann cell body remained over the endplate and the cytoplasmic processes were unlabelled. This indicates that the distal parts of the cell may become affected before the cell body (Appendix 15). By contrast, in the SOD1 mice, endplates were devoid of tSC cell bodies and only covered by the cytoplasmic processes of pre-terminal Schwann cells, while other endplates had tSCs with displaced (non-synaptic) nuclei (Carrasco, Seburn and Pinter, 2016).

The small size of NMJs and the presence of multiple nuclei at the synaptic region hindered the precise identification of cell bodies, especially in the WT animals. TSCs sprouts, which have been previously reported in the SOD1 model (Tremblay, Martineau and Robitaille, 2017), were observed in a higher proportion in hTDP-43 compared to WT mice (Appendix 16). In hTDP-43 mice, tSC sprouts were identified in 130 NMJs, while in WT mice, they were found in only 70 NMJs, a difference that was not statistically significant. This is most likely due to the rapid disease progression, as Kang et al., 2019 showed that the proportion of NMJs with tSC sprouts correlates with the duration of denervation (Kang, Tian and Thompson, 2019).

Quantification of tSCs revealed similar regional distribution pattern to nerve terminals, but less severe. About 60% of pelvic limb NMJs were denervated with an equivalent proportion (~50%) of tSCs loss (Figure 21D, E). Similarly, in cranial muscles, less than

20% of the NMJs were denervated and 10% of them had lost their tSC labelling (Figure 21D, E). Correlation analysis also showed that in muscles with a higher percentage of innervation, NMJs were fully covered by tSCs, while in denervated muscles, NMJs had more tSC loss (Figure 21F). Finally, comparing the severity of tSC loss between partially and vacant NMJs showed that the majority of vacant NMJs (60.3%) were associated with total loss of the S100b labelling, whilst 90% of the partially denervated NMJs had parallel, partial loss of S100b labelling (Figure 21G). Some fully denervated endplates were still fully covered by tSCs (Appendix 17). Taken together, these findings imply that changes in tSCs are consequences rather than causes of denervation. TSC pathology is most likely caused by the loss of neuregulin 1 (NRG1) which is released by nerve terminals and binds to ErbB receptors (receptor tyrosine kinase) on tSC surfaces to promote their proliferation and survival (Lin *et al.*, 2000; Escher *et al.*, 2005).

There is currently a paucity of information in the literature regarding the influence of TDP-43 pathology on tSCs. The data presented here fills this gap and represents the first known analysis of tSC pathology in an ALS-TDP-43 mouse model. In comparison, there are some studies of myelinating Schwann cells. Two recently published studies reported a cytoplasmic accumulation of TDP-43 and phosphorylated TDP-43 at myelinating Schwann cells in motor nerves of ALS patients (Nakamura-shindo and Sakai, 2020; Riva *et al.*, 2022). A third study investigated the effect of TDP-43 deletion in myelinating Schwann cells in mice and found that these mice had impaired motor function that was caused by delayed nerve conduction (Chang *et al.*, 2021).

Most studies that reported changes in the structure and function of tSCs were performed on the SOD1 mice or were derived from patient tissue samples. Downregulation of S100b and p75^{NTR} has been reported in ALS patients and SOD1^{G93A} mice (Liu *et al.*, 2013; Carrasco, Seburn and Pinter, 2016; Harrison and Rafuse, 2020). Additional pathological changes in tSCs that have been previously reported include invasion of synaptic cleft by the cytoplasmic processes (Bruneteau *et al.*, 2015), and impaired phagocytic and repair functions in the SOD1^{G37R} mice at pre-symptomatic stage (Arbour *et al.*, 2015; Martineau *et al.*, 2020).

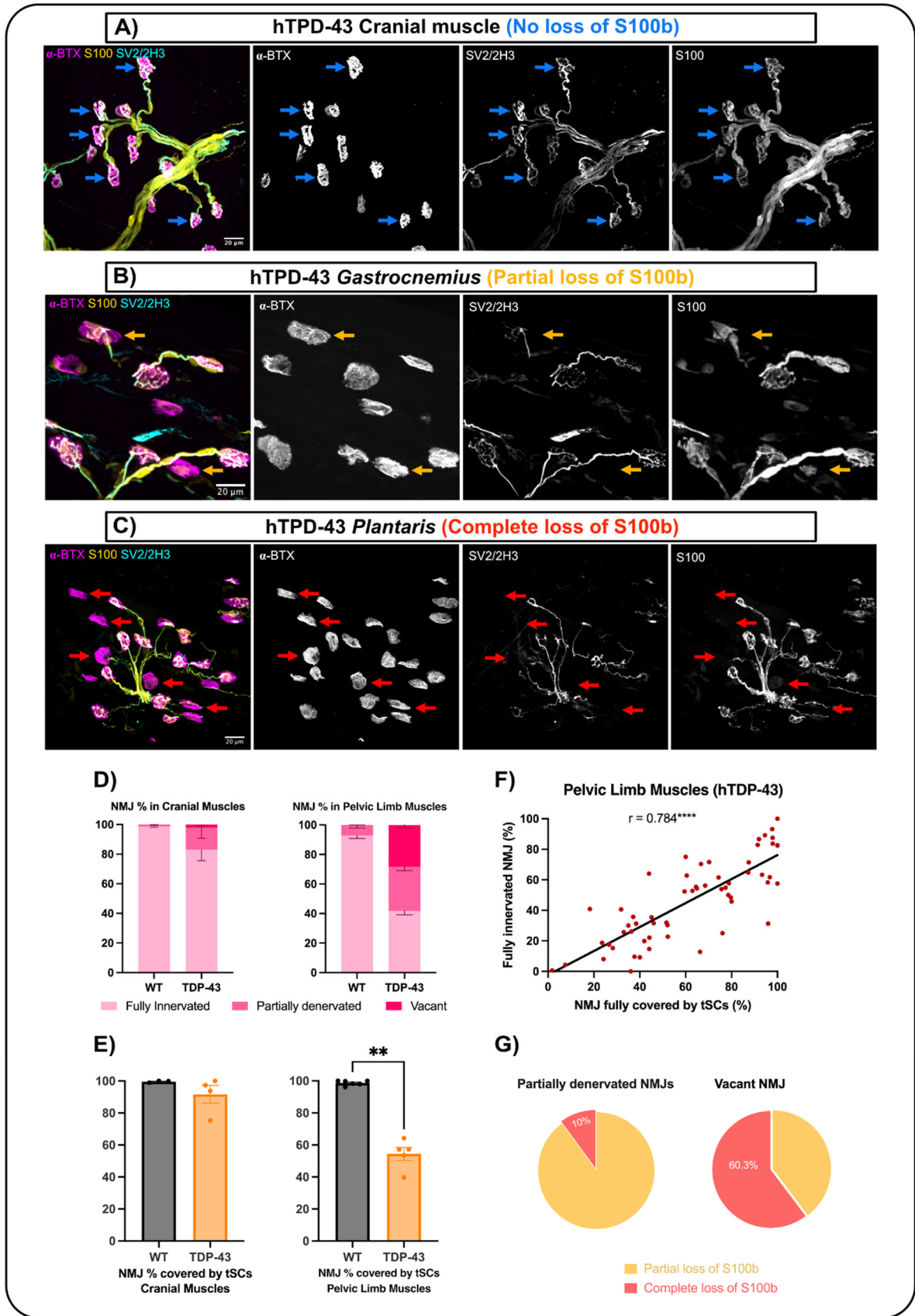


Figure 21: tSC pathology in pelvic limb and cranial muscles of hTDP-43 mice at disease end-stage

(A-C) Confocal micrographs of NMJs from hTDP-43 show variable degrees of tSC loss. **(A)** Fully innervated NMJs are completely covered by tSCs (blue arrows) in cranial muscles. **(B)** Partially denervated NMJs from *gastrocnemius* (orange arrows) with partial loss of S100b labelling. **(C)** Vacant NMJs from plantaris (red arrows) with complete loss of S100b labelling. **(D)** Bar charts illustrating the percentages of innervation and **(E)** the percentages of NMJs completely covered by tSCs in pooled data from cranial and pelvic limb muscles show a similar degree of pathology. **(F)** A linear graph demonstrating a strong positive correlation between the percentage of fully innervated NMJs and NMJs fully covered by tSCs. Each data point represents pooled NMJs of one muscle. **(G)** Pie charts show that 90% of partially denervated NMJs were partially covered by tSCs, while the majority of vacant NMJs (60.3%) had a complete loss of tSC coverage. α -BTX (α -bungarotoxin) was used to label AChR (magenta), anti S100b antibody was used to label tSCs (yellow), anti SV2 and anti 2H3 antibodies were used to label synaptic vesicles (to visualize nerve terminals) and neurofilaments (to visualize axon), respectively (cyan). Scale bar = 20 μ m in all images. *Adapted from* (Alhindi *et al.*, 2023)

3. Within-region assessment of NMJ pathology at disease end-stage

Selective vulnerability of motor neuron pools innervating anatomically distinct muscles is a feature observed in aging and in many MNDs (Vinsant *et al.*, 2013b; Tremblay, Martineau and Robitaille, 2017; Woschitz *et al.*, 2022). In several ALS models, pathological signs such as denervation, mitochondrial abnormalities, a decline in motor unit number and whole muscle contractile force were found in the early disease stages in fast-twitch muscles such as TA, EDL, and GC. However, in SOL (a slow-twitch muscle), reinnervation signs such as poly-innervation, the appearance of nerve terminals and tSC sprouts were more prominent, and denervation did not appear until the late symptomatic stage (Frey *et al.*, 2000; Gould *et al.*, 2006; Pun *et al.*, 2006; Hegedus, Putman and Gordon, 2007; Narai *et al.*, 2009; Valdez *et al.*, 2012; Vinsant *et al.*, 2013b; Sharma *et al.*, 2016; Tremblay, Martineau and Robitaille, 2017; Ebstein, Yagudayeva and Shneider, 2019). Therefore, an assessment of individual cranial and pelvic limb muscles was performed to identify resistant and vulnerable muscles in these regions (Figure 22, Appendix 12-14).

Proportions of denervation varied between muscles in both regions. In the pelvic limbs, 5 muscles showed more than 60% denervation, namely FDB (72% denervation), plantaris (66% denervation), PL (65% denervation), GC (63% denervation), and PB (60% denervation), while the rest had less than 45% denervation: lumbricals (44%

denervation), TA (35% denervation), EDL (34% denervation), and SOL (24% denervation) (Figure 22A). Subsequent analysis revealed that the plantaris had the greatest percentage of vacant NMJs (44%) and SOL had the least (4%) (Figure 22C). In the cranial muscles, only AS and IS had a significant amount of denervated NMJs, with most of them being partially denervated (Figure 22B, D). It is important to note that the changes in AAL and LALc could have been obscured by the high level of heterogeneity between animals. Selective involvement of AAL, AS, and LALc has been well documented in SMA mouse models ($SMN^{\Delta 7}$ and $SMN^{-/-};SMN^2$) (Woschitz *et al.*, 2022). Nonetheless, this is the first study to explore selective vulnerability within cranial muscles in an ALS mouse model.

The spread of data that was observed in some muscles (such as TA, EDL, GC, plantaris, LALc, AAL) was expected (Figure 22A, B). Samples were taken from either body side in this analysis and asymmetrical denervation, which is a characteristic feature of ALS, might explain this variation (Ebstein, Yagudayeva and Shneider, 2019). Sex differences might also play a role; males have an earlier onset, faster progression, and a shorter survival time than females (Logroscino *et al.*, 2010; McCombe and Henderson, 2010; Esmaeili *et al.*, 2013; Bros-Facer *et al.*, 2014; Renzini *et al.*, 2023). Future studies will therefore need to explore symmetry and sex-specific differences in the hTDP-43 ALS model.

Another explanation for wide variance of data within TA and GC is the distribution of fibre types within these muscles. In TA and GC, the slow-twitch fibres are not evenly distributed within the muscle, being exclusively located at the deeper part of the muscle (adjacent to the bone) in both WT and hTDP-43 mice (see Chapter 5: muscle fibre assessment). This phenomenon was also demonstrated in $SOD1^{G93A}$ mice, where the outer two-thirds of TA (adjacent to the skin) contained FF fibres and denervated earlier than the inner third (Pun *et al.*, 2006; Vinsant *et al.*, 2013b). This, however, was taken into consideration during muscle fibre dissection and fibres were always sampled from every part of the muscle. Additionally, the small percentage of slow-twitch fibres in these muscles makes their contribution negligible (see Chapter 5: muscle fibre assessment).

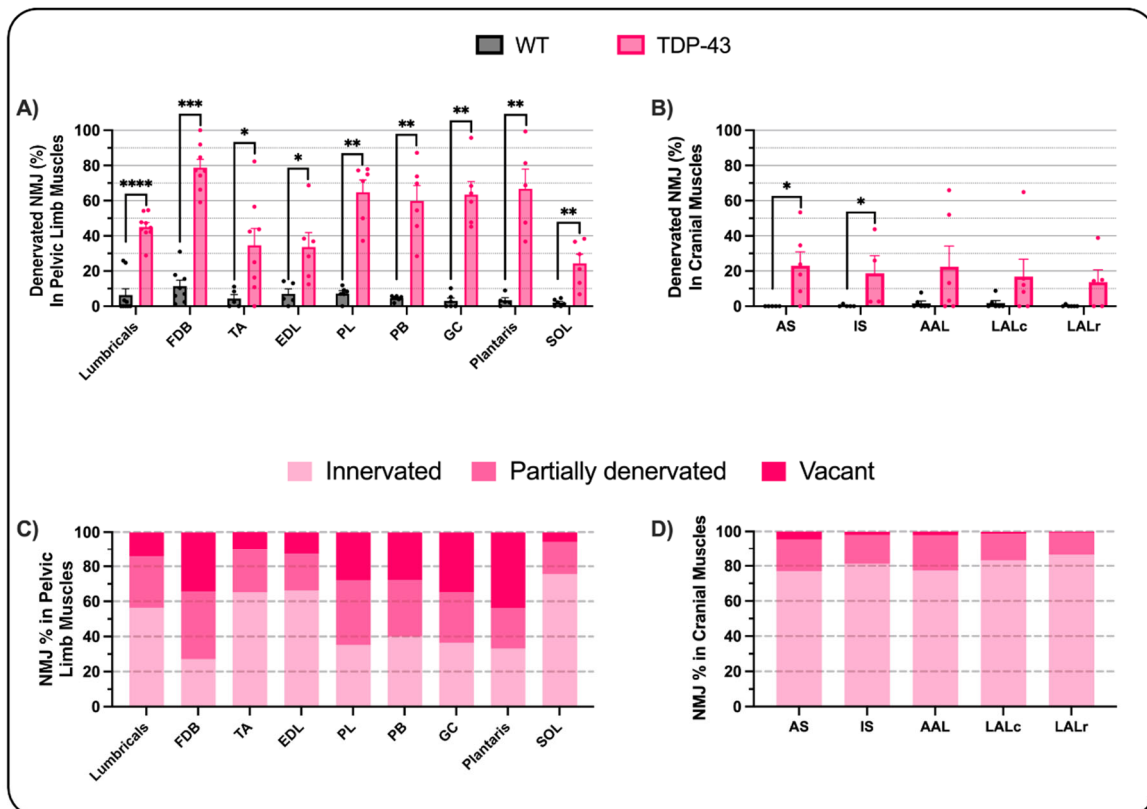


Figure 22: Selective vulnerability in the pelvic limb and cranial muscles of hTDP-43 mice

Bar charts showing significant differences between muscles of the pelvic limbs (**A, C**) and head (**B, D**) at the disease's end-stage. **A**) demonstrates the percentage of denervated NMJs (vacant and partially denervated combined) in each pelvic limb muscle. Charts show significant denervation in all hTDP-43 pelvic limb muscles. PL, PB, GC, and plantaris were the most affected muscles (>60% denervation). While lumbricals, TA, EDL, and SOL had less than 45% denervated NMJs. **C**) Bar chart demonstrating the percentage of innervated, partially denervated, and vacant NMJs in pelvic limb muscles. The graph showed more vacant NMJs in the most vulnerable muscles (plantaris 44%, FDB 34%, GC 34%, PL 27%, PB 27%) compared to the less vulnerable ones (Lumbricals 14%, EDL 12%, TA 11%, SOL 4%). **B**) In cranial muscles, significant denervation was only seen in AS and IS, with the majority of NMJs being partially denervated (**D**). (**A, B**) Bars depict the mean \pm SEM. Data points represent the average of a minimum of 30 NMJs of one animal, N = 6 – 8 animals, Mann-Whitney test, $p^* \leq 0.05$, $p^{**} \leq 0.01$. (**C, D**) Bars depict the mean of all animals. *Adapted from (Alhindi et al., 2023)*

4. Selective involvement of pre-synaptic structures during NMJ pathology

Morphological analysis of pre- and post-synaptic structures at the NMJ was performed using aNMJ-morph on muscle specimens from the pelvic limb to quantify NMJ alterations as a result of denervation (Minty *et al.*, 2020). As expected in this model with MN-restricted overexpression of hTDP-43, significant changes were only observed at pre-synaptic structures, whilst the post-synaptic structures were completely unaffected (Table 3). Consistent with the initial innervation analysis, the plantaris was the most affected muscle followed by PB, GC, and PL. The axon diameter was significantly smaller in all muscle samples from hTDP-43. Nerve terminal area, perimeter and overlap were reduced in all muscles except TA. Significant changes were not detected in TA. This is probably due to the high-level of variability between animals, as discussed in the previous section.

The selective involvement of pre-synaptic structures makes the hTDP-43 model ideal for studying NMJ defects caused solely by MN pathology and in the absence of any intrinsic muscle pathology. However, the rapid progression of disease in this model might not allow sufficient time for alterations to occur in the post-synaptic region, unlike other models with slower disease progression such as the mutated TDP-43 (Q331K and M337V) model, in which decreased endplate size was observed (Chand *et al.*, 2018; Gordon *et al.*, 2019). Additionally, post-synaptic alterations appeared later with disease progression in the relatively slowly progressive SOD1^{G93A} model. These included: a reduction in endplate area (Comley *et al.*, 2016; Mejia Maza *et al.*, 2021) and the length of the post-junctional folds (Vinsant *et al.*, 2013b), increased endplate fragmentation (5 or more AChR islands), the presence of faint AChRs (dimmer areas compared to those at the same confocal plane) and ectopic AChRs (a cluster located 5µm or more from another cluster on the same fibre) (Valdez *et al.*, 2012; Tremblay, Martineau and Robitaille, 2017). Post-synaptic changes were also evident in models with muscle expression of the mutant protein (Picchiarelli *et al.*, 2019; Martin and Wong, 2020) and in ALS patients (Bjornskov *et al.*, 1975; Bruneteau *et al.*, 2015).

Morphometrical variables		TA		PB		PL		SOL		GC		Plantaris	
		WT	hTDP-43	WT	hTDP-43	WT	hTDP-43	WT	hTDP-43	WT	hTDP-43	WT	hTDP-43
Pre-Synaptic Variables	Axon diameter (μm)	1.06	0.6**	0.76	0.28**	0.86	0.23***	1.03	0.7*	0.78	0.24**	0.79	0.23***
	NT area (μm^2)	83.88	72.7	74.71	29.74****	73.24	37.65**	88.34	64.62**	79.35	33.69***	65.67	23.3****
	NT perimeter (μm)	134.7	130	111.6	54.5***	108.1	63**	108.3	89.6**	129.9	65.17**	110	40.2***
	NT complexity	3.6	3.4	3.3	2.6	3.2	2.4**	3.4	3.2	3.68	3.07	3.2	1.9**
Post-Synaptic Variables	AChR area (μm^2)	163.7	170.4	138.5	157.9	142.9	152.3	141.6	147.8	163	180.6	128.9	134
	Endplate area (μm^2)	273.5	288.8	213.9	237.3	224.1	234.6	230	238.6	244.6	261.0	210.2	203.1
	Compactness (%)	59	57.5	64.3	65.8	63.2	66.6	62.8	62.9	66.93	68.84	63.6	65.3
	AChR cluster number	1.05	1.1	0.98	0.95	0.99	1.00	0.97	1.01	0.99	0.98	0.99	0.93
	Fragmentation	0.03	0.08	0.02	0.02	0.01	0.03	0.03	0.04	0.02	0.02	0.03	0.01
Others	Overlap (%)	44	32.6	48.4	16.5***	44.3	17.8***	51.2	36.3*	43.90	17.20**	44.6	14.2**

Table 3: Selective disruption of the pre-synaptic structures in hTDP-43 mice

Morphological analysis of the NMJs in the pelvic limb muscles of WT and hTDP-43 mice was conducted using aNMJ-morph. The table shows complete preservation of the post-synaptic region in all muscles. Values are the mean of 60 - 40 NMJs per animal, N = 6 - 8 animals. (See chapter 3 for a detailed description of each variable). NT: nerve terminals, AChR: acetylcholine receptors, TA: tibialis anterior; PB: peroneus brevis; PL: peroneus longus; SOL: soleus; GC: gastrocnemius. Unpaired T-test was used for parametric variables: axon diameter, NT area, AChR area, NT perimeter, endplate area, and Mann-Whitney test was used for the remaining non-parametric variables. *P \leq 0.05, **P \leq 0.01, ***P \leq 0.001, ****P \leq 0.0001. Adapted from (Alhindi *et al.*, 2023)

5. Timeline of NMJ denervation in pelvic limb muscles

To gain a thorough understanding of the NMJ's contribution to disease progression, the severely affected pelvic limb muscles (plantaris and PL) and the most resistant pelvic limb muscle (SOL) were examined at pre-symptomatic (P8) and early symptomatic stages (P15). Results showed no denervation in any muscle before the onset of symptoms (Figure 23B). The first evidence of denervation was seen in plantaris and coincided with the symptom onset and MN death in the lumbar spinal cord (Figure 23, Appendix 18, Figure 19, Figure 24). In contrast, both PL and SOL remained fully innervated at this stage. The labelling of tSCs was preserved across all muscles (Appendix 18). By the end-stage of the disease, PL and plantaris demonstrated a dramatic drop in the percentage of innervated NMJs, while SOL displayed only a mild loss of innervated NMJs (Figure 23B). Although PL and plantaris showed similar degrees of denervation at the end-stage, disease onset was delayed

in PL, which might indicate that the disease progressed more rapidly in PL once initiated. Collectively, these data show differences in the onset and the progression rate of denervation between muscles, with the SOL being the most resistant muscle, i.e., the slowest to degenerate. It also emphasises the early involvement of the NMJ in the pathogenesis of ALS in this model.

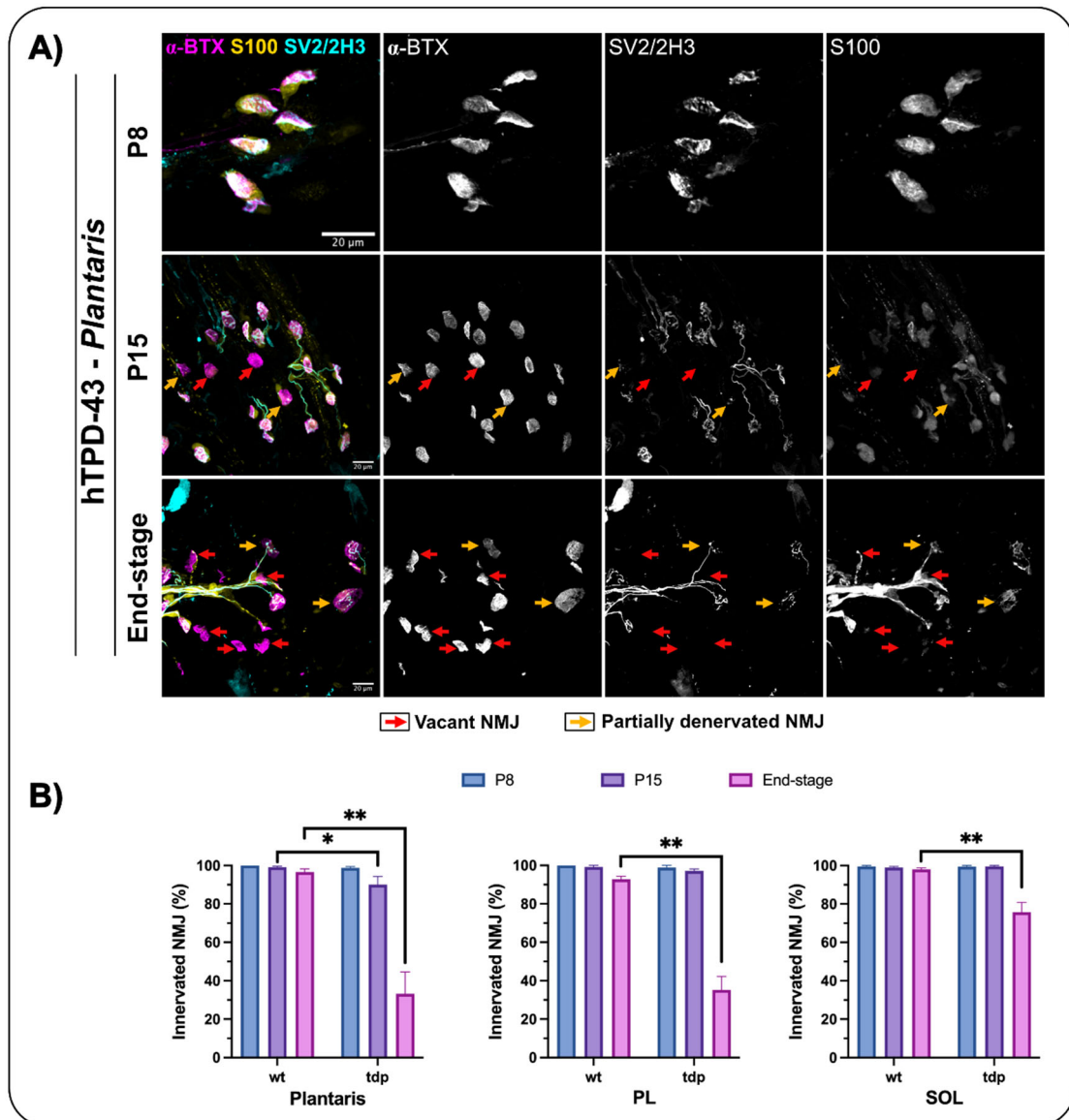


Figure 23: NMJ denervation at early symptomatic stages in plantaris

A) Representative confocal micrographs of hTDP-43 NMJs from plantaris at different time points: pre-symptomatic (P8), early symptomatic (P15), and disease end-stage (P19,20). The images show preservation of NMJ structure at P8, and some vacant (red arrows) and partially denervated NMJs (orange arrows) with loss of S100b labelling at P15 and end-stage. **B)**

Quantitative analysis of innervated NMJ in plantaris, PL, and SOL. Despite having a similar percentage of innervation at end-stage, only plantaris showed significant denervation at P15 while PL remained fully innervated. Denervation was evident in PL and SOL at end-stage only. Bars depict mean \pm SEM, Mann-Whitney test, $p^* \leq 0.05$. α -BTX (α -bungarotoxin) was used to label AChR (magenta), anti S100b antibody was used to label tSCs (yellow), anti SV2 and anti 2H3 antibodies were used to label synaptic vesicles (to visualize nerve terminals) and neurofilaments (to visualize axon), respectively (cyan). Scale bar = 20 μ m in all images. Adapted from (Alhindi *et al.*, 2023)

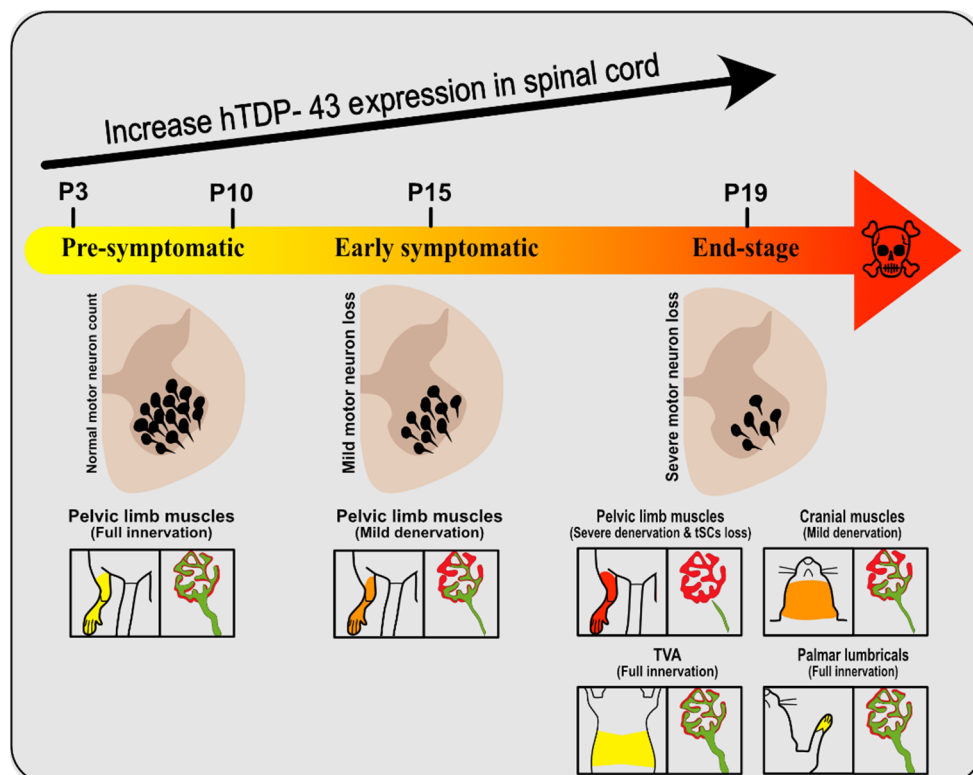


Figure 24: Progression of pathological changes in the hTDP-43 mouse model.

A schematic diagram summarising the changes in hTDP-43 expression, MN count in the lumbar region, and NMJ integrity in muscles over the disease's course. Spinal expression of hTDP-43 gradually increases from P3 onwards. The elevation in hTDP-43 level triggered ALS-like symptoms at P15. MN death and mild denervation of pelvic limb muscles coincided with symptoms onset, with further increase in MN death and NMJ pathology increasing in severity in pelvic limbs and spreading to cranial muscles by the end-stage. The black circles in the half sections of the spinal cord represent MN cell bodies in the ventral horn. The different colours of body regions illustrate the severity of denervation (yellow indicates full innervation, orange indicates mild denervation, and red indicates severe denervation). Drawings of NMJs illustrate nerve terminals in green and AChRs in red. Adapted from (Alhindi *et al.*, 2023)

Conclusions

The aim of the study was to comprehensively examine MN pathology in the *Thy-1* hTDP-43 model. It involved a detailed analysis of the progression of hTDP-43 overexpression in the spinal cord, lumbar MN loss, and NMJ pathology in different body regions. This rapidly fatal model of ALS developed a severe NMJ pathology of pelvic limb muscles, affecting pre-synaptic structures only, accompanied by a significant MN loss at the disease end-stage. Both pathologies were first detected at the early symptomatic stage, at P15. Cranial muscles showed only a mild denervation at the disease end-stage, whilst abdominal and thoracic limb muscles were completely spared. In the pelvic limb, plantaris showed the highest percentage of vacant NMJs followed by GC, PB, and PL. In contrast, the slow twitch muscle, SOL, demonstrated the lowest percentage of vacant NMJs. The selective overexpression of hTDP-43 in MNs facilitated studying the pathological alterations of tSCs that are secondary to MN degeneration. The degree of tSC pathology correlated with the severity of NMJ denervation: pelvic limb muscles, showed the severest denervation and demonstrated a severe loss of tSCs at the disease end-stage, while cranial muscles showed a mild denervation with no loss of tSCs. Overall, this model developed a clear MN pathology, making it a suitable tool to study MN-specific pathology in ALS. Additionally, the rapid progression of disease makes it an ideal option for brief experiments that save both time and costs.

Chapter 5: Histological changes in muscle fibres of the Thy-1 hTDP-43 ALS mouse model

Introduction

Skeletal muscle weakness is the predominant feature of ALS. It has been postulated that skeletal muscle might be a site of primary injury at an early stage in the ALS disease process and is affected prior to MN degeneration and symptom onset. As such, skeletal muscle is an accessible primary target for novel therapies (Dobrowolny *et al.*, 2008; Marcuzzo *et al.*, 2011; Pikatza-Menoio *et al.*, 2021).

The gross anatomical morphology of skeletal muscle in ALS is of great interest. Most of the studies that investigate the involvement of muscles in the pathogenesis of ALS are performed in SOD1 mouse models or otherwise use skeletal muscle samples from ALS patients. Muscle fibre atrophy has been reported in ALS patients and SOD1 mice (Dobrowolny *et al.*, 2008; Ahmadi *et al.*, 2010; Marcuzzo *et al.*, 2011; Mueller *et al.*, 2022), in addition to mitochondrial changes including aggregations, enlargement, vacuolization, swelling, formation of myelin-like figures, and abnormal cristae (Afifi *et al.*, 1966; Chung and Suh, 2002; Dobrowolny *et al.*, 2008). Post mortem sampling of skeletal muscle from ALS patients have shown fibre grouping, fibre splitting, an increase in connective tissue and fat content (Ahmadi *et al.*, 2010), and muscle fibrosis (Gonzalez *et al.*, 2017). Examination of pelvic limb muscles in SOD1^{mus} transgenic mice revealed formation of crystalline inclusions, satellite cell apoptosis, mitochondrial vesiculation and swelling, disruption of sarcomeres (Dobrowolny *et al.*, 2008; Martin and Wong, 2020) and a shift from glycolytic to oxidative metabolism (Dobrowolny *et al.*, 2008). This shift in metabolic activity is more likely due to an increase in oxidative stress and reactive oxygen species (ROS) (Dobrowolny *et al.*, 2008). In addition, several genes that are implicated in metabolic pathways, myogenesis, and axon regeneration are dysregulated in the muscles of ALS patients and SOD1 mouse models (Jokic *et al.*, 2005; Dobrowolny *et al.*, 2008; Manzano *et al.*, 2011).

TDP-43 is an essential protein that is required for normal myoblast differentiation, proliferation, and survival. It forms myo-granules that binds to sarcomeric mRNA transcripts during muscle formation and regeneration (Vogler *et al.*, 2018). Few

studies have examined pathological muscle changes in ALS-TDP-43 mouse models. While Prp-TDP-43^{A315T} mice displayed pronounced muscle fibre atrophy in TA and GC muscles at disease end-stage (Wegorzewska *et al.*, 2009), TDP-43_{prP} mice did not develop similar changes in GC (Xu *et al.*, 2010).

In the current study, the restricted overexpression of hTDP-43 in MNs caused severe pelvic limb denervation and loss of MNs in mice (see previous chapter). Thus, this model provides the opportunity to explore whether rapidly progressive MN pathology affects skeletal muscle or not, and whether histological differences exist between vulnerable and resistant muscles.

Hypothesis of the study:

Based on the findings of the previous chapter (chapter 4), the restricted overexpression of hTDP-43 in MNs is not expected to have a detrimental effect on the histological features of the muscles.

Aims of the study:

- To investigate features of muscle histology in the Thy1-hTDP-43 mouse model of ALS by examining cross sections of pelvic limb muscles at disease end-stage.
- To investigate whether selective vulnerability of muscles is related to fibre type by correlating NMJ denervation with the proportion of slow-twitch fibres.

Methods

Animals and tissue collection

See previous chapter for details on animal models. Cross sections of pelvic limb muscles were studied at disease end-stage in WT and hTDP-43 mice (N = 3 in each group). Pelvic limbs were dissected and immediately fixed with 4 % PFA (Electron Microscopy Sciences, 15710) for 2 hours, then washed thoroughly with 1x PBS. The same muscles that were analysed for NMJ pathology (in the previous chapter) were dissected (lumbricals, FDB, TA, EDL, PL, PB, SOL, GC, and plantaris) and immersed in 30% sucrose overnight. The next day, these muscles were placed in a solution of

1:1 OCT-30% sucrose for 30 minutes, then embedded in OCT. To allow comparison between WT and hTDP-43 mice, the block was labelled with a marker at the thickest part of the muscle belly from which sections were collected at 16 μ m thickness with a cryostat. Slides were allowed to air dry for 60 minutes, then stored at -20°C overnight and stained the next day.

Muscle fibre staining

Slides were allowed to thaw, then rinsed with 1x PBS and placed in pre-cooled methanol at -20°C for 6 minutes. After that, heat-mediated antigen retrieval was performed with tris EDTA (pH 9) solution for 10 minutes. Slides were allowed to cool before washing with warm tap water and 1xPBS (2 x 5 minutes). Slides were blocked with 2% BSA (Sigma Aldrich) for 1 hour; then incubated in the following primary antibodies at 4°C, overnight: mouse supernatant anti BA-D5 IgG (made in BSA at 1:250 dilution, from developmental studies hybridoma bank) to label myosin heavy chain type-1 (slow-twitch muscle fibres), and rabbit polyclonal anti laminin 1+2 IgG (in BSA at 1:500 dilution, ab7463, Abcam) to label muscle fibre basal lamina. Slides were then washed 3 \times 5 minutes with 1xPBS and incubated in the secondary antibodies: AlexaFluor-488-conjugated donkey anti-mouse IgG antibody (made in PBS at 1:500 dilution, a21202, Life Technologies), and AlexaFluor-594-conjugated donkey anti-rabbit IgG antibody (made in PBS at 1:500 dilution, A10043, Life Technologies) for 6 hours at room temperature, away from light. Finally, samples were washed for 3 \times 5 minutes with 1xPBS, then, mounted in Vectashield mounting media with DAPI (H-1200-10, 2BScientific). Coverslips were sealed by clear nail polish and slides were stored at -20°C.

Muscle cross sectional imaging

Images were recorded with a Nikon A1R FLIM confocal laser scanning microscope with 20 \times objective. Images were taken at 16-bit, Z-stack images with 4 μ m interval; red channel-561 nm excitation; green channel-488 nm excitation; blue channel-405 nm excitation. The maximum intensity projection images were used for analysis.

Muscle fibre analysis

Muscle fibre analysis was performed using Fiji software. The entire muscle cross section was analysed for the following parameters: total muscle fibre count, total count of slow-twitch fibres, group atrophy, fibre type grouping (grouping of fibres of the same type), and centrally located nuclei (nuclei that are located at the centre rather than the periphery of the muscle fibres). Muscle fibre counting was performed manually using the cell counter function in Fiji; BA-D5 positive fibres were considered slow-twitch fibres, while the remained unstained fibres were considered fast-twitch fibres. Muscle fibre area was measured manually at randomly selected microscopic fields, using the tracing tool in Fiji, and the mean of areas for more than 200 muscle fibres was calculated. Finally, muscles were visually examined for the presence of central nuclei and for fibre type grouping.

Statistical analysis

Statistical analysis was performed using GraphPad Prism Software (version 9). Mann Whitney test was used to compare the non-continuous variables (number of muscle fibres and the percentage of slow-twitch fibres) of each muscle between WT and hTDP-43. Unpaired t-test was used to compare the continuous variable (muscle fibre area) between WT and hTDP-43 mice. All results were expressed as mean \pm standard error of the mean (SEM). P values < 0.05 were considered statistically significant.

Results and discussion

1. Gross skeletal muscle atrophy with no regenerative changes in hTDP-43 mice

Muscle cross sections were labelled to investigate the differences in the muscle size, fibre type and nuclear position between WT and hTDP-43 mice. Initial qualitative assessment suggested gross atrophy of all pelvic limb muscles in hTDP-43 compared to WT muscles (Figure 25).

Plasticity (remodelling of fibre type or size in response to functional demands) is a characteristic feature of skeletal muscle fibres. Fibre type composition is primarily determined during development (Jiwlawat *et al.*, 2018) but it can be altered in response to pathological conditions that causes progressive denervation such as ALS

(Hegedus *et al.*, 2008). In ALS, denervated muscle fibres are re-innervated by neighbouring, more resistant MNs, which causes a change in fibre type composition and leads to the characteristic phenotype of fibre type grouping and hybrid fibres (Hegedus *et al.*, 2008).

To investigate fibre type switching in hTDP-43 muscles, slow-twitch fibres were labelled in muscle cross sections. As expected, SOL showed the highest proportion of slow-twitch fibres. Almost half of the muscle fibres in SOL were composed of the slow-twitch type in WT and hTDP-43 mice. Moreover, in both WT and hTDP-43 mice, slow-twitch fibres appeared similar in number and distribution, implying no fibre type grouping or switching in the hTDP-43 muscles (Figure 25).

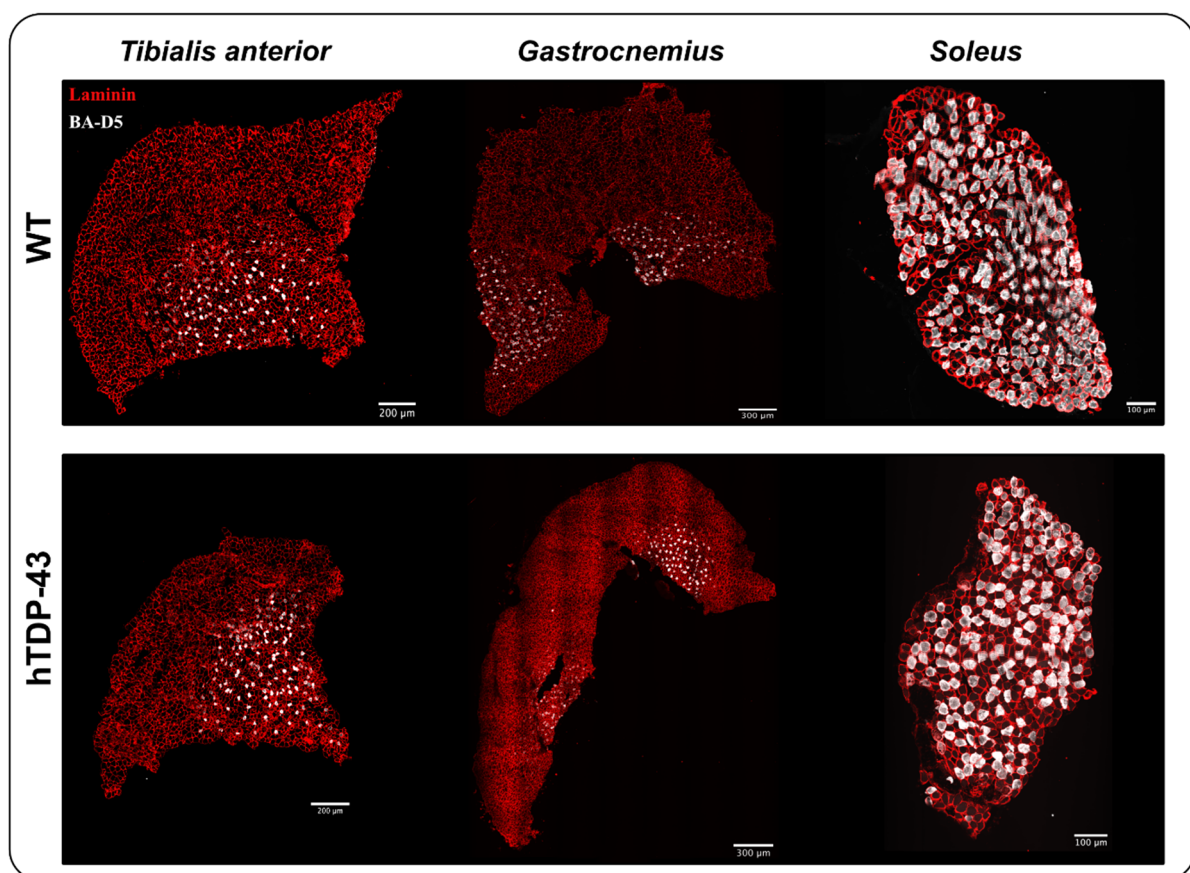


Figure 25: Decreased muscle mass in hTDP-43 mice.

Representative cross sections of pelvic limb muscles (M. tibialis anterior, gastrocnemius, and soleus) in WT and hTDP-43 mice. hTDP-43 muscles were visibly smaller than WT. No apparent changes in the number or the distribution of slow-twitch fibres was noted. The muscle fibre basal laminae were labelled with anti-laminin antibody (red), and slow-twitch fibres were labelled with anti-BA-D5 antibody (white). The scale bar in M. tibialis anterior = 200 μm , in gastrocnemius = 300 μm , and in soleus = 100 μm .

Muscle cross sections were then evaluated for the presence of centrally located nuclei. During muscle fibre maturation, nuclei migrate from the centre of the fibre to the periphery (Roman and Gomes, 2018). Centrally located nuclei have been reported in many muscular disorders that exhibit muscle wasting and their presence indicates an ongoing muscle remodelling (Folker and Baylies, 2013). Examination of muscle cross sections revealed that all nuclei were normally located at the periphery (Figure 26). These initial observations of small muscles, i.e., absence of fibre type grouping and central nuclei are suggestive of degenerative, rather than regenerative, changes in muscle fibres. This is in keeping with the presented data of NMJ pathology in the previous chapter, where NMJ denervation was predominant over re-innervation. This is expected in this rapidly progressive ALS model. The rate of MN degeneration most likely exceeded the regenerative rate.

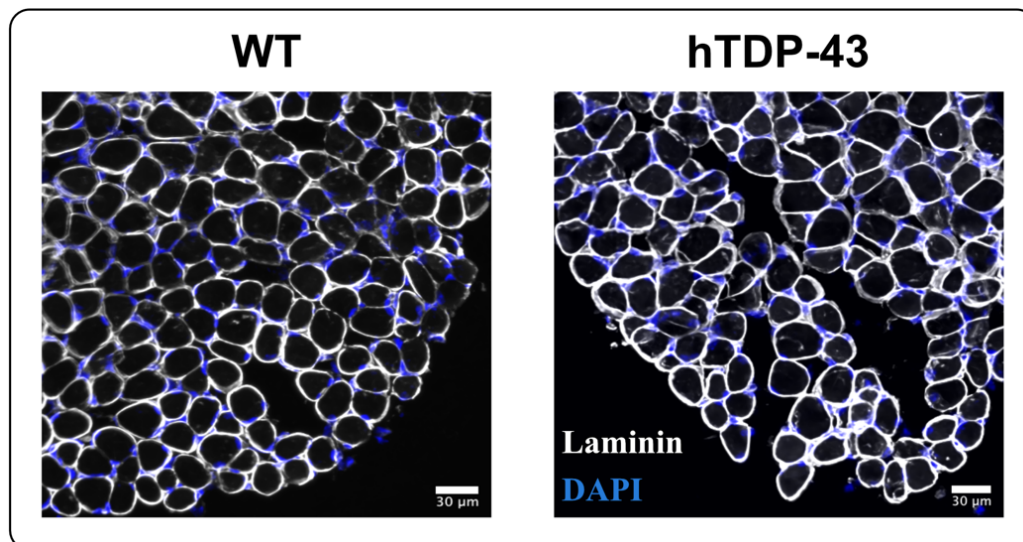


Figure 26: No evidence of centrally located nuclei in hTDP-43 muscles.

Representative cross sections of pelvic limb muscles in WT and hTDP-43 to illustrate the location of myofibre nuclei. In both mice, all nuclei were located at the periphery of the muscle fibres. Muscle fibre basal laminae were labelled with anti-laminin antibody (white), and nuclei were stained with DAPI (blue). The scale bars = 30 μm.

This observation is further supported by the presence of fibre type grouping, and centrally located nuclei in models in which disease progression is less rapid, indicating an ongoing degeneration/regeneration process. For instance, centrally located nuclei and fibre atrophy were observed after 8 weeks of hTDP-43^{ΔNLS} expression (which has

an average survival time of 10-18 weeks) (Walker *et al.*, 2015), and at 10 months in TDP-43^{Q331K} mice, which develop motor deficits at around 3 months and significant MN degeneration and denervation at 10 (Arnold *et al.*, 2013). Significant increases in centrally located nuclei have also been observed in the SOD1^{G93A} model and was associated with marked atrophy of genioglossus (a tongue muscle) (Mueller *et al.*, 2022) and biceps femoris (Marcuzzo *et al.*, 2011). Fibre type grouping was reported in patients (Jensen *et al.*, 2016) in addition to the presence of hybrid fibres (mixed fibres that express more than one myosin isoform) (Baloh *et al.*, 2007). Conversely, TDP-43^{Q331K-Low} and TDP-43^{M337V} models, which did not show NMJ loss at 10 months, had no histological muscle changes at all (Arnold *et al.*, 2013). Taken together, these findings indicate that the rate of progression of MN pathology influences skeletal muscle changes, i.e., the fast rate of MN degeneration prevents compensatory muscle regeneration.

2. Muscle fibre atrophy in the absence of compensatory changes in the pelvic limb muscles of hTDP-43 mice

To confirm initial qualitative observations, quantitative analysis of muscle fibre variables was performed. Cross-sectional fibre area and muscle fibre counts were used as indicators of muscle atrophy, and compensatory changes, including muscle fibre hypertrophy and fibre type switching, were also evaluated in the pelvic limb muscles of hTDP-43 and WT mice.

There was no significant difference in the total muscle fibre count between hTDP-43 and WT mice in all muscles, implying that the small size of hTDP-43 muscles was not the result of muscle fibre loss (Figure 27). Consistent with initial observations, SOL had the largest percentage of slow-twitch fibres across all muscles. Almost 40% of muscle fibres were slow-twitch in both WT and TDP-43 mice, compared to between 4% and 22% in the other muscles. A slight increase in the proportion of slow-twitch fibres was found in most hTDP-43 muscles (lumbricals, TA, PL, PB, plantaris, and SOL) but none of these were significantly different from WT (Figure 27). The absence of changes in fibre type proportion might suggest the lack of compensatory muscle regeneration due to the rapidly progressive nature of the disease. Alternatively, changes might have occurred between the subtypes of the fast-twitch fibres. In the SOD1 model, several studies have reported a significant reduction of the vulnerable

fast-fatigue fibres with a corresponding increase in the fast-intermediate fatigue and fatigue-resistant fibres (Hegedus, Putman and Gordon, 2007; Hegedus *et al.*, 2008; Stallings *et al.*, 2010; Dobrowolny, Aucello and Musarò, 2011; Peggion *et al.*, 2017).

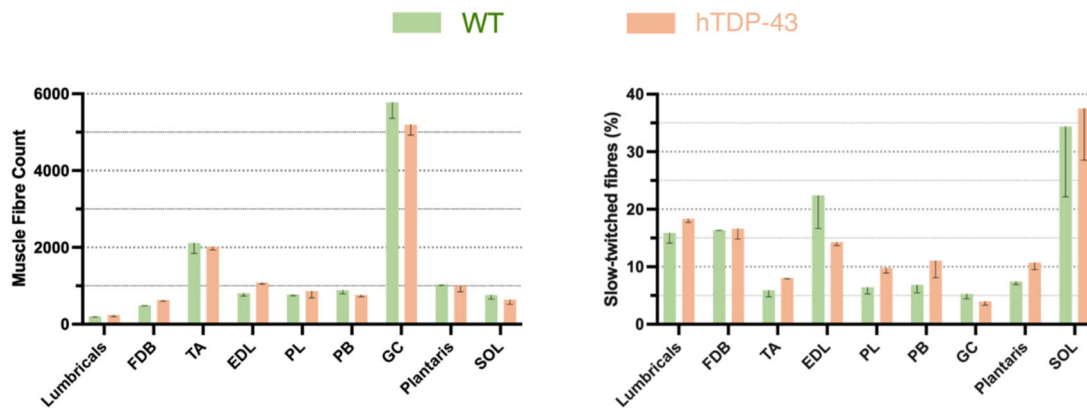


Figure 27: No difference in total muscle fibre count or percentage of slow- to fast- twitch fibres between WT and hTDP-43 mice.

A) Muscle fibres were manually counted in the whole cross section and the average \pm SEM of 3 muscles was depicted. The high number of muscle fibres in GC (in both WT and hTDP-43 mice) compared to other muscles reflect its large size (gross anatomy). **B)** The percentage of slow-twitch fibres in 3 muscles per genotype was calculated and the average \pm SEM depicted for each muscle. N = 3, Mann-Whitney test.

Muscle fibre atrophy was found in almost all pelvic limb muscles in the hTDP-43 mice. Muscle fibre cross-sectional area was lower in most hTDP-43 muscles, showing a statistical difference in lumbricals, FDB, TA, and plantaris (Figure 28A). The reduction in muscle fibre area explains the gross atrophy of the muscles that was previously observed (Figure 25). The degree of muscle fibre atrophy varied between muscles with FDB and GC having the highest percentages of atrophy (over 30%) with PL and PB having the lowest (less than 10%) (Figure 28B). Moreover, frequency distribution analysis of the muscle fibre area of TA and GC demonstrated a shift in the values for hTDP-43 mice to the left (towards small sized fibres) (Figure 28 C, D). This indicates that atrophy without compensatory hypertrophy has occurred, which is perhaps to be expected in a rapidly progressing model as demonstrated previously in studies using human tissue samples; several studies have found that muscle atrophy was more likely in patients with a rapidly-progressing disease, while patients with a slower

progression showed compensatory type switching and fibre hypertrophy (Krivickas *et al.*, 2002; Jensen *et al.*, 2016; DI Pietro *et al.*, 2017).

Although PL and PB showed severe NMJ denervation (previous chapter) they did not develop muscle fibre atrophy (Figure 28A, B). The reason for this is unclear. One possible explanation is that atrophied muscles have an earlier onset of NMJ denervation than non-atrophied muscles. As shown in the previous chapter (Figure 23), NMJ denervation started at the early symptomatic stage (P15) in plantaris but not in PL. consequently, there may have been enough time for fibre atrophy to occur in plantaris but not in PL. Furthermore, FDB and GC, which developed the most severe atrophy (Figure 28b), showed higher percentages of vacant NMJs (34%; chapter 4, Figure 22C), while PL and PB both had 27% vacant NMJs. Thus, disease duration, as well as the severity of denervation might be contributing to muscle atrophy in ALS (Figure 28b).

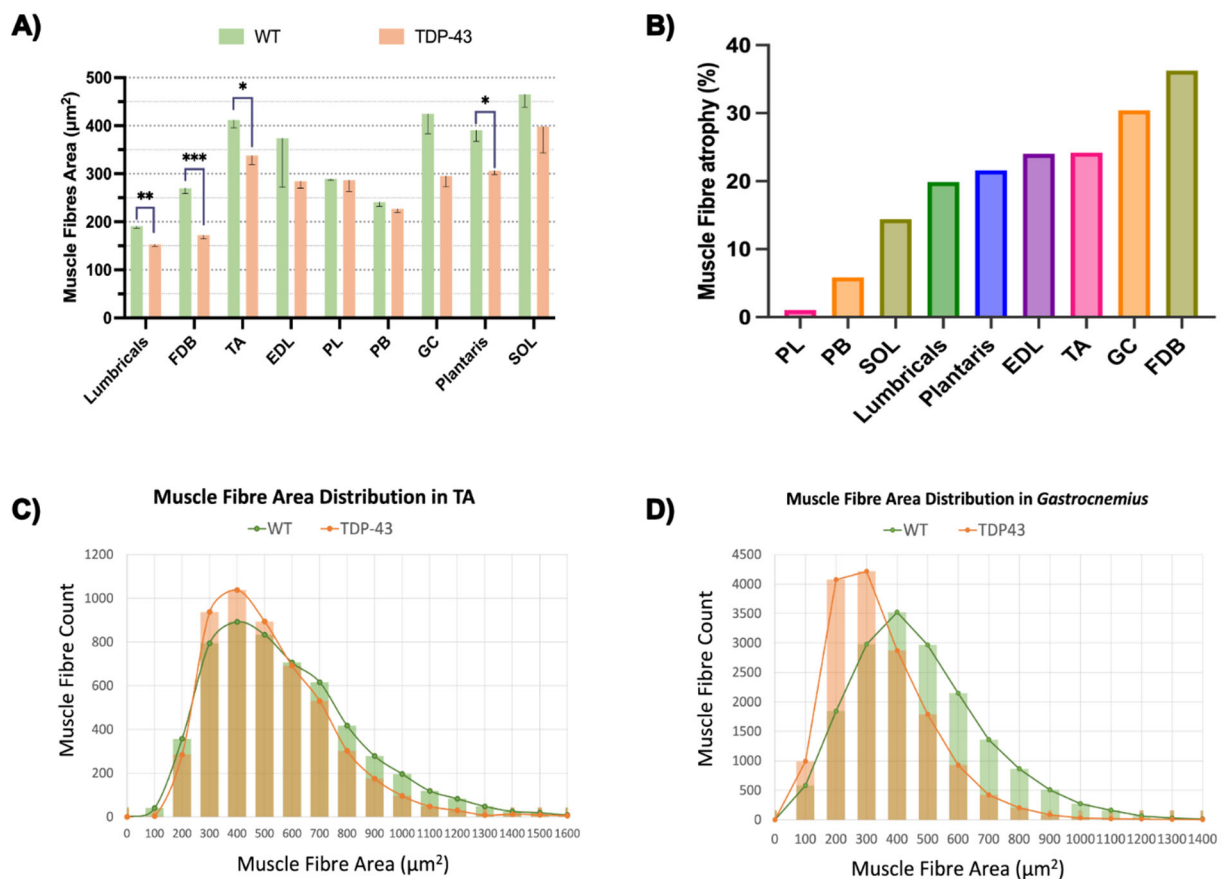


Figure 28: Significant muscle fibre atrophy in hTDP-43 mice at disease end-stage.

(A) Almost all pelvic limb muscles in hTDP-43 mice had a smaller total muscle fibre area compared to WT but the difference was only significant in 4: lumbricals, FDB, TA, and *plantaris*. N = 3. Bars depict mean \pm SEM, Unpaired t-test, $P^* \leq 0.05$, $P^{**} \leq 0.01$, $P^{***} \leq 0.001$. (B) Bar chart showing variable degree of muscle fibre atrophy between the different pelvic limb muscles in hTDP-43 mice. FDB and GC had the highest percentage of fibre atrophy, while PL and PB had the least. (C, D) Muscle fibre area distribution in TA and *gastrocnemius* illustrates left shift of hTDP-43 values (orange bars) indicating an increase in the small fibres (atrophy) and a decrease in the large ones (absence of compensatory hypertrophy). N = 3 in all charts.

Conclusions

The aim of this study was to provide a meticulous characterisation of skeletal muscle pathology in the Thy1-hTDP-43 mouse model of ALS. Examining the influence of MN degeneration on skeletal muscle morphology provided valuable insights into disease progression. It presented an overview of the histological changes in pelvic limb muscles and showed a mild atrophy affected primarily the most denervated muscles. This implies that muscular changes were most likely induced by MN degeneration. Furthermore, the severe, rapidly progressing MN degeneration prevented compensatory changes such as fast to slow fibre type switching and fibre grouping. Taken together, the findings from this chapter and the previous one demonstrated that the *Thy-1* hTDP-43 ALS mouse is a powerful model for studying MN pathology, in addition to the secondary degenerative changes affecting muscles and tSC in ALS.

Chapter 6: General Discussion

The involvement of the NMJ in many neurodegenerative diseases (Murray, Talbot and Gillingwater, 2010) makes it an area of interest for both basic research and as a potential therapeutic target. Until recently, NMJ research has relied on rodent models, particularly the mouse. However, Jones *et al.*, revealed marked differences exist between mouse and human NMJs (Jones *et al.*, 2017), highlighting interspecies differences and questioning the reliability of the mouse as a model of the human NMJ. These findings have encouraged further investigations of mouse and human NMJ differences and fuelled the need to identify a more appropriate animal model. The main aims of this project were to highlight the importance of studying the NMJ as a target in MND, particularly in ALS, and to explore other species to find a more representative model of the human NMJ.

Morphological comparison of mouse and human terminal Schwann cells

This study presented a robust methodology for morphometric analysis of tSCs at the mammalian NMJ. Whilst tSC labelling is an established technique, the more detailed morphometric analyses of tSCs developed here will allow more extensive studies in disease models and facilitate comparative anatomical studies. Furthermore, this approach has been validated by identifying the differences in tSCs at the NMJs of the pelvic limb muscles between mice and humans (chapter 2).

This study (chapter 2) was built on the previously published study by Jones *et al.*, 2017 which identified the major differences between the human and murine NMJ. It only explored two of the three main components of the NMJ: the MN terminal and the endplate, while tSCs were not studied (Jones *et al.*, 2017). The findings presented in this project (chapter 2) provide a description of the morphological differences between mouse and human tSCs.

The mouse NMJ is considerably larger than the human NMJ, so the corresponding increase in size (but not number) of tSCs indicates that tSCs have the capacity to expand, rather than divide, to support larger synapses. The strong positive correlation between tSC area and NMJ size, in contrast to the weak correlation with tSC number,

further supports this notion. The presence of non-synaptic nuclei and lesser coverage of AChRs in humans are also clinically relevant findings. While these two features were observed in healthy human NMJs, they have been documented in diseased mouse models of neurodegenerative disorders. For example, the presence of vacant AChRs area was reported in SMA (Murray *et al.*, 2013; Neve *et al.*, 2016) and ALS mouse models (Liu *et al.*, 2013; Carrasco, Seburn and Pinter, 2016; Harrison and Rafuse, 2020), as well as a significant increase in the proportion of NMJs with non-synaptic tSC nuclei in the SOD1 ALS mouse model (45% compared to 8% in WT)(Carrasco, Seburn and Pinter, 2016). Therefore, findings from animal models should be translated cautiously into humans.

2.1 Study limitations and future directions

The analysis of tSC morphology was done using one muscle only (PB) because of the limited availability of human tissue samples at the lab and the difficulty in obtaining new human tissue samples.

One major concern was related to the use of tissue harvested from amputated limbs of patients with peripheral vascular diseases. No study up to date has investigated the effect of chronic ischemia, hypertension, or inflammation due to peripheral vascular disease on the morphology of tSC. However, a study has found dramatic changes in nerve terminals morphology and significant denervation in response to 2 hours of hypoxia followed by 2 hours of perfusion in young and old mice (Baxter, Gillingwater and Parson, 2008). In the current study, the absence of apparent pathological signs such as denervation, nerve terminal sprouting, or retraction provide strong evidence for the validity of the results. Moreover, during surgery, the level of amputation is determined based on the presence of adequate blood flow to ensure wound healing, and samples were always collected close to the line of incision (level of amputation) to ensure collecting healthy samples. Additionally, qualitative comparison of tSC morphology between the lower limb muscle samples (PB, obtained from discarded amputated limbs) and M. rectus abdomens samples (obtained during abdominal surgery) showed a similarity in the overall morphology and argues against any major impact of the underlying condition on the morphology of tSC.

Future studies are recommended to further explore and characterize tSCs in both humans and mice, and in muscles from other body regions. Investigating the

morphological changes of tSCs across the lifespan will shed light on tSC responses to ageing in both species. In addition, investigating the NMJ coverage capacity of a single tSC in a time-course experiment will be informative, as the ability of a single myelinating Schwann cell to support a large segment of the axon increases with age (Berthold and Nilsson, 1987).

As shown previously, humans have a different architecture of the active zone protein SNAP25 with larger and denser puncta than mice (Jones *et al.*, 2017). With the presence of these molecular differences between mouse and human at the nerve terminals, it is entirely possible that there will be parallel molecular differences in tSCs as well. However, as discussed in chapter 1, a major hurdle in the progress of tSC research is the absence of a tSC specific marker in mammals. Finding a specific cell marker for tSCs will open opportunities for future molecular studies.

Comparative anatomy of NMJ morphology in larger mammals

Conventionally, most NMJ studies rely on rodent and amphibian models and there has been a paucity of data from large mammalian species (Slater, 2015). More importantly, in light of the considerable morphological differences between mouse and human NMJs, it was imperative to explore other alternative models that more closely resemble the human NMJ. Through this study, for the first time, there is a repository of comparative NMJ morphological data in higher mammals, including cat, dog, sheep and pig. In addition, this research project has generated and validated a workflow and data that can be employed for further investigative and comparative NMJ research.

The analysis conducted on heavier mammals revealed that sheep and pig NMJs show promising trends for modelling the human NMJ. As such, sheep are potentially a more appropriate model of the human NMJ than the mouse. The overall NMJ size, nerve terminal branching pattern, post-synaptic architecture and overlap percentage, in addition to muscle fibre size, all showed remarkable similarity between sheep and humans. Furthermore, sheep and humans were the only species whose NMJ size significantly correlated with both muscle fibre and axon diameter. Pig could be considered a second choice to sheep as a suitable model of the human NMJ, by virtue of it having slightly longer and more numerous nerve terminal branch points, whilst its overall size did not correlate with axon diameter. Sheep and pigs are already used in

research: sheep are used to model Batten's disease and peripheral nerve injuries (Starritt, Kettle and Glasby, 2011; Weber and Pearce, 2013), while pigs can develop MND (Wohlsein *et al.*, 2012) and has been used as a model of ALS (Holm, Alstrup and Luo, 2016) and SMA (Duque *et al.*, 2015) . A thorough understanding of NMJ structure and function of these models will enhance our understanding of the human NMJ in health and disease.

2.2 Study limitations

The induced lockdown due to COVID-19 interrupted the laboratory work, and thus samples could not be fully processed to label and assess tSCs in these mammals. Furthermore, this study was limited by the availability of animals at the time when sampling was conducted. Therefore, it was not possible to obtain enough N numbers to perform a sex comparison in these mammals.

2.3 NMJ morphology in large mammals

Future research must further investigate the pig and sheep NMJs to provide a more comprehensive understanding of the extent of similarity between these two animals and the human NMJ. Further investigations should focus on characterizing tSC morphology in sheep and pigs, as it is one of the main components of the NMJ. The human NMJ has a low quantal content (the amount of ACh released by each action potential being approximately 20 quanta/impulse) compared to rodent and frog NMJs (40-100 and approximately 200 quanta/impulse, respectively) (Slater, 2008). The human NMJ also possess deeper and more numerous post-synaptic folds than the mouse and frog (Slater, 2008). Using electrophysiological methods to record mEPP and EPPs and estimating quantal content in sheep and pig NMJs, in addition to visualizing the post-synaptic folds with an electron microscope would provide critical insights into the functional and structural characterization of the NMJ in these species. Furthermore, age-related degenerative changes are well documented in rodents (Courtney and Steinbach, 1981; Valdez *et al.*, 2010, 2012), contrary to the human NMJ which was found to be stable across several decades of life (Wokke *et al.*, 1990; Jones *et al.*, 2017). Thus, future studies will need to investigate sheep and pig NMJ stability throughout their lifespan. Additionally, the presence of intense hot spots of SV2 labelling in sheep and pig NMJs warrants an exploration of the structural architecture and distribution of active zone proteins, as the presence of similar hot

spots in human NMJs was attributed to the high density of the active zone protein SNAP25 (Jones *et al.*, 2017). Finally, further investigation into the composition of neurofilaments in these species will be needed given the spotted labelling of neurofilaments at the axon by anti-2H3 antibody in sheep and pig NMJs.

The present study showed a great degree of homogeneity in NMJ morphology within species. However, it is important to keep in mind that only one body region, the pelvic limb, was explored. High levels of morphological variation were observed between different body regions in mice (Jones *et al.*, 2016). It will be useful to investigate if variations are present between pelvic limb muscles and other body regions in higher body mass mammals. Furthermore, biological sex differences in NMJ morphology are well documented in human studies, in contrast to mice in which biological sex has no effect on NMJ morphology (Jones, 2017). In the present study, due to the low sample size and the limited availability of large mammals sexual dimorphism could not be assessed. Hence, biological sex matching opens up a new area of research for exploration.

2.2 Factors influencing NMJ size

Several factors have been noted to influence NMJ size in different species. These include muscle-specific variables such as muscle fibre type (Prakash *et al.*, 1996) and diameter (Kuno, Turkanis and Weakly, 1971; Oda, 1985; Jones, 2017), MN axon diameter (Jones, 2017), and more generally gross body mass (Slater, 2017). The findings of this study refute any correlation of body mass with NMJ size, since there was no trend towards an increase or a decrease in NMJ size across animals with different body mass: mouse (19 g), cat (4.3 kg), dog (39 kg), and sheep (75 kg). However, it is possible that other factors might influenced the results. Considering that only the pelvic limb muscles were examined in this study, it may be necessary to investigate other body regions and to examine other mammals, such as horses and cows, to make a conclusive conclusion regarding the relationship between the size of the NMJ and the body mass of species.

The strongest relationship was observed between muscle fibre and MN axon diameter and NMJ size within species. A statistically significant direct relationship between NMJ size and muscle fibre diameter was observed in both pig and sheep. In contrast, MN axon diameter showed a strong correlation with NMJ size in sheep only. Muscle fibre

type showed a trend where the slow twitch muscle (SOL) had smaller NMJs, and fast twitch muscles (EDP, PL, PB) had larger NMJs. Similarly, ponies had a significantly smaller NMJ in SOL compared to EDL and *tibialis cranialis* (Cahalan, Perkins, *et al.*, 2022) while murine and human NMJs were larger in SOL (Jones *et al.*, 2017). Further investigations can focus on single fibre preparations to directly assess the relationship of muscle fibre size and type to NMJ size.

2.3 The choice of animal models in NMJ research

Research into modelling a structurally and functionally consistent human NMJ will always come with caveats. Models developed so far have their advantages and limitations. Rodents are accessible, affordable, and easy to maintain and breed. They are also convenient to work with for surgical intervention, for dissecting and extracting muscles for whole mount preparations, and give an accurate readout of muscle status. Conversely, muscle tissue from large animals and humans must be teased into fibres from larger biopsy specimens, which is technically challenging. Furthermore, the breeding and maintenance of larger mammals is a logistical challenge due to costs, pregnancy duration, number of fetuses per pregnancy, the period to reach adulthood and ageing. However, large animal models, for example horses (Cahalan, Perkins, *et al.*, 2022), can be used for studying the role of the length of the nerve in disease vulnerability. In addition, the long lifespan of these animals might be useful for better understanding the pathophysiology of chronic neurodegenerative diseases and in long-term follow-up studies.

Pathological characterization of the NMJ and skeletal muscle in the *Thy-1* hTDP-43 mouse model

3.1 The Thy1-TDP-43 mouse is a favourable model for studying MN pathology in ALS

ALS is a fatal multisystem disease, primarily affecting both UMNs and LMNs (Rowland, 2001). One of the recurrent challenges faced in ALS treatment is the limited translation of otherwise promising preclinical research into successful clinical treatments (Mitsumoto, Brooks and Silani, 2014; Tosolini and Sleight, 2017). As seen from the extreme differences in the mouse and the human NMJ (chapter 2 and (Jones

et al., 2017)), even the most widely employed models can have system specific differences. This can be partially solved by finding a model species that better represents the human condition. As illustrated in chapter 3, sheep and pig would provide more suitable options to study the human NMJ. Nevertheless, even with the availability of an alternative model, full-scale disease modelling in those species is often limited – ALS is more complicated in humans than in laboratory animals, as humans are subject to multiple environmental and sporadic risk factors, as discussed in chapter 1. Gene mutations account for the minority of sALS cases (only 5.2%) and less than half of familial cases (47.7%) (Zou *et al.*, 2017). Thus, a large proportion of patients develop disease from non-mutational causes. Conversely, laboratory animals, such as rodents, are maintained in a controlled environment and usually express a single causal factor i.e., gene manipulation. These experimental approaches limit the precise replication of pathological processes in humans. Finally, while most therapeutic studies have used the SOD1 models (Mitsumoto, Brooks and Silani, 2014; Tosolini and Sleight, 2017), they lack the formation of TDP-43 aggregations which is a characteristic feature of disease pathogenesis and present in 90% of ALS patients (Mackenzie *et al.*, 2007). Thus, using an ALS-TDP-43 model might translate more appropriately to humans and help develop a better understanding of disease pathogenesis.

In this study, the restricted overexpression of hTDP-43 in MNs led to the development of systematic signs which recapitulate many aspects of ALS seen in patients, including progressive paralysis, muscle weakness, and weight loss (Rowland, 2001). Furthermore, the *Thy1*-hTDP-43 ALS mouse model has demonstrated many pathological key aspects that were reported in studies on ALS patients including severe MN degeneration, progressive NMJ denervation and pathological changes in tSC such as intrusion of their cytoplasmic processes into the synaptic cleft (Maselli *et al.*, 1993; Fischer *et al.*, 2004; Liu *et al.*, 2013; Bruneteau *et al.*, 2015) However, the rapid progression of the in this model limited the development of secondary pathological changes in the motor endplate and muscle fibre which are documented in previous studies on ALS patients. These changes include endplate fragmentation (Bjornskov *et al.*, 1975; Bjornskov, Norris and Mower-Kuby, 1984), decreased area of endplate (Tsujiyata *et al.*, 1984) muscle fibre loss, group atrophy, fibre type grouping, and fibre type switching (Maselli *et al.*, 1993; Fischer *et al.*, 2004). The rapid progression of the

disease has also limited the study of compensatory changes such as sprouting of tSCs. Although this model might have limitations for studying the compensatory mechanisms of MN degeneration, it is ideal for studying TDP-43 mediated MN pathology and the pathological events associated with a rapidly progressing disease course.

3.2 Study limitations and future directions

3.2.1 Further characterization of the Thy-1 hTDP-43 mouse model

Biological sex is one of the established risk factors for ALS. Males have higher incidence, earlier onset, and a more rapidly progressing disease course than females (Logroscino *et al.*, 2010; McCombe and Henderson, 2010; Esmaeili *et al.*, 2013; Bros-Facer *et al.*, 2014; Renzini *et al.*, 2023). ALS is also characterized by an asymmetrical onset (Ravits and La Spada, 2009) and mutant TDP-43 mouse models have demonstrated asymmetrical denervation of pelvic limbs (Ebstein, Yagudayeva and Shneider, 2019). In the present study, both sides of the body were studied in 4 male and 2 female mice. Therefore, evaluation of sex-specific differences was not possible due to the low sample size for each sex, and the effect of laterality on NMJ denervation could not be assessed as tissue from each side was combined and processed together. Future studies are needed to investigate these two factors in more depth. Potential differences between male and female mice, and laterality effects might explain the variations observed between animals (chapter 4 - Figure 22).

In this study, the time course of pelvic limb denervation was recorded in PL, plantaris, and SOL only, and revealed preserved innervation at P10 (the pre-symptomatic stage). Additionally, plantaris was the only muscle that showed significant denervation at P15 and at disease end-stage, had the highest percentage of vacant NMJs (44%) and significant muscle fibre atrophy (21.6%). Examining other muscles that showed higher percentages of vacant NMJs and muscle fibre atrophy such as GC and FDB (34% vacant NMJs and more than 30% atrophy) and muscles that exhibited the lowest percentages such as PB (27% vacant NMJs and 6% atrophy) at pre- and early symptomatic stages will guide in tracing the disease progression and understanding the influence of MN degeneration on skeletal muscle fibres.

This study has showed that a significant loss of S100b labelling occurs at tSCs of pelvic limb muscles in hTDP-43 mice. Findings from ALS patients and the SOD1 mouse models demonstrated intrusion of tSC processes into the primary synaptic cleft (Arbour *et al.*, 2015; Bruneteau *et al.*, 2015). It will be interesting to explore whether similar changes exist in the present model in cranial muscles in which preservation of S100 labelling was observed (chapter 4, Figure 21E). Furthermore, studying the influence of MN degeneration on muscle fibres would also provide valuable insights into the mechanisms of disease progression. This study has detected mild muscle fibre atrophy of some pelvic limb muscles with no changes in slow-twitch fibre percentage. Further exploration of muscular changes, including metabolic shift (from glycolytic to oxidative) and fast-twitch fibre switch (from FF to FR) is also necessary, as these changes have been reported previously in other ALS mouse models (Dobrowolny *et al.*, 2008; Peggion *et al.*, 2017; Molotsky *et al.*, 2022).

This thesis focused on illustrating the importance of studying the NMJ in ALS; as such, only LMN structures were thoroughly explored. It is however necessary to examine the involvement of the nervous system holistically and expand beyond the LMN to include cells such as UMNs and glia. UMN degeneration, if present, would improve our understanding of disease progression and indicate whether it is a dying-forward or backward pathology (Eisen, Kim and Pant, 1992; Chou and Norris, 1993). Glial cells also play a role in the pathogenesis of the disease; astrocytes and microglia drive disease progression and oligodendrocytes contribute to the initiation of the disease (Boillée *et al.*, 2006; Yamanaka *et al.*, 2008; Kang *et al.*, 2013). Investigating glial alterations in the brain and spinal cord would provide a more comprehensive picture of the disease process.

3.2.2 Identifying the primary site of pathology in MND

The involvement of UMN soma (Eisen, Kim and Pant, 1992), LMN soma (Chou and Norris, 1993), NMJ (Murray, Talbot and Gillingwater, 2010) and skeletal muscle (Dobrowolny *et al.*, 2008) has been widely investigated, and there is still an extensive debate in the literature regarding the primary target of ALS. It is pertinent to note that each model has a distinct genetic mechanism with a different pace of disease progression and phenotype (Picher-Martel *et al.*, 2016; Mejzini *et al.*, 2019). Nonetheless, it is important to identify the primary site of insult in each gene mutation

and to tailor therapies to patients based on their underlying causative factor (Picher-Martel *et al.*, 2016). The detection of MN loss and NMJ structural changes simultaneously with symptoms onset, as observed in this study (chapter 4), encourages further investigations to accurately pinpoint the primary site of pathology between the MN soma and the NMJ. Further investigations including the study of ultrastructural changes, such as the mitochondria at the MN soma and the NMJ (Vinsant *et al.*, 2013b) as well as electrophysiological studies to detect changes in neurotransmission (Tremblay, Martineau and Robitaille, 2017) would provide valuable insights into the onset of the pathological changes. Investigating whether ultrastructural changes appear first at the MN soma or nerve terminals will help delineate the primary site of insult.

3.2.3 Selective vulnerability of muscles in MND

Several studies have clearly demonstrated that pathological changes appear earlier in the fast-twitch muscles, such as TA and EDL, than the slow-twitch muscles, such as SOL (Frey *et al.*, 2000; Gould *et al.*, 2006; Pun *et al.*, 2006; Hegedus, Putman and Gordon, 2007; Narai *et al.*, 2009; Valdez *et al.*, 2012; Vinsant *et al.*, 2013b; Sharma *et al.*, 2016; Tremblay, Martineau and Robitaille, 2017; Ebstein, Yagudayeva and Shneider, 2019). The data presented in this study was consistent with those published previously. It showed that SOL (which contains more than 40% slow-twitch fibres) was the most resistant in the pelvic limb with less than 5% vacant NMJs. By contrast, plantaris, FDB, and GC contained 10-16% slow-twitch fibres and displayed the most severe NMJ pathology (34-44% vacant NMJs). Co-investigating NMJ denervation and tSC changes in individual muscle fibres will further elucidate fibre type-specific vulnerability in ALS. This can be done by co-labelling NMJs and muscle fibres to monitor if the NMJ and tSCs on the fast-twitch muscle fibre are degenerated and those on the slow-twitch muscle fibre are spared.

The reasons for selective vulnerability in ALS remain unknown. Understanding the mechanisms that drive selective vulnerability to degeneration and/or contribute to disease resistance would be beneficial for the development of novel therapies. Studying the intrinsic properties of MNs is crucial for understanding vulnerability differences. MNs of the resistant muscles might have resistant tendencies to insults or have a regenerative capacity that allows them to survive longer (Woschitz *et al.*,

2022). One way to explore this is by performing a proteomic profiling of the MNs innervating vulnerable versus resistant pelvic muscles using two different retrograde MN tracers to identify MNs supplying each muscle. Comparing cervical MNs (supplying the thoracic limbs) and lumbosacral MNs (supplying the pelvic limbs), would also provide valuable insights into the role of MNs in ALS. Lastly, performing proteomic muscle profiling to investigate pathway differences between vulnerable and resistant muscles in hTDP-43 mice would help clarify whether intrinsic molecular muscle changes are responsible for selective vulnerability in this model.

Conclusions

Disruption of NMJ morphology is one of the early signs of neurodegeneration in MND. Hence, studying the NMJ is essential for understanding disease pathogenesis and developing novel therapeutic interventions. Since obtaining human muscle biopsies of sufficient quantity and quality comes with ethical and technical challenges, the use of animal models is imperative for the study of the NMJ. However, the genetic and biological diversity between different species compared to humans leads to the poor translation of such animal studies to the human condition, which has a large impact on resources and time. Therefore, choosing the appropriate model for studying the system under investigation (the NMJ) is necessary for an accurate translation of the results from animal studies to human diseases.

[The first aim of this thesis was to investigate the morphological differences between tSCs in mice and humans.](#)

Despite the clinical significance of tSCs in neuromuscular diseases, there has been a paucity of data describing human tSC morphology. This thesis has thoroughly examined the structural characteristics of human tSCs and conducted a comprehensive comparison between mouse and human tSCs. The results showed considerable species-specific differences; human tSCs were remarkably smaller than those of the mouse, with more extended cytoplasm, less AChR coverage, and more non-synaptic nuclei.

The second aim of this thesis was to identify an appropriate animal model of the human NMJ.

Given the stark differences between mouse and human NMJs, it is important to identify alternative animal models that mimic the human condition. The NMJ morphology in cats, dogs, sheep, and pigs was thoroughly explored in this thesis. The major contributions of this study were:

1. Establishing the first morphometric database for NMJs in non-rodent mammals including cats, dogs, sheep, and pigs.
2. Identifying that the sheep NMJ was the most similar to the human NMJ, followed by the pig NMJ.
3. Revealing that the size of the NMJ in mammals is not proportional to body size.
4. Identifying that muscle fibre and axon diameter correlate with the NMJ size in some species.

The third and final aim of this thesis was to conduct a comprehensive analysis of NMJ pathology in the *Thy-1* hTDP-43 ALS mouse model.

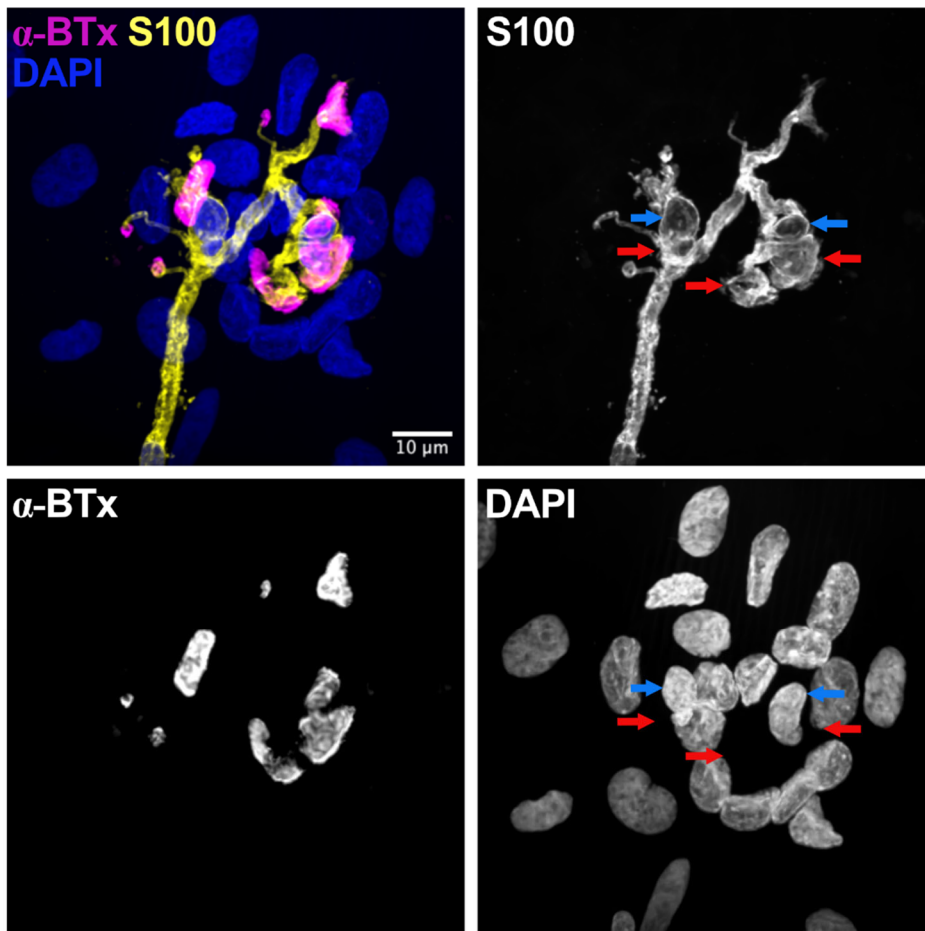
To emphasise the significance of the NMJ in neurodegenerative diseases, a novel ALS mouse model was used to investigate the pathological changes at the NMJ throughout the animal's lifespan. This study provides the first comprehensive characterization of NMJ pathology in the *Thy1*-hTDP-43 mouse model. The major findings of the study were:

1. The overexpression of human TDP-43 under the *Thy1* promoter in mice induces an ALS-like phenotype at P15, with a gradual loss of α MNs in the lumbar region of the spinal cord and an increased denervation of pelvic limb muscles.
2. The *Thy1*-hTDP-43 mouse model of ALS showed severe MN-restricted NMJ pathology in pelvic limbs with a varying degree of vulnerability and resistance between different muscles. In contrast, cranial muscles showed mild denervation, while thoracic limb and abdominal muscles were completely spared.
3. The MN degeneration induced secondary changes at tSCs and muscle fibres in pelvic limb muscles including loss of S100b labelling at tSCs and muscle fibre atrophy.

Overall, the findings of this thesis have deepened our understanding of the comparative anatomy of the NMJ in humans, mice, cats, dogs, sheep, and pigs., which now encourages further exploration of the sheep and pig for future NMJ studies. It has also emphasised the importance of the NMJ to our understanding of MND and its early involvement in the pathogenesis of ALS.

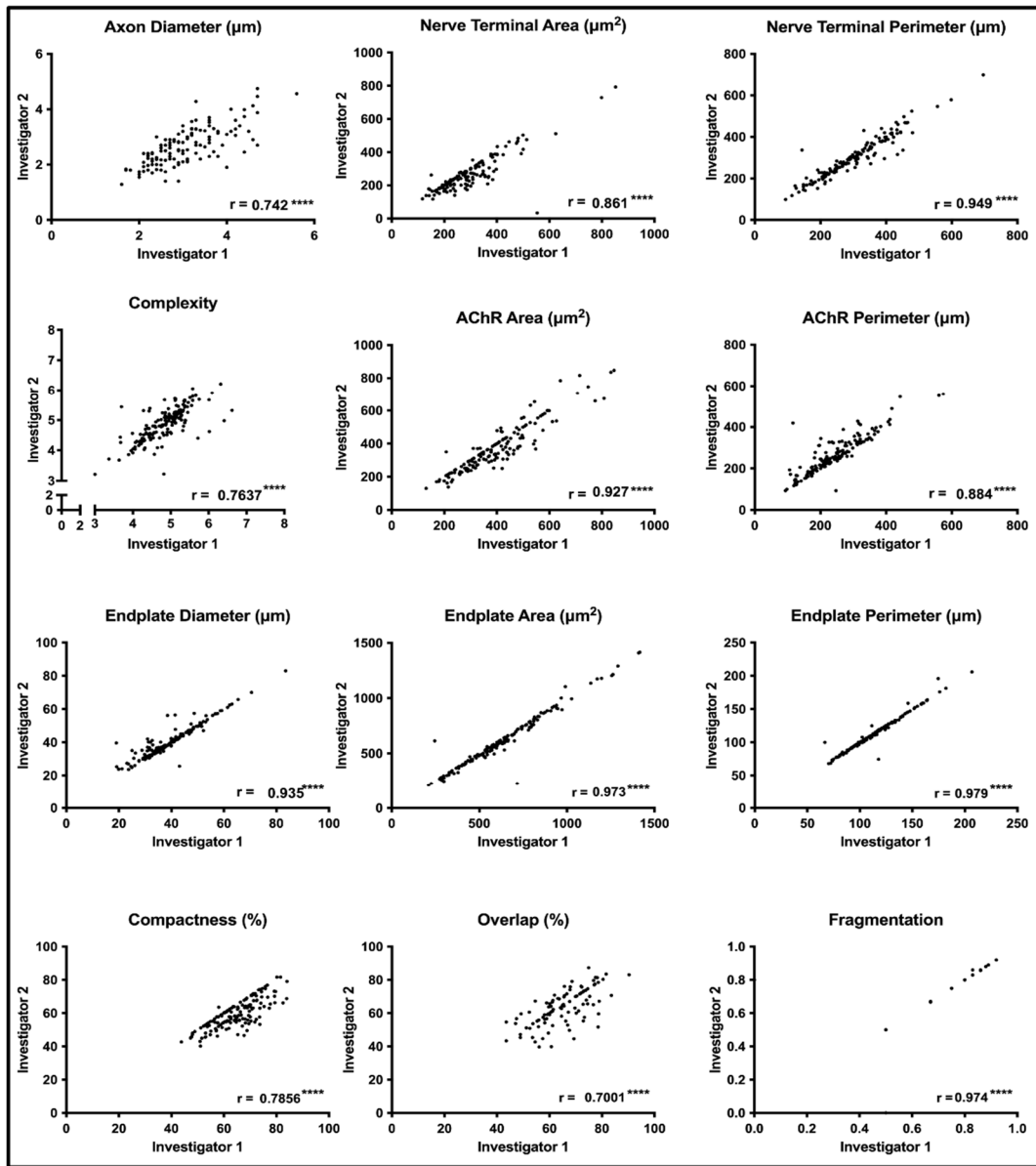
Appendices

Chapter 2: Morphology of terminal Schwann cells at mouse and human NMJs



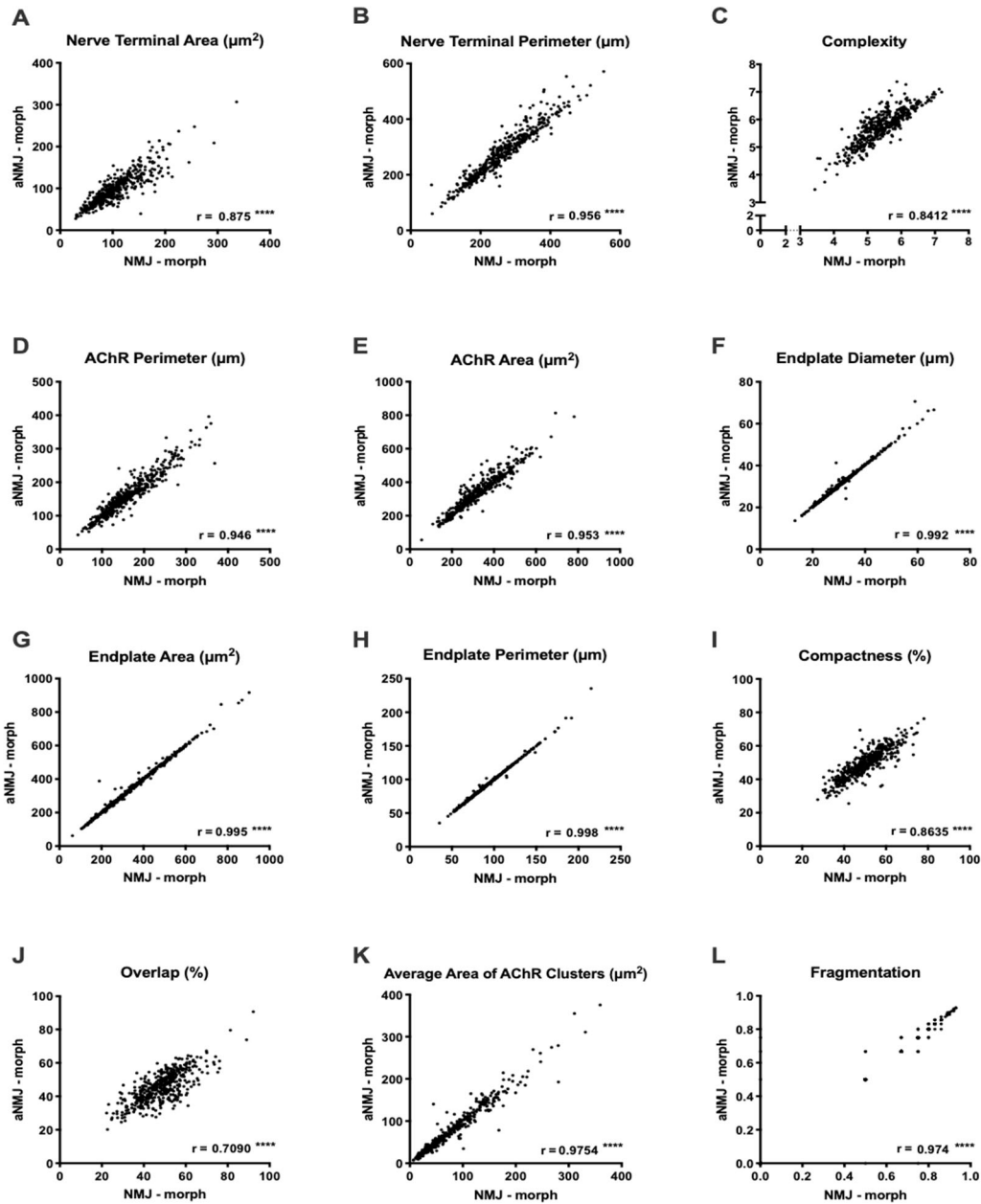
Appendix 1: Identifying the cell bodies of tSCs.

A representative confocal micrograph of human tSCs. To identify tSC bodies a nucleus must be located within a cytoplasmic halo over or near the endplate. Blue arrows indicate true cell bodies, while red arrows indicate cytoplasmic haloes that can be falsely identified as cell bodies. The merged image shows tSCs labelled with antibodies against S100 (yellow), AChRs labelled with α -BTx (magenta), and nuclei stained by DAPI (blue). Scale bar = 10 μ m



Appendix 2: Validation of NMJ-morph user proficiency

Strong correlations between training (investigator 1) and reference data (investigator 2). A total of 120 mouse NMJs were analysed. Each data point represents one NMJ. Pearson and Spearman correlation coefficients (r) for parametric and non-parametric variables, respectively. All $r > 0.7$ with all $P < 0.0001$.



Appendix 3: Validatin of aNMJ-morph

A total of 465 cat NMJs were analysed by a single user using NMJ-morph (manual approach) and aNMJ-morph (semi-automated approach). Strong correlations were found across all variables which validates the use of aNMJ-morph in NMJ analysis. Each data point represents one NMJ. Pearson and Spearman correlation coefficients (r) for parametric and non-parametric variables, respectively. All $r > 0.7$ with all $P < 0.0001$.

	Mouse (PB) N = 6; n = 126 NMJ 214 tSCs	Human (PB) N = 5; n = 151 NMJ 247 tSCs
Number of tSCs per NMJ	1.74 ± 0.06	1.73 ± 0.07
Total tSCs perimeter (μm)	280.8 ± 8.92**	178.3 ± 6.14
Total tSCs area (μm²)	258.51 ± 8.48**	199.15 ± 7.11
Synaptic area of tSCs (μm²)	184.33 ± 6.07****	89.27 ± 3.86
Coverage (%)	68.89 ± 0.71*	54.14 ± 1.06
Non-synaptic area of tSCs (μm²)	74.17 ± 3.47****	109.88 ± 4.79
Extension (%)	28.23 ± 0.86**	54.55 ± 1.27

Appendix 4: Morphological comparison of mouse and human tSCs from peroneus brevis muscle. Values are averages ± SEM.

Chapter 3: The NMJ morphology of large mammals

NMJ variables	Notes
Pre-synaptic variables	
Axon diameter:	Calculated by averaging the measurements at three different points along the axon (thickest, thinnest, and proximal to bifurcation)
Nerve terminal measurements:	area and perimeter
Branching analysis:	number of terminal branches, number of branch points, total length of branches, average length of branches
Post-synaptic variables	
Endplate measurements:	area, perimeter, and diameter (The maximum linear dimension of the endplate)
AChR-related measurements:	area, perimeter, and number of AChR clusters
Derived variables	
NT Complexity	= $\text{Log}_{10}(\text{number of terminal branches} \times \text{number of branch points} \times \text{total length of branches})$.
Average area of AChR cluster	= AChR area/number of AChR clusters
Endplate Fragmentation	= $1 - (1/\text{number of AChR clusters})$ A value of 0 is given to a plaque-like endplate, and values close to 1 indicate more fragmentation.
Endplate Compactness	= (AChR area/Endplate area) \times 100
Area of synaptic contact	= Total area of AChRs – unoccupied area of AChRs
Overlap	= Area of synaptic contact/Total area of AChRs \times 100

Appendix 5: Morphological variables measured by aNMJ-morph.

Cat N=3	PL n = 120 NMJ	PB n = 120 NMJ	EDL n = 111 NMJ	SOL n = 114 NMJ
Presynaptic core variables				
Axon diameter	0.87	0.96	0.75	1.28
NT area (μm^2)	103.21	104.26	84.97	101.53
NT perimeter (μm)	300.48	281.68	234.98	271.23
Number of terminal branches	128.10	96.00	74.95	106.63
Number of branch points	89.02*	52.76	36.94	51.59
Total length of branches (μm)	151.42	131.25	104.99	126.94
Average length of branches (μm)	1.31	1.49	1.58	1.306
Postsynaptic core variables				
AChR area (μm^2)	170.79	175.39	157.15	134.89
AChR perimeter (μm)	365.30	348.60	290.84	326.04
Endplate area (μm^2)	328.26	367.88	327.29	309.23
Endplate perimeter (μm)	90.26	97.75	86.78	90.96
Endplate diameter (μm)	30.17	34.05	29.05	30.41
Number of AChR clusters	2.78	2.78	2.34	4.76
Derived variables				
NT Complexity	6.079	5.70	5.32	5.70
Average area of AChR cluster (μm^2)	84.99	91.71	85.98	40.42
Endplate Fragmentation	0.49	0.46	0.44	0.66
Endplate Compactness	53.95*	48.86	49.23	46.02
Area of synaptic contact (μm^2)	91.88	98.12	91.08	67.72
Pre and post synaptic overlap (%)	45.99	44.95	42.53	50.00

Appendix 6: A Comparison of morphological variables in the NMJs of four feline muscles. PL: *peroneus longus*, PB: *peroneus brevis*, EDL: M. extensor digitorum longus, SOL: M. soleus. Values are the means of 3 animals. Values in red are significantly different from values in bold; PL had significantly more branch points and more compact endplate than EDL and SOL, respectively. One-way ANOVA with Dunnett's post hoc analysis (parametric variables) and Kruskal-Wallis test with Dunn's post hoc analysis (non-parametric variables). *P < 0.05.

Dog N=3	PL n = 110 NMJ	PB n = 145 NMJ	EDL n = 128 NMJ
Presynaptic core variables			
Axon diameter	1.87	1.50	2.13
NT area (μm^2)	338.32	247.45	330.11
NT perimeter (μm)	501.32	359.27	462.50
Number of terminal branches	112.61	77.77	96.41
Number of branch points	63.57	55.61	66.97
Total length of branches (μm)	234.44	182.71	229.95
Average length of branches (μm)	2.365	2.64	2.66
Postsynaptic core variables			
AChR area (μm^2)	503.62	326.77	432.14
AChR perimeter (μm)	618.33	442.39	548.77
Endplate area (μm^2)	1055.80	633.59	887.30
Endplate perimeter (μm)	159.51	114.61	143.22
Endplate diameter (μm)	55.12	40.413	48.81
Number of AChR clusters	5.00	2.70	3.73
Derived variables			
NT Complexity	6.04	5.73	6.05
Average area of AChR cluster (μm^2)	162.59	176.17	187.34
Endplate Fragmentation	0.69	0.41	0.52
Endplate Compactness	48.71	52.84	49.51
Area of synaptic contact (μm^2)	255.71	176.92	240.58
Pre and post synaptic overlap (%)	51.21	53.14	55.02

Appendix 7: A Comparison of morphological variables in the NMJs of three canine muscles. No statistically significant difference between muscles across all variables. PL: *peroneus longus*, PB: *peroneus brevis*, EDL: *M. extensor digitorum longus*. Values are the means of 3 animals. One-way ANOVA with Dunnett's post hoc analysis (parametric variables) and Kruskal–Wallis test with Dunn's post hoc analysis (non-parametric variables). *P < 0.05.

Sheep N=3	PL n = 111 NMJ	EDL n = 94 NMJ	SOL n = 108 NMJ
Presynaptic core variables			
Axon diameter	0.93	1.26	1.16
NT area (μm^2)	145.88	173.66	142.12
NT perimeter (μm)	214.62	257.06	223.47
Number of terminal branches	37.07	52.22	47.29
Number of branch points	25.76	29.53	23.82
Total length of branches (μm)	103.71	123.18	101.69
Average length of branches (μm)	3.55	2.67	2.87
Postsynaptic core variables			
AChR area (μm^2)	189.96	200.50	156.08
AChR perimeter (μm)	224.92	262.19	237.79
Endplate area (μm^2)	341.64	387.36	367.18
Endplate perimeter (μm)	78.74	86.65	90.05
Endplate diameter (μm)	28.18	30.58	32.01
Number of AChR clusters	4.18	5.47	5.26
Derived variables			
NT Complexity	4.80	5.13	4.88
Average area of AChR cluster (μm^2)	76.30*	48.16	39.81
Endplate Fragmentation	0.59	0.75	0.68
Endplate Compactness	56.72	52.29	44.05
Area of synaptic contact (μm^2)	124.33	133.32	108.59
Pre and post synaptic overlap (%)	65.04	65.27	68.76

Appendix 8: A Comparison of morphological variables in the NMJs of three ovine muscles. PL: *peroneus longus*, EDL: *M. extensor digitorum longus*, SOL: *M. soleus*. Values are the means of 3 animals. Values in red are significantly different from the values in bold; PL had a significantly larger area of AChR clusters than SOL. One-way ANOVA with Dunnett's post hoc analysis (parametric variables) and Kruskal-Wallis test with Dunn's post hoc analysis (non-parametric variables). *P < 0.05.

Pig N=3	PL n = 120 NMJ	EDL n = 120 NMJ	SOL n = 126 NMJ
Presynaptic core variables			
Axon diameter	1.24	1.32	1.16
NT area (μm^2)	240.61	234.86	117.21
NT perimeter (μm)	240.92	246.08	217.11
Number of terminal branches	29.80	31.77	58.58
Number of branch points	37.68	40.75	37.03
Total length of branches (μm)	146.82	147.75	109.08
Average length of branches (μm)	5.77***	5.25	2.05
Postsynaptic core variables			
AChR area (μm^2)	286.00	269.34	163.10
AChR perimeter (μm)	213.06	222.05	230.18
Endplate area (μm^2)	286.00	269.34	163.10
Endplate perimeter (μm)	99.33	104.06	82.97
Endplate diameter (μm)	34.36	33.41	28.77
Number of AChR clusters	3.73	3.43	3.98
Derived variables			
NT Complexity	5.08	5.12	5.22
Average area of AChR cluster (μm^2)	137.02*	131.16	70.71
Endplate Fragmentation	0.49	0.47	0.51
Endplate Compactness	67.71	69.17	56.66
Area of synaptic contact (μm^2)	222.36	210.94	91.80
Pre and post synaptic overlap (%)	78.30	78.01	57.05

Appendix 9: A Comparison of morphological variables in the NMJs of three porcine muscles. PL: *peroneus longus*, EDL: *M. extensor digitorum longus*, SOL: *M. soleus*. Values are the means of 3 animals. Values in red are significantly different from bold values; PL had significantly longer branches than EDL and SOL and larger AChR clusters than SOL. One-way ANOVA with Dunnett's post hoc analysis (parametric variables) and Kruskal-Wallis test with Dunn's post hoc analysis (non-parametric variables). *P < 0.05, **P < 0.001.

A) Correlation of NMJ size with muscle fibre diameter

	Cat (r) N = 3, n = 12 465 NMJs	Dog (r) N = 3, n = 9 341 NMJs	Sheep (r) N = 3, n = 9 313 NMJs	Pig (r) N = 3, n = 9 366 NMJs
NT area (μm^2)	0.11	-0.31	0.56	0.81**
AChR area (μm^2)	-0.39	-0.36	0.76*	0.86**
Endplate area (μm^2)	-0.15	-0.17	0.37	0.82**
Endplate diameter (μm)	-0.076	-0.21	-0.25	0.81**

B) Correlation of NMJ size with MN axon diameter

	Cat (r) N = 3, n = 12 465 NMJs	Dog (r) N = 3, n = 9 341 NMJs	Sheep (r) N = 3, n = 9 313 NMJs	Pig (r) N = 3, n = 9 366 NMJs
NT area (μm^2)	0.24	-0.091	0.72*	0.067
AChR area (μm^2)	-0.13	-0.16	0.49	0.036
Endplate area (μm^2)	0.051	-0.17	0.81*	-0.13
Endplate diameter (μm)	0.36	-0.25	0.36	-0.13

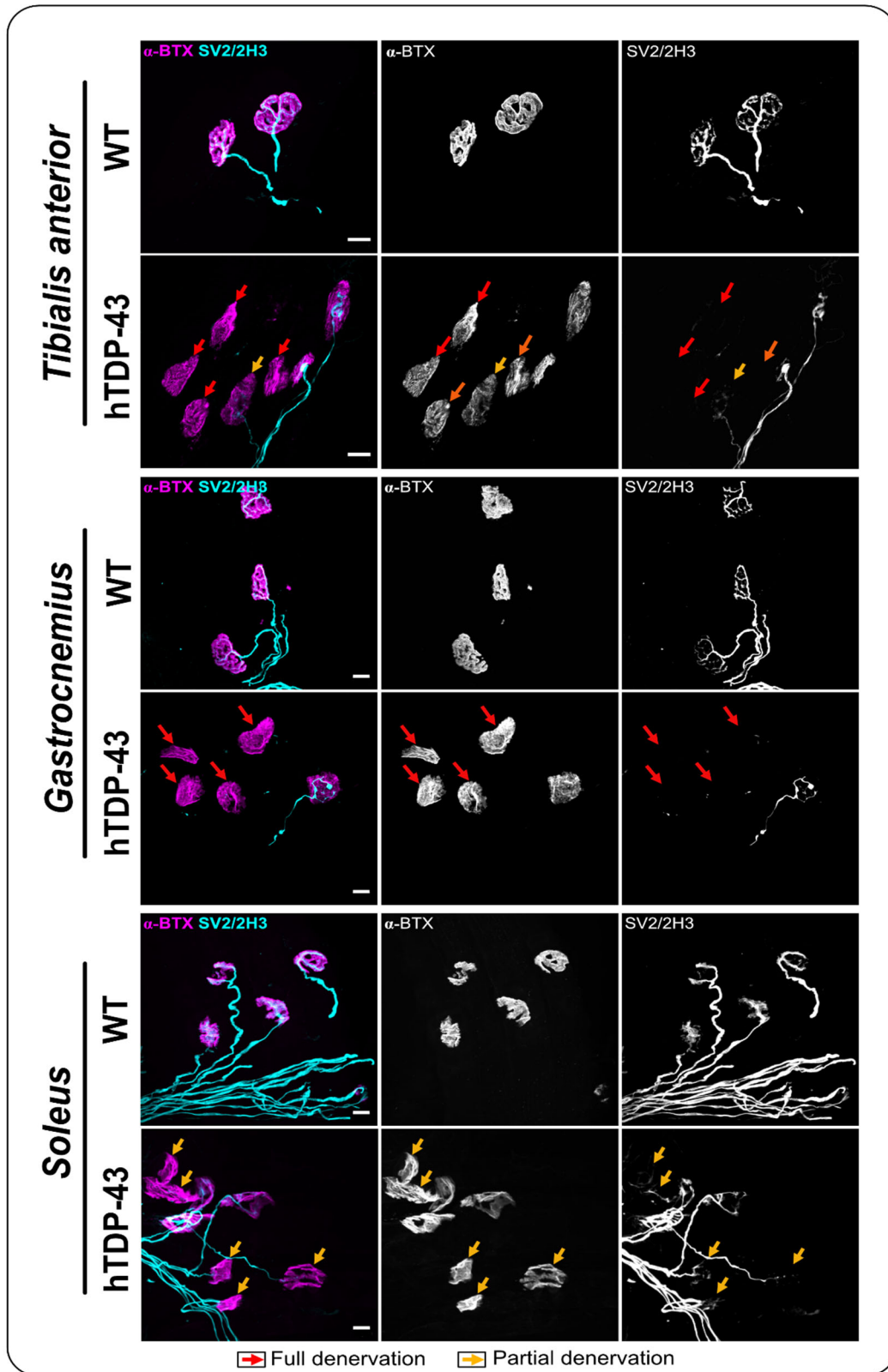
Appendix 10: A) A strong positive correlations between NMJ size and muscle fibre diameter identified in sheep and pig. B) Strong positive correlations between NMJ size and MN axon diameter identified in sheep only. Correlation coefficients (r) and the significance level of the P-value determined through Pearson correlation conducted on variable averages of each muscle (n). *P < 0.05; **P < 0.01.

Chapter 4: Pathological changes at the NMJ in the Thy-1 hTDP-43 ALS mouse model

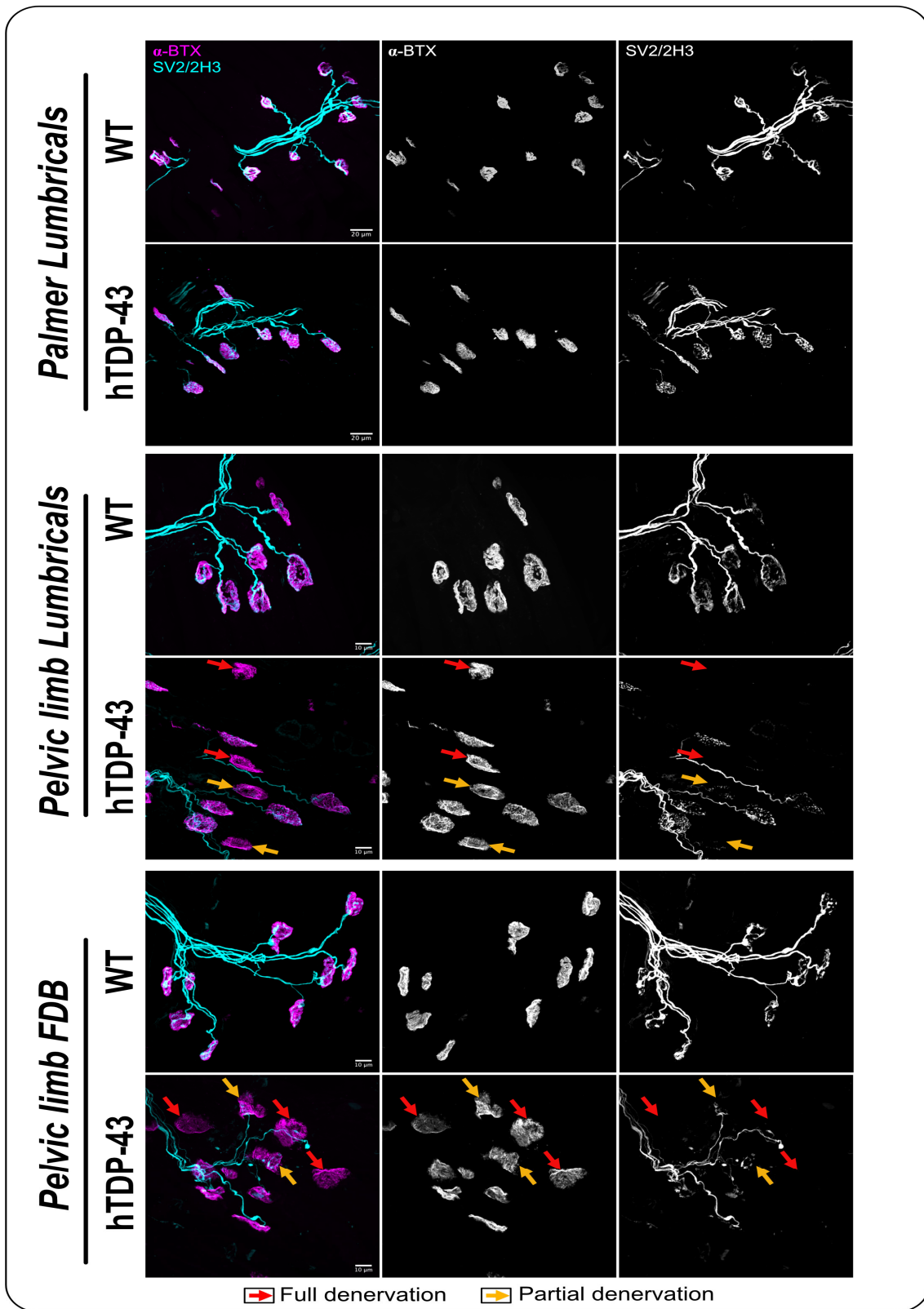
Score	Suspension test When the animal is suspended by the tail:	Grip test When the animal is suspended by the tail:	Free movement
0	Both pelvic limbs are consistently splayed outwards fully.	Both hind feet can grip strongly onto the rim of a cup.	The mouse moves freely, all four limbs support body weight
1	One pelvic limb is retracted to the abdomen (not splayed outwards) for half the time tested.	One hind foot is not able to grip strongly onto the rim of a cup.	The mouse has a mild tremor and may have a limp while walking.
2	Both pelvic limbs are retracted to the abdomen (not splayed outwards) for half the time tested.	One hind foot or both are not able to grip strongly onto the rim of a cup.	The mouse has a severe tremor, limp, and feet may point outward while walking (duck feet).
3	Both pelvic limbs are fully retracted to the abdomen for more than half of the time tested.	Both hind feet are unable to grip the rim of a cup.	The mouse has difficulty moving forward due to severe paralysis and drags its abdomen along the ground.

Appendix 11: Criteria for scoring muscle strength in a murine model of ALS. Animals reach the disease end-stage when scoring 3 in all tests.

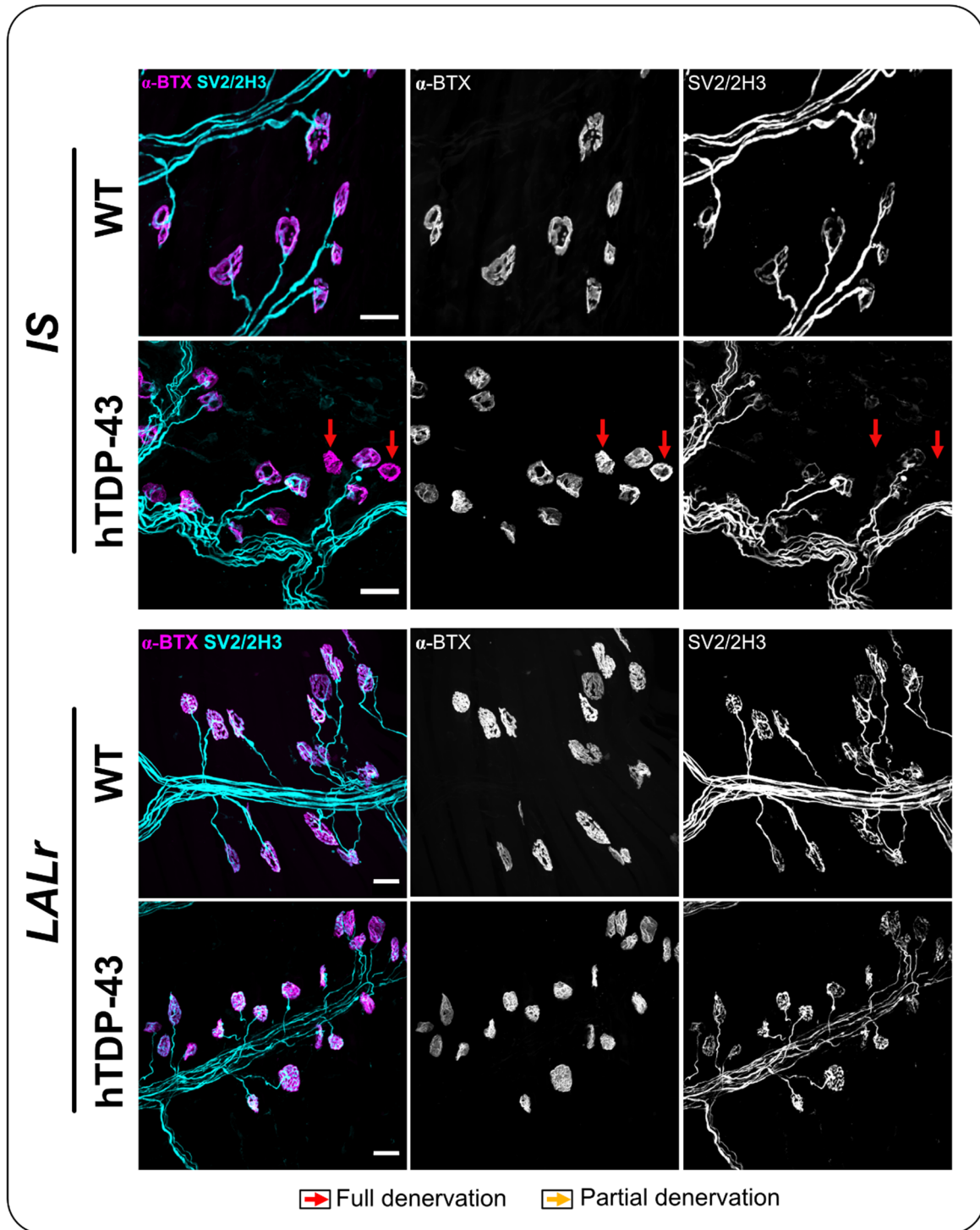
(Rogers *et al.*, 1997; Guyenet *et al.*, 2010; Yerger *et al.*, 2022)



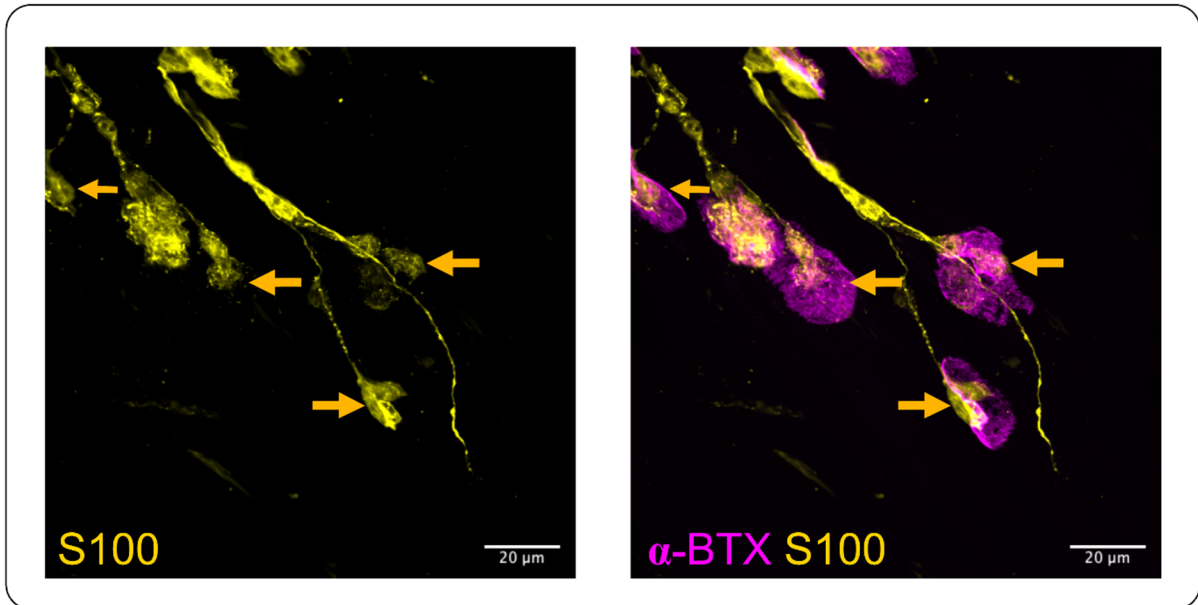
Appendix 12: Variable degree of pelvic limb denervation at the disease end-stage in hTDP-43 and WT mice. Alpha-BTX (α -bungarotoxin) labels acetylcholine receptors (magenta); S100b labels tSCs (yellow). SV2/2H3 label synaptic vesicles and neurofilaments to visualize nerve terminals and axon, respectively (cyan).



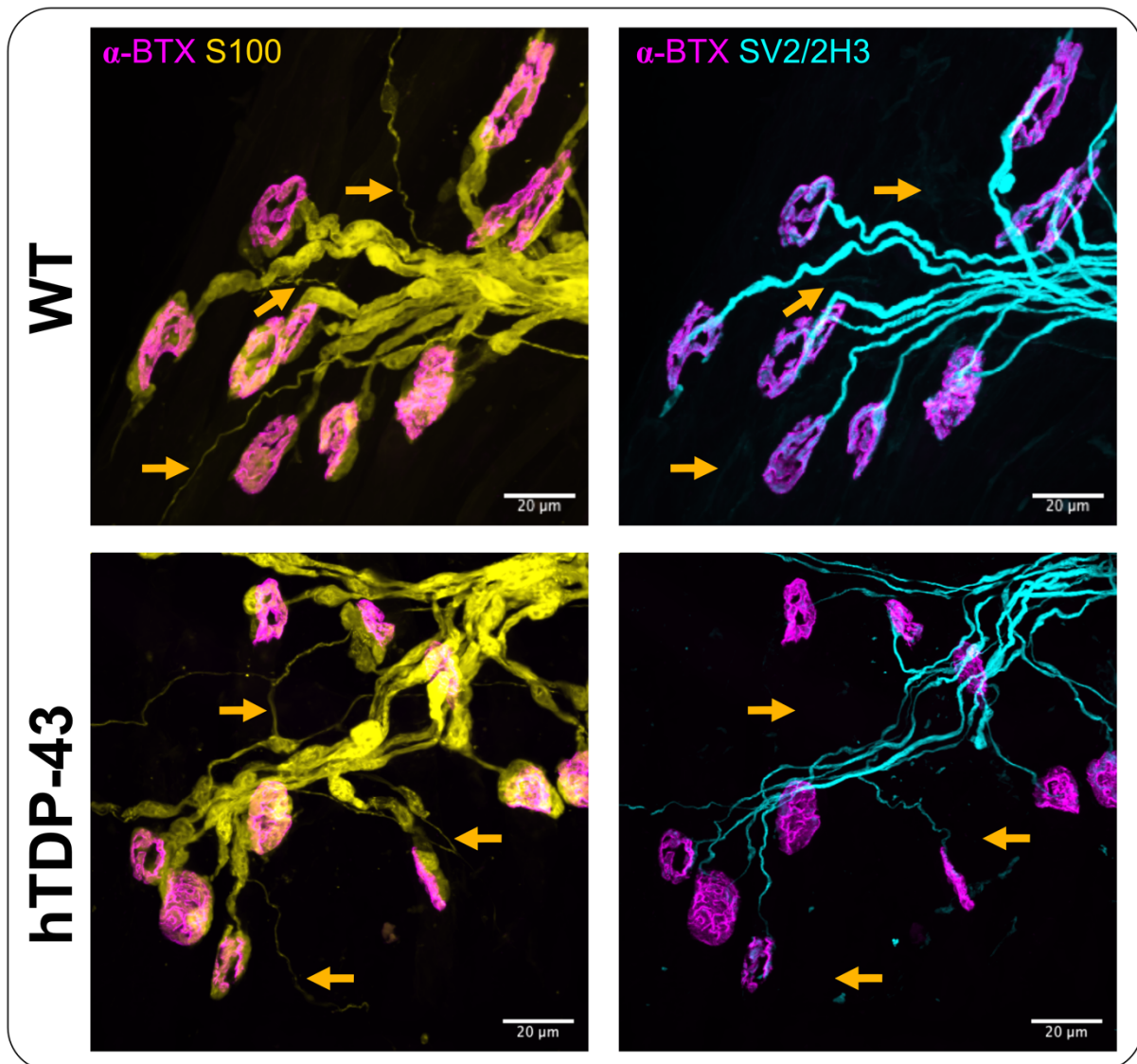
Appendix 13: Variable degree of denervation in selected limb muscles at the disease end-stage in a murine model of ALS. Alpha-BTX (α -bungarotoxin) labels acetylcholine receptors (magenta); SV2/2H3 label synaptic vesicles and neurofilaments to visualize nerve terminals and axon, respectively (cyan).



Appendix 14: Variable degree of denervation in cranial muscles at the disease end-stage in a murine model of ALS. Alpha-BTX (α -bungarotoxin) labels acetylcholine receptors (magenta); SV2/2H3 label synaptic vesicles and neurofilaments to visualize nerve terminals and axon, respectively (cyan).

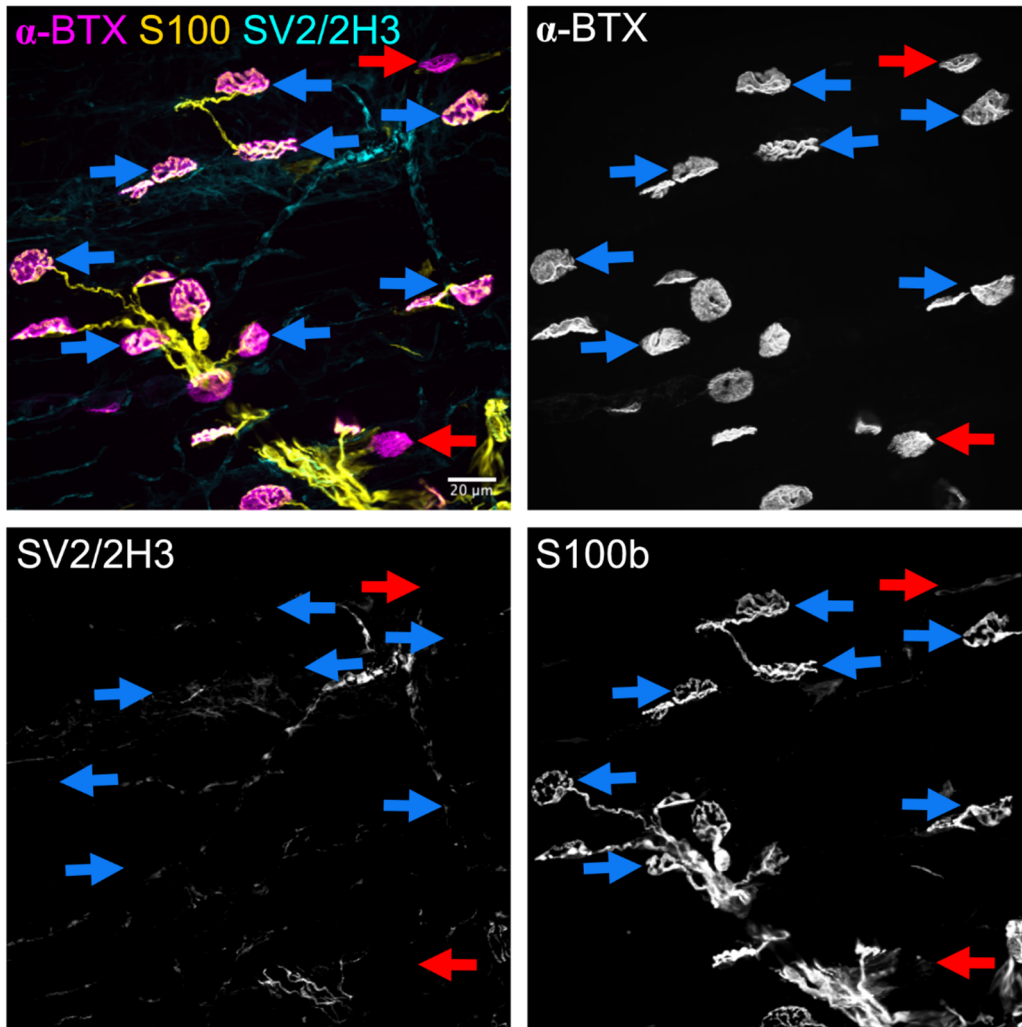


Appendix 15: Loss of tSCs cytoplasmic processes preceded the loss of cell bodies (arrows). Alpha-BTX (α -bungarotoxin) labels acetylcholine receptors (magenta); S100b labels tSCs (yellow).



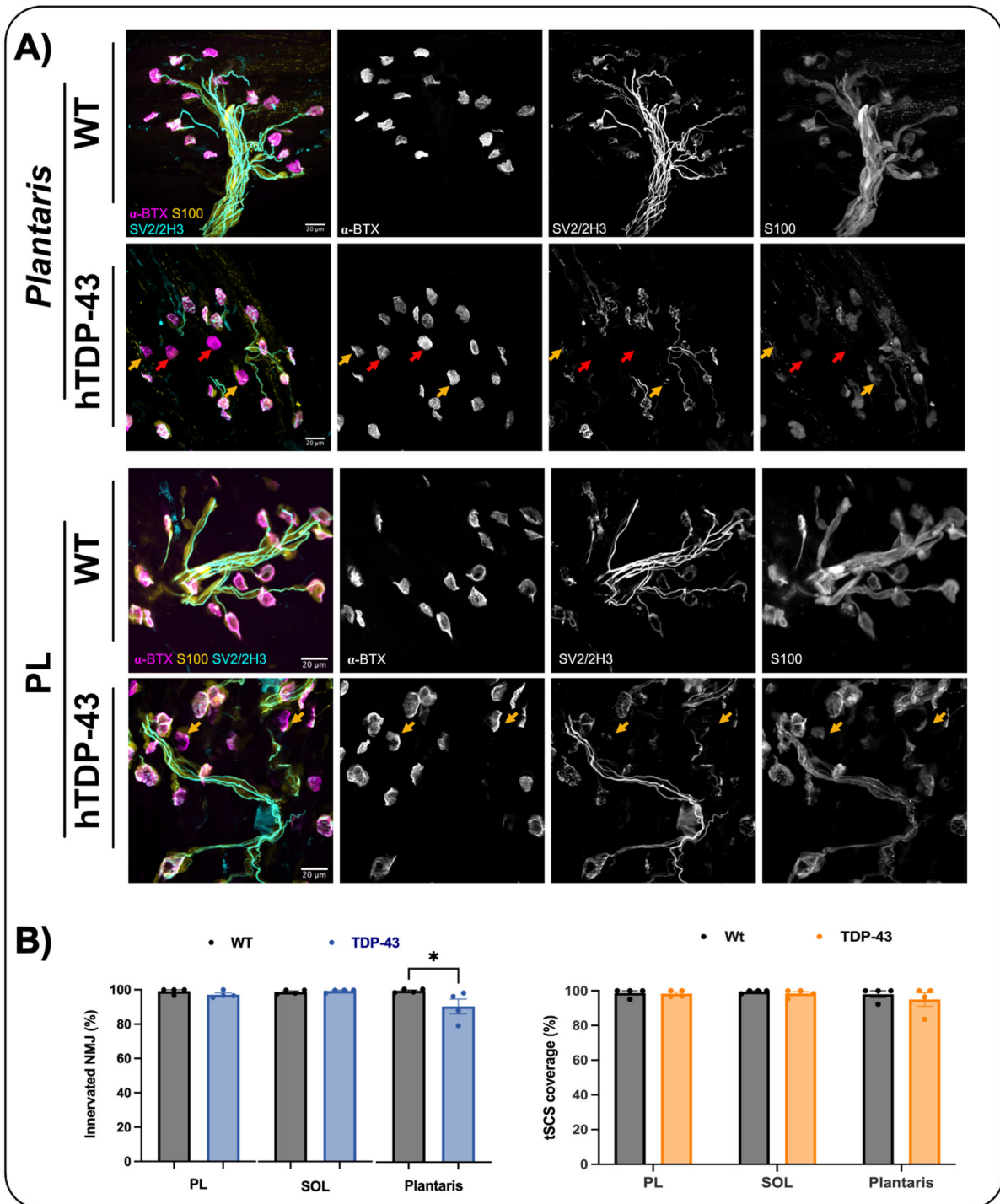
Appendix 16: TSC sprouts (arrows) were more frequently observed in the muscles of hTDP-43 mice compared with those from WT animals. Alpha-BTX (α -bungarotoxin) labels acetylcholine receptors (magenta); S100b labels tSCs (yellow). SV2/2H3 label synaptic vesicles and neurofilaments to visualize nerve terminals and axon, respectively (cyan).

Gastrocnemius in hTDP-43 mice at end-stage



→ Complete loss of S100b → No loss of S100b

Appendix 17: Variable degrees of tSCs loss in the hTDP-43 mouse model. A representative confocal micrograph from hTDP-43 mice tissue showing vacant NMJs (blue and red arrows) with full coverage of tSCs (blue arrows) and two NMJs with complete loss of tSCs coverage (red arrows). Alpha-BTX (α -bungarotoxin) labels acetylcholine receptors (magenta); S100b labels tSCs (yellow). SV2/2H3 label synaptic vesicles and neurofilaments to visualize nerve terminals and axon, respectively (cyan).



Appendix 18: Assessment of NMJ denervation and tSC loss in PL, SOL, and plantaris at early symptomatic stage (P15) in hTDP-43 mice. A) representative confocal micrographs show vacant and partially denervated α BTX NMJs (red and orange arrows, respectively) in plantaris with complete or total loss of the S100b labelling, and partial denervation in PL (orange arrows). α -BTX (α -bungarotoxin) labels acetylcholine receptors (magenta); S100b labels tSCs (yellow). SV2/2H3 label synaptic vesicles and neurofilaments to visualize nerve terminals and axon, respectively (cyan). **B)** Bar charts illustrating the percentages of innervated NMJs and

NMJs fully covered by tSCs in PL, SOL, and plantaris at P15 with a significant reduction of innervation observed in plantaris only.

Publications

1. Minty, G., Hoppen, A., Boehm, I., **Alhindi, A.**, Gibb, L., Potter, E., *et al.* (2020) 'ANMJ-morph: A simple macro for rapid analysis of neuromuscular junction morphology', *Royal Society Open Science*, 7(4).
2. Boehm, I., **Alhindi, A.**, Leite, A. S., Logie, C., Gibbs, A., Murray, O., *et al.* (2020) 'Comparative anatomy of the mammalian neuromuscular junction', *Journal of Anatomy*, (March), pp. 1–10.
3. **Alhindi, A.**, Boehm, I., Forsythe, R. O., Miller, J., Skipworth, R. J. E., Simpson, H., *et al.* (2021) 'Terminal Schwann cells at the human neuromuscular junction', *Brain Communications*, 3(2), pp. 1–12.
4. **Alhindi, A.**, Boehm, I. and Chaytow, H. (2021) 'Small junction, big problems: Neuromuscular junction pathology in mouse models of amyotrophic lateral sclerosis (ALS).', *Journal of Anatomy*, (May), pp. 1–19.
5. **Alhindi, A.**, Shand, M., Smith, H. L., Leite, A. S., Huang, Y. T., van der Hoorn, D., *et al.* (2023) 'Neuromuscular junction denervation and terminal Schwann cell loss in the hTDP-43 overexpression mouse model of amyotrophic lateral sclerosis', *Neuropathology and Applied Neurobiology*, 49(4), pp. 1–17.

Presentations at conferences:

1. Work from chapter 2 was presented at **the XV European meeting on Glial cells in health and disease, 2021.**
Poster title: Morphological Differences Between Terminal Schwann Cell at the Mouse and Human Neuromuscular Junction.
2. Work from chapter 4 and 5 was presented at **the European network to cure ALS conference, 2022.**
Poster title: Characterization of NMJ pathology in hTPD-43 ALS mouse model.
3. Work from chapter 4 and 5 was also presented at **the 3rd international scientific congress on spinal muscular atrophy, 2022.**
Poster title: Characterisation of NMJ pathology in a motor neuron disease mouse model.

References

- Afifi, A. K. *et al.* (1966) 'Ultrastructure of atrophic muscle in amyotrophic lateral sclerosis', *Neurology*. AAN Enterprises, 16(5), p. 475.
- Ahmadi, M. *et al.* (2010) 'Human extraocular muscles in ALS', *Investigative Ophthalmology and Visual Science*, 51(7), pp. 3494–3501. doi: 10.1167/iovs.09-5030.
- Albuquerque, E. . *et al.* (1976) 'An electrophysiological and morphological study of the neuromuscular junction in patients with myasthenia gravis', *Experimental Neurology*. Elsevier Inc, 51(3), pp. 536–563. doi: 10.1016/0014-4886(76)90179-5.
- Alhindi, A. *et al.* (2021) 'Terminal Schwann cells at the human neuromuscular junction', *Brain Communications*, 3(2), pp. 1–12. doi: 10.1093/braincomms/fcab081.
- Alhindi, A. *et al.* (2023) 'Neuromuscular junction denervation and terminal Schwann cell loss in the hTDP-43 overexpression mouse model of amyotrophic lateral sclerosis', *Neuropathology and Applied Neurobiology*, 49(4), pp. 1–17. doi: 10.1111/nan.12925.
- Altman, T. *et al.* (2021) 'Axonal TDP-43 condensates drive neuromuscular junction disruption through inhibition of local synthesis of nuclear encoded mitochondrial proteins', *Nature Communications*, 12(1). doi: 10.1038/s41467-021-27221-8.
- Alvarez-Suarez, P., Gawor, M. and Prószyński, T. J. (2020) 'Perisynaptic schwann cells - The multitasking cells at the developing neuromuscular junctions', *Seminars in Cell and Developmental Biology*. Elsevier, (February), pp. 0–1. doi: 10.1016/j.semcdb.2020.02.011.
- An, D. *et al.* (2019) 'Stem cell-derived cranial and spinal motor neurons reveal proteostatic differences between ALS resistant and sensitive motor neurons', *Elife*. eLife Sciences Publications, Ltd, 8, p. e44423.
- Andersen, P. M. *et al.* (1996) 'Autosomal recessive adult-onset amyotrophic lateral sclerosis associated with homozygosity for Asp90Ala CuZn-superoxide dismutase mutation: a clinical and genealogical study of 36 patients', *Brain*. Oxford University Press, 119(4), pp. 1153–1172.
- Andreadou, E. *et al.* (2008) 'Plasma glutamate and glycine levels in patients with amyotrophic lateral sclerosis: The effect of riluzole treatment', *Clinical Neurology and Neurosurgery*. Elsevier, 110(3), pp. 222–226.
- Ang, E.-T. *et al.* (2010) 'Motor Axonal Sprouting and Neuromuscular Junction Loss in an Animal Model of Charcot-Marie-Tooth Disease', *Journal of Neuropathology & Experimental Neurology*, 69(3), pp. 281–293. doi: 10.1097/NEN.0b013e3181d1e60f.
- Arbour, D. *et al.* (2015) 'Early and persistent abnormal decoding by glial cells at the neuromuscular junction in an ALS model', *Journal of Neuroscience*, 35(2), pp. 688–706. doi: 10.1523/JNEUROSCI.1379-14.2015.
- Ariano, M. ., Armstrong, R. . and Edgerton, V. R. (1973) 'Hindlimb Muscle Fiber Populations of Five Mammals', *The Journal of Histochemistry and Cytochemistry*, 21(1), pp. 51–55.

- Armon, C. (2009) 'Smoking may be considered an established risk factor for sporadic ALS', *Neurology*, 73(20), pp. 1693–1698. doi: 10.1212/WNL.0b013e3181c1df48.
- Arnold, E. S. *et al.* (2013) 'ALS-linked TDP-43 mutations produce aberrant RNA splicing and adult-onset motor neuron disease without aggregation or loss of nuclear TDP-43', *Proceedings of the National Academy of Sciences of the United States of America*, 110(8). doi: 10.1073/pnas.1222809110.
- Arriza, J. L. *et al.* (1994) 'Functional comparisons of three glutamate transporter subtypes cloned from human motor cortex', *Journal of Neuroscience*. Soc Neuroscience, 14(9), pp. 5559–5569.
- Aspinall, V. and Cappello, M. (2009) *Introduction to Veterinary Anatomy and Physiology Textbook*. 2nd edn. Butterworth Heinemann Elsevier.
- Astrow, S. H., Qiang, H. and Ko, C. P. (1998) 'Perisynaptic Schwann cells at neuromuscular junctions revealed by a novel monoclonal antibody', *Journal of Neurocytology*, 27(9), pp. 667–681. doi: 10.1023/A:1006916232627.
- Ayala, Y. M. *et al.* (2008) 'Structural determinants of the cellular localization and shuttling of TDP-43', *Journal of Cell Science*. Company of Biologists, 121(22), pp. 3778–3785.
- Bae, J. S. *et al.* (2014) 'Cortical hyperexcitability and the split-hand plus phenomenon: Pathophysiological insights in ALS', *Amyotrophic Lateral Sclerosis and Frontotemporal Degeneration*. Taylor & Francis, 15(3–4), pp. 250–256. doi: 10.3109/21678421.2013.872150.
- Baloh, R. H. *et al.* (2007) 'Frequent atrophic groups with mixed-type myofibers is distinctive to motor neuron syndromes', *Muscle and Nerve*, 36(1), pp. 107–110. doi: 10.1002/mus.20755.
- Baralle, M., Buratti, E. and Baralle, F. E. (2013) 'The role of TDP-43 in the pathogenesis of ALS and FTL D', *Biochemical Society Transactions*, 41(6), pp. 1536–1540. doi: 10.1042/BST20130186.
- Barrett, E. F., Barrett, J. N. and David, G. (2011) 'Mitochondria in motor nerve terminals: Function in health and in mutant superoxide dismutase 1 mouse models of familial ALS', *Journal of Bioenergetics and Biomembranes*, 43(6), pp. 581–586. doi: 10.1007/s10863-011-9392-1.
- Batista, A. F. R. and Hengst, U. (2016) 'Intra-axonal protein synthesis in development and beyond', *International Journal of Developmental Neuroscience*. Elsevier, 55, pp. 140–149.
- Baxter, B., Gillingwater, T. H. and Parson, S. H. (2008) 'Rapid loss of motor nerve terminals following hypoxia-reperfusion injury occurs via mechanisms distinct from classic Wallerian degeneration', *Journal of Anatomy*, 212(6), pp. 827–835. doi: 10.1111/j.1469-7580.2008.00909.x.
- Bendotti, C. *et al.* (2001) 'Transgenic SOD1 G93A mice develop reduced GLT-1 in spinal cord without alterations in cerebrospinal fluid glutamate levels', *Journal of Neurochemistry*. Wiley Online Library, 79(4), pp. 737–746.

- Berger, M. M. *et al.* (2000) ‘Detection and cellular localization of enterovirus RNA sequences in spinal cord of patients with ALS’, *Neurology*, 54(1), pp. 20–25. doi: 10.1212/wnl.54.1.20.
- Berthold, C. H. and Nilsson, I. (1987) ‘Redistribution of Schwann cells in developing feline L7 ventral spinal roots’, *Journal of Neurocytology*, 16(6), pp. 811–828. doi: 10.1007/BF01611988.
- Bilsland, L. G. *et al.* (2010) ‘Deficits in axonal transport precede ALS symptoms in vivo’, *Proceedings of the National Academy of Sciences of the United States of America*, 107(47), pp. 20523–20528. doi: 10.1073/pnas.1006869107.
- Bishop, D. L. *et al.* (2004) ‘Axon branch removal at developing synapses by axosome shedding’, *Neuron*, 44(4), pp. 651–661. doi: 10.1016/j.neuron.2004.10.026.
- Bjornskov, E. K. *et al.* (1975) ‘End-Plate Morphology in Amyotrophic Lateral Sclerosis’, *Archives of Neurology*, 32(10), pp. 711–712. doi: 10.1001/archneur.1975.00490520081016.
- Bjornskov, E. K., Norris, F. H. and Mower-Kuby, J. (1984) ‘Quantitative Axon Terminal and End-plate Morphology in Amyotrophic Lateral Sclerosis’, *Archives of Neurology*, 41(5), pp. 527–530. doi: 10.1001/archneur.1984.04050170073021.
- Blecher, R. *et al.* (2019) ‘Contact sports as a risk factor for amyotrophic lateral sclerosis: a systematic review’, *Global Spine Journal*. SAGE Publications Sage CA: Los Angeles, CA, 9(1), pp. 104–118.
- Boehm, I., Alhindi, A., *et al.* (2020) ‘Comparative anatomy of the mammalian neuromuscular junction’, *Journal of Anatomy*, (March), pp. 1–10. doi: 10.1111/joa.13260.
- Boehm, I., Miller, J., *et al.* (2020) ‘Neuromuscular junctions are stable in patients with cancer cachexia’, *Journal of Clinical Investigation*, 130(3), pp. 1461–1465. doi: 10.1172/JCI128411.
- Boillée, S. *et al.* (2006) ‘Onset and progression in inherited ALS determined by motor neurons and microglia’, *Science*. American Association for the Advancement of Science, 312(5778), pp. 1389–1392.
- Boriek, A. M., Miller, C. C. and Rodarte, J. R. (1998) ‘Muscle fiber architecture of the dog diaphragm’, *Journal of Applied Physiology*, 84(1), pp. 318–326. doi: 10.1152/jappl.1998.84.1.318.
- Van Den Bosch, L. *et al.* (2006) ‘The role of excitotoxicity in the pathogenesis of amyotrophic lateral sclerosis’, *Biochimica et Biophysica Acta - Molecular Basis of Disease*, 1762(11–12), pp. 1068–1082. doi: 10.1016/j.bbadis.2006.05.002.
- Bradley, W. G. *et al.* (1983) ‘Morphometric and biochemical studies of peripheral nerves in amyotrophic lateral sclerosis’, *Annals of Neurology*, 14(3), pp. 267–277. doi: 10.1002/ana.410140304.
- Brill, M. S. *et al.* (2011) ‘Spatial constraints dictate glial territories at murine neuromuscular junctions’, *Journal of Cell Biology*. The Rockefeller University Press, 195(2), pp. 293–305.

- Brill, M. S., Marinković, P. and Misgeld, T. (2013) 'Sequential photo-bleaching to delineate single Schwann cells at the neuromuscular junction.', *Journal of Visualized Experiments: JoVE*, (71), pp. 1–7. doi: 10.3791/4460.
- Bristol, L. A. and Rothstein, J. D. (1996) 'Glutamate transporter gene expression in amyotrophic lateral sclerosis motor cortex', *Annals of Neurology*, 39(5), pp. 676–679. doi: 10.1002/ana.410390519.
- Brockes, J. P., Fields, K. L. and Raff, M. C. (1979) 'Studies on cultured rat Schwann cells. I. Establishment of purified populations from cultures of peripheral nerve', *Brain research*. Elsevier, 165(1), pp. 105–118.
- Bros-Facer, V. *et al.* (2014) 'Treatment with an antibody directed against nogo-a delays disease progression in the SOD1G93A mouse model of Amyotrophic lateral sclerosis', *Human Molecular Genetics*, 23(16), pp. 4187–4200. doi: 10.1093/hmg/ddu136.
- Brown, M. C., Jansen, J. K. and Van Essen, D. (1976) 'Polyneuronal innervation of skeletal muscle in new-born rats and its elimination during maturation.', *The Journal of Physiology*. Wiley Online Library, 261(2), pp. 387–422.
- Brown, R. H. and Al-Chalabi, A. (2017) 'Amyotrophic lateral sclerosis', *New England Journal of Medicine*. Mass Medical Soc, 377(2), pp. 162–172.
- Bruijn, L. I. *et al.* (1997) 'ALS-linked SOD1 mutant G85R mediates damage to astrocytes and promotes rapidly progressive disease with SOD1-containing inclusions', *Neuron*. Elsevier, 18(2), pp. 327–338.
- Brull, S. J. and Naguib, M. (2011) 'Review of Neuromuscular Junction Anatomy and Function', in *Neuroscientific Foundations of Anesthesiology*. Oxford University Press. doi: 10.1093/med/9780195398243.003.0104.
- Bruneteau, G. *et al.* (2015) 'Endplate denervation correlates with Nogo-A muscle expression in amyotrophic lateral sclerosis patients', *Annals of Clinical and Translational Neurology*, 2(4), pp. 362–372. doi: 10.1002/acn3.179.
- Cahalan, S. D., Perkins, J. D., *et al.* (2022) 'A method to identify, dissect and stain equine neuromuscular junctions for morphological analysis', *Journal of Anatomy*, (May), pp. 1133–1147. doi: 10.1111/joa.13747.
- Cahalan, S. D., Boehm, I., *et al.* (2022) 'Recognising the potential of large animals for modelling neuromuscular junction physiology and disease', *Journal of Anatomy*, (September). doi: 10.1111/joa.13749.
- Camu, W., Billiard, M. and Baldy-Moulinier, M. (1993) 'Fasting plasma and CSF amino acid levels in amyotrophic lateral sclerosis: a subtype analysis', *Acta Neurologica Scandinavica*. Wiley Online Library, 88(1), pp. 51–55.
- Carpenter, S. (1968) 'Proximal axonal enlargement in motor neuron disease', *Neurology*. AAN Enterprises, 18(9), p. 841.

- Carrasco, D. I., Seburn, K. L. and Pinter, M. J. (2016) 'Altered terminal Schwann cell morphology precedes denervation in SOD1 mice', *Experimental Neurology*. Elsevier Inc., 275(10), pp. 172–181. doi: 10.1016/j.expneurol.2015.09.014.
- Castro, R. *et al.* (2020) 'Specific labeling of synaptic schwann cells reveals unique cellular and molecular features', *eLife*, 9, pp. 1–19. doi: 10.7554/eLife.56935.
- Chand, K. K. *et al.* (2018) 'Defects in synaptic transmission at the neuromuscular junction precede motor deficits in a TDP-43 Q331K transgenic mouse model of amyotrophic lateral sclerosis', *The FASEB Journal*, 32(5), pp. 2676–2689. doi: 10.1096/fj.201700835R.
- Chang, K. *et al.* (2021) 'TDP-43 maximizes nerve conduction velocity by repressing a cryptic exon for paranodal junction assembly in Schwann cells', *eLife*, 10, pp. 1–26. doi: <https://doi.org/10.7554/eLife.64456>.
- Chiang, P. M. *et al.* (2010) 'Deletion of TDP-43 down-regulates Tbc1d1, a gene linked to obesity, and alters body fat metabolism', *Proceedings of the National Academy of Sciences of the United States of America*, 107(37), pp. 16320–16324. doi: 10.1073/pnas.1002176107.
- Chiò, A. *et al.* (2001) 'Incidence of ALS in Italy: Evidence for a uniform frequency in Western countries', *Neurology*, 56(2), pp. 239–244. doi: 10.1212/WNL.56.2.239.
- Chiu, A. Y. *et al.* (1995) 'Age-dependent penetrance of disease in a transgenic mouse model of familial amyotrophic lateral sclerosis', *Molecular and Cellular Neurosciences*, pp. 349–362. doi: 10.1006/mcne.1995.1027.
- Choquer, M. *et al.* (2020) 'Insomnia is frequent in amyotrophic lateral sclerosis at the time of diagnosis', *Sleep and Biological Rhythms*. Springer Japan, (0123456789). doi: 10.1007/s41105-020-00296-4.
- Chou, S. M. (1991) 'Neuropathology of upper motor neurons in amyotrophic lateral sclerosis', *Proc XI Intl Cong Neuropathol*, pp. 595–598.
- Chou, S. M. (1992) 'Pathology: light microscopy of amyotrophic lateral sclerosis', *Handbook of Amyotrophic Lateral Sclerosis*. Marcel Dekker, pp. 133–181.
- Chou, S. and Norris, F. (1993) 'Amyotrophic Lateral Sclerosis: Lower Motor Neuron Disease Spreading to Upper Motor Neurons', *Muscle & Nerve*, (August), pp. 864–869.
- Chung, M. J. and Suh, Y. L. (2002) 'Ultrastructural changes of mitochondria in the skeletal muscle of patients with amyotrophic lateral sclerosis', *Ultrastructural Pathology*, 26(1), pp. 3–7. doi: 10.1080/01913120252934260.
- Chung, W.-S. and Barres, B. A. (2009) 'Selective remodeling: refining neural connectivity at the neuromuscular junction', *PLoS biology*. Public Library of Science San Francisco, USA, 7(8), p. e1000185.
- Cipriani, S. *et al.* (2018) 'Neuromuscular junction changes in a mouse model of Charcot-Marie-Tooth Disease Type 4C', *International journal of molecular sciences*. MDPI, 19(12), p. 4072.

- Clark, J. A. *et al.* (2016) ‘Axonal degeneration, distal collateral branching and neuromuscular junction architecture alterations occur prior to symptom onset in the SOD1G93A mouse model of amyotrophic lateral sclerosis’, *Journal of Chemical Neuroanatomy*. Elsevier B.V., 76, pp. 35–47. doi: 10.1016/j.jchemneu.2016.03.003.
- Collard, J.-F., Côté, F. and Julien, J.-P. (1995) ‘Defective axonal transport in a transgenic mouse model of amyotrophic lateral sclerosis’, *Nature*. Nature Publishing Group UK London, 375(6526), pp. 61–64.
- Comley, L. H. *et al.* (2016) ‘Cross-disease comparison of amyotrophic lateral sclerosis and spinal muscular atrophy reveals conservation of selective vulnerability but differential neuromuscular junction pathology’, *Journal of Comparative Neurology*, 524(7), pp. 1424–1442. doi: 10.1002/cne.23917.
- Coughlin, S. R. (2000) ‘Thrombin signalling and protease-activated receptors’, *Nature*, 407(6801), pp. 258–264. doi: 10.1038/35025229.
- Courtney, J. and Steinbach, J. H. (1981) ‘Age changes in neuromuscular junction morphology and acetylcholine receptor distribution on rat skeletal muscle fibres.’, *The Journal of Physiology*, 320(1), pp. 435–447. doi: 10.1113/jphysiol.1981.sp013960.
- Cozzi, B. *et al.* (2017) ‘Aging and Veterinary Care of Cats, Dogs, and Horses through the Records of Three University Veterinary Hospitals’, *Frontiers in Veterinary Science*. Available at: <https://www.frontiersin.org/articles/10.3389/fvets.2017.00014>.
- Cudkowicz, M. E. *et al.* (1997) ‘Epidemiology of mutations in superoxide dismutase in amyotrophic lateral sclerosis’, *Annals of Neurology*, 41(2), pp. 210–221. doi: 10.1002/ana.410410212.
- Dadon-Nachum, M., Melamed, E. and Offen, D. (2011) ‘The “dying-back” phenomenon of motor neurons in ALS’, *Journal of Molecular Neuroscience*, 43(3), pp. 470–477. doi: 10.1007/s12031-010-9467-1.
- Darabid, H., Arbour, D. and Robitaille, R. (2013) ‘Glial cells decipher synaptic competition at the mammalian neuromuscular junction’, *Journal of Neuroscience*, 33(4), pp. 1297–1313. doi: 10.1523/JNEUROSCI.2935-12.2013.
- DeChiara, T. M. *et al.* (1996) ‘The receptor tyrosine kinase MuSK is required for neuromuscular junction formation in vivo’, *Cell*. Elsevier, 85(4), pp. 501–512.
- DeJesus-Hernandez, M. *et al.* (2011) ‘Expanded GGGGCC Hexanucleotide Repeat in Noncoding Region of C9ORF72 Causes Chromosome 9p-Linked FTD and ALS’, *Neuron*. Elsevier Inc., 72(2), pp. 245–256. doi: 10.1016/j.neuron.2011.09.011.
- Dengler, R. *et al.* (2005) ‘Amyotrophic lateral sclerosis: new developments in diagnostic markers’, *Neurodegenerative Diseases*. Karger Publishers, 2(3–4), pp. 177–184.
- DePaul, R. and Brooks, B. R. (1993) ‘Multiple orofacial indices in amyotrophic lateral sclerosis’, *Journal of Speech, Language, and Hearing Research*. ASHA, 36(6), pp. 1158–1167.

- Desaki, J. and Uehara, Y. (1981) 'The overall morphology of neuromuscular junctions as revealed by scanning electron microscopy', *Journal of Neurocytology*, 10(1), pp. 101–110. doi: 10.1007/BF01181747.
- Deschenes, M. R. *et al.* (2016) 'Effects of exercise training on neuromuscular junction morphology and pre- to post-synaptic coupling in young and aged rats', *Neuroscience*, 316, pp. 167–177. doi: <https://doi.org/10.1016/j.neuroscience.2015.12.004>.
- Deschenes, M. R. (2019) 'Adaptations of the neuromuscular junction to exercise training', *Current Opinion in Physiology*, 10, pp. 10–16. doi: <https://doi.org/10.1016/j.cophys.2019.02.004>.
- Devoy, A. *et al.* (2017) 'Humanized mutant FUS drives progressive motor neuron degeneration without aggregation in 'FUSDelta14' knockin mice', *Brain*. Oxford University Press, 140(11), pp. 2797–2805.
- Dewil, M. *et al.* (2007) 'Inhibition of p38 mitogen activated protein kinase activation and mutant SOD1G93A-induced motor neuron death', *Neurobiology of Disease*. Elsevier, 26(2), pp. 332–341.
- Dimitrova, D. M. *et al.* (2009) 'Polyneuronal innervation of single muscle fibers in cat eye muscle: Inferior oblique', *Journal of Neurophysiology*, 101(6), pp. 2815–2821. doi: 10.1152/jn.90828.2008.
- Dirren, E. *et al.* (2015) 'SOD1 silencing in motoneurons or glia rescues neuromuscular function in ALS mice', *Annals of Clinical and Translational Neurology*. Wiley Online Library, 2(2), pp. 167–184.
- Dobrowolny, G. *et al.* (2008) 'Skeletal Muscle Is a Primary Target of SOD1G93A-Mediated Toxicity', *Cell Metabolism*, 8(5), pp. 425–436. doi: 10.1016/j.cmet.2008.09.002.
- Dobrowolny, G., Aucello, M. and Musarò, A. (2011) 'Muscle atrophy induced by SOD1G93A expression does not involve the activation of caspase in the absence of denervation', *Skeletal Muscle*, 1(1), pp. 1–8. doi: 10.1186/2044-5040-1-3.
- Done, S. *et al.* (2009) *Color Atlas of Veterinary Anatomy, the Cat and Dog*. 2ne edn. Elsevier Inc.
- Duque, S. I. *et al.* (2015) 'A large animal model of spinal muscular atrophy and correction of phenotype', *Annals of Neurology*. Wiley Online Library, 77(3), pp. 399–414.
- Ebstein, S. Y., Yagudayeva, I. and Shneider, N. A. (2019) 'Mutant TDP-43 Causes Early-Stage Dose-Dependent Motor Neuron Degeneration in a TARDBP Knockin Mouse Model of ALS', *Cell Reports*. ElsevierCompany., 26(2), pp. 364-373.e4. doi: 10.1016/j.celrep.2018.12.045.
- Eisen, A., Kim, S. and Pant, B. (1992) 'Amyotrophic lateral sclerosis (ALS): A phylogenetic disease of the corticomotoneuron?', *Muscle & Nerve*, 15(2), pp. 219–224. doi: 10.1002/mus.880150215.

- Eisen, A. and Weber, M. (2001) 'The motor cortex and amyotrophic lateral sclerosis', *Muscle and Nerve*, 24(4), pp. 564–573. doi: 10.1002/mus.1042.
- Escher, P. *et al.* (2005) 'Synapses form in skeletal muscles lacking neuregulin receptors', *Science*. American Association for the Advancement of Science, 308(5730), pp. 1920–1923.
- Esmaeili, M. A. *et al.* (2013) 'Premature death of TDP-43 (A315T) transgenic mice due to gastrointestinal complications prior to development of full neurological symptoms of amyotrophic lateral sclerosis', *International Journal of Experimental Pathology*, 94(1), pp. 56–64. doi: 10.1111/iep.12006.
- Fahim, M. A., Holley, J. A. and Robbins, N. (1984) 'Topographic comparison of neuromuscular junctions in mouse slow and fast twitch muscles', *Neuroscience*, 13(1). doi: 10.1016/0306-4522(84)90273-2.
- Fails, A. D. and Magee, C. (2018) *Anatomy and Physiology of Farm Animals*. John Wiley & Sons.
- Fang, J. *et al.* (2016) 'Pattern differences of small hand muscle atrophy in amyotrophic lateral sclerosis and mimic disorders', *Chinese Medical Journal*, 129(7), pp. 792–798. doi: 10.4103/0366-6999.178953.
- Fawcett, J. W. and Keynes, R. J. (1990) 'Peripheral nerve regeneration', *Annual review of neuroscience*. Annual Reviews 4139 El Camino Way, PO Box 10139, Palo Alto, CA 94303-0139, USA, 13(1), pp. 43–60.
- Feng, Z. and Ko, C.-P. (2008) 'Schwann cells promote synaptogenesis at the neuromuscular junction via transforming growth factor- β 1', *Journal of Neuroscience*. Soc Neuroscience, 28(39), pp. 9599–9609.
- Ferguson, T. A. and Elman, L. B. (2007) 'Clinical presentation and diagnosis of Amyotrophic Lateral Sclerosis', *NeuroRehabilitation*. IOS Press, 22, pp. 409–416. doi: 10.3233/NRE-2007-22602.
- Fischer, L. R. *et al.* (2004) 'Amyotrophic lateral sclerosis is a distal axonopathy: Evidence in mice and man', *Experimental Neurology*, 185(2), pp. 232–240. doi: 10.1016/j.expneurol.2003.10.004.
- Folker, E. S. and Baylies, M. K. (2013) 'Nuclear positioning in muscle development and disease', *Frontiers in Physiology*. Frontiers Media SA, 4, p. 363.
- Fratta, P. *et al.* (2018) 'Mice with endogenous TDP-43 mutations exhibit gain of splicing function and characteristics of amyotrophic lateral sclerosis', *The EMBO Journal*, 37(11), p. e98684.
- Frey, D. *et al.* (2000) 'Early and selective loss of neuromuscular synapse subtypes with low sprouting competence in motoneuron diseases', *Journal of Neuroscience*, 20(7), pp. 2534–2542. doi: 10.1523/jneurosci.20-07-02534.2000.

- Fu, H., Hardy, J. and Duff, K. E. (2018) 'Selective vulnerability in neurodegenerative diseases', *Nature Neuroscience*. Springer US, 21(10), pp. 1350–1358. doi: 10.1038/s41593-018-0221-2.
- Fuertes-Alvarez, S. and Izeta, A. (2021) 'Terminal Schwann Cell Aging: Implications for Age-Associated Neuromuscular Dysfunction', *Aging and disease*, 12(2), p. 494. doi: 10.14336/AD.2020.0708.
- Gallo, V. *et al.* (2009) 'Smoking and risk for amyotrophic lateral sclerosis: analysis of the EPIC cohort', *Annals of neurology*. Wiley Online Library, 65(4), pp. 378–385.
- Galvas, P. E. and Gonyea, W. J. (1980) 'Motor-end-plate and nerve distribution in a histochemically compartmentalized pennate muscle in the cat', *American Journal of Anatomy*, 159(2), pp. 147–156. doi: 10.1002/aja.1001590203.
- Gambino, D. R., Malmgren, L. T. and Gacek, R. R. (1990) 'Age-related changes in the neuromuscular junctions in the human posterior cricoarytenoid muscles: a quantitative study', *The Laryngoscope*. Wiley Online Library, 100(3), pp. 262–268.
- Genin, E. C. *et al.* (2019) 'Mitochondrial defect in muscle precedes neuromuscular junction degeneration and motor neuron death in CHCHD10S59L/+ mouse', *Acta Neuropathologica*. Springer, 138(1), pp. 123–145.
- Glass, D. J. *et al.* (1996) 'The receptor tyrosine kinase MuSK is required for neuromuscular junction formation and is a functional receptor for agrin', in *Cold Spring Harbor Symposia on Quantitative Biology*. Cold Spring Harbor Laboratory Press, pp. 435–444.
- Goetz, C. G. (2009) *Chapter 15 Jean-Martin Charcot and the Anatomico-Clinical Method of Neurology*. 3rd edn, *Handbook of Clinical Neurology*. 3rd edn. Elsevier B.V. doi: 10.1016/S0072-9752(08)02115-5.
- Gonzalez, D. *et al.* (2017) 'ALS skeletal muscle shows enhanced TGF- β signaling, fibrosis and induction of fibro/adipogenic progenitor markers', *PLOS ONE*. Public Library of Science, 12(5), p. e0177649. Available at: <https://doi.org/10.1371/journal.pone.0177649>.
- Gordon, D. *et al.* (2019) 'Single-copy expression of an amyotrophic lateral sclerosis-linked TDP-43 mutation (M337V) in BAC transgenic mice leads to altered stress granule dynamics and progressive motor dysfunction', *Neurobiology of Disease*. Elsevier Inc, 121, pp. 148–162. doi: 10.1016/j.nbd.2018.09.024.
- Gordon, D. C. *et al.* (1989) 'Muscle-fiber architecture, innervation, and histochemistry in the diaphragm of the cat', *Journal of Morphology*, 201(2), pp. 131–143. doi: 10.1002/jmor.1052010204.
- Gould, T. W. *et al.* (2006) 'Complete dissociation of motor neuron death from motor dysfunction by Bax deletion in a mouse model of ALS', *Journal of Neuroscience*, 26(34), pp. 8774–8786. doi: 10.1523/JNEUROSCI.2315-06.2006.
- Gould, T. W. *et al.* (2019) 'Glial cells maintain synapses by inhibiting an activity-dependent retrograde protease signal', *PLoS genetics*. Public Library of Science San Francisco, CA USA,

15(3), p. e1007948.

Grant, K. *et al.* (1979) 'Morphological characteristics of lateral rectus motoneurons shown by intracellular injection of HRP.', *Journal de Physiologie*, 75(5), pp. 513–519.

Griffin, J. W. and Thompson, W. J. (2008) 'Biology and pathology of nonmyelinating schwann cells', *Glia*, 56(14), pp. 1518–1531. doi: 10.1002/glia.20778.

Gurney, M. E. *et al.* (1994) 'Motor neuron degeneration in mice that express a human Cu,Zn superoxide dismutase mutation', *Science*, 264(5166), pp. 1772–1775. doi: 10.1126/science.8209258.

Gurney, M. E. *et al.* (1996) 'Benefit of vitamin E, riluzole, and gababapentin in a transgenic model of familial amyotrophic lateral sclerosis', *Annals of Neurology*. Wiley Online Library, 39(2), pp. 147–157.

Guyenet, S. J. *et al.* (2010) 'A simple composite phenotype scoring system for evaluating mouse models of cerebellar ataxia', *JoVE (Journal of Visualized Experiments)*, (39), p. e1787.

Halstead, S. K. *et al.* (2005) 'Anti-disialosyl antibodies mediate selective neuronal or Schwann cell injury at mouse neuromuscular junctions', *Glia*. Wiley Online Library, 52(3), pp. 177–189.

Harding, B. N. *et al.* (2015) 'Spectrum of neuropathophysiology in spinal muscular atrophy type i', *Journal of Neuropathology and Experimental Neurology*. © 2015 by American Association of Neuropathologists, Inc., 74(1), pp. 15–24. doi: 10.1097/NEN.0000000000000144.

Harrison, J. M. and Rafuse, V. F. (2020) 'Muscle fiber-type specific terminal Schwann cell pathology leads to sprouting deficits following partial denervation in SOD1G93A mice', *Neurobiology of Disease*. Elsevier, 145(July), p. 105052. doi: 10.1016/j.nbd.2020.105052.

Hassan, S. M. *et al.* (1994) 'GAP-43 and p75 NGFR immunoreactivity in presynaptic cells following neuromuscular blockade by botulinum toxin in rat', *Journal of neurocytology*. Springer, 23, pp. 354–363.

Hegedus, J. *et al.* (2008) 'Preferential motor unit loss in the SOD1 G93A transgenic mouse model of amyotrophic lateral sclerosis', *Journal of Physiology*, 586(14), pp. 3337–3351. doi: 10.1113/jphysiol.2007.149286.

Hegedus, J., Putman, C. T. and Gordon, T. (2007) 'Time course of preferential motor unit loss in the SOD1G93A mouse model of amyotrophic lateral sclerosis', *Neurobiology of Disease*, 28(2), pp. 154–164. doi: 10.1016/j.nbd.2007.07.003.

Herranz-Martin, S. *et al.* (2017) 'Viral delivery of *C9orf72* hexanucleotide repeat expansions in mice leads to repeat-length-dependent neuropathology and behavioural deficits', *Disease Models & Mechanisms*, 10(7), pp. 859–868. doi: 10.1242/dmm.029892.

Herrera, A. A., Qiang, H. and Ko, C. P. (2000) 'The role of perisynaptic Schwann cells in

development of neuromuscular junctions in the frog (*Xenopus laevis*)', *Journal of Neurobiology*, 45(4), pp. 237–254. doi: 10.1002/1097-4695(200012)45:4<237::AID-NEU5>3.0.CO;2-J.

Herrera, A. A. and Werle, M. J. (1990) 'Mechanisms of elimination, remodeling, and competition at frog neuromuscular junctions', *Journal of Neurobiology*, 21(1), pp. 73–98. doi: 10.1002/neu.480210106.

Hess, D. M. *et al.* (2007) 'Localization of TrkC to Schwann cells and effects of neurotrophin-3 signaling at neuromuscular synapses', *Journal of Comparative Neurology*. Wiley Online Library, 501(4), pp. 465–482.

Hesselmans, L. F. G. M. *et al.* (1993) 'Development of Innervation of Skeletal Muscle Fibers in Man: Relation to Acetylcholine Receptors', *The Anatomical Record*, 236, pp. 553–562.

Hirata, K. *et al.* (1997) 'Postnatal development of Schwann cells at neuromuscular junctions, with special reference to synapse elimination', *Journal of Neurocytology*. doi: 10.1023/A:1018570500052.

Holm, I. E., Alstrup, A. K. O. and Luo, Y. (2016) 'Genetically modified pig models for neurodegenerative disorders', *The Journal of Pathology*. Wiley Online Library, 238(2), pp. 267–287.

Howland, D. S. *et al.* (2002) 'Focal loss of the glutamate transporter EAAT2 in a transgenic rat model of SOD1 mutant-mediated amyotrophic lateral sclerosis (ALS)', *Proceedings of the National Academy of Sciences*. National Acad Sciences, 99(3), pp. 1604–1609.

Huisman, M. H. B. *et al.* (2011) 'Population based epidemiology of amyotrophic lateral sclerosis using capture-recapture methodology', *Journal of Neurology, Neurosurgery and Psychiatry*, 82(10), pp. 1165–1170. doi: 10.1136/jnnp.2011.244939.

Iguchi, Y. *et al.* (2013) 'Loss of TDP-43 causes age-dependent progressive motor neuron degeneration', *Brain*, 136(5), pp. 1371–1382. doi: 10.1093/brain/awt029.

Ingre, C. *et al.* (2015) 'Risk factors for amyotrophic lateral sclerosis', *Clinical Epidemiology*, 7, pp. 181–193. doi: 10.2147/CLEP.S37505.

Ioghen, O. *et al.* (2020) 'Non-Myelinating Schwann Cells in Health and Disease', in *Schwann Cells*. intechopen, p. 17. doi: <http://dx.doi.org/10.5772/intechopen.91930>.

Jans, H., Salzman, R. and Wernig, A. (1986) 'Sprouting and nerve retraction in frog neuromuscular junction during ontogenesis and environmental changes', *Neuroscience*, 18(3), pp. 773–781. doi: 10.1016/0306-4522(86)90069-2.

Jensen, L. *et al.* (2016) 'Skeletal Muscle Remodelling as a Function of Disease Progression in Amyotrophic Lateral Sclerosis', *BioMed Research International*, 2016. doi: 10.1155/2016/5930621.

Jiwlawat, N. *et al.* (2018) 'Current progress and challenges for skeletal muscle differentiation

from human pluripotent stem cells using transgene-free approaches', *Stem Cells International*. Hindawi, 2018.

Johnston, J. A. *et al.* (2000) 'Formation of high molecular weight complexes of mutant Cu,Zn-superoxide dismutase in a mouse model for familial amyotrophic lateral sclerosis', *Proceedings of the National Academy of Sciences of the United States of America*, 97(23), pp. 12571–12576. doi: 10.1073/pnas.220417997.

Jokic, N. *et al.* (2005) 'Nogo expression in muscle correlates with amyotrophic lateral sclerosis severity', *Annals of Neurology*, 57(4), pp. 553–556. doi: 10.1002/ana.20420.

Jones, R. A. *et al.* (2016) 'NMJ-morph reveals principal components of synaptic morphology influencing structure - Function relationships at the neuromuscular junction', *Royal Society Open Science*, 6(12). doi: 10.1098/rsob.160240.

Jones, R. A. *et al.* (2017) 'Cellular and Molecular Anatomy of the Human Neuromuscular Junction', *Cell Reports*. Elsevier Company., 21(9), pp. 2348–2356. doi: 10.1016/j.celrep.2017.11.008.

Jones, R. A. (2017) *Comparative Anatomy of the Human Neuromuscular Junction*. Doctoral Thesis. The University of Edinburgh.

Jordan, C. L. and Williams, T. J. (2001) 'Testosterone regulates terminal Schwann cell number and junctional size during developmental synapse elimination', *Developmental Neuroscience*, 23(6), pp. 441–451. doi: 10.1159/000048731.

Kang, H. *et al.* (2007) 'Regulation of the intermediate filament protein nestin at rodent neuromuscular junctions by innervation and activity', *Journal of Neuroscience*. Soc Neuroscience, 27(22), pp. 5948–5957.

Kang, H. *et al.* (2014) 'Terminal schwann cells participate in neuromuscular synapse remodeling during reinnervation following nerve injury', *Journal of Neuroscience*, 34(18), pp. 6323–6333. doi: 10.1523/JNEUROSCI.4673-13.2014.

Kang, H., Tian, L. and Thompson, W. J. (2019) 'Schwann cell guidance of nerve growth between synaptic sites explains changes in the pattern of muscle innervation and remodeling of synaptic sites following peripheral nerve injuries', *Journal of Comparative Neurology*. Wiley Online Library, 527(8), pp. 1388–1400.

Kang, S. H. *et al.* (2013) 'Degeneration and impaired regeneration of gray matter oligodendrocytes in amyotrophic lateral sclerosis', *Nature Neuroscience*. Nature Publishing Group US New York, 16(5), pp. 571–579.

Kariya, S. *et al.* (2008) 'Reduced SMN protein impairs maturation of the neuromuscular junctions in mouse models of spinal muscular atrophy', *Human Molecular Genetics*. Oxford University Press, 17(16), pp. 2552–2569. doi: 10.1093/hmg/ddn156.

Karpati, G., Carpenter, S. and Durham, H. (1988) 'A hypothesis for the pathogenesis of amyotrophic lateral sclerosis', *Revue Neurologique*. Department of Neurology and

Neurosurgery, McGill University, Montréal, Québec, Canada., 144(11), pp. 672–675. Available at: <http://europepmc.org/abstract/MED/3231956>.

Katz, J. S., Dimachkie, M. M. and Barohn, R. J. (2015) ‘Amyotrophic Lateral Sclerosis: A Historical Perspective’, *Neurologic Clinics*. Elsevier Inc, 33(4), pp. 727–734. doi: 10.1016/j.ncl.2015.07.013.

Kiernan, J. A. and Hudson, A. J. (1991) ‘Changes in sizes of cortical and lower motor neurons in amyotrophic lateral sclerosis’, *Brain*. Oxford University Press, 114(2), pp. 843–853.

Kiernan, M. C. *et al.* (2011) ‘Amyotrophic lateral sclerosis’, *The Lancet*. Elsevier Ltd, 377(9769), pp. 942–955. doi: 10.1016/S0140-6736(10)61156-7.

Kim, J. E. *et al.* (2015) ‘Pattern difference of dissociated hand muscle atrophy in amyotrophic lateral sclerosis and variants’, *Muscle and Nerve*, 51(3), pp. 333–337. doi: 10.1002/mus.24323.

Ko, C. P. (1987) ‘A lectin, peanut agglutinin, as a probe for the extracellular matrix in living neuromuscular junctions’, *Journal of Neurocytology*. Springer, 16(4), pp. 567–576. doi: 10.1007/BF01668509.

Kong, J. and Xu, Z. (1998) ‘Massive mitochondrial degeneration in motor neurons triggers the onset of amyotrophic lateral sclerosis in mice expressing a mutant SOD1’, *Journal of Neuroscience*, 18(9), pp. 3241–3250. doi: 10.1523/jneurosci.18-09-03241.1998.

Konno, T. and Watanabe, K. (2012) ‘Distribution of myofiber types in the crural musculature of sheep’, *Okajimas Folia Anatomica Japonica*, 89(2), pp. 39–45. doi: 10.2535/ofaj.89.39.

Kraemer, M., Buerger, M. and Berlit, P. (2010) ‘Diagnostic problems and delay of diagnosis in amyotrophic lateral sclerosis’, *Clinical Neurology and Neurosurgery*, 112(2), pp. 103–105. doi: <https://doi.org/10.1016/j.clineuro.2009.10.014>.

Krivickas, L. S. *et al.* (2002) ‘Skeletal muscle fiber function and rate of disease progression in amyotrophic lateral sclerosis’, *Muscle & Nerve: Official Journal of the American Association of Electrodiagnostic Medicine*. Wiley Online Library, 26(5), pp. 636–643.

Kuno, M., Turkanis, S. A. and Weakly, J. N. (1971) ‘Correlation between nerve terminal size and transmitter release at the neuromuscular junction of the frog’, *The Journal of Physiology*. Wiley-Blackwell, 213(3), p. 545.

Kwiatkowski, T. J. *et al.* (2009) ‘Mutations in the FUS/TLS Gene on Chromosome 16 Cause Familial Amyotrophic Lateral Sclerosis’, *Science*. American Association for the Advancement of Science, 323(5918), pp. 1205–1208. doi: 10.1126/science.1166066.

Lagier-Tourenne, C. *et al.* (2012) ‘Divergent roles of ALS-linked proteins FUS/TLS and TDP-43 intersect in processing long pre-mRNAs’, *Nature Neuroscience*. Nature Publishing Group, 15(11), pp. 1488–1497. doi: 10.1038/nn.3230.

Langmore, S. E. and Lehman, M. E. (1994) ‘Physiologic deficits in the orofacial system underlying dysarthria in amyotrophic lateral sclerosis’, *Journal of Speech, Language, and*

Hearing Research. ASHA, 37(1), pp. 28–37.

LaPointe, N. E. *et al.* (2009) ‘The amino terminus of tau inhibits kinesin-dependent axonal transport: implications for filament toxicity’, *Journal of Neuroscience Research*. Wiley Online Library, 87(2), pp. 440–451.

Lauriat, T. L. and McInnes, L. A. (2007) ‘EAAT2 regulation and splicing: relevance to psychiatric and neurological disorders’, *Molecular Psychiatry*, 12(12), pp. 1065–1078. doi: 10.1038/sj.mp.4002065.

Lee, Y. *et al.* (2011) ‘Muscles in a mouse model of spinal muscular atrophy show profound defects in neuromuscular development even in the absence of failure in neuromuscular transmission or loss of motor neurons’, *Developmental Biology*. Elsevier Inc., 356(2), pp. 432–444. doi: 10.1016/j.ydbio.2011.05.667.

Lee, Y. and Thompson, W. J. (2012) ‘The vertebrate neuromuscular junction’, in *Muscle-Fundamental Biology and Mechanisms of Disease: the vertebrate neuromuscular junction*. Elsevier Inc., pp. 775–787. doi: 10.1016/B978-0-12-381510-1.00054-5.

Leigh, P. N. *et al.* (1988) ‘Ubiquitin deposits in anterior horn cells in motor neurone disease’, *Neuroscience Letters*. Elsevier, 93(2–3), pp. 197–203.

Letinsky, M. S. and Morrison-Graham, K. (1980) ‘Structure of developing frog neuromuscular junctions’, *Journal of Neurocytology*, 9(3), pp. 321–342. doi: 10.1007/BF01181540.

Li, S.-H. and Li, X.-J. (2004) ‘Huntington and its role in neuronal degeneration’, *The Neuroscientist*. Sage Publications Sage CA: Thousand Oaks, CA, 10(5), pp. 467–475.

Lin, W. *et al.* (2000) ‘Aberrant development of motor axons and neuromuscular synapses in erbB2-deficient mice’, *Proceedings of the National Academy of Sciences*. National Acad Sciences, 97(3), pp. 1299–1304.

Liu, J. X. *et al.* (2013) ‘Distinct Changes in Synaptic Protein Composition at Neuromuscular Junctions of Extraocular Muscles versus Limb Muscles of ALS Donors’, *PLoS ONE*, 8(2). doi: 10.1371/journal.pone.0057473.

Liu, Y. *et al.* (2016) ‘C9orf72 BAC Mouse Model with Motor Deficits and Neurodegenerative Features of ALS/FTD’, *Neuron*. Elsevier Inc., 90(3), pp. 521–534. doi: 10.1016/j.neuron.2016.04.005.

Liu, Z. *et al.* (2015) ‘Specific marker expression and cell state of Schwann cells during culture in vitro’, *PLoS ONE*, 10(4), pp. 1–17. doi: 10.1371/journal.pone.0123278.

Loeb, G. E. *et al.* (1987) ‘Distribution and innervation of short, interdigitated muscle fibers in parallel-fibered muscles of the cat hindlimb’, *Journal of Morphology*, 191(1), pp. 1–15. doi: 10.1002/jmor.1051910102.

Logroscino, G. *et al.* (2010) ‘Incidence of amyotrophic lateral sclerosis in Europe’, *Journal of Neurology, Neurosurgery and Psychiatry*, 81(4), pp. 385–390. doi: 10.1136/jnnp.2009.183525.

López-Erauskin, J. *et al.* (2018) 'ALS/FTD-linked mutation in FUS suppresses intra-axonal protein synthesis and drives disease without nuclear loss-of-function of FUS', *Neuron*. Elsevier, 100(4), pp. 816–830.

Love, F. M. and Thompson, W. J. (1998) 'Schwann cells proliferate at rat neuromuscular junctions during development and regeneration', *Journal of Neuroscience*, 18(22), pp. 9376–9385. doi: 10.1523/jneurosci.18-22-09376.1998.

Lubischer, J. L. and Thompson, W. J. (1999) 'Neonatal Partial Denervation Results in Nodal But Not Terminal Sprouting and a Decrease in Efficacy of Remaining Neuromuscular Junctions in Rat Soleus Muscle', 19(20), pp. 8931–8944.

Mackenzie, I. R. A. *et al.* (2007) 'Pathological TDP-43 distinguishes sporadic amyotrophic lateral sclerosis from amyotrophic lateral sclerosis with SOD1 mutations', *Annals of Neurology: Official Journal of the American Neurological Association and the Child Neurology Society*. Wiley Online Library, 61(5), pp. 427–434.

Magrané, J. *et al.* (2014) 'Abnormal mitochondrial transport and morphology are common pathological denominators in SOD1 and TDP43 ALS mouse models', *Human Molecular Genetics*, 23(6), pp. 1413–1424. doi: 10.1093/hmg/ddt528.

Malek, A. M. *et al.* (2012) 'Pesticide exposure as a risk factor for amyotrophic lateral sclerosis: A meta-analysis of epidemiological studies: Pesticide exposure as a risk factor for ALS', *Environmental Research*, 117, pp. 112–119. doi: <https://doi.org/10.1016/j.envres.2012.06.007>.

Manjaly, Z. R. *et al.* (2010) 'The sex ratio in amyotrophic lateral sclerosis: A population based study', *Amyotrophic Lateral Sclerosis*. Taylor & Francis, 11(5), pp. 439–442. doi: 10.3109/17482961003610853.

Mantilla, C. B. and Sieck, G. C. (2001) 'Plasticity in Respiratory Motor Control Invited Review: Mechanisms underlying motor unit plasticity in the respiratory system', *Journal of Applied Physiology*, 49, pp. 1230–1241.

Manzano, R. *et al.* (2011) 'Altered expression of myogenic regulatory factors in the mouse model of amyotrophic lateral sclerosis', *Neurodegenerative diseases*. Karger Publishers, 8(5), pp. 386–396.

Marcuzzo, S. *et al.* (2011) 'Hind limb muscle atrophy precedes cerebral neuronal degeneration in G93A-SOD1 mouse model of amyotrophic lateral sclerosis: A longitudinal MRI study', *Experimental Neurology*. Elsevier Inc., 231(1), pp. 30–37. doi: 10.1016/j.expneurol.2011.05.007.

Marques, M. J. and Lichtman, J. W. (2000) 'From Plaque to Pretzel: Fold Formation and Acetylcholine Receptor Loss at the Developing Neuromuscular Junction', 20(10), pp. 3663–3675.

Martin, L. J. and Wong, M. (2020) 'Skeletal Muscle-Restricted Expression of Human SOD1 in Transgenic Mice Causes a Fatal ALS-Like Syndrome', 11(December), pp. 1–26. doi:

10.3389/fneur.2020.592851.

Martineau, É. *et al.* (2018) 'Dynamic neuromuscular remodeling precedes motor-unit loss in a mouse model of ALS', *eLife*, 7, pp. 1–19. doi: 10.7554/eLife.41973.

Martineau, É. *et al.* (2020) 'Properties of glial cell at the neuromuscular junction are incompatible with synaptic repair in the SOD1G37R ALS mouse model', *Journal of Neuroscience*, 40(40), pp. 7759–7777. doi: 10.1523/JNEUROSCI.1748-18.2020.

Mascarello, F. *et al.* (1982) 'The tensor tympani muscle of cat and dog contains IIM and slow-tonic fibres: an unusual combination of fibre types', *Journal of Muscle Research and Cell Motility*, 3(3), pp. 363–374. doi: 10.1007/BF00713043.

Maselli, R. A. *et al.* (1993) 'Neuromuscular transmission in amyotrophic lateral sclerosis.', *Muscle & Nerve*, (16), pp. 1193–1203.

Mattsson, P. *et al.* (2012) 'Physical fitness, but not muscle strength, is a risk factor for death in amyotrophic lateral sclerosis at an early age', *Journal of Neurology, Neurosurgery & Psychiatry*. BMJ Publishing Group Ltd, 83(4), pp. 390–394.

Mayr, R. (1971) 'Structure and distribution of fibre types in the external eye muscles of the rat', *Tissue and Cell*. Elsevier, 3(3), pp. 433–462.

McCombe, P. A. and Henderson, R. D. (2010) 'Effects of gender in amyotrophic lateral sclerosis', *Gender Medicine*. Elsevier HS Journals, Inc., 7(6), pp. 557–570. doi: 10.1016/j.genm.2010.11.010.

McGown, A. *et al.* (2013) 'Early interneuron dysfunction in ALS: insights from a mutant sod1 zebrafish model', *Annals of neurology*. Wiley Online Library, 73(2), pp. 246–258.

Mech, A. M. *et al.* (2020) 'Morphological variability is greater at developing than mature mouse neuromuscular junctions', *Journal of Anatomy*, (April), pp. 1–15. doi: 10.1111/joa.13228.

Mejia Maza, A. *et al.* (2021) 'NMJ-Analyser identifies subtle early changes in mouse models of neuromuscular disease', *Scientific Reports*. Nature Publishing Group UK, 11(1), pp. 1–17. doi: 10.1038/s41598-021-91094-6.

Mejzini, R. *et al.* (2019) 'ALS Genetics, Mechanisms, and Therapeutics: Where Are We Now?', *Frontiers in Neuroscience*, 13(December), pp. 1–27. doi: 10.3389/fnins.2019.01310.

Menon, P., Kiernan, M. C. and Vucic, S. (2014) 'Cortical dysfunction underlies the development of the split-hand in amyotrophic lateral sclerosis', *PLoS ONE*, 9(1). doi: 10.1371/journal.pone.0087124.

Minty, G. *et al.* (2020) 'ANMJ-morph: A simple macro for rapid analysis of neuromuscular junction morphology', *Royal Society Open Science*, 7(4). doi: 10.1098/rsos.200128.

Mitchell, J. C. *et al.* (2015) 'Wild type human TDP-43 potentiates ALS-linked mutant TDP-43 driven progressive motor and cortical neuron degeneration with pathological features of ALS',

- Acta Neuropathologica Communications*. 3, p. 36. doi: 10.1186/s40478-015-0212-4.
- Mitsumoto, H., Brooks, B. R. and Silani, V. (2014) ‘Clinical trials in amyotrophic lateral sclerosis: why so many negative trials and how can trials be improved?’, *The Lancet Neurology*. Elsevier, 13(11), pp. 1127–1138.
- Moller, A. *et al.* (2017) ‘Amyotrophic lateral sclerosis-associated mutant SOD1 inhibits anterograde axonal transport of mitochondria by reducing Miro1 levels’, *Human Molecular Genetics*. Oxford University Press, 26(23), pp. 4668–4679.
- Molotsky, E. *et al.* (2022) ‘Neuromuscular junction pathology is correlated with differential motor unit vulnerability in spinal and bulbar muscular atrophy’, *Acta Neuropathologica Communications*. BioMed Central, 10(1), pp. 1–22. doi: 10.1186/s40478-022-01402-y.
- Monk, K. R., Feltri, M. L. and Taveggia, C. (2015) ‘New insights on schwann cell development’, *Glia*, 63(8), pp. 1376–1393. doi: 10.1002/glia.22852.
- Morfini, G. A. *et al.* (2009) ‘Axonal transport defects in neurodegenerative diseases’, *Journal of Neuroscience*, 29(41), pp. 12776–12786. doi: 10.1523/JNEUROSCI.3463-09.2009.
- Morfini, G. A. *et al.* (2012) ‘Chapter 8 - Axonal Transport’, in *Basic Neurochemistry: Principles of Molecular, Cellular, and Medical Neurobiology: Eighth Edition*. Elsevier Inc., pp. 146–164. doi: 10.1016/B978-0-12-374947-5.00008-0.
- Mueller, M. *et al.* (2022) ‘Impact of Limb Phenotype on Tongue Denervation Atrophy, Dysphagia Penetrance, and Survival Time in a Mouse Model of ALS’, *Dysphagia*. Springer US, 37(6), pp. 1777–1795. doi: 10.1007/s00455-022-10442-4.
- Murray, L. M. *et al.* (2008) ‘Selective vulnerability of motor neurons and dissociation of pre- and post-synaptic pathology at the neuromuscular junction in mouse models of spinal muscular atrophy’, *Human Molecular Genetics*, 17(7), pp. 949–962. doi: 10.1093/hmg/ddm367.
- Murray, L. M. *et al.* (2010) ‘Pre-symptomatic development of lower motor neuron connectivity in a mouse model of severe spinal muscular atrophy’, *Human Molecular Genetics*, 19(3), pp. 420–433. doi: 10.1093/hmg/ddp506.
- Murray, L. M. *et al.* (2013) ‘Defects in neuromuscular junction remodelling in the *Smn2B*^{-/-} mouse model of spinal muscular atrophy’, *Neurobiology of disease*. Elsevier, 49, pp. 57–67.
- Murray, L. M., Talbot, K. and Gillingwater, T. H. (2010) ‘Review: Neuromuscular synaptic vulnerability in motor neurone disease: Amyotrophic lateral sclerosis and spinal muscular atrophy’, *Neuropathology and Applied Neurobiology*, 36(2), pp. 133–156. doi: 10.1111/j.1365-2990.2010.01061.x.
- Musarella, M. *et al.* (2006) ‘Expression of Nav1.6 sodium channels by Schwann cells at neuromuscular junctions: role in the motor endplate disease phenotype’, *Glia*. Wiley Online Library, 53(1), pp. 13–23.
- Nakamura-shindo, K. and Sakai, K. (2020) ‘Accumulation of phosphorylated TDP-43 in the

cytoplasm of Schwann cells in a case of sporadic amyotrophic lateral sclerosis', *Case Report*. (April), pp. 606–610. doi: 10.1111/neup.12673.

Narai, H. *et al.* (2009) 'Early detachment of neuromuscular junction proteins in ALS mice with SODG93A mutation', *Neurology International*, 1(1), p. 16. doi: 10.4081/ni.2009.e16.

Neve, A. *et al.* (2016) 'Central and peripheral defects in motor units of the diaphragm of spinal muscular atrophy mice', *Molecular and Cellular Neuroscience*. Elsevier, 70, pp. 30–41.

Nguyen, H. P., Van Broeckhoven, C. and van der Zee, J. (2018) 'ALS Genes in the Genomic Era and their Implications for FTD', *Trends in Genetics*, 34(6), pp. 404–423. doi: <https://doi.org/10.1016/j.tig.2018.03.001>.

Niimi, S. *et al.* (1979) 'Some basic studies on recording and processing techniques in EMG data assessment', *Ann. Bull. RILP*, 13, pp. 27–41.

Nijssen, J., Comley, L. H. and Hedlund, E. (2017) 'Motor neuron vulnerability and resistance in amyotrophic lateral sclerosis', *Acta Neuropathologica*. Springer Berlin Heidelberg, 133(6), pp. 863–885. doi: 10.1007/s00401-017-1708-8.

O'Malley, J. P., Waran, M. T. and Balice-Gordon, R. J. (1999) 'In vivo observations of terminal Schwann cells at normal, denervated, and reinnervated mouse neuromuscular junctions', *Journal of Neurobiology*, 38(2), pp. 270–286. doi: 10.1002/(SICI)1097-4695(19990205)38:2<270::AID-NEU9>3.0.CO;2-F.

O'Rourke, J. G. *et al.* (2015) 'C9orf72 BAC Transgenic Mice Display Typical Pathologic Features of ALS/FTD', *Neuron*. Elsevier, 88(5), pp. 892–901. doi: 10.1016/j.neuron.2015.10.027.

Oda, K. (1984) 'Age changes of motor innervation and acetylcholine receptor distribution on human skeletal muscle fibres', *Journal of the Neurological Sciences*, 66(2–3), pp. 327–338. doi: 10.1016/0022-510X(84)90021-2.

Oda, K. (1985) 'The Relationship between Motor Endplate Size and Muscle Fiber Diameter in Different Muscle Groups of the Rat', *Japanese Journal of Physiology*, 35, pp. 1091–1095.

Ogata, T. (1988) 'Structure of Motor Endplates in the Different Fiber Types of Vertebrate Skeletal Muscles', *Archives of Histology and Cytology*, 51(5), pp. 385–424. doi: 10.1679/aohc.51.385.

Okut, H. *et al.* (1999) 'Genotypic expression with different ages of dams: III. Weight traits of sheep1', *Journal of Animal Science*, 77(9), pp. 2372–2378. doi: 10.2527/1999.7792372x.

Ou, S. H. *et al.* (1995) 'Cloning and characterization of a novel cellular protein, TDP-43, that binds to human immunodeficiency virus type 1 TAR DNA sequence motifs.', *Journal of virology*, 69(6), pp. 3584–3596. doi: 10.1128/jvi.69.6.3584-3596.1995.

Pacelli, C. *et al.* (2015) 'Elevated mitochondrial bioenergetics and axonal arborization size are key contributors to the vulnerability of dopamine neurons', *Current Biology*. Elsevier, 25(18),

pp. 2349–2360.

Pamphlett, R., Kril, J. and Hng, T. M. (1995) ‘Motor neuron disease: a primary disorder of corticomotoneurons?’, *Muscle & Nerve: Official Journal of the American Association of Electrodiagnostic Medicine*. Wiley Online Library, 18(3), pp. 314–318.

Paul, A. C. (2001) ‘Muscle length affects the architecture and pattern of innervation differently in leg muscles of mouse, guinea pig, and rabbit compared to those of human and monkey muscles’, *Anatomical Record*, 262(3), pp. 301–309. doi: 10.1002/1097-0185(20010301)262:3<301::AID-AR1045>3.0.CO;2-H.

Pawson, P. A., Grinnell, A. D. and Wolowske, B. (1998) ‘Quantitative freeze-fracture analysis of the frog neuromuscular junction synapse - II. Proximal-distal measurements’, *Journal of Neurocytology*, 27(5), pp. 379–391. doi: 10.1023/A:1006995010453.

Peggion, C. *et al.* (2017) ‘Absolute quantification of myosin heavy chain isoforms by selected reaction monitoring can underscore skeletal muscle changes in a mouse model of amyotrophic lateral sclerosis’, *Analytical and Bioanalytical Chemistry*. Analytical and Bioanalytical Chemistry, 409(8), pp. 2143–2153. doi: 10.1007/s00216-016-0160-2.

Penfield, W. and Boldrey, E. (1937) ‘Somatic motor and sensory representation in the cerebral cortex of man as studied by electrical stimulation’, *Brain*. Citeseer, 60(4), pp. 389–443.

Périé, S., St Guily, J. L. and Sebillé, A. (1999) ‘Comparison of perinatal and adult multi-innervation in human laryngeal muscle fibers’, *Annals of Otolaryngology, Rhinology & Laryngology*. SAGE Publications Sage CA: Los Angeles, CA, 108(7), pp. 683–688.

Personius, K. E. and Sawyer, R. P. (2005) ‘Terminal Schwann cell structure is altered in diaphragm of mdx mice’, *Muscle and Nerve*, 32(5), pp. 656–663. doi: 10.1002/mus.20405.

Picchiarelli, G. *et al.* (2019) ‘FUS-mediated regulation of acetylcholine receptor transcription at neuromuscular junctions is compromised in amyotrophic lateral sclerosis’, *Nature Neuroscience*. Springer US, 22(11), pp. 1793–1805. doi: 10.1038/s41593-019-0498-9.

Picher-Martel, V. *et al.* (2016) ‘From animal models to human disease: A genetic approach for personalized medicine in ALS’, *Acta Neuropathologica Communications*. Acta Neuropathologica Communications, 4(1), pp. 1–29. doi: 10.1186/s40478-016-0340-5.

Pickles, S. *et al.* (2016) ‘ALS-linked misfolded SOD1 species have divergent impacts on mitochondria’, *Acta Neuropathologica Communications*, 4(1), p. 43. doi: 10.1186/s40478-016-0313-8.

DI Pietro, L. *et al.* (2017) ‘Potential therapeutic targets for ALS: MIR206, MIR208b and MIR499 are modulated during disease progression in the skeletal muscle of patients’, *Scientific Reports*. Springer US, 7(1), pp. 1–11. doi: 10.1038/s41598-017-10161-z.

Pikatzia-Menoio, O. *et al.* (2021) ‘The skeletal muscle emerges as a new disease target in amyotrophic lateral sclerosis’, *Journal of Personalized Medicine*, 11(7), pp. 1–33. doi: 10.3390/jpm11070671.

- Porter, R. and Lemon, R. (1995) *Corticospinal Function and Voluntary Movement*. Oxford University Press. doi: 10.1093/acprof:oso/9780198523758.001.0001.
- Prakash, Y. S. *et al.* (1996) 'Morphology of diaphragm neuromuscular junctions on different fibre types', *Journal of Neurocytology*, 25(1), pp. 88–100. doi: 10.1007/bf02284788.
- Pun, S. *et al.* (2006) 'Selective vulnerability and pruning of phasic motoneuron axons in motoneuron disease alleviated by CNTF', *Nature Neuroscience*, 9(3), pp. 408–419. doi: 10.1038/nn1653.
- Quinn, R. (2005) 'Comparing rat's to human's age: how old is my rat in people years?', *Nutrition*. Elsevier Limited, 21(6), p. 775.
- Ravits, J. M. and La Spada, A. R. (2009) 'Als motor phenotype heterogeneity, focality, and spread: Deconstructing motor neuron degenerationsymbol', *Neurology*, 73(10), p. 805. doi: 10.1212/WNL.0b013e3181b6bbbd.
- Reddy, L. V *et al.* (2003) 'Glial Cells Maintain Synaptic Structure and Function and Promote Development of the Neuromuscular Junction In Vivo', *Neuron*, 40(3), pp. 563–580. doi: [https://doi.org/10.1016/S0896-6273\(03\)00682-2](https://doi.org/10.1016/S0896-6273(03)00682-2).
- Renton, A. E. *et al.* (2011) 'A hexanucleotide repeat expansion in C9ORF72 is the cause of chromosome 9p21-linked ALS-FTD', *Neuron*, 72(2), pp. 257–268. doi: 10.1016/j.neuron.2011.09.010.
- Renton, A. E., Chiò, A. and Traynor, B. J. (2014) 'State of play in amyotrophic lateral sclerosis genetics', *Nature Neuroscience*. Nature Publishing Group, 17(1), pp. 17–23. doi: 10.1038/nn.3584.
- Renzini, A. *et al.* (2023) 'Sex and HDAC4 Differently Affect the Pathophysiology of Amyotrophic Lateral Sclerosis in SOD1-G93A Mice', *International Journal of Molecular Sciences*, 24(1). doi: 10.3390/ijms24010098.
- Reynolds, M. L. and Woolf, C. J. (1992) 'Terminal Schwann cells elaborate extensive processes following denervation of the motor endplate', *Journal of Neurocytology*, 21(1), pp. 50–66. doi: 10.1007/BF01206897.
- Richmond, F. J. R. and Abrahams, V. C. (1975) 'Morphology and enzyme histochemistry of dorsal muscles of the cat neck', *Journal of Neurophysiology*, 38(6), pp. 1312–1321. doi: 10.1152/jn.1975.38.6.1312.
- Riemslogh, F. W. *et al.* (2021) 'Inducible expression of human C9ORF72 36x G 4 C 2 hexanucleotide repeats is sufficient to cause RAN translation and rapid muscular atrophy in mice', *Disease Models & Mechanisms*, (January), p. dmm.044842. doi: 10.1242/dmm.044842.
- Riva, N. *et al.* (2022) 'Phosphorylated TDP-43 aggregates in peripheral motor nerves of patients with amyotrophic lateral sclerosis', (145), pp. 276–284.
- Robinson, D. A. (1970) 'Oculomotor unit behavior in the monkey.', *Journal of*

neurophysiology, 33(3), pp. 393–403.

Rogers, D. C. *et al.* (1997) ‘Behavioral and functional analysis of mouse phenotype: SHIRPA, a proposed protocol for comprehensive phenotype assessment’, *Mammalian Genome*. Springer, 8(10), pp. 711–713.

Rogers, R. S. *et al.* (2017) ‘Impaired mitophagy plays a role in denervation of neuromuscular junctions in ALS mice’, *Frontiers in Neuroscience*. Frontiers Media SA, 11, p. 473.

Roman, W. and Gomes, E. R. (2018) ‘Nuclear positioning in skeletal muscle’, *Seminars in Cell and Developmental Biology*. Elsevier Ltd, 82, pp. 51–56. doi: 10.1016/j.semcdb.2017.11.005.

Rosen, D. R. *et al.* (1993) ‘Mutations in Cu/Zn superoxide dismutase gene are associated with familial amyotrophic lateral sclerosis’, *Nature*, 362(6415), pp. 59–62. doi: 10.1038/362059a0.

Rosenblum, L. T. and Trotti, D. (2017) ‘EAAT2 and the molecular signature of amyotrophic lateral sclerosis’, *Advances in Neurobiology*, 16, pp. 117–136. doi: 10.1007/978-3-319-55769-4_6.

Rothstein, J. D. *et al.* (1993) ‘Chronic inhibition of glutamate uptake produces a model of slow neurotoxicity.’, *Proceedings of the National Academy of Sciences*. National Acad Sciences, 90(14), pp. 6591–6595.

Rouaux, C. *et al.* (2007) ‘Sodium valproate exerts neuroprotective effects in vivo through CREB-binding protein-dependent mechanisms but does not improve survival in an amyotrophic lateral sclerosis mouse model’, *Journal of Neuroscience*. Soc Neuroscience, 27(21), pp. 5535–5545.

Rowland, L. P. (2001) ‘How Amyotrophic Lateral Sclerosis Got Its Name’, *Archives of Neurology*, 58(3), pp. 512–515. doi: 10.1001/archneur.58.3.512.

Roy, S. *et al.* (2005) ‘Axonal transport defects: A common theme in neurodegenerative diseases’, *Acta Neuropathologica*, 109(1), pp. 5–13. doi: 10.1007/s00401-004-0952-x.

Ruskamo, S. *et al.* (2017) ‘Molecular mechanisms of Charcot-Marie-Tooth neuropathy linked to mutations in human myelin protein P2’, *Scientific Reports*. Nature Publishing Group UK London, 7(1), p. 6510.

Sanes, J. R. and Lichtman, J. W. (1999) ‘Development of the Vertebrate Neuromuscular Junction’, pp. 389–442.

Saporta, M. A. (2014) ‘Charcot-Marie-Tooth disease and other inherited neuropathies’, *CONTINUUM: Lifelong Learning in Neurology*. LWW, 20(5), pp. 1208–1225.

Sasaki, S. *et al.* (1988) ‘Swelling of neuronal processes in motor neuron disease’, *Neurology*. AAN Enterprises, 38(7), p. 1114.

Scekic-Zahirovic, J. *et al.* (2017) ‘Motor neuron intrinsic and extrinsic mechanisms contribute to the pathogenesis of FUS-associated amyotrophic lateral sclerosis’, *Acta Neuropathologica*. Springer Berlin Heidelberg, 133(6), pp. 887–906. doi: 10.1007/s00401-017-1687-9.

- Schaefer, A. M., Sanes, J. R. and Lichtman, J. W. (2005) 'A compensatory subpopulation of motor neurons in a mouse model of amyotrophic lateral sclerosis', *Journal of Comparative Neurology*, 490(3), pp. 209–219. doi: 10.1002/cne.20620.
- Schmidt, M. L. *et al.* (1987) 'Phosphate dependent and independent neurofilament epitopes in the axonal swellings of patients with motor neuron disease and controls.', *Laboratory Investigation; A Journal of Technical Methods and Pathology*, 56(3), pp. 282–294.
- Scotter, E. L., Chen, H. J. and Shaw, C. E. (2015) 'TDP-43 Proteinopathy and ALS: Insights into Disease Mechanisms and Therapeutic Targets', *Neurotherapeutics*, 12(2), pp. 352–363. doi: 10.1007/s13311-015-0338-x.
- Seals, R. M. *et al.* (2017) 'Occupational formaldehyde and amyotrophic lateral sclerosis', *European Journal of Epidemiology*. Springer, 32, pp. 893–899.
- Sephton, C. F. *et al.* (2010) 'TDP-43 is a developmentally regulated protein essential for early embryonic development', *Journal of Biological Chemistry*. © 2010 ASBMB. Currently published by Elsevier Inc; originally published by American Society for Biochemistry and Molecular Biology., 285(9), pp. 6826–6834. doi: 10.1074/jbc.M109.061846.
- Shan, X. *et al.* (2010) 'Altered distributions of Gemini of coiled bodies and mitochondria in motor neurons of TDP-43 transgenic mice', *Proceedings of the National Academy of Sciences of the United States of America*, 107(37), pp. 16325–16330. doi: 10.1073/pnas.1003459107.
- Sharma, A. *et al.* (2016) 'ALS-associated mutant FUS induces selective motor neuron degeneration through toxic gain of function', *Nature Communications*. Nature Publishing Group, 7. doi: 10.1038/ncomms10465.
- Sherrington, C. S. (1929) 'Ferrier lecture. —Some functional problems attaching to convergence', *Proceedings of the Royal Society of London. Series B, Containing Papers of a Biological Character*. The Royal Society London, 105(737), pp. 332–362.
- Siklós, L. *et al.* (1996) 'Ultrastructural evidence for altered calcium in motor nerve terminals in amyotrophic lateral sclerosis', *Annals of Neurology*. Wiley Online Library, 39(2), pp. 203–216.
- Slater, C. R. (2008) 'Structural factors influencing the efficacy of neuromuscular transmission', *Annals of the New York Academy of Sciences*, 1132, pp. 1–12. doi: 10.1196/annals.1405.003.
- Slater, C. R. (2015) 'The functional organization of motor nerve terminals', *Progress in neurobiology*. Elsevier, 134, pp. 55–103.
- Slater, C. R. (2017) 'The structure of human neuromuscular junctions: Some unanswered molecular questions', *International Journal of Molecular Sciences*, 18(10). doi: 10.3390/ijms18102183.
- Sleigh, J. N., Mech, A. M. and Schiavo, G. (2020) 'Developmental demands contribute to early neuromuscular degeneration in CMT2D mice', *Cell Death & Disease*. Nature Publishing Group, 11(7), pp. 1–10.

- Smith, I. W. *et al.* (2013) 'Terminal Schwann cells participate in the competition underlying neuromuscular synapse elimination', *Journal of Neuroscience*, 33(45), pp. 17724–17736. doi: 10.1523/JNEUROSCI.3339-13.2013.
- Smittkamp, S. E. *et al.* (2010) 'Measures of bulbar and spinal motor function, muscle innervation, and mitochondrial function in ALS rats', *Behavioural Brain Research*. Elsevier B.V., 211(1), pp. 48–57. doi: 10.1016/j.bbr.2010.03.007.
- Snyder-Warwick, A. K. *et al.* (2018) 'Hypothalamic Sirt1 protects terminal Schwann cells and neuromuscular junctions from age-related morphological changes', *Aging Cell*, 17(4). doi: 10.1111/acel.12776.
- So, E. *et al.* (2018) 'Mitochondrial abnormalities and disruption of the neuromuscular junction precede the clinical phenotype and motor neuron loss in hFUSWT transgenic mice', *Human Molecular Genetics*, 27(3), pp. 463–474. doi: 10.1093/hmg/ddx415.
- Sobue, G. *et al.* (1990) 'Phosphorylated high molecular weight neurofilament protein in lower motor neurons in amyotrophic lateral sclerosis and other neurodegenerative diseases involving ventral horn cells', *Acta Neuropathologica*. Springer, 79, pp. 402–408.
- Spaulding, E. L. *et al.* (2016) 'Synaptic deficits at neuromuscular junctions in two mouse models of Charcot–Marie–Tooth type 2d', *Journal of Neuroscience*. Soc Neuroscience, 36(11), pp. 3254–3267.
- Spreux-Varoquaux, O. *et al.* (2002) 'Glutamate levels in cerebrospinal fluid in amyotrophic lateral sclerosis: a reappraisal using a new HPLC method with oculometric detection in a large cohort of patients', *Journal of the Neurological Sciences*. Elsevier, 193(2), pp. 73–78.
- Stallings, N. R. *et al.* (2010) 'Progressive motor weakness in transgenic mice expressing human TDP-43', *Neurobiology of Disease*. Elsevier Inc., 40(2), pp. 404–414. doi: 10.1016/j.nbd.2010.06.017.
- Standring, S., Wiseman, S. and Brennan, P. (2019) *Gray's Surgical Anatomy*. Elsevier.
- Starritt, N. E., Kettle, S. A. J. and Glasby, M. A. (2011) 'Sutureless repair of the facial nerve using biodegradable glass fabric', *The Laryngoscope*. Wiley Online Library, 121(8), pp. 1614–1619.
- Talbot, K. (2009) 'Motor neuron disease', *Practical Neurology*, 9(5), pp. 303–309. doi: 10.1136/jnnp.2009.188151.
- Talbot, S. R. *et al.* (2019) 'Defining body-weight reduction as a humane endpoint: a critical appraisal', *Laboratory Animals*. SAGE Publications, 54(1), pp. 99–110. doi: 10.1177/0023677219883319.
- Tiryaki, E. and Horak, H. A. (2014) 'ALS and other motor neuron diseases', *CONTINUUM: Lifelong Learning in Neurology*. LWW, 20(5), pp. 1185–1207.
- Todd, K. J., Darabid, H. and Robitaille, R. (2010) 'Perisynaptic glia discriminate patterns of

- motor nerve activity and influence plasticity at the neuromuscular junction', *Journal of Neuroscience*. Soc Neuroscience, 30(35), pp. 11870–11882.
- Torres-Torrelo, J. *et al.* (2012) 'Glutamate modulates the firing rate in oculomotor nucleus motoneurons as a function of the recruitment threshold current', *The Journal of Physiology*. Wiley Online Library, 590(13), pp. 3113–3127.
- Torres-Torrelo, J., Torres, B. and Carrascal, L. (2014) 'Modulation of the input–output function by GABAA receptor-mediated currents in rat oculomotor nucleus motoneurons', *The Journal of Physiology*. Wiley Online Library, 592(22), pp. 5047–5064.
- Tosolini, A. P. and Sleight, J. N. (2017) 'Motor neuron gene therapy: lessons from spinal muscular atrophy for amyotrophic lateral sclerosis', *Frontiers in Molecular Neuroscience*. Frontiers Media SA, 10, p. 405.
- Tremblay, E., Martineau, É. and Robitaille, R. (2017) 'Opposite synaptic alterations at the neuromuscular junction in an ALS mouse model: When motor units matter', *Journal of Neuroscience*, 37(37), pp. 8901–8918. doi: 10.1523/JNEUROSCI.3090-16.2017.
- Tsujihata, M. *et al.* (1984) 'The motor end-plate fine structure and ultrastructural localization of acetylcholine receptors in amyotrophic lateral sclerosis', *Muscle & Nerve*, 7(3), pp. 243–249. doi: 10.1002/mus.880070310.
- Turgeon, V. L. *et al.* (1998) 'Thrombin perturbs neurite outgrowth and induces apoptotic cell death in enriched chick spinal motoneuron cultures through caspase activation', *Journal of Neuroscience*. Soc Neuroscience, 18(17), pp. 6882–6891.
- Turner, B. J., Lopes, E. C. and Cheema, S. S. (2003) 'Neuromuscular accumulation of mutant superoxide dismutase 1 aggregates in a transgenic mouse model of familial amyotrophic lateral sclerosis', *Neuroscience Letters*, 350(2), pp. 132–136. doi: 10.1016/S0304-3940(03)00893-0.
- Turner, M. R. *et al.* (2005) 'Distinct cerebral lesions in sporadic and 'D90A'SOD1 ALS: studies with [11C] flumazenil PET', *Brain*. Oxford University Press, 128(6), pp. 1323–1329.
- Turner, M. R. *et al.* (2013) 'Autoimmune disease preceding amyotrophic lateral sclerosis', *Neurology*, 81(14), pp. 1222 LP – 1225. doi: 10.1212/WNL.0b013e3182a6cc13.
- Ulfhake, B. and Kellerth, J. (1981) 'A quantitative light microscopic study of the dendrites of cat spinal α -motoneurons after intracellular staining with horseradish peroxidase', *Journal of Comparative Neurology*. Wiley Online Library, 202(4), pp. 571–583.
- Valdez, G. *et al.* (2010) 'Attenuation of age-related changes in mouse neuromuscular synapses by caloric restriction and exercise', 107(33), pp. 14863–14868. doi: 10.1073/pnas.1002220107.
- Valdez, G. *et al.* (2012) 'Shared resistance to aging and als in neuromuscular junctions of specific muscles', *PLoS ONE*, 7(4). doi: 10.1371/journal.pone.0034640.
- Valdez, G. (2020) 'Formation and maturation of neuromuscular junctions', in *Patterning and*

Cell Type Specification in the Developing CNS and PNS. 2nd edn. Elsevier Inc., pp. 157–184. doi: 10.1016/b978-0-12-814405-3.00008-4.

Verma, S. *et al.* (2022) ‘Neuromuscular Junction Dysfunction in Amyotrophic Lateral Sclerosis’, *Molecular Neurobiology*. Springer US, 59(3), pp. 1502–1527. doi: 10.1007/s12035-021-02658-6.

Versluys, L. *et al.* (2022) ‘Expanding the TDP-43 Proteinopathy Pathway From Neurons to Muscle: Physiological and Pathophysiological Functions’, *Frontiers in Neuroscience*, 16(February), pp. 1–22. doi: 10.3389/fnins.2022.815765.

Vincent, A. (2002) ‘Unravelling the pathogenesis of myasthenia gravis’, *Nature Reviews Immunology*. Nature Publishing Group UK London, 2(10), pp. 797–804.

Vinsant, S. *et al.* (2013a) ‘Characterization of early pathogenesis in the SOD1G93A mouse model of ALS: Part I, background and methods’, *Brain and Behavior*, 3(4), pp. 335–350. doi: 10.1002/brb3.143.

Vinsant, S. *et al.* (2013b) ‘Characterization of early pathogenesis in the SOD1G93A mouse model of ALS: Part II, results and discussion’, *Brain and Behavior*, 3(4), pp. 431–457. doi: 10.1002/brb3.142.

Vogler, T. O. *et al.* (2018) ‘TDP-43 and RNA form amyloid-like myo-granules in regenerating muscle’, *Nature*, 563(7732), pp. 508–513. doi: 10.1038/s41586-018-0665-2.

De vos, K. J. *et al.* (2007) ‘Familial amyotrophic lateral sclerosis-linked SOD1 mutants perturb fast axonal transport to reduce axonal mitochondria content’, *Human Molecular Genetics*, 16(22), pp. 2720–2728. doi: 10.1093/hmg/ddm226.

Walker, A. K. *et al.* (2015) ‘Functional recovery in new mouse models of ALS/FTLD after clearance of pathological cytoplasmic TDP-43’, *Acta Neuropathologica*. Springer Berlin Heidelberg, 130(5), pp. 643–660. doi: 10.1007/s00401-015-1460-x.

Wang, M. D. *et al.* (2017) ‘Identification of risk factors associated with onset and progression of amyotrophic lateral sclerosis using systematic review and meta-analysis’, *NeuroToxicology*. Elsevier B.V., 61, pp. 101–130. doi: 10.1016/j.neuro.2016.06.015.

Wang, W. *et al.* (2013) ‘The ALS disease-associated mutant TDP-43 impairs mitochondrial dynamics and function in motor neurons’, *Human Molecular Genetics*, 22(23), pp. 4706–4719. doi: 10.1093/hmg/ddt319.

Weber, K. and Pearce, D. A. (2013) ‘Large animal models for Batten disease: a review’, *Journal of Child Neurology*. SAGE Publications Sage CA: Los Angeles, CA, 28(9), pp. 1123–1127.

Wegorzewska, I. *et al.* (2009) ‘TDP-43 mutant transgenic mice develop features of ALS and frontotemporal lobar degeneration’, *Proceedings of the National Academy of Sciences of the United States of America*, 106(44), pp. 18809–18814. doi: 10.1073/pnas.0908767106.

- Wieczorek, D. F. *et al.* (1985) 'Co-expression of multiple myosin heavy chain genes, in addition to a tissue-specific one, in extraocular musculature.', *The Journal of Cell Biology*, 101(2), pp. 618–629.
- Wilbourn, A. J. (2000) 'The split hand syndrome', *Muscle and Nerve*, 23(1), p. 138. doi: 10.1002/(SICI)1097-4598(200001)23:1<138::AID-MUS22>3.0.CO;2-7.
- Wilbourn, A. J. and Sweeney, P. J. (1994) 'Dissociated wasting of medial and lateral hand muscles with motor neuron disease', *Canadian Journal of Neurological Sciences*, 21(Suppl 2), p. S9.
- Williamson, T. L. and Cleveland, D. W. (1999) 'Slowing of axonal transport is a very early event in the toxicity of ALS-linked SOD1 mutants to motor neurons', *Nature neuroscience*. Nature Publishing Group, 2(1), pp. 50–56.
- Wils, H. *et al.* (2010) 'TDP-43 transgenic mice develop spastic paralysis and neuronal inclusions characteristic of ALS and frontotemporal lobar degeneration', *Proceedings of the National Academy of Sciences of the United States of America*, 107(8), pp. 3858–3863. doi: 10.1073/pnas.0912417107.
- Winter, F. De *et al.* (2006) 'The expression of the chemorepellent Semaphorin 3A is selectively induced in terminal Schwann cells of a subset of neuromuscular synapses that display limited anatomical plasticity and enhanced vulnerability in motor neuron disease', *Molecular and Cellular Neuroscience*, 32(1–2), pp. 102–117. doi: 10.1016/j.mcn.2006.03.002.
- Wohlsein, P. *et al.* (2012) 'Spontaneous degenerative polioencephalomyelopathy in feeder pigs--a new motor neuron disease?', *Berliner und Munchener tierarztliche Wochenschrift*, 125(11–12), pp. 520–528.
- Wokke, J. H. J. *et al.* (1990) 'Morphological changes in the human end plate with age', *Journal of the Neurological Sciences*, 95(3), pp. 291–310. doi: 10.1016/0022-510X(90)90076-Y.
- Wood, S. J. and Slater, C. R. (2001) 'Safety factor at the neuromuscular junction', *Progress in Neurobiology*, 64(4), pp. 393–429. doi: 10.1016/S0301-0082(00)00055-1.
- Worne, F. (2011) 'Color Atlas of Veterinary Anatomy. Volume 3: the dog and cat', *Australian Veterinary Journal*, 5(89), p. 159.
- Woschitz, V. *et al.* (2022) 'Mouse models of SMA show divergent patterns of neuronal vulnerability and resilience', *Skeletal Muscle*. BioMed Central, pp. 1–20. doi: 10.1186/s13395-022-00305-9.
- Xu, Y. F. *et al.* (2010) 'Wild-type human TDP-43 expression causes TDP-43 phosphorylation, mitochondrial aggregation, motor deficits, and early mortality in transgenic mice', *Journal of Neuroscience*, 30(32), pp. 10851–10859. doi: 10.1523/JNEUROSCI.1630-10.2010.
- Yamanaka, K. *et al.* (2008) 'Astrocytes as determinants of disease progression in inherited amyotrophic lateral sclerosis', *Nature Neuroscience*. Nature Publishing Group US New York, 11(3), pp. 251–253.

- Yang, J.-F. *et al.* (2001) 'Schwann cells express active agrin and enhance aggregation of acetylcholine receptors on muscle fibers', *Journal of Neuroscience*. Soc Neuroscience, 21(24), pp. 9572–9584.
- Yerger, J. *et al.* (2022) 'Phenotype assessment for neurodegenerative murine models with ataxia and application to Niemann–Pick disease, type C1', *Biology Open*. The Company of Biologists Ltd, 11(4), p. bio059052.
- Yoshihara, T. *et al.* (1998) 'Ultrastructural and histochemical study of the motor end plates of the intrinsic laryngeal muscles in amyotrophic lateral sclerosis', *Ultrastructural Pathology*, 22(2), pp. 121–126. doi: 10.3109/01913129809032266.
- Young, P. *et al.* (2005) 'LNX1 is a perisynaptic Schwann cell specific E3 ubiquitin ligase that interacts with ErbB2', *Molecular and Cellular Neuroscience*. Elsevier, 30(2), pp. 238–248.
- Zenker, W., Snobl, D. and Boetschi, R. (1990) 'Multifocal innervation and muscle length: a morphological study on the role of myo-myonal junctions, fiber branching and multiple innervation in muscles of different size and shape', *Anatomy and Embryology*. Springer, 182, pp. 273–283.
- Zhou, Y. and Danbolt, N. C. (2014) 'Glutamate as a neurotransmitter in the healthy brain', *Journal of Neural Transmission*. Springer, 121, pp. 799–817.
- Zou, Z. Y. *et al.* (2017) 'Genetic epidemiology of amyotrophic lateral sclerosis: A systematic review and meta-analysis', *Journal of Neurology, Neurosurgery and Psychiatry*, 88(7), pp. 540–549. doi: 10.1136/jnnp-2016-315018.